FREIE UNIVERSITÄT BERLIN

INSTITUT FÜR GEOLOGISCHE WISSENSCHAFTEN

Evaluating Volatile Induced Surface Features on Vesta and Ceres

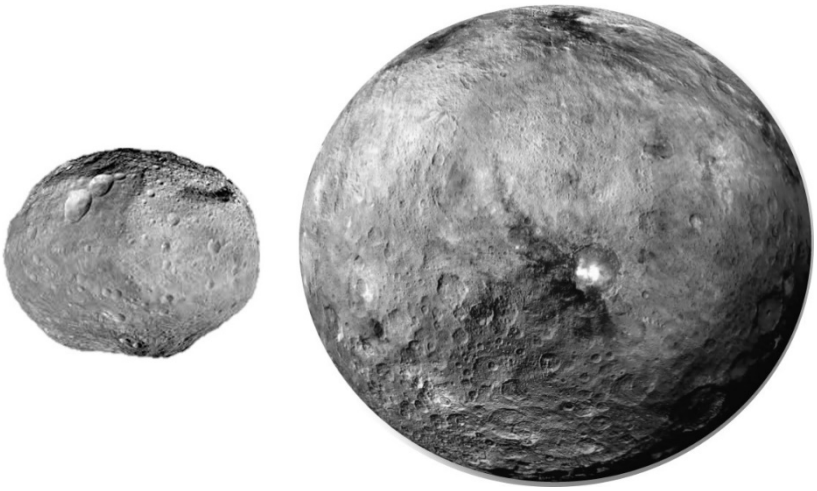

Dissertation
zur Erlangung des akademischen Grades eines
Doktors der Naturwissenschaften (Dr. rer. nat)

vorgelegt als kumulative Arbeit
am Fachbereich Geowissenschaften
der Freien Universität Berlin

Von

RUTU PAREKH

Berlin, 2021

About the cover images:

Mosaics of Vesta (left) and Ceres (right) prepared from the data acquired from the Dawn mission. Marcia impact crater is observed near the central latitudes on Vesta which consists of volatile bearing regolith material. On Ceres, Occator impact crater with bright spot is seen. The bright region is rich with brine salts which indicates excavation and deposition of subsurface materials. *Image source: Vesta- https://solarsystem.nasa.gov/news/725/vesta-and-ceres-what-we-knew-about-these-worlds-before-and-after-dawn/, Ceres- https://www.nationalgeographic.com/science/article/dwarf-planet-ceres-churns-briny-fluids-icy-volcanoes-nasa-dawn ; Image credit: NASA/JPL-Caltech/UCLA/MPS/DLR/IDA.*

Erstgutachter: Prof. Dr. Ralf Jaumann
Freie Universität Berlin
Institut für Geologische Wissenschaften
Arbeitsbereich Planetologie
Email: ralf.jaumann@fu-berlin.de

Zweitgutachter: Prof. Dr. Lena Noack
Freie Universität Berlin
Institut für Geologische Wissenschaften
Arbeitsbereich Geodynamik
Email: lena.noack@fu-berlin.de

Tag der Disputation: *15th March, 2022*

EIDESSTATTLICHE ERKLÄRUNG

Hiermit erkläre ich, dass ich die beigefügte Dissertation selbständig verfasst und keine anderen als die angegebenen Hilfsmittel genutzt habe.

Ich versichere weiterhin, dass ich die beigefügte Dissertation nur in diesem und keinem anderen Promotionsverfahren eingereicht habe und, dass diesem Promotionsverfahren keine endgültig gescheiterten Promotionsverfahren vorausgegangen sind.

Berlin, November 2021 Rutu Parekh

To,

Swati Parekh (moma)

Ashwin Parekh (pops)

श्रेयान्स्वधर्मो विगुणः परधर्मात्स्वनुष्ठितात् ।
स्वधर्मे निधनं श्रेयः परधर्मो भयावहः ॥३५॥
श्रीमद्भगवद्गीता, अध्याय ३

It is far better to live own destiny, dreams and nature imperfectly than to live an imitation of someone else's perfection.
Shrimad Bhagavat Gita, Chapter 3, verse 35

ACKNOWLEDGMENTS

Past 3 years have been one of the most evolving and unforgetting experiences of my life. During this roller coaster ride I had the privilege to visit new places, experienced different cultures, met some of the most amazing groups of people, learnt new scientific techniques and gained some valuable research opportunities. In true sense I was able to explore myself and expanded my skill sets both personally and professionally. All these experiences have truly enriched my journey which would not have been possible without constant encouragement, freedom, trust and support from my adviser Dr. Katharina Otto. I am deeply grateful to her for offering me a PhD position and stood strongly by me at every step. I am fortunate to be able to work with her and deeply appreciate countless discussion hours and professional advice. I am very much grateful to Prof. Dr. Ralf Jaumann for providing the opportunity to work with an international team and for sharing his valuable feedback on manuscripts and thesis. I am truly grateful for his patience, wisdom, unwavering support and being an inspiring mentor to me throughout this journey. Thank you!

I am also grateful to Prof. Dr. Lena Noack, Freie Universität Berlin, Institut für Geologische Wissenschaften, who kindly agreed to register me under her supervision and helped me to navigate through the committee formulation process. Following, I would also like to thank my entire doctoral committee.

My colleagues at Nachwusgruppe, David Haack for sharing his knowledge on history and Geology, Tanja Michalik for always adjusting the office hours despite challenges, Manuel Sachse for his 'coffee hours' wisdom and David Kappel for their discussion sessions. Your support and encouragement are implacable. I would like to extend my thanks to colleagues at planetary geology group Ernst Hauber, Katrin Stephan, Klaus-Dieter Matz, Stephan Schröder, Thomas Roatsch, Thomas Weigelt, Daniela Tirsch, Elke Kersten, Katrin Krohn, Stephan Elgner for their critical feedback, support on data processing and to always accommodate my last-minute requirements. I will not forget timely help from Claudia Hauschild and Plaul Stephanie with all the requests on visa processing. To all my friends at DLR, I would not have survived without your jokes, Flammenkuchen luncheon breaks, menza coffee discussions and many more unforgettable memories. Thank you Nasia, Sabrina, Max, Mika, Gianluigi. I am grateful to Solmaz Adeli who has become my go-to person in a very short time. I cannot imagine my venture without unconditional love and friendship I received from Indhu and Giulia.

My PhD journey is certainly incomplete without members of Europlanet Diversity Committee and my EPEC (Europlanet Early career) fellows. Since 2017, you have been part of my professional journey and it has been an absolute honor to work with them. I especially like to thank Prof. Dr. Victoria Pearson (chair) and Prof. Dr. Lena Noack (vice-chair) of the diversity committee who enlightened my knowledge related to diversity and inclusivity. I will certainly miss our gathering during the EPSC conferences. At EPEC committee, I got the opportunity to develop professional network and personal friendship with Indhu, Solmaz, Maike, Erica, Noah, Hans, Ana, Melinda, Joanna and entire EPEC network. Special thanks to Anita Heward and Maarten Roos for helping

me launch the ‘Motivational Journey’ series at EPEC diversity. My special thanks to Nigel Mason for providing an amazing opportunity to become part of Europlanet RI.

I would also like to thank the Dawn Team members, Carol Raymond, Julie Castillo-Rogez, Hanna Sizemore, Jennifer Scully, Debra Buczkowski, Christopher Russell for providing me with a friendly and helpful environment to discuss and improvise my work. Thank you DLR-DAAD for all the financial help and support.

I would not have managed to complete this thesis without love, unconditional support, emotional strength and care I received form Dr. Riddhi Patel. My special thanks to Parthiv Patel for helping me with proof reading and thesis formatting. I am truly thankful to Devangi Patel and Tejas Patel for regularly their evening calls and hysterical talks. I would like to extend my thanks to Shailendu Shroff, Suresh Chaudhary, Dhruval Patel for all the laughter, memories and fun-time we had over past 3 years. You all have become an essential part of my life and truly made Berlin home for me, I will adore this bond forever.

This PhD thesis is dedicated to my parents. I thank my mom for always being a strong and critical support, I would not have made this far without her. Pappa, thank you for being my silent cheerleader and supporting me under all circumstances. I thank both of them for teaching me important life lessons that helped me to land on my feet every time I fell. Thanks to my brother Akash, sister-in-law, Neetal and little nephew, Ayansh for being my stress buster in difficult times. I am particularly grateful to my nana (grandfather) for the joyful time we had, I miss him forever. Finally, last and very special acknowledgement to my then boyfriend and now fiancé, Harshil Shah, for being the emotional anchor throughout the courtship period, for being equally passionate about my dreams, for being an infinite source of endurance and to stand beside me during my busiest period. Thank you for filling this venture with love and support.

ABSTRACT

This work evaluates volatile induced surface features on Vesta and Ceres, two of the largest asteroids present within the asteroid belt. Both the planetary objects have similar surface acceleration but different regolith nature. Vesta is a relatively dry body whereas Ceres is rich with water ice. Direct measurement of volatiles is challenging due to harsh space conditions. However, when they are mixed with regolith, it produces peculiar landforms due to melting and/or sublimation and affects the overall evolution of a planetary body. Therefore, in this study the surface features which have direct or indirect link to ice and/or volatiles are examined in order to understand the volatile distribution. For this, regional and global scale investigations related to ponded deposits, pit chains and mass wasting analysis were conducted on Vesta and Ceres.

In the vicinity of Marcia and Cornelia impact craters of Vesta, two types of pond deposits were observed. Type 1 melt ponds have smooth, shallow deposits (depth <100 m) and are produced from the downslope movement of volatile bearing impact melt material. In contrast, type 2 dust ponds deposit consist of rough surface with ~200 m depth. These deposits are produced from the mobility of granular dust via infrequent high-amplitude seismic diffusivity and/or short-lived volatile outgassing activity. Due to low amounts of volatiles, the dusty material did not achieve kinetic sieving and thus do not attain typical smooth pond morphology. The findings of this study strongly support the hypothesis related to presence of low amounts of volatiles within Vesta's regolith.

To understand the volatile distribution on Ceres, the analysis of pit chains is carried out within three impact craters namely; Occator, Azacca and Urvara. Radial pit chain pattern of Occator is related to subsurface laccolith swelling of volatile rich cryomagmatic material. Linear pit chain clusters at floors of Azacca and Urvara are attributed to seasonal thermal contraction of ice layer present near the surface. Additionally, based on the pit chains depth the depicted average minimum thickness of regolith within Azacca, located at equator is ~200 m. On the contrary, within Occator and Urvara, the localized thickness is 30 m and 800 m, respectively, which is attributed to their distinct subsurface condition. Hence, this investigation favors the presence of ice layer within the subsurface layer and reveals that it is not distributed homogeneously on Ceres.

Lastly, the global scale comparative examination of the mass wasting process on Vesta and Ceres shows few common and some distinct characteristics. In general, granular sliding on Vesta and flow-like movements on Ceres are observed as dominant population. Further, slides and slumping features are restricted to mid-latitudes on Ceres which implies ice-rock fractionation at regional scale. Additionally, the volatile concentration also influences the deposit mobility on Vesta and Ceres and is analyzed by estimating height, width and effective coefficient of friction; *H/L*. The outcome suggests that deposits become immobile at shorter distances on Vesta in comparison to Ceres (avg. distance 4.5 km and 11.2 km, respectively). The difference in morphology and mobility is related to contrast in the amounts of volatiles present within regolith of both the bodies. While comparing the effective coefficient of friction of Vesta and Ceres with

planetary objects in outer solar system, the examination shows that lower temperature may have more influence on mobility.

Together, all the above-mentioned studies summarize the volatile induced surface landforms and provide evidences related to their distribution on Vesta and Ceres. This work also presents the first-time comparative investigation that reveals the influence of volatile content on the morphological characteristics of Vesta and Ceres.

KURZFASSUNG

In dieser Arbeit werden durch Volatile beeinflusste Oberflächenmerkmale auf Vesta und Ceres, zwei der größten Asteroiden im Asteroidengürtel, untersucht. Beide planetarischen Objekte haben eine ähnliche Oberflächenbeschleunigung, aber eine unterschiedliche Regolithbeschaffenheit. Vesta ist ein relativ trockener Körper, während Ceres reich an Wassereis ist. Die direkte Messung von volatilen Stoffen ist aufgrund der rauen Weltraumbedingungen schwierig. Wenn diese jedoch mit Regolithmaterial vermischt sind, entstehen durch Schmelzen/Sublimation auffällige Landformen und beeinflussen die Gesamtentwicklung eines Planetenkörpers. Daher werden in dieser Studie die Oberflächenmerkmale untersucht, die in direktem oder indirektem Zusammenhang mit Eis und/oder volatilen Stoffen stehen, um die Verteilung der Volatile zu verstehen. Zu diesem Zweck wurden auf Vesta und Ceres regionale und globale Untersuchungen zu Ablagerungen in Senken, zu pit chains und Massenbewegungen durchgeführt.

In der Nähe der Einschlagskrater Marcia und Cornelia auf Vesta wurden zwei Arten von Ablagerungen in Senken beobachtet. Senken des Typs 1 haben glatte, flache Ablagerungen (Tiefe <100 m) und entstehen durch die Abwärtsbewegung von flüchtigem geschmolzenem Material während Einschlägen. Im Gegensatz dazu weisen staubige Ablagerungen in Senken des Typs 2 eine raue Oberfläche und eine Tiefe von etwa 200 m auf. Diese Ablagerungen entstehen durch die Mobilität von granularem Staubregolith durch seltene seismische Diffusivität mit hoher Amplitude und/oder kurzlebige Ausgasungsaktivität von volatilen Stoffen. Aufgrund der geringen Mengen an volatilen Stoffen wurde das staubige Material nicht kinetisch gesiebt und weist daher keine typische glatte Senkenmorphologie auf. Die Ergebnisse dieser Studie stützen die Hypothese vom Vorhandensein geringer Mengen an volatilen Stoffen im Regolith von Vesta.

Um die Verteilung der flüchtigen Stoffe auf Ceres zu verstehen, wurde eine Analyse der pit chains in drei Einschlagskratern durchgeführt: Occator, Azacca und Urvara. Das Muster der radialen pit chains in Occator steht im Zusammenhang mit dem Aufquellen von volatilem, kryomagmatischem Material unter der Oberfläche des Lakkoliths. Die linearen pit chains auf dem Grund von Azacca und Urvara sind auf die saisonale thermische Kontraktion der oberflächennahen Eisschicht zurückzuführen. Die Tiefe der pit chains zeigt außerdem, dass die durchschnittliche Mindestdicke des Regoliths in Azacca am Äquator ca. 200 m beträgt. In Occator und Urvara hingegen liegt die Mächtigkeit bei 30 m bzw. 800 m, was auf die unterschiedlichen Bedingungen im Untergrund zurückzuführen ist. Diese Untersuchung spricht also für das Vorhandensein einer Eisschicht im Untergrund und zeigt, dass diese nicht homogen auf Ceres verteilt ist.

Schließlich zeigt die vergleichende Untersuchung der Massenbewegungen auf Vesta und Ceres im globalen Maßstab einige gemeinsame und einige unterschiedliche Merkmale. Im Allgemeinen dominiert auf Vesta das körnige Gleiten, während auf Ceres vor allem fließende Bewegungen zu beobachten sind. Außerdem sind Rutschungen und Einbrüche auf Ceres auf die mittleren Breiten beschränkt, was auf eine Fraktionierung von Gestein und Eis auf regionaler Ebene schließen lässt. Darüber hinaus beeinflusst die Konzentration volatiler Stoffe die Mobilität der Ablagerungen auf

Vesta und Ceres und wird durch Schätzung von Höhe, Breite und effektivem Reibungskoeffizienten (*H/L*) analysiert. Die Ergebnisse deuten darauf hin, dass die Ablagerungen auf Vesta im Vergleich zu Ceres bei kürzeren Entfernungen unbeweglich werden (durchschnittliche Entfernung 4,5 km bzw. 11,2 km). Der Unterschied in der Morphologie und Mobilität hängt mit den unterschiedlichen Mengen an flüchtigen Stoffen zusammen, die im Regolith beider Körper vorhanden sind. Beim Vergleich der effektiven Reibungskoeffizienten von Vesta und Ceres mit planetarischen Objekten im äußeren Sonnensystem zeigt die Untersuchung, dass eine niedrigere Temperatur einen größeren Einfluss auf die Mobilität haben kann.

Alle oben genannten Studien fassen die durch Volatile beeinflussten Oberflächenformen zusammen und liefern Beweise für ihre Verteilung von Volatilen auf Vesta und Ceres. Diese Arbeit stellt auch die erste vergleichende Untersuchung dar, die den Einfluss des Gehalts an volatilen Stoffen auf die morphologischen Eigenschaften von Vesta und Ceres aufzeigt.

TABLE OF CONTENTS

1. INTRODUCTION

1.1 Motivation

Every planetary object in the solar system is rich in various geological impressions and chemical composition regardless of their size or location. The upper layer of all planetary bodies has undergone extensive resurfacing events after their formation and possess some distinct geological characteristics. Understanding geological processes which can lead to variations in the physical and chemical properties is key to interpret the evolution of planetary systems. In the solar system, asteroids are considered as small, rocky, airless bodies which are neither planets nor natural satellites. However, they are suspected as remnants of planetary evolution and contain the record of earliest composition of solar nebula in which planets are formed. Therefore, this thesis is focused on the surface investigation of (4) Vesta and (1) Ceres, two of the exceptional asteroids located within inner solar system.

Some of the most commonly observed geological process includes impact cratering, volcanism, mass wasting processes and various types of fracturing events, all of which have the capability to modify the surface of asteroids at a global scale. These processes have successfully addressed the relation of the surface geology and the composition, interior and planetary evolution of the bodies. For instance, the huge impact basin Rheasilvia on asteroid Vesta has blanketed the entire southern region with its ejecta and reshaped the surface of Vesta (Thomas et al., 1997; Otto et al., 2019, Jaumann et al., 2012; Schenk et al., 2012), whereas the distribution, mobility and morphology of the mass movements is proven to be closely related to the presence of ice in subsurface on dwarf-planet Ceres (Schmidt et al., 2017; Chilton et al., 2019; Hughson et al., 2018; Parekh et al., 2021a).

Such geological events not only influence the shape and size of the body, but also modify the thermal attributes of the surfaces. Sudden temperature rise induced by impacts or mass motion invoke the release of H_2O ice and other volatiles trapped within subsurface. The direct observation of volatiles can be challenging since they sublimate at heliocentric distances of about 3 AU or less when present on an airless planetary surface, however, they can be detected using reflectance spectroscopy. One of the aspects of the volatile related investigation is to find and establish the relation between volatile degassing and planetary landforms which is indicative of the involvement of H_2O ice (Schmidt et al., 2017; Otto et al., 2019; Sizemore et al., 2018; Denevi et al., 2012). Knowledge of volatile content and composition on small planetary bodies is crucial to determine the source of water on Earth (Michel et al., 2015) and within the extraterrestrial objects for future human activities in space as well as the formation of life in our solar system.

NASA's Dawn mission has explored Vesta and Ceres and acquired high-resolution images as well as spectral images (Russell and Raymond, 2011). The Framing camera (FC) on board the spacecraft (Sierks et al., 2011) has revealed surface dichotomy on both Vesta and Ceres. The topographic data generated from the stereopairs images of FC exhibits large scale elevation difference within landscapes on Vesta (Jaumann et al., 2012). Additionally, clusters of pitted terrain

(Denevi et al., 2012) and gullies formation (Scully et al., 2015) suspected localized involvement of volatile activities. At the mid latitudes of Ceres, the crater Occator gained particular attention due to its young age (Nathues et al., 2020) and bright surface spots (Nathues et al., 2015; Buczkowski et al., 2018). Based on the spectral analysis and study of volatile related surface impressions, subsurface brine reservoir beneath Occator is suspected on Ceres (Scully et al., 2020; Schmidt et al., 2020, Schenk et al., 2020; De Sanctis et al., 2020).

Using such studies as a base, it reasonable to implicate that H_2O ice and/or other volatiles plays a crucial role in material transportation and eventually alter the surface of asteroids. Thus, keeping this as a central objective, this thesis summarizes diverse volatile related surface expressions present on Vesta and Ceres. The outcome of this study not only emphasize the association of volatiles with the geomorphology but also provide measures to relate surface impressions with regolith composition. A similar approach can also be carried out for other planetary bodies. In addition, comparative studies of planetary bodies also show promising result. For example, the surfaces of Vesta and Ceres are similar in terms of the geological events that shape them (e.g. mass wasting, impact cratering) and their gravitational acceleration, but the geomorphology and mobility are contrasting due to different regolith properties and bulk compositions. Comparing and understanding the involvement of volatiles in geological activities provides the opportunity to constrain the sources and link abundance of water ice within the asteroid belt and bares the potential to be expanded to other planetary bodies in solar system. Since water is an import element for life, studying volatile influenced geological events are therefore provide significant possibility to sustain life on extra-terrestrial objects.

1.2 Outline of thesis

This cumulative dissertation consists of seven further chapters. In Chapter **2** the general context, including the scientific background on small bodies, asteroids and the Dawn mission as well as asteroid Vesta and dwarf planet Ceres is introduced. The following Chapter **3**, includes brief knowledge of volatile related morphological features and their geological background in association with extraterrestrial objects. Chapter **4** describes various type of data utilized from the Dawn mission in order to achieve the objectives. The following three chapters (Chapters **5, 6, 7**) includes the original research papers published and/or submitted in peer-reviewed journals (as described below). In last Chapter **8**, the summary of all three papers and their conclusion is derived. All three research papers are stand-alone articles, and therefore contain individual introduction and conclusions. As a first authors of all three papers, I selected the study area, reviewed relevant literature, utilized the required data, approach the methodology accordingly, analyzed data, interpret the results and derived conclusion. Individual contribution of the co-authors is described below.

Chapter **5** contains paper published as R. Parekh, K. A. Otto, K.D. Matz, R. Jaumann, K. Krohn, T. Roatsch, E. Kersten, S. Elgner, C. T. Russell, C. A. Raymond (2021b), Formation of ejecta and dust pond deposits on asteroid Vesta. *Journal of Geophysical Research: Planets*, doi: 10.1029/2021JE006873. For these study surface data of the Moon and small bodies such as Eros,

Itokawa is processed by K.D. Matz, K. A. Otto and R. Jaumann participated in discussion and in draft review, C.T. Russell reviewed the language and grammatical errors. The paper describes investigation related to ponded features on Vesta and further highlight their morphological similarities and differences with ponded candidate observed on Eros, Itokawa and the Moon.

Chapter **6** represents a paper submitted as R. Parekh, K. A. Otto, R. Jaumann, E. Hauber, C.T Russell, C.A. Raymond. Small-scale pit chains on Ceres and their relation with surface regolith, submitted to *Icarus*. K. A. Otto provided guidance, R. Jaumann and E. Hauber participated in discussion, C.T. Russell reviewed grammatical errors. This paper focuses on the distribution of pit chains present on the crater floor of Occator, Azacca and Urvara on Ceres. This paper establish link between subsurface endogenic activity with the pit chains on Ceres. Further, the pit chain dimensions (depth, length, width) reveals the thickness heterogeneity of surface regolith on Ceres.

Chapter **7** includes a paper published as R. Parekh, K. A. Otto, R. Jaumann, K. D. Matz, T. Roatsch, E. Kersten, S. Elgner, and C. Raymond (2021a). Influence of volatiles on mass wasting processes on Vesta and Ceres, *Journal of Geophysical Research: Planets*, 126 (3). doi: 10.1029/2020JE006573. K. A. Otto and R. Jaumann provided guidance and participated, K. D. Matz and T. Roatsch provided data and C. Raymond reviewed the language errors. The paper deals with the mass wasting features with the aim of better understating related to volatile presence and their abundance at a global scale on Vesta and Ceres. Additionally, the effective coefficient of friction of Vesta and Ceres is compared with the outer solar system objects (Iapetus, Rhea, Charon) in order to investigate the role of volatiles on mass mobility.

2. THEORETICAL BACKGROUND

2.1 Small bodies in the solar system

Small planetary objects are irregular brittle and/or icy objects which are relatively small compared to the larger planets. Their size ranges from meters to a few hundred kilometers (~940 km) and are distributed throughout the solar system (Vernazza & Beck; 2016). Following the recommendation of the Small Bodies Assessment Group, main belt asteroids, near-earth objects, the Martian moons, irregular moons of the outer planets, centaurs, Kuiper belt objects, Trojans asteroids, Trans-Neptunian objects, dwarf planets, interstellar objects, meteorites, comets and other similar objects (SBAG, 2020; Vernazza & Beck, 2016) all fall under the category of 'small bodies'. Studies related to small bodies started with earth-based telescope observations in early 1800s. During the early analysis the definition of small objects was relatively simple, however, as new techniques advanced in telescopic surveillance (including earth and space based) more categories were defined and the line between the above-mentioned categories became blurred.

In the solar system, small bodies are thought to be the left-over blocks which has formed the terrestrial planets and other giant objects. They have survived a long history of violent collision, numerous resurfacing events and harsh thermal evolution which has shaped their current physical and chemical characteristics (Vernazza & Beck, 2016). Thus, they serve as an important constituent of our solar system. Additionally, they provide a window to trace the earliest formation of the solar system. Their diverse distribution offers large spectrum of material composition and interaction under different environmental conditions. From their unique size and shape to distinct orbital characteristics, each parameter has capacity to unravel the information which are often missing on the larger planets. By its very nature, they carry the pristine record of the primitive production condition that date back to 4.6 billion years ago (Bottke et al, 2002; SBAG,2020; Vernazza & Beck, 2016). Due to mutual nebular origin, such small objects contain organic materials and also preserve evidences for water and other volatiles that plays vital role for the existence and development of life. Finally, numerous small objects are a natural laboratory to conduct in-situ measurements and sample collection that offer powerful tools for planetary formation models.

In a nutshell, the investigation and exploration of the diverse range of small planetary bodies will not only amplify the scientific insights related to evolution of the solar system and future human exploration of space, but will also provide crucial fundamental knowledge related to volatiles and other life developing elements such as organics.

2.2 Asteroids

Asteroids, formally called minor planets (Cellino, 2021), are one of the most populated categories in small bodies. Figure **2.1** illustrates the distribution of asteroids within our solar system, namely main asteroid belt, Trojan asteroids and Kuiper belt asteroids. Additionally, there are also, Near-Earth Objects (NEO's), group of small objects that often crosses the orbit of earth, with perihelion distance of ≤1.3 AU (Harris & D'Abramo, 2015; Section **2.2.4**). The main asteroid belt is located between Mars and Jupiter at roughly 3.2 AU. Trojan asteroids orbit the Sun within

Jupiter's Lagrange points (Emery et al., 2015; ~5 AU). Moving far outside the solar system, at ~50 AU from the Sun, the Kuiper belt objects are located. Till now, spacecrafts were able to reach and orbit main belt asteroids as well as near-Earth asteroids (Table **2.1**). Whereas, for Trojans asteroids, NASA's Lucy mission launched in October 2021 and the New Horizon mission explored, the Kuiper belt objects of the Pluto system and MU69 (Arrokoth).

The era of asteroid research began in early 1801, with earth-based telescope observation (Gehrels, 1971). Giuseppe Piazzi discovered Ceres which was though a planet but later on it was defined as an asteroid and in 2006 the IAU classified it as the dwarf planet (Russell & Raymond, 2011). Up to date 1.1×10^5 (Oct., 2021; https://solarsystem.nasa.gov/) asteroids are identified with the help of newly developed earth-based telescopes and highly sophisticated space missions and many more are yet to be recognized. During their primitive study, asteroids were considered as starlink points of light (Bottke et al., 2015). However, after more than twenty decades of research, technological developments and theoretical and/or numerical modeling proved that asteroid-related exploration has the capacity to unfold the unique history of the solar system's evolution.

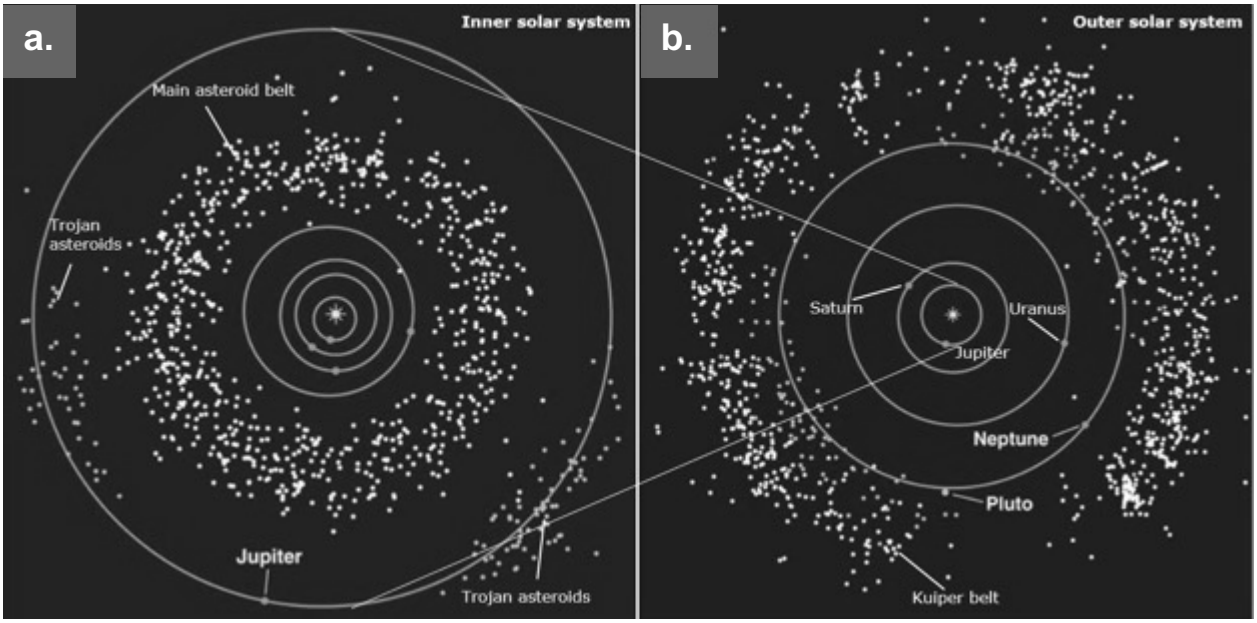

Figure 2.1 Overview of the major asteroid groups present in the solar system. Within the inner solar system, the main asteroid belt and Trojan asteroids are present where as in the outer solar system a large population of Kuiper belt asteroids (white dots in b.) along with Plutonians (grey dots) are located. The image is only for the purpose of representation and is not up to the scale. The image has been reproduced from the article by Soter, 2007 with Copyright permission of American Scientist, magazine of Sigma Xi, The Scientific Research Honor Society.

The main asteroid belt is the highest reservoir of asteroids in the inner solar system. Approximately 1.1-1.9 million asteroids ≥1 km in diameter are estimated in the main belt (Garlick, 2003) out of which Ceres (dia.: 930 km), Pallas (dia.: 512 km) and Vesta (dia.: 525.4 km; Cellino, 2021; Foderà Seri et al., 2002; Raymond & Russel, 2011) are the largest ones. During the early

formation of the solar system, numerous rocky objects violently collided with each other, forming the asteroids (Bottke et., 2016; Weidenschilling, 2000).

Table 2.1 The main-belt asteroids visited by space missions. The table shows a list of asteroids of the main asteroid belt followed by their heliocentric distance from the sun (AU) and explored by spacecrafts. The table was prepared from image published by Vissiniti, 2020 at http://tiny.cc/asteroid_missions

Asteroids	Semi-major axis (AU)	Mission
Ida & Dactyl	2.86	Galileo
Mathilde	2.65	NEAR Shoemaker
Lutetia	2.44	Rosetta
Vesta	2.36	Dawn
Annefrrank	2.21	Stardust
Braille	2.34	Deep Space 1
Steins	2.36	Rosetta
Toutatis	2.53	Chang'e 2
Ceres	2.78	Dawn

Within the asteroid belt, the asteroid orbit is marked by gaps at various distances (Figure **2.2**). These gaps in semi-major axes are called Kirkwood gaps (Garlick, 1888) caused by orbital resonance with Jupiter (Britt et al., 2007). Another powerful resonance is ν_6 secular resonance and occurs when the asteroid's longitude of perihelion orbit is equal to the Saturn's perihelion orbit (Morbidelli et al., 2002). These resonances increase the eccentricity of asteroids (due to frequent high gravitation conditions) and as a consequence, the asteroids pushed out of asteroid belt, often crosses the orbits of planetary bodies (such as Earth, Venus; Morbidelli et al., 2002; Michel et al.,

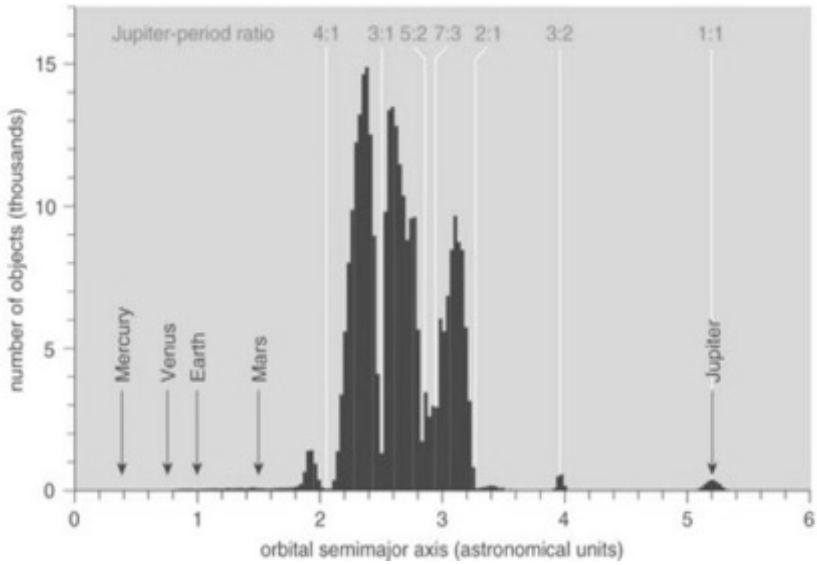

Figure 2.2 Heliocentric distance of main belt asteroids. The main asteroid belt expands between the 4:1 and 2:1 orbital resonance with Jupiter. The gaps between resonances are known as 'Kirkwood' gaps. 1AU=151.31 million km (distance between Earth and Sun). Image Credit: Soter, 2007, Copyright permission of American Scientist, magazine of Sigma Xi, The Scientific Research Honor Society.

2015). Today, the total mass of main asteroid belt population is about 4.5×10^{-4} Earth masses (Cellino, 2021).

To understand the asteroid composition, their surface has been investigated by the reflectance spectra of various light wavelengths. These spectra are sensitive towards surface minerals and expose the heterogenous composition of asteroids. Based on their composition different taxonomic class have been assigned. Each class corresponds to specific spectral characteristics, indicating different surface composition and amalgamation of various minerals. Overall, four main categories were derived: S-complex-, C- complex, X-complex and others (includes T, D, O, R, A, L, K and V-complex; Bus & Binzel 2002 a, b; Bus et al., 2002). Table **2.2** summaries the synopsis of different taxonomic classes and their composition. The majority of asteroids are S, C and X type. Inner asteroid belt (near 2.1 AU) is dominant in S-complex which was traditionally characterized as silicaceous composition with absorption at 1-2 µm (Chapman et al., 1975). Within the outer asteroid belt (at ~3 AU) most of the asteroids belongs to the C-complex (Gradie and Tedesco, 1982; Cellino, 2021) with low- absorption at 0.7 µm implying aqueous alteration of phyllosilicates (Vilas & Gaffey, 1989). X-complex comprises darkest and brightest asteroids (Michel et al., 2015) and their spectra overlaps with C-type but the clear division is possible considering albedo estimations (Bus & Binzel, 2002a). Very rare group of asteroids belongs to V-type and has spectra similar to basaltic achondrites (Michel et al., 2015). Vesta falls under the category of V-complex where as Ceres is a C-type, both the objects are the focus of this thesis.

Table 2.2 Summary of asteroid taxonomy classes. The table describes each taxonomy class, associated minerals and meteorite. Each class is further categorized based on their absorption in visible and near-infrared wavelengths. The summary is collected from Michel et al., 2015 and Cellino, 2021.

Class	Minerals and possible meteorite analogs
S-complex	*Minerals*: olivine, pyroxene *Meteorite*: many types of chondrites including primitive and basaltic achondrites
C-complex	*Minerals*: carbons, phyllosilicates, weak absorption of olivine, pyroxene *Meteorite*: carbonaceous chondrites
X-complex	*Minerals*: carbons, pyroxene (low-iron), enstatite, oldhamite *Meteorite*: carbonaceous chondrite (CB), silicate-rich irons
V-complex	*Minerals*: pyroxene, plagioclase *Meteorite*: Howardite, Eucrite and Diogenite (HEDs)

Figure **2.3** shows the spectrum of Vesta and Ceres using Infrared Telescope Facility (IRTF) in 2011 and 2005, respectively. After calibration the plotted data shows strong absorption centered at 0.9 µm and 1.9 µm on Vesta, favors the electronic absorption of Fe^{+2} common in orthopyroxene. Hence, based on absorption properties it was concluded that V-type asteroids, such as Vesta consists brittle fragments of impacts (McSween et al., 2011). On Ceres, the absorption feature centered at 1.2 µm and is likely due to magnetite or lizardite (Rivkin et al., 2006). The strong surface sensitivity at 3 µm wavelength is of particular interest due to indication of hydrated minerals expected on C-type asteroid such as Ceres (Lebofsky et al., 1978; Rivkin et al., 2010).

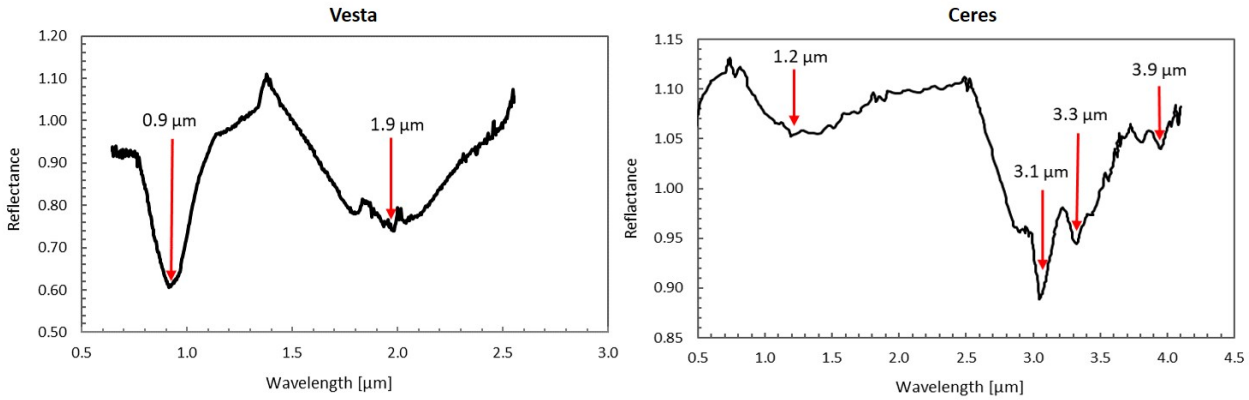

Figure 2.3 Near infrared reflectance spectrum of Vesta and Ceres. The data for spectrum is measured from the NASA Infrared Telescope Facility (IRTF) in 2011 and 2005 and calibrated by Reddy et al., 2011; 2020 and Rivkin et al., 2006; 2010 respectively. On left the absorption at 0.9 µm and 1.9 µm indicating Vesta as V-type asteroid. On right is the graph of absorption at 1.2 µm, 3.1 µm, 3,3 µm and 3.9 µm suggests that Ceres has experience aqueous alteration as C-type asteroid. The plotted data for Vesta is retrieved from the Planetary Data System (PDS) available at https://sbn.psi.edu/pds/resource/reddyvesta.html and data for Ceres, it is from Rivkin et al., 2006; 2010 digitized with plot digitizer.

2.2.1 Link between asteroids and meteorites

Meteorites are piece of solid debris and/or metal from comets and asteroids which pass through the space and falls on the Earth surface. When the debris enter the Earth's atmosphere, it interacts with atmospheric gases thermally, causing them to lighten up, and often burn out. The heated debris produces long streaks of light in the sky, thus known as meteor fire balls or shooting stars.

Meteorites have different compositions which belongs to various parent objects within solar system. Majority of the meteorites are originated from the asteroid surfaces but small amount of them are also related to the comets and large objects like Mars, Moon or Vesta (Cloutis et al., 2014). Therefore, the 'free fall' samples have potential to withhold not only information related to chemical and physical composition of planetary objects but also represent diverse asteroid compositions which may or may not be discovered yet (Burbine et al., 2002). By including the meteorite study technique, an approximate idea of asteroid properties can be gained in advance. Additionally, results emerging from meteorite analyses serve as an archive which later can be matched with surface data of certain parent bodies.

A subset of achondritic meteorites; Howardites, Eucrite and Diogenites (HED) is observed from mid to lower latitudes on V-type asteroid Vesta. HEDs are brassicas composed of fragmented igneous brittle rocks. Eucrites are rich with basalts and indicates the involvement of igneous process whereas diogenites are of ultramafic pyroxene-rich meteorite and indicates influence of intrusive events. Both of them compose howardite as breccias. Thus, the composition of HEDs lead to conclude that their parent body must be a differentiated object with mafic process (McSween et al., 2013b; 2011; Duke & Silver et al., 1967). Vesta surface has shown spectral characteristics which are similar to the HEDs (Adams, 1974; Reddy et al., 2012; McCord et al., 1970; McSween

et al., 2013b). However, due to the distribution heterogeneity of HEDs on Vesta, it is also possible that Vesta is a parent object of HEDs meteorite (Russell et al., 2013).

Similarly, rarer type of carbonaceous chondrite meteorites belongs to C-type asteroid. The bulk composition of Ceres surface is consistent with some chondrites (CM/CI; Gaffey 1976; McSween & Treiman, 2018a). CM and CI are altered chondrite subsets and are associated with modification process (Rivkin et al. 2011). CM chondrites are mixture of both altered aqueous minerals and unaltered phases whereas CI chondrites are almost completely altered (King et al., 2015a, b). On Ceres, the surface has relatively high proportion of carbonates with lesser organic matter (McSween et al., 2018b) and experienced sever surface transformation process. Figure **2.4** illustrates the images of HEDs and carbonaceous chondrites collected from different locations on Earth.

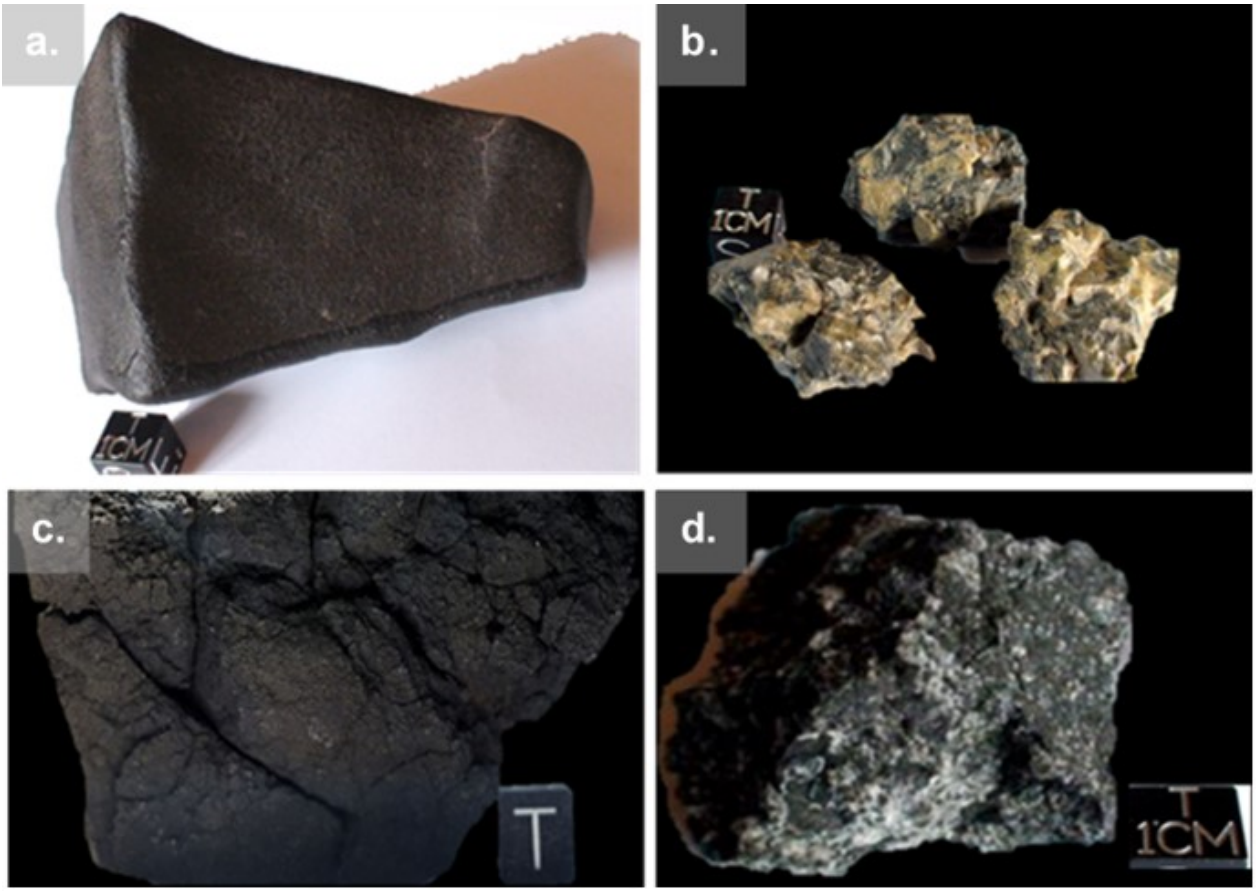

Figure 2.4 Examples of HED and carbonaceous chondrites. (a.) Piece of Agout Eucrite derived from Morocco in 2000. (b.) Pieces of crystalline Diogenites derived from Tunisia in 1931. (c.) Piece of CM1/2 carbonaceous chondrite derived from Africa. It is rarest of all and so far, only 20 meteorites are present worldwide. Photo credit: NASA/JPL (~1 cm), source: http://www.meteorite.fr/en/forsale/HED.htm. (d.) Piece of CI carbonaceous chondrite derived from Tanzania in 1939, image source: http://www.meteorite.fr/en/forsale/ivuna.htm. Copyright for image (a.), (b.) and (d.); 1998-2020, Photo credit: The Earth's Memory SARL, France (~1 cm).

2.2.2 Migration of volatiles within the asteroid belt

With the advancement of astronomical instrumentations, laboratory studies and theoretical models, it has been proven that some of the asteroid belt objects had water ice and other volatiles incorporated during the early formation of the solar system (Mousis et al., 2008). The volatiles and ice particles were produced during the early stage of planetary formation (Rivkin et al., 2015) and later migrated into the asteroid belt (Mousis & Alibert, 2005). There are two possible mechanism via which large fractions of volatiles crossed the so called 'snow line' and delivered volatiles into the asteroid belt; (i) through the inward flux of icy planetesimals (Mousis et al., 2008) and (ii) transportation of asteroids originating from giant planets from the outer solar system (Rivkin et al., 2015). The concept of 'snow line' is often used while discussing the presence of volatiles and ice particles within the inner solar system and refers to the heliocentric boundary beyond which water ice is stable in space (Rivkin et al., 2015). At present day, the location of the snow line has fallen within the asteroid belt (Su et al., 2013) although, prior to the planet formation, the location was uncertain (Luine & Reid, 2006). Protoplanetary disc model suggested that the icy particles originated from ~5 AU were migrated up to ~3 AU without any sublimation process (Mousis et al., 2008). Between 3-2 AU ice might have melted and ≤2 AU, solar insolation has caused ice to vaporized (Mousis et al., 2008). Thus, asteroids ≥3 AU distance may have unaltered ice within their regolith which did not react with surface minerals (Cyr et al., 1998; Mousis et al., 2008). According to the analysis of 'Grand Tack' model, asteroids is transferred into main belt via inward migration of Jupiter and Saturn (Walsh et al., 2011). Hence, the presence of volatile rich asteroids within main asteroid belt is justified. However, few asteroids have relatively dry brittle surface within main belt. Following the arguments of dynamical models, widening of the asteroid belt towards sun in the past may have caused the evaporation of volatiles (Bottke et al., 2012). Therefore, asteroids such as Eros, Itokawa, Ryugu, Bennu or Vesta do not show presence of large quantities of volatiles within their subsurface regolith (Cyr et al., 1998) whereas a few asteroids like Ceres have an ice-rich mantle (Russell et al., 2005). In summary, above proposed theories justify the presence of relatively dry and wet surface materials within the asteroid belt.

2.2.3 The regolith of asteroids

Regolith is a terrestrial term which was also used in context of the Moon (Hartmann et al.,1973) while observing incoherent surface material. The upper most layer of granular-like (Clark, 2008) and secondarily cemented material covered over a stable bedrock surface, which formed by weathering, erosion, transportation, excavation and/or deposition of the relatively older subsurface mixtures (Merrill et al., 1897; Küppers et al., 2014). On asteroidal objects, unconsolidated regolith surfaces usually consist of coarser material, fragmented mixtures of bedrocks and impact ejecta (McKay et al. 1991; Eggleton et al., 2001; Küppers et al., 2014; Figure **2.5**).

The surface of airless asteroids is exposed to space weathering and other modification events (such as impact cratering, solar sputtering, solar wind implantation) which produces the regolith layer (Clark et al, 2002). The ongoing formation of a regolith cover is considered as a final stage of surface evolution (Basu & Molinaroli 2011). The production and transportation of regolith

mixtures is divided into two epochs on asteroids: (i) an era of impacts resulting into melting and accumulation of debris which later converted into cohesive materials due to heating and/or gravitational compaction (Housen & Wilening, 1982); followed by (ii) comminution of megaregolith debris into coarser and finer particles (Gundlach & Blum 2012) by hypervelocity impacts and influx of micrometeorites (Housen & Wilening, 1982; Küppers et al, 2014). Due to the ongoing exposure of regolith to the space environment, electro-magnetic radiation and particle impacts, trigger physical and chemical alterations on a global scale. Various velocity of large impactors constantly bombards the uppermost part of the surface and often result into complex craters. In contrast, the smaller impacts do not deeply penetrate the surface layer but produce fragments, induce mixing-stirring of the existing particles and in turn, affects the porosity of the regolith (Shoemaker 1971; Hartmann et al. 2001). Depending on the porosity, regolith has the ability to hold and trap volatiles (Küppers et al, 2014; Brunetto et al., 2015) over the time. Thus, regolith studies provide the opportunity to identify and interpret processes that dominate on the surface of asteroids.

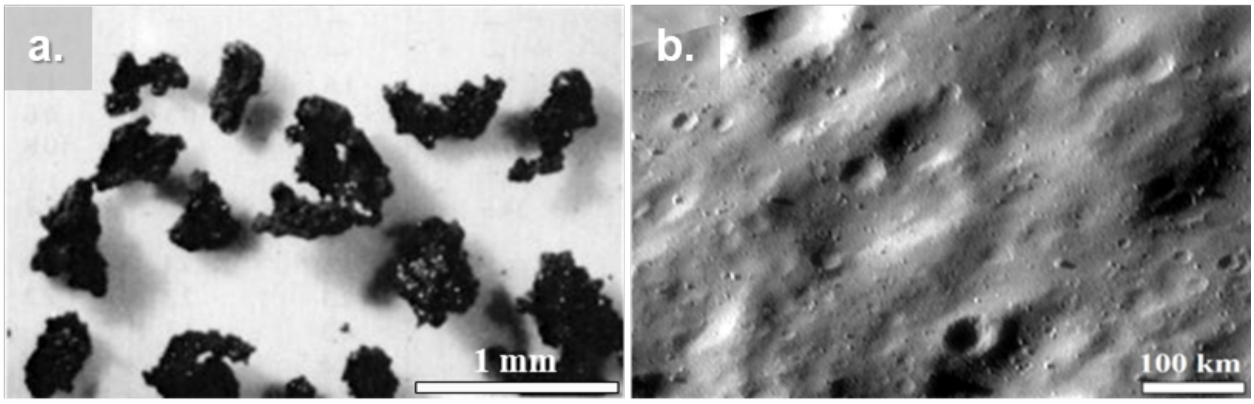

Figure 2.5 Various types of regolith examples. (a.) optical microscope image of lunar regolith. The samples are retrieved from the Apollo 11 mission. The samples are known as agglutinates comprised of minerals and glasses glued together and produced from micrometeorite impacts on the Moon. The agglutinated samples have an edgy, uneven, rough texture (McKay et al., 1991). Image modified from document by McKay et al.,1991, source: https://www.lpi.usra.edu/publications/books/lunar_sourcebook/pdf/LunarSourceBook.pdf#page=319. Image id: NASA Photo S69-54827. (b.) The surface of asteroid (433) Eros composed of large boulders to fine-grained fractions resulting from the transport and breakdown of regolith over time. Image id: tm-m0134185586f4_2p_iof_dbl.cub retrieved from http://tiny.cc/eros.

2.2.4 Near-Earth Asteroids (NEA)

By definition NEAs are asteroids that cross the Earth trajectory with perihelion distances, $q \leq 1.3$ AU and aphelion distances, $Q \geq 0.983$ AU (Rabinowitz et al., 1994; Morbidelli et al., 2002). As of June 2015, in total 12,697 NEAs (≥1 km in diameter with an absolute magnitude of ≤17.75) were detected (Harris & D'Abramo, 2015), however, many more have been added (39; Center for Near Earth object studies, 2021) to the list since then. Most NEAs are remnants (usually ≤1 km in size) formed by collision events involving larger asteroids within the main asteroid belt millions of years ago (McFadden et al., 1989; Bottke et al., 2000). The fragments consist of irregular shapes deflected onto near Earth orbits by accelerating into the inner solar system due to orbital resonance

with Jupiter (Harris & D'Abramo, 2015). Spectral observations of NEAs show that they have a relatively low number (6 out of 88) of C-type asteroids in comparison to main belt asteroids, (Rivkin et al., 2012; Fornasier et al., 2014; Binzel et al., 2004) implying possible low amounts of volatiles and ice particles (Marchi et al., 2009) within their regolith layer.

In past two decades, the interest to study and explore the NEAs with space missions increased tremendously due to their easy accessible near-Earth orbit and knowledge appeal related to their physical and chemical composition. Several sample return missions and lander maneuvers to these bodies have provided great scientific as well engineering potential. Figure **2.6** summarizes the spacecrafts that visited NEAs.

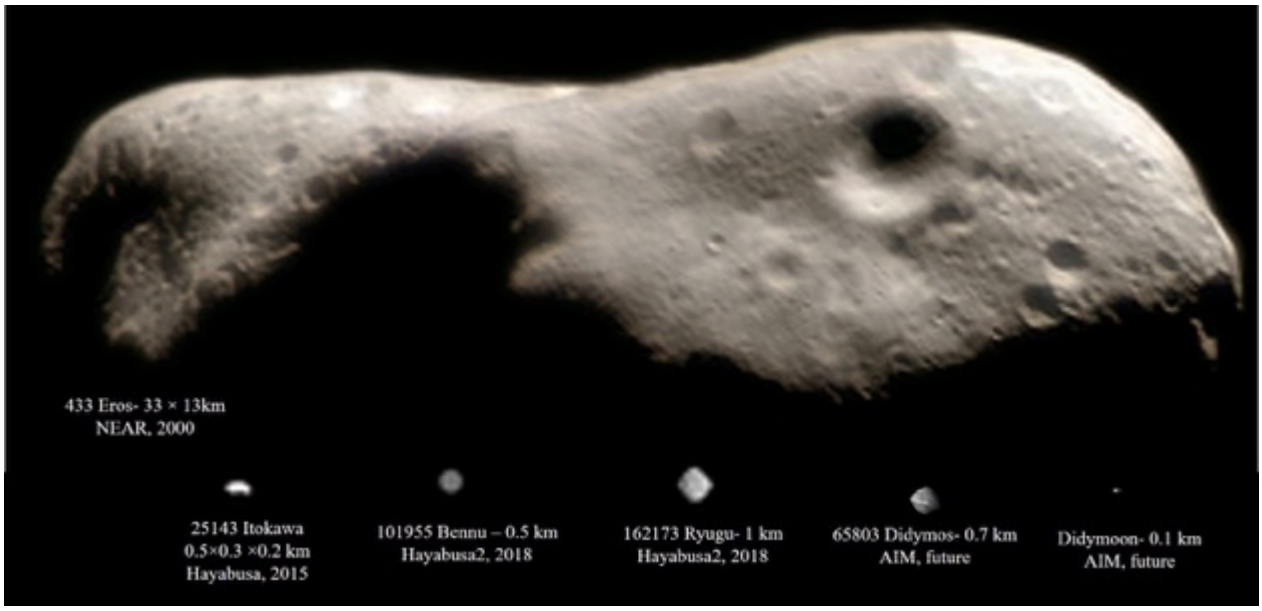

Figure 2.6 Near earth asteroids orbited by spacecraft. Listed are name of asteroids, their dimensions, visiting spacecraft and the year of maneuver. The image was modified and updated from a version published at https://cutt.ly/qEWSivS, Copyrights Planetary Soc., Emily Lakdawala.

2.3 The Dawn mission- at a glance

After 11 years of successful flight operations, the Dawn mission was terminated in October 2018. It orbited 1.1 year around Vesta and 3.7 years around Ceres. During its extraterrestrial adventure, Dawn has overcome challenges and untangle a whole new world of science and engineering. The motivation behind designing the Dawn mission was not only to increase the understanding related to two of the unexceptionally massive planetary objects, Vesta and Ceres but also to better interpret the condition during their formation (Russell & Raymond, 2011; Russell et al., 2013). Keeping this as a dominant objective, the Dawn spacecraft began its journey to the center of the main asteroid belt in the year 2007. During its early planning phase, Dawn was designed to explore Vesta (due to its similar characteristics to the moon) however, because of adequate preserved resources it was later extended to visit Ceres. In the following sections, the details related to the Dawn mission objectives (Section **2.3.1**), on-board instruments (Section **2.3.2**) and the operational plans (Section **2.3.3**) is described.

2.3.1 Mission objectives

The main objective of the Dawn mission was to understand processes related to the formation and evolution of Vesta and Ceres. Both are located within main asteroid belt (Vesta at 2.36 AU and Ceres at 2.76 AU) but has significant contrast in their composition (Russell & Raymond, 2011; Russell et al., 2004). To achieve this enormous goal, multiple interim objectives were clarified as follows.

- Determine external and internal forces that influenced the shape, axis and spinning of Vesta and Ceres.
- Construct shape models for precise map projection, to derive gravitational anomaly and understand the surface thermal condition.
- Acquire maximum surface data (both optical and spectral, gravity, topography, photometry) to conduct geological mapping and estimate the chronology.
- Clarify and refine pre-existing knowledge related to surface mineralogy and geochemistry of both the bodies.

2.3.2 Mission instruments

To achieve the above-mentioned objectives the Dawn spacecraft carried three instruments: A Framing Cameras (FC; Sierks et al., 2011), a Visual and InfraRed spectrometer (VIR; De Sanctis et al., 2011) and a Gamma Ray and Neutron Detector (GRaND; Prettyman et al., 2011). Additionally, the framing camera is also used for the gravity examination and topography investigation of the surface of Vesta and Ceres (Russell et al., 2004; Russell and Raymond, 2011).

The visible and infrared spectrometer (VIR, Figure **2.7a**) acquired the surface data in visible (0.25-0.1 µm) and infrared (0.1-0.5 µm) wavelength. The VIR determined mineralogical composition of the surface material on Vesta and Ceres. The resolution of the VIR images is ~ 70 $m \cdot pixel^{-1}$ for Vesta and ~34 $m \cdot pixel^{-1}$ for Ceres (McSween et al., 2013). The data gathered form the VIR suggested strong absorption at 1 µm and 2 µm has indicated the pyroxene presence on Vesta (De Sanctis et al., 2013; Russell et al., 2016). On Ceres, deep absorption at 1.28 µm, 1.65 µm, 2.00 µm exhibit the presence of H_2O minerals, absorption feature at 3.05-3.1 µm are related to organics, crystalline water ice, ammonia phyllosilicates and strong deep at 3.3-3.5 µm, 3.9 µm supports the existence of hydrocarbons within regolith (De Sanctis et al., 2015a; Ammannito et al., 2016; Combe et al., 2019).

The Gamma Ray and Neutron Detector (GRaND, Figure **2.7b**) instrument was design to provide constrain on the surface elements of Vesta and Ceres with 100 $g \cdot cm^{-2}$ depth-sensitivity (=density of surface material [$g \cdot cm^{-3}$] × distance beneath the surface [cm]; Prettyman et al., 2011). The instrument detects thermal and epithermal neutrons of the top layer soil by emission of gamma and hydrogen (Prettyman et al., 2011). It has successfully mapped the mixing ratio of HEDs, determined the relative abundance of plagioclase and other mafic minerals on the surface of Vesta (Prettyman et al., 2012). At Ceres, GRaND has detected ammoniated phyllosilicates, carbonates

and other hydrated salt on the surface of Ceres which was also supported by the data gathered from spectrometer (Prettyman et al., 2017).

The two Framing Cameras (FC, Figure **2.7c**) on the spacecraft was designed to explore the geological context of Vesta and Ceres along with VIR and GRaND. The camera uses focal length of 150 nm, field of view of 5:5°×5:5° and frame-transfer CCD[1] with 1024×1024 sensitive pixels (Russell et al., 2004; Sierks et al., 2011). It operates within range of 500-100 nm with 7 multi-color band filter wheel and a clear filter (Sierks et al., 2011). To acquire color-based images the FC is operated between 450-950 nm (Sierks et al., 2011) which is sensitive for the surface of Vesta and Ceres. A single clear filter is used for the navigation purpose of the spacecraft and for the enhancement of the surficial features with high SNR[2] observation was considered. The two FCs

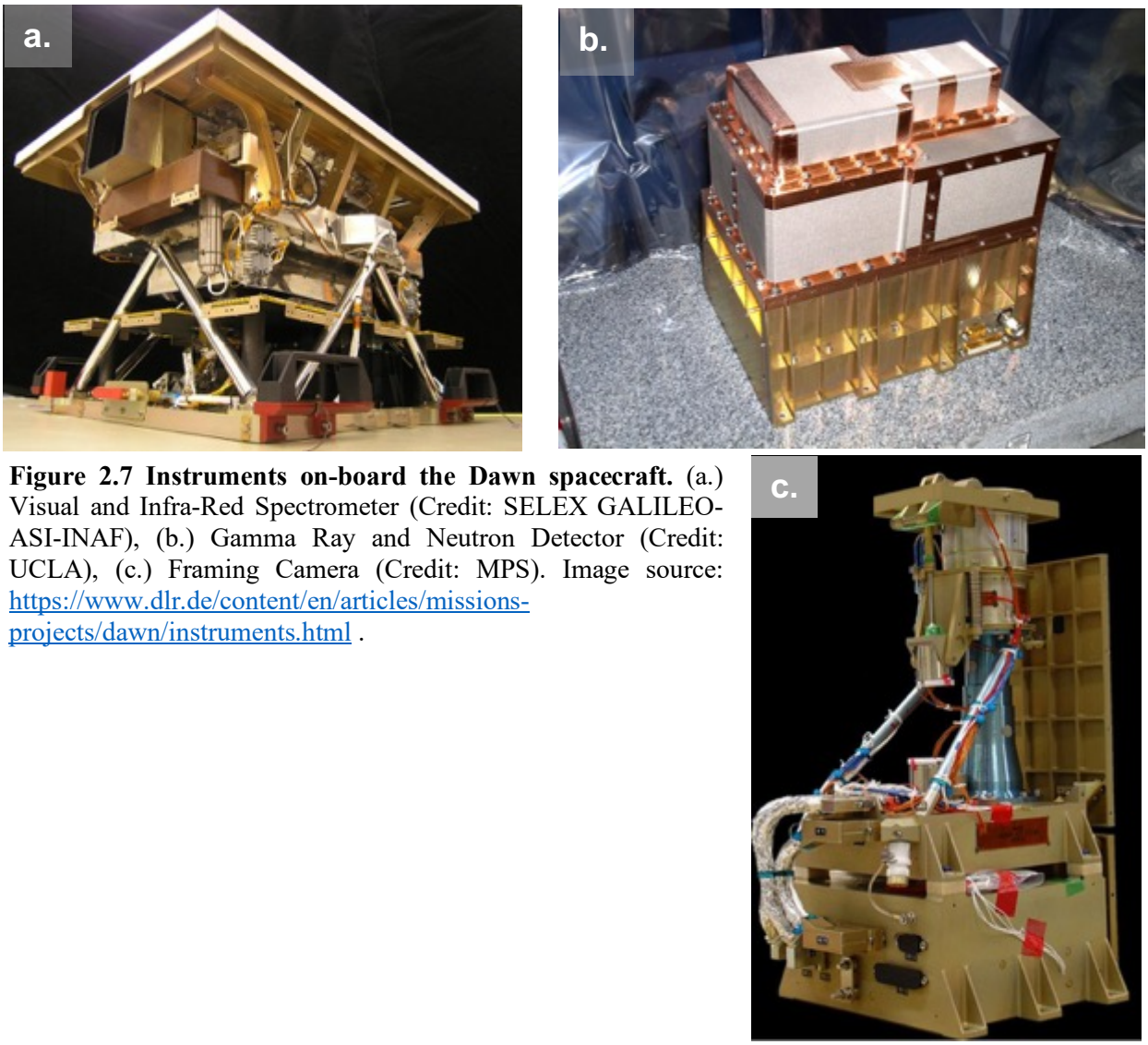

Figure 2.7 Instruments on-board the Dawn spacecraft. (a.) Visual and Infra-Red Spectrometer (Credit: SELEX GALILEO-ASI-INAF), (b.) Gamma Ray and Neutron Detector (Credit: UCLA), (c.) Framing Camera (Credit: MPS). Image source: https://www.dlr.de/content/en/articles/missions-projects/dawn/instruments.html .

[1] Charged coupled device
[2] Signal-to-noise

also allow to prepare the surface Digital Terrain Model (DTM) and to produce the shape models for geological and geophysical analysis. (Sierks et al., 2011; Raymond et al., 2011).

Serval scientific studies conducted using imaging data from framing camera (FC), absorption data from the visible and infrared spectrometer (VIR) and elemental composition maps prepared form the Gamma Ray and Neutron Detector (GRaND) instrument suggested that Vesta has relatively dry regolith (e.g. Jaumann et al., 2012; O'Brien et al., 2014) whereas Ceres is rich with water ice (e.g. Russell et al., 2016; Buczkowski et al., 2016).

2.3.3 Operation duration and cycle on Vesta and Ceres

After launched from Cape Carnival, the Dawn spacecraft did its gravity maneuver at Mars in February 2009 and arrived in Vesta orbit on July 16, 2011. From here the spacecraft left for the journey towards Ceres on September 2012. It arrived in Ceres' orbit in the March 2016 and was operational until October 30, 2018. It has collected data while orbiting in different scientific orbits at Vesta and Ceres (Figure **2.8**). The spacecraft initiated the data gathering at both targets with a survey orbit to acquire the VIR data. Followed by, it entered into a High Altitude Mapping Orbit (HAMO) phase which was mainly dedicated to FC observation. Later on, the spacecraft descend to a Low Altitude Mapping orbit (LAMO) to obtain GRaND spectra. Before leaving for Ceres, it entered into a HAMO-2 phase and mapped the northern region of Vesta which was under shadow during previous HAMO observations due to its rotational axis. In the case of Ceres, extended mission orbits focused on imaging the highest possible resolution of the Occator crater using the FCs, GRaND and the VIR instruments.

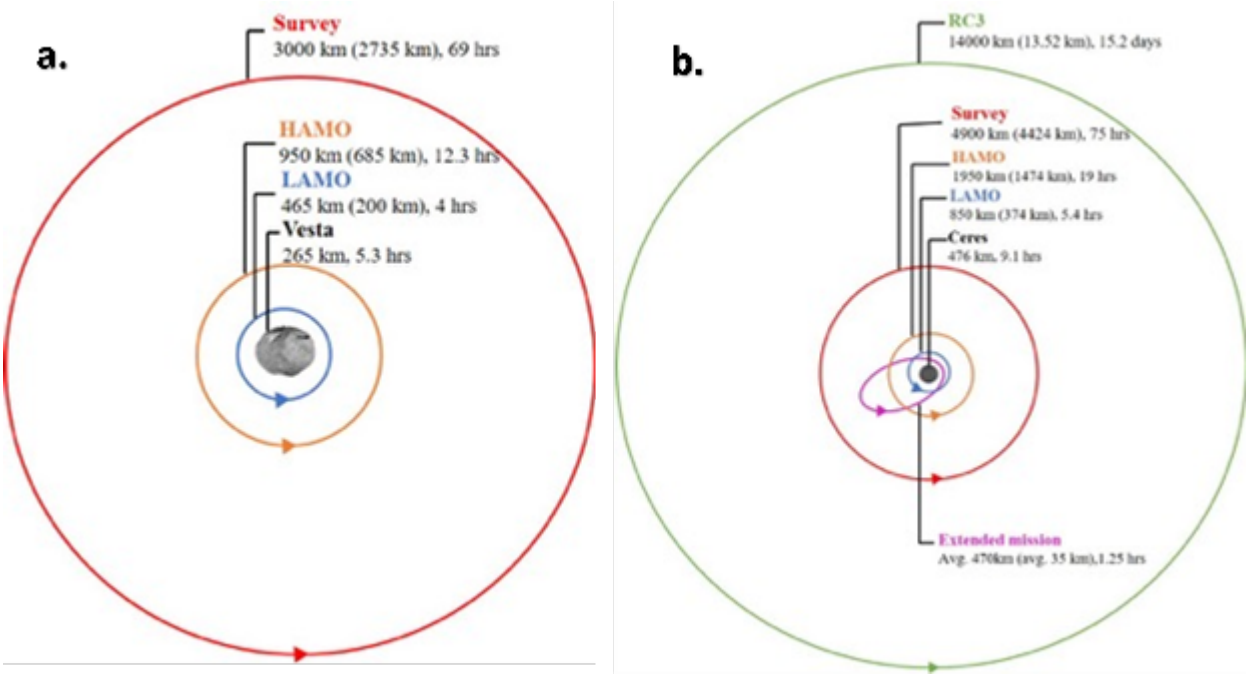

Figure 2.8 Illustration of the Dawn orbital phase on Vesta(a) and Ceres(b). Listed are radius (altitude in bracket) and the period the orbits around both the bodies. The equatorial radius and rotation of Vesta and Ceres are shown in the center. The illustrations are edited based on the updates in science orbits. Credit: UCLA/McREL.(Russell & Raymond, 2011).

Although each scientific orbit was design for a specific instrument, all three were functional throughout the mission maneuvers around Vesta and Ceres. As a result, entire Vesta surface was mapped at ~70 m·pixel^{-1} resolution in HAMO cycle. The global Digital Terrain Model (DTM) of 80% of the Vesta's surface were derived in HAMO orbit phase and ~66 % of the surface were in higher resolution (~20 m·pixel^{-1}) using data from LAMO orbit phase (Russell et al., 2013; Preusker et al., 2012). Similarly, during Dawn operation around Ceres, 99% of the surface (~140 m·pixel^{-1}) along with the corresponding DTM was mapped from the data acquired during HAMO orbit and higher resolution (~35 m·pixel^{-1}) surface maps were produced from LAMO data (Preusker et al., 2016).

2.4 Asteroid (4) Vesta

The ample amount of data acquired from the Dawn mission has immensely increased our understanding related to Vesta's formation, gravity field, rotational axis, inclination, internal and external surface structure.

Table **2.3** summarizes the physiological parameters of Vesta derived using the Dawn data. And Figure **2.9** exhibits the HAMO mosaic of Vesta. It is the second largest differential asteroid with tri-axial ellipsoid axis (286.3 × 278.6 × 223.2 km) (Russell et al., 2012; Preusker et al., 2012; Jaumann et al., 2012) comprises of iron core with the eucrite diogenite crust (De Sanctis et al., 2012; Ammannito et al., 2013). The northern hemisphere of Vesta is believed to be one of the earliest, produced heavily cratered surface (Russell et al., 2012). The elemental and mineral composition suggested their close relation with HED parent body (Russell et al., 2012, 2013).

Vesta reveals diverse geological structures including dichotomy of impact cratering within northern and southern latitudes, well-preserved mass wasting features (Otto et al., 2013; Krohn et al., 2014; Parekh et al., 2021a), albedo heterogeneity (Ammannito et al., 2013), exceptionally large impact basin (Rheasilvia and Veneneia) in the south (Jaumann et al., 2012; Schenk et al., 2012) and extensive elevation differences (Jaumann et al., 2012). The upper regolith of Vesta is dry (Jaumann et al., 2012) with very low amount of H or OH.

Table 2.3 Physical parameters of Vesta derived from the Dawn mission data. (Russell et al., 2012*)*

Parameters	Value	Error
Mean radius [km]	262.7	±0.1
Volume* [km^3]	74.970×10^6	±0.05×10^6
Mass [kg]	2.5907	±0.00001x10^{20}
Semi-major axis [AU]	2.3615	±8.85 x 10^{-10}
Surface temperature [K]	85.5- 255.5	-
Bulk density [kg·m^{-3}]	3456	±35
Rotation rate# [°·day^{-1}]	1617.333110	±0.000003

*Derived from best fit ellipsoid, #1617.333128°·day^{-1} after Konopliv et al., 2014

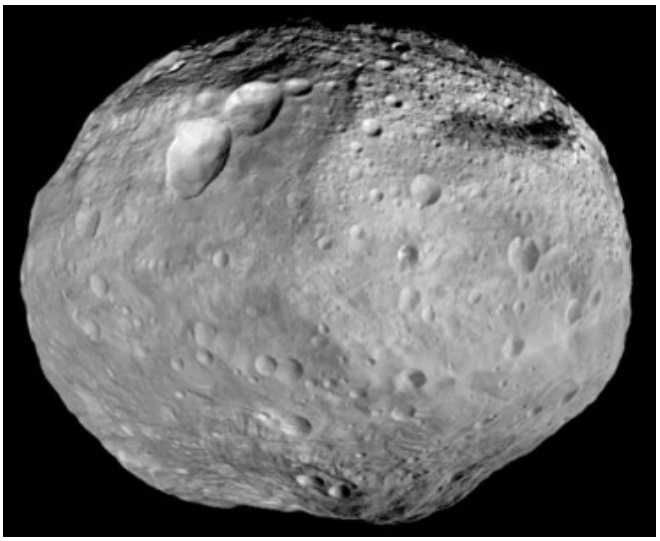

Figure 2.9 Mosaic of asteroid Vesta (4). The first high resolution (~70 m·pixel^{-1}) was prepared from the Dawn data (HAMO). Credit: NASA/JPL-Caltech/UCLA/MPS/DLR/IDA, source: https://solarsystem.nasa.gov/news/725/vesta-and-ceres-what-we-knew-about-these-worlds-before-and-after-dawn/

2.4.1 Geology

The Dawn instruments has rigorously covered the surface of Vesta, revealing the violent collision dominated history. Figure **2.10** exhibits the global map of Vesta showing distinct geological surface features exposed by data acquired from the FC instrument.

Due to low gravitational condition and bombardment history, the elevation difference on Vesta with respect to the ellipsoid of 285 × 229 km (Jaumann et al., 2012) is high (-22.3 km to 19.1 km). Overall the topography holds intense slopes (reaches up to ~55˚) but deposit mobility is relatively less (in comparison to Moon and Mars; Kleinhans et al., 2011). The surface of Vesta can be divided into three geological major units: (i) highly cratered northern terrain; (ii) densely populated ridges, troughs surface at the equatorial and central region and (iii) large impact basins resting at southern latitudes (Jaumann et al., 2012; Yingst et al., 2014; Williams et al., 2014b; Schenk et al., 2012).

The northern highland of Vesta is dominated by the surface features such as troughs and grooves, small crater chains and various impact craters (Ruesch et al., 2014b). The troughs and ridges are present within a region called Saturnalia Fossa (lat.: 208.05˚E, long.: 37.05˚N), which are ~1.5 km wide with an average length of 4.7 km, oriented in north-south direction and shows considerable amount of debris infilling suggesting their older age (Buczkowski et al., 2012). Small crater chains are oriented radially around fresh craters and their close proximity to the large crater suggested that they must formed from the secondary impact debris (Ruesch et al., 2014a). Moving on to the equator, relatively larger scale troughs (Divalia Fossa; lat.: 349˚E-84˚E, long.: 30˚S-30˚N) has wide, flat-floored, muted grooves and pit chains (Buczkowski et al., 2012; Jaumann et al., 2012). Additionally, the three prominent craters namely Marcia, Calpurnia, and Minucia are aligned with overlapping rims mimicking a 'Snowman' impression (Section **2.4.2**; Williams et al., 2014b) at mid latitudes. Down in the southern latitudes, the large Rheasilvia and Veneneia basins have reshaped the southern hemisphere and their impact ejecta blanketed the southern hemisphere (Schenk et al., 2012). Both the basins are located within Vestalia Terra (lat.: 25˚N-35˚N, long.: 200˚E-300˚E) and cover ~80,000 km^2 area (Buczkowski et al., 2014; Jaumann et al., 2012). The Rheasilvia basin is located at 300˚E, 78˚S and has a diameter of 500±25 km whereas Veneneia

basin is centered at 173˚E, 51˚S and has a diameter 400±25 km (Jaumann et al., 2012; Schenk et al., 2012). The rim of Veneneia basin is partially overlapped by and extend into the Rheasilvia basin implying Veneneia to be the oldest out of two (Russell et al., 2012; Jaumann et al., 2012; Schenk et al., 2012).

The steep topography of Vesta encourages the formation of variety of mass wasting features, asymmetric craters, pitted terrain and gullies at a global scale (Denevi et al., 2012; Krohn et al., 2014a; Otto et al., 2013; Parekh et al., 2021a; Williams et al., 2014a). Various mass wasting impressions with slumping block, granular flows, alcoves and furrows were observed on the slopes of craters and basin walls (Parekh et al., 2021a; Otto et al., 2013; Krohn et al., 2014b; Jaumann et al., 2012). Based on the deposit mobility it is reasonable to depict that the topography and dry regolith environment plays a vital role in transportation of the surface material (Parekh et al., 2021a; Otto et al., 2013). The extensive elevation contrast result in sharp inclination, forming distinct morphology such as asymmetric craters (Krohn et al., 2014a; 2019). They are produced due to collapse of uphill slope of craters causing wider wall on one side and relatively narrower on the other. In regions where the slope is ≥20˚, the elevation terminates the distribution of ejecta in uphill direction and diverted the downslope movement (Krohn et al., 2014a). Numerous examples of pitted terrain noted within interior of craters are identified by irregular rims and supports violent outgassing of the volatiles in the past (Denevi et al., 2012). Some of Vesta's craters reveal significant attributes of linear to curvilinear gullies at the crater rim and floor which are related to dry granular flow whereas curvilinear ones are formed by transient water flow present within ice bearing regolith on Vesta (Sarafian et al., 2013; Scully et al., 2015; 2021).

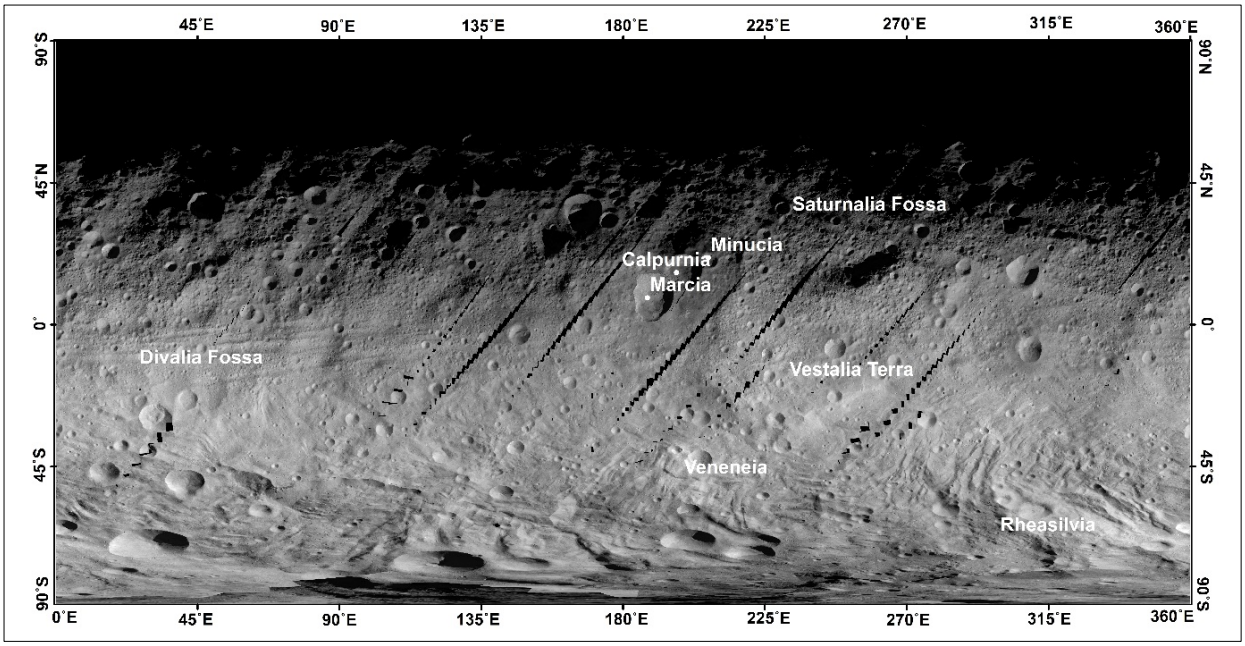

Figure 2.10 Map of Vesta. Global equidistance mosaic is prepared from LAMO orbit data (resolution: ~70 m·pixel^{-1}; Roatsch et al., 2012). The geological features tagged are discussed in the text.

2.4.2 Marcia crater

Marcia crater is located on the western edge of Vestalia Terra. It is the largest (dia.: ~67.9 km) amongst three followed by Calpurnia (dia.: ~50.1 km) and Minucia (dia.: ~23.1 km; Williams et al., 2014). It is located at ~10˚N and ~190˚E and surrounded by the young mixed impact ejecta from all the three craters (Jaumann et al., 2014; William et al., 2014b; Figure **2.11**). The Marcia crater is sustained by the pristine geological characters such as well-defined rim structure, preserved fresh and bright material at SW crater wall (William et al., 2014b), pitted terrain (Denevi et al., 2012) and ponded features (Jaumann et al., 2012; Parekh et al., 2021b). The VIR analysis depicted bright material as pyroxene (McCord et al., 2012; Li et al., 2012) and the outcrop is interpreted to be the youngest (Williams et al., 2014b). The smooth, featureless small pond-like depressions within vicinity of Marcia are infilled by the impact ejecta melt (Parekh et al., 2021b; Chapter **5**) whereas pristine pitted terrain displayed at the floor of Marcia and Calpurnia is enriched with volatile bearing (OH- or H-) mixture (Denevi et al., 2012; Prettyman et al., 2012; De Sanctis et al., 2012) probably excavated due to the Marcia impact. The strong evidence of ponded features and pitted terrain suggested that the small amount of localized ice-bearing deposit must be present within subsurface layers of Vesta (Denevi et al., 2012; Scully et al., 2015).

To derive the age of Marcia and Calpurnia, seven smooth units within the ejecta blanket were mapped (Williams et al., 2014b). The smooth units consist of muted craters and hummocky to lobate morphology suggesting impact melt flow movements (Williams et al., 2014a; Denevi et al., 2012). Based on the analysis of the geological units and estimation of chronological models, it is

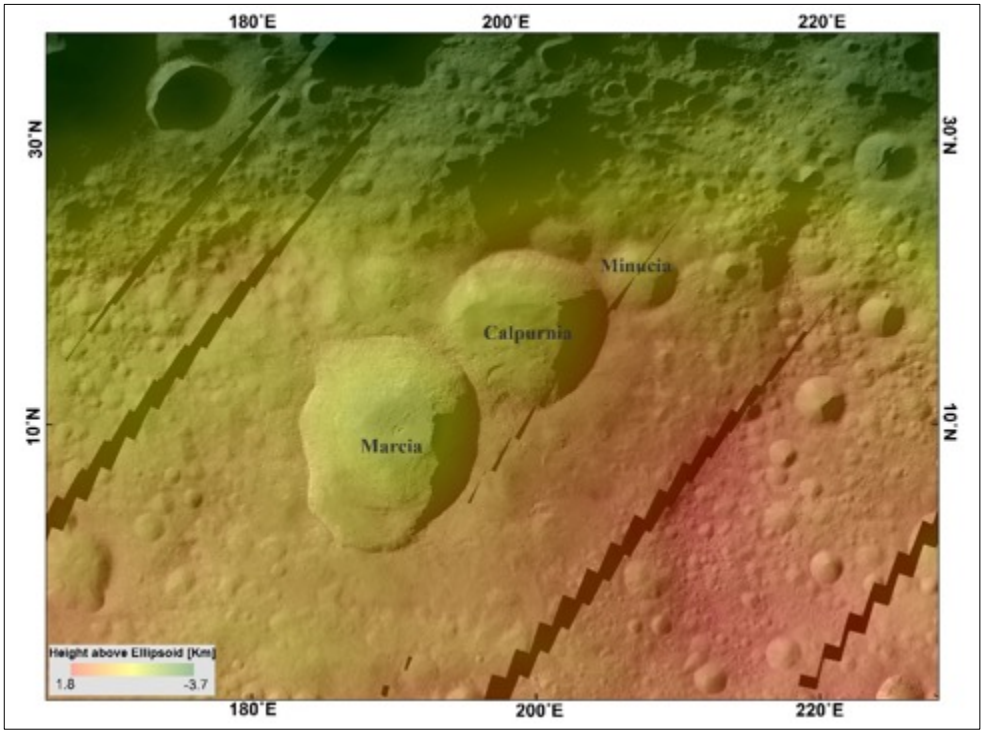

Figure 2.11 Map of Marcia impact crater. Three craters namely Marcia, Calpurnia and Minucia are partially adjoined via rims and surrounded by smooth intermixed ejecta material (Williams et al., 2014b). The HAMO DTM is overlaid on the LAMO mosaic and the map is on equidistance projection.

reasonable to conclude that parts of the Marcia's impact ejecta (120-390 Myr) are relatively older than the crater (40-60 Myr) itself (Williams et al., 2014b).

2.4.3 Regolith of Vesta

Unlike rest of the airless dry bodies such as Moon, Itokawa, Eros (Noguchi et al., 2011), the weathering process on Vesta is different. On both Moon and Itokawa, nanophase metallic particles were observed due to solar wind and micrometeorite process which left behind unique spectral signature that is not observed on Vesta at available resolutions (Pieters et al., 2012). Instead the regolith material of Vesta is well-mixed of bright and dark diverse components (McCord et al., 2012). This heterogeneity is confirmed by the study of photometric and thermal properties of the regolith. Schröder et al. (2014) observed substantial contrast in the phase curves of different regolith materials where fresh impact ejecta has steep a phase curve and is related to the physical roughness of the regolith. To obtain quantitative understanding, Martikainen et al. (2019) developed a spectral model and compare it with the spectral data acquired by the Dawn mission. The Vesta spectral signature of the surface matches best with the finer regolith of ≤25 μm HED particles (Martikainen et al., 2019; Hiroi et al., 1995).

The low velocity (5-8 $km \cdot s^{-1}$; Williams et al., 2014a) of impactors has continuously gardened the regolith and exposed the subsurface (Pieters et al., 2012) throughout the history of Vesta's

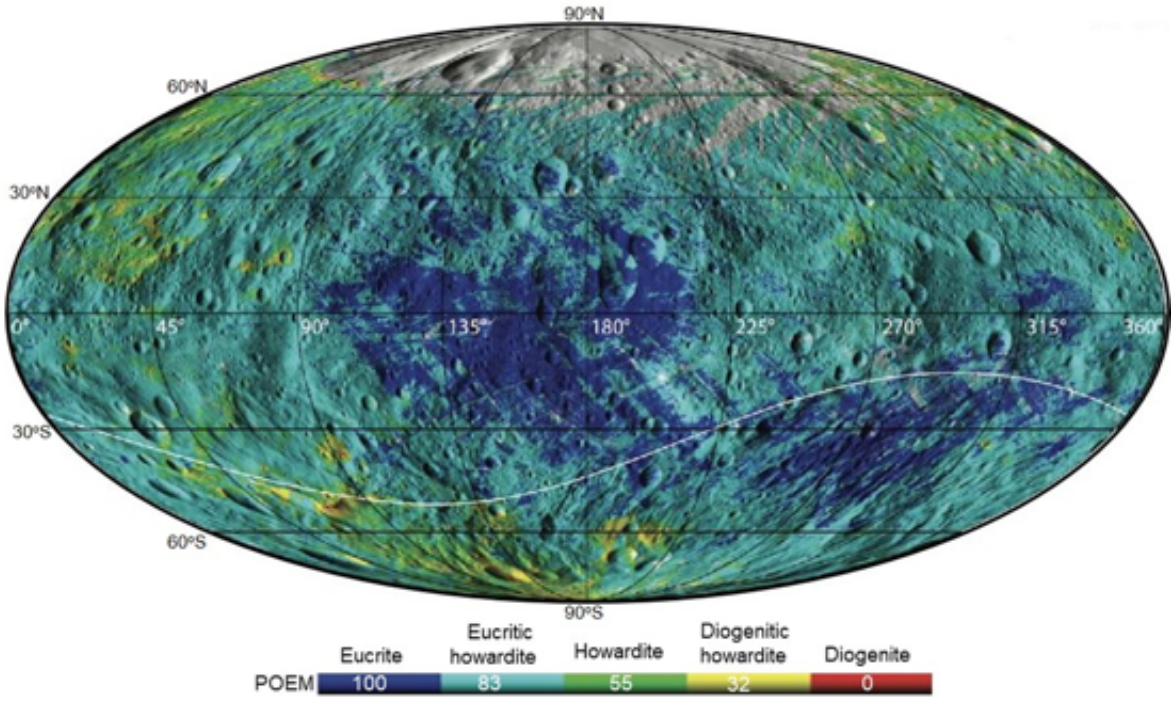

Figure 2.12 HED map of Vesta. The global surface composition map is prepared from the VIR spectrometer (From McSween Jr. et al., 2019, Copyrights 2019 with permission from Elsevier GmbH). The numbers denote average POEM (Percent Of Eucritic Material) values estimated from the absorption band centered approximately at 0.9 μm (BI) and 1.9 μm (BII), in relation to pure Eucrite and Diogenite. The high concentration of diogenitic howardite rocks in southern and western flank of Rheasilvia whereas high amount of eucrite and eucritic howardite is exposed near the equator. The white line denotes the outline of Rheasilvia basin. The map is in Mollweide projection (area in equal projection).

evolution. Some of the youngest impactor material uncovered at the crater walls and/or ejecta patches is mixed with the regolith (Jaumann et al., 2014), whereas deposits of dark presumably impactor material are also prominent on the surface of Vesta with low-albedo reflectivity (Jaumann et al., 2012; McCord et al., 2012; Reddy et al., 2012a). The source of the dark material is thought to be exogenic carbon rich low velocity impactor material (Jaumann et al., 2014; Reddy et al., 2012b).

Howardites are mixture of both eucrites and diogenites with minor elements of olivine, Mg, Fe and quartz (Ammannito et al., 2013). The presence of HED on Vesta was first obtained via images acquired from the HST[3] (Thomas et al. 1997a; Zellner et al. 1997) and noticed significant longitudinal variability (Binzel et al., 1997). The VIR images were able to reveal the presence of diogenites within Rheasilvia basin floor where as eucrite within regolith were located near to the equatorial latitudes (Ammannito et al., 2013; De Sanctis et al., 2012). The distribution variability of HED and their relations with surface features implies that eucrite was present within upper the regolith of the Vesta which was later redistributed due to the large Rheasilvia and Veneneia impact (Schenk et al. 2012; Jutzi et al. 2013; Figure **2.12**). Similarly, these impacts also excavated the diogenites and howardites from the deepest layer of Vesta and disseminate with ejecta blanket (Ammannito et al., 2013).

2.4.4 Gravity

The gravity field of Vesta was determined by monitoring the motion of the ground based Doppler tracking of the Dawn spacecraft along with FC data. The measurements were significantly improved as the spacecraft gradually acquired the imaging data at better resolution. The gravity field is influenced by the interior structure of Vesta which is divided into three layers: core, mantle and crustal (Zuber et al., 2011) as determined from HST measurements. The core has a thickness of ~110 km (Russell et al., 2011) with a density of 6000-8000 $kg \cdot m^{-3}$ (Toplis et al., 2013) whereas the crustal density is in the range of 2310-3440 $kg \cdot m^{-3}$ (Konopliv et al., 2014), determined based on a three-layer model (or Bouguer anomalies; Konopliv et al., 2014) and contribute to the surface gravity anomaly. Thus, gravitational heterogeneity of the surface reflects the poorly defined crustal boundaries (Raymond et al., 2014a).

The gravitational acceleration on Vesta ranges from 0.20 $m \cdot s^{-2}$ to 0.25 $m \cdot s^{-2}$ (Ermakov et al., 2014). Figure **2.13** illustrate the map of the gravity field of Vesta. It is clear that the region within vicinity of Marcia crater has high positive gravity anomalies and is related to a high density of mafic minerals (Konopliv et al., 2013; Ruesch et al., 2014a) whereas the Rheasilvia and Veneneia basins have low gravitational region and are probably connected to a thin crustal thickness (Ermakov et al., 2014).

[3] Hubble Space Telescope

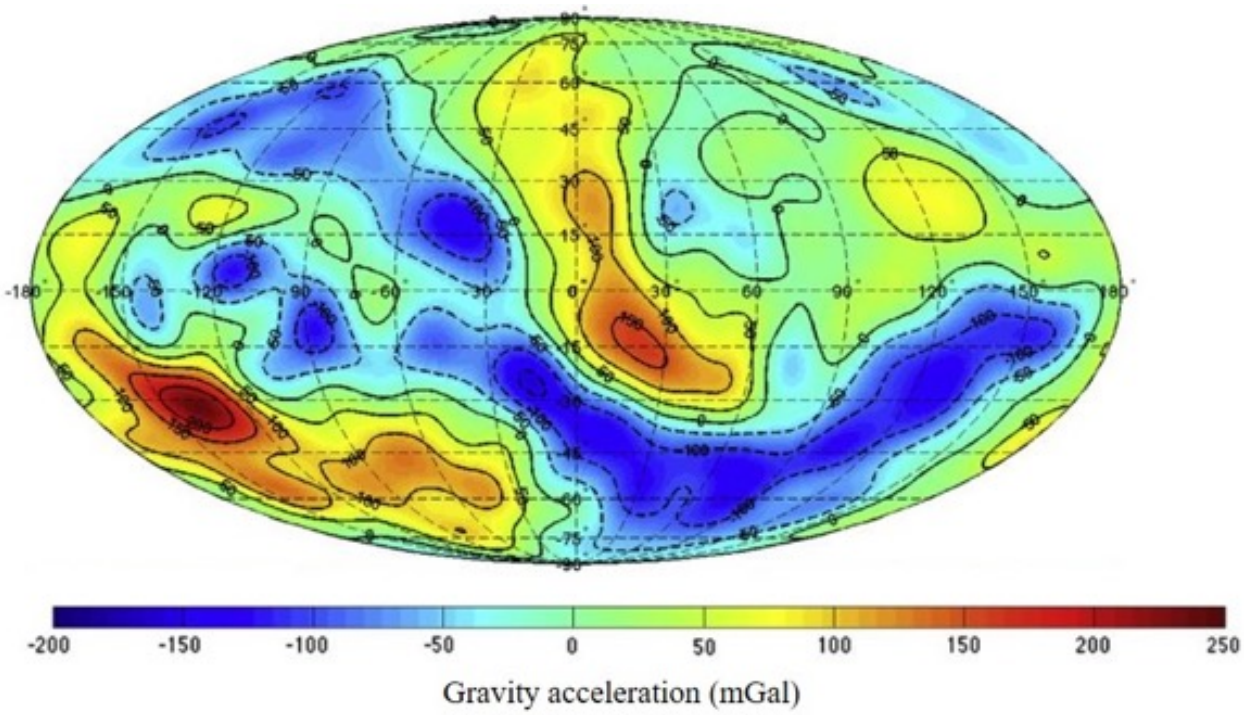

Figure 2.13 Bouguer anomaly gravity map of Vesta. The map is prepared on 290 ×265 km ellipsoid through harmonic degree 15 (from Konopliv et al., 2014, Copyright 2013 with permission from Elsevier Inc). Note that the highest anomaly region at lower left, Vestalia Terra. 1 m·Gal=0.01 m·s^{-2}. The map is in Mollweide projection (area in equal projection).

2.5 Asteroid (1) Ceres

The Dawn spacecraft orbited around Ceres for nearly 3.5 years from 2015 to 2018. During its maneuver, the spacecraft collected data at different altitudes and went down to ~35 km altitude during its extended phase. Table **2.4** summarizes the physical properties of Ceres estimated form the observation of the Dawn data.

Table 2.4 Physical properties of Ceres derived from the Dawn data (from Park et al., 2016a; 2018)

Parameters	Value	Error
Mean radius [km]	469.7	±0.3
Volume* [km^3]	434.13	±1.5×10^6
Mass [kg]	9.3833	±0.0001x10^{20}
Semi-major axis [AU]	2. 7670962	±1.01×10^{-11}
Surface temperature [K]	110-155	-
Bulk density [kg·m^{-3}]	2161	±2.5
Rotation rate# [°·day^{-1}]	952.1532	± 0.0001

*Derived from the best fit ellipsoid after Park et al., 2016a, # 950.1532635 °·day^{-1} derived after Park et al., 2018

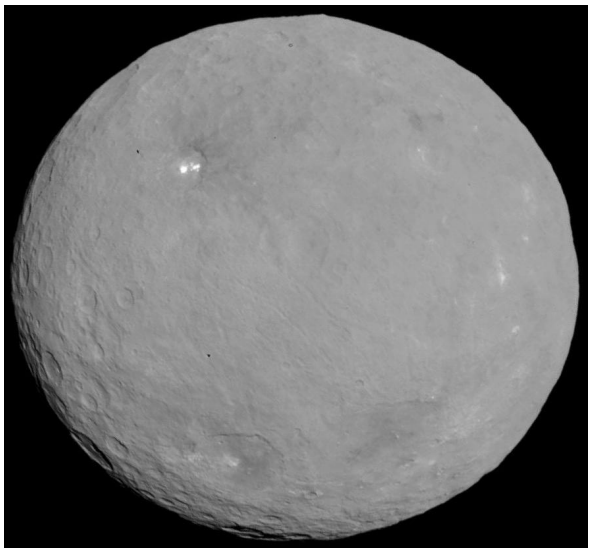

Figure 2.14 Mosaic of Ceres. The first high resolution (~140 m·pixel^{-1}) was prepared from the Dawn data (HAMO). Credit: NASA/JPL-Caltech/UCLA/MPS/DLR/IDA, source: https://photojournal.jpl.nasa.gov/catalog/PIA19562 .

Due to its size (483.1 × 481 × 445.9 km; Park et al., 2016a), Ceres is categorized as dwarf planet. Figure **2.14** illustrate the first mosaic derived from the Dawn LAMO datasets. The onboard FC instrument revealed various types of geological features including large variety of impact craters, tectonic features (Buczkowski et al., 2018a, b; Scully et al., 2017) diverse mass wasting impressions, flow features (Schmidt et al; 2017, Chilton et al., 2019; Hughson et al., 2019; Parekh et al., 2021a) and possible existence of viscous cryovolcanic features like the Ahuna mons dome (Ruesch et al., 2016; Sori et al., 2017). The VIR spectrometer helped to assert the large amounts of volatiles (mixed with magnesium, ammoniated phyllosilicates, carbonates and other salts) in the upper regolith layer Ceres (De Sanctis et al., 2016; 2018; Carrozzo et al., 2018). The data acquired form the GRaND complement the VIR imaging by confirming the presence of H_2O traces accurately within 1m of the surface layer near the poles (Prettyman et al., 2017; 2019b). Additionally, the elemental maps confirm the presence of abundance of carbon (8-14 wt%) and small amount of iron (15-17 wt%) which lead to conclude that Ceres has a relatively wet crust (Russell et al., 2016) and a partially differentiated interior (Prettyman et al., 2017).

2.5.1 Geology

Dawn observations expose the crustal complexity of Ceres by revealing the complicated surface morphology and composition. Overall, the surface of Ceres has been subject to constant resurfacing events due to distribution of local ejecta, exposure of fresh material (Palomba et al., 2019), blending and amalgamation of regolith with ice (Prettyman et al., 2019b) and impact heat driven excavation and/or vaporization (Raymond et al., 2020). The identified physical characters such as albedo, structures, morphology and topography are related to possible geological processes including volcanism, tectonism, impact catering and redeposition of material (Buczkowski et al., 2016).

The topographic maps prepared from the stereopairs of FCs' showed no sharp elevation discrimination (up to ~15 km relief), however distinct topographic advancement was noted in Hanami Planum region (lat.: 15˚N, long.: 240˚E) with strong a gravitational anomaly (Buczkowski et al., 2016; Ermakov et al., 2017). The stratigraphic model divides the surface of Ceres into two

parts: (i) younger Hanami Planum highland which is >2 Gyr old (Frigeri et al., 2018) and (ii) relatively older surrounding planitiae with absence of 100 km or larger crater (Marchi et al., 2016).

The surface of Ceres is rich with complex impact craters (Hiesinger et al., 2016), crisp impressions of linear structures, bright faculae and cryovolcanic domes and mounds (Buczkowski et al., 2016; Figure **2.15**). Impact crater on the Ceres has dynamic range of morphological features and are associated with varying degree of relaxation phenomena (Bland et al., 2013; Hiesinger et al., 2016). Most of resurfacing events by ejecta spread were led via formation of large craters such as Occator, Urvara, Yalode and Kerwan (Hiesinger et al., 2016). One of the most distinguished and highly complex craters, Occator (dia.: ~92 km) is stretched form equator to northern highlands and consist of bright spots at its floor which are formed due to the outgassing and/or desiccation of brine materials (Raymond et al., 2020; Section **2.5.2**). Several impact craters also have floor fractures which are distributed radially (Buczkowski et al., 2016; 2018b). Based on the orientation of fractures and their distribution, the possible involvement of subsurface magnetic intrusion (Buczkowski et al., 2018b) or viscous relaxation was proposed (Bland et al., 2016). The fresh exposed water ice traces were also detected via VIR observation above ~30˚ latitudes including Oxo crater (Combe et al., 2019) whereas VIR observation detected Mg-bearing and NH_4-bearing phyllosilicates within Haulani crater (Tosi et al., 2018). Few sets of regional linear structures (pit chains, troughs, grooves and graben) were noted within the Samhain Catenae region (lat.: 6.13˚N; long.: 247.4˚E; Buczkowski et al., 2016; Scully et al., 2017). Even though their similar morphology, the formation of linear structures is either related to subsurface tectonic activities (Buczkowski et al., 2018b; Scully et al., 2017) or linked to impact crater formation (Otto et al., 2019). A large number of dome-like features were also significant on Ceres with varying sizes. Among them, Ahuna mons (lat.: 10.5˚S; long.: 316.4˚E) is one of the tallest (~4 km high and ~21 km wide) mountains and most likely a cryovolcanic edifice (Ruesch et al., 2016) produced from the recent extrusion of the silicate, brines and water ice mixtures (Ruesch et al., 2016; Sori et al., 2017). Some of the smaller mounds known as pingo-like structures (<10 km in dia.; < 1 km in height) are populated within smooth impact material (Sizemore et al., 2019; Schmidt et al., 2020) and are influenced by the periglacial activities within interiors of the asteroid. Global distribution of mass wasting flows (Chapter **7**) with discrete characteristics and flow patterns suggest the involvement of water ice within the upper regolith layer (Schmidt et al., 2017; Duarte et al., 2019, Chilton et al., 2019, Parekh et al., 2021a). The morphometrical measurements of the mass wasting deposit mobility and their comparative analysis disclose the strong dichotomy with deeper water ice within the equatorial region in comparison to the poles where ice is present close to the surface (Schmidt et al., 2017; Parekh et al., 2021a). In coming section, brief geological background of three craters namely Occator, Azacca and Urvara is discussed due to their close association with pit chains (Chapter **6**; Section **6.4**).

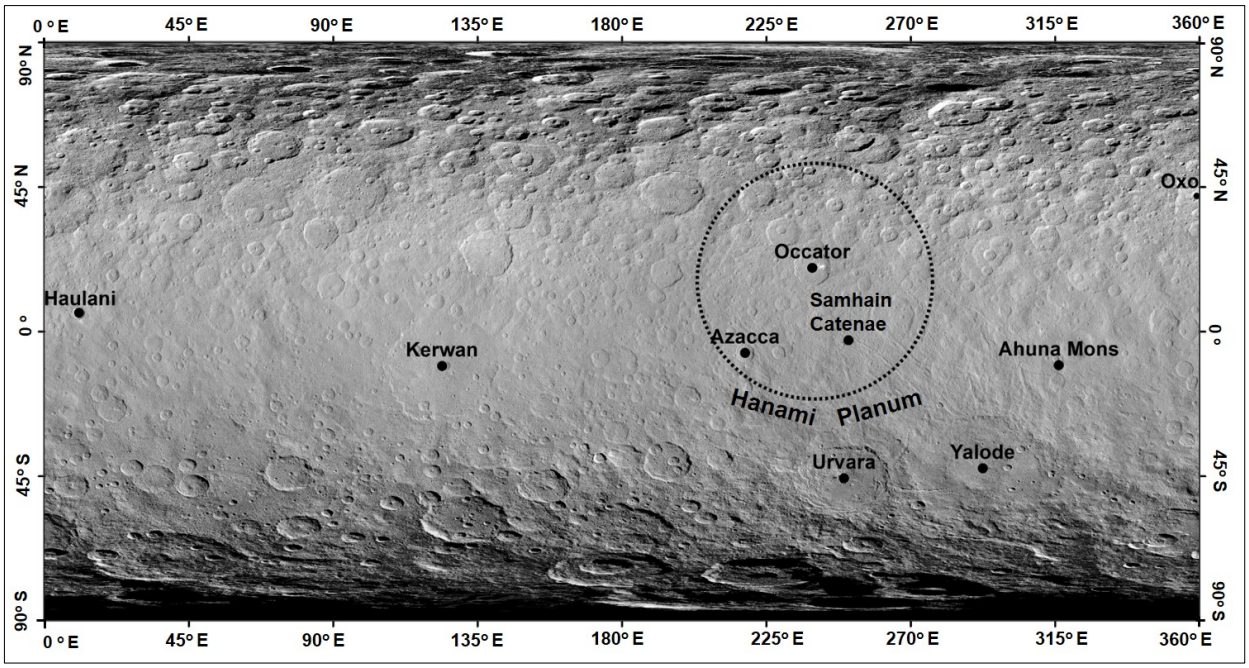

Figure 2.15 Map of Ceres. Global equidistance map of Ceres prepared from LAMO data (resolution: 35 m·pixel^{-1}; Roatsch et al., 2017). The highlighted geological features are discussed in the text. The dotted black line highlights the region of Hanami Planum.

2.5.2 Occator crater

The LAMO images (~35 m·pixel^{-1}) and XM02 data (up to 2.5 m·pixel^{-1}) exposed the minor surface features within the floor of Occator carter. The crater with the diameter of ~92 km (lat.: 19.8˚ N, long.: 239.3˚E) and consists of chaotic terrain (Buczkowski et al., 2018; Schenk et al., 2018). Occator lays within Hanami Planum (Figure **2.15**) where the crustal thickness is ~52 km (Scully et al., 2018; Ermakov et al., 2017). The floor of Occator has multiple features which denotes that the crater is geologically active region until recent time (~2 Myr; Neesemann et al., 2019; Nathues et al., 2020). The crater has a central pit with a complex dome structure at the center of the floor (Schenk et al., 2016; Nathues et al., 2020). Extensive lobate flow features rich in phyllosilicates cover large areas in southeast floor of the crater indicating impact melt deposits with mud-like consistency (Schenk et al., 2020). The entire crater floor is cut by the diverse group of linear structures including pit chains, toughs, grooves (Buczkowski et al., 2018a; Scully et al., 2020; Nathues et al., 2020) whereas few fractures are also present around the crater rim and the ejecta covered surface (Otto et al., 2019). The bright spots of Vinalia Faculae (north-east) and Cerealia Faculae (center of the crater) is rich with salts and carbon (including Sodium) which are possibly transported to the surface from either the deep-rooted hydrothermal reservoirs (Castillo-Rogez et al., 2019; Hesse & Castillo-Rogez, 2019; Quick et al., 2019; Raymond et al., 2020; Scully et al., 2018) or delivered via an exogenic impactor (Schenk et al., 2020; Scully et al., 2020). Recently, the data from the extended Dawn mission revealed pingo-like mounds (~10 m tall; Schmidt et al., 2020; Schenk et al., 2020). These pingos are associated with relatively young water rich flow features that are deposited post impact and later refroze with ice in its core (Schmidt et

al., 2020). Schenk et al. (2020) also summarizes the other small-scale features (like pit chains, fractures) within the crater floor which improvised understanding related to brine distribution. Based on the morphological, chronological and compositional evidence it is reasonable to infer that a large-scale post-impact surface evolution process has taken place within Occator crater floor which involves multiple expressions of volatile and brine transportation (Schenk et al., 2019; 2020; Nathues et al., 2020; Scully et al., 2020; Raymond et al., 2020; Schmidt et al., 2020; Park et al., 2020; Section **6.6.1**).

2.5.3 Azacca crater

Azacca crater is ~49.9 km in diameter located at 61˚S, 218˚E. The crater has flat smooth floor with central peak, floor fractures and some degraded pits (Sizemore et al., 2017). The stratigraphic model derived the age of Azacca crater ~76±10 Myr (Schmedemann et al., 2017). Otto et al. (2019) observed large population of fracture in northeast direction beyond the rim of the crater and modeled the horizontal surface stress require to generate the fractures, suggesting the presence of a low-viscosity crustal layer resting at the top of a rocky-brittle regolith layer under equilibrium condition (Otto et al., 2019; Section **6.6.2**).

2.5.4 Urvara crater

Urvara basin has diameter of ~170 km and located at 45˚S, 250˚E. This large basin reveals varying degrees of preserved morphological features including terraced rim structure, intermixed smooth ejecta materials, lobate mass deposits, central peak, set of floor fractures and relatively small younger impact craters (Crown et al., 2018). The estimated age for the Urvara impact basin is 550±50 Myr with younger ejecta material (~420±70 to190±20 Myr; Crown et al., 2018). The younger Urvara basin is adjacent to the Yalode impact basin and thus the northern floor of Urvara comprise material from both basins (Crown et al., 2018). The terraced rim wall at the southern and western part of Urvara exhibits localized ice-rich mass movement and steep scarps (at northeast) indicating the high friction of the crustal material (Crown et al., 2018). The shallow, linear to curvilinear troughs and grooves are closely packed in a group, short in length, parallel to each other present on the Urvara floor material and Urvara/Yalode mixed material implying the different timeline for their formation (Crown et al., 2018). The observed morphological characteristics and geological environment within the Urvara impact basin reveals the extrusion and redistribution of volatile rich material via localized transportation (Section **6.6.3**).

2.5.5 Regolith of Ceres

The GRaND instrument has detected the presence of hydrogen with higher concentration at the poles reflecting abundance of aqueously altered regolith rich with water ice and other volatiles (Figure **2.16**; Prettyman et al., 2017; Schörghofer et al., 2016). According to physical models, the ice within the regolith layer was lost due to sublimation (Prettyman et al., 2018; 2017) and is highest in the warmer equatorial regions in comparison to the poles due to which the ice is present at greater depth on mid latitudes (Bland et al., 2016; Sizemore et al., 2019). However, this does not imply that the ice is completely scarce at mid latitudes. LAMO images expose small bright patches (Combe et al., 2016; 2019), pitted terrain (Sizemore et al., 2017) and lobate flow related

morphology (Schmidt et al., 2017; Hughson et al., 2019; Parekh et al., 2021a) which is controlled by the abundance of ice within the regolith suggesting small amount of ice within the upper regolith of the equatorial belt.

The mineralogy map obtained by VIR of Ceres' regolith shows that the surface is rich in Mg-phyllosilicates, ammonium-bearing carbonates, magnetite or graphitized carbon (De Sanctis et al., 2015b; Ammannito et al., 2016; Figure **2.16**). Due to the warm interior at the equator the ice melted and produced liquid water that converted silicates to generate Fe-serpentine and clay minerals (McSween et al., 2017). The neutron detector captured the Fe distribution and reveled the profound decrease of the concentration towards the poles (Prettyman et al., 2017). The gravity measurement suggested that Ceres has a rocky interior and a volatile enriched unstable crustal material related to CI and CM carbonaceous chondrites (Prettyman et al., 2017; 2019). Thus, combined evidences from the GRaND and VIR data implies that ice-rock fractionation occurred on a global scale and the presence of ice rich regolith from lower to higher latitudes confirms the survival of ice for billions of years within a few meters of the surface of an airless body (Prettyman et al., 2017). In general, Cere's regolith is consisting of extensively aqueously altered regolith which is highly exceptional case considering the carbonaceous chondrite as closet analogue of Ceres.

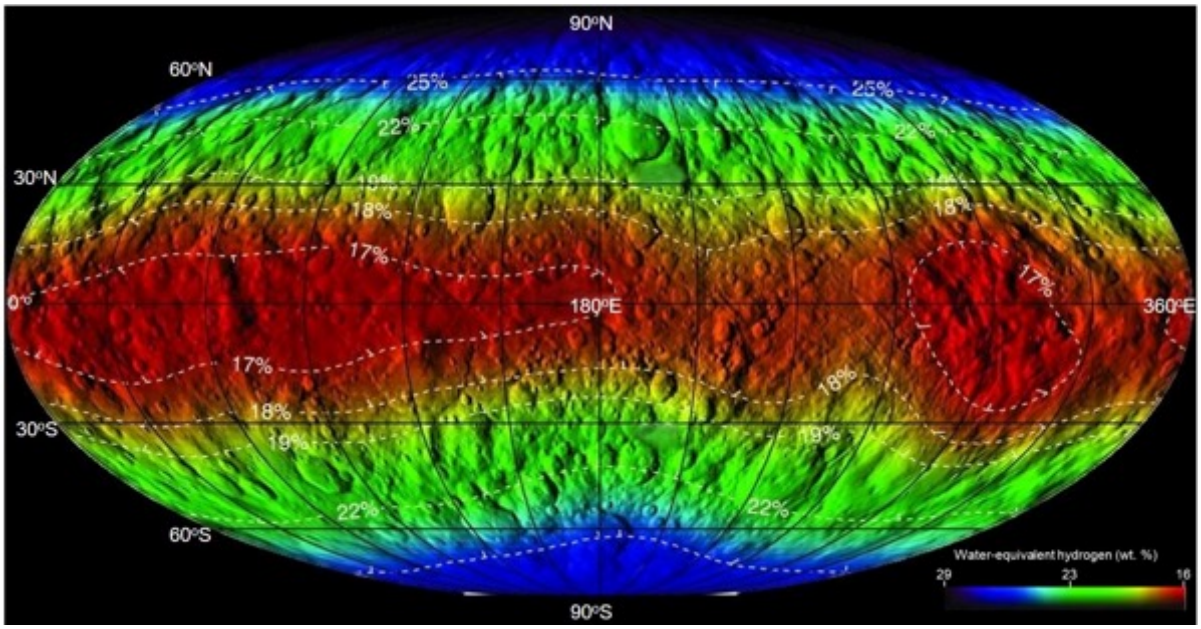

Figure 2.16 Map of distribution of Hydrogen on global scale on Ceres. It is prepared from the thermal and neutron counting data. The white dashed lines highlighted the percentage of hydrogen within Ceres regolith. The hydrogen is reported in terms of Water Equivalent Hydrogen (WEH) which mean the percentage (by weight) of H_2O within the regolith is equal to all the detected hydrogen present in the form of H_2O. The map is in Mollweide projection (equal area projection). It is reproduced from the paper by Prettyman et al., 2017, Copyright 2017, with permission from American Association for the Advancement of Science

2.5.6 Gravity

Likewise Vesta, the gravity field of Ceres is also determined from radiometric Doppler tracking and FC data acquired by the Dawn spacecraft (Konopliv et al., 2018). The gravity field on Ceres is relatively lower due to airy isotopic interior compensation (Park et al., 2016; Ermakov et al., 2017; Fu et al., 2017). The mean gravitational acceleration on Ceres amounts to 0.27 $m \cdot s^{-2}$ (Sori et al., 2020; Bland et al., 2019). The Bouguer anomaly map is determined by variations of the topography with a constant crustal density of 1400 $kg \cdot m^{-3}$. Figure **2.17** illustrate the map of the gravity field on the surface of Ceres. It is clear that the region within vicinity of Urvara crater has one of the highest positive gravity anomalies whereas Occator and Hanami Planum have a low negative anomaly which are probably connected to large brine reservoir beneath the crust (Raymond et al., 2020).

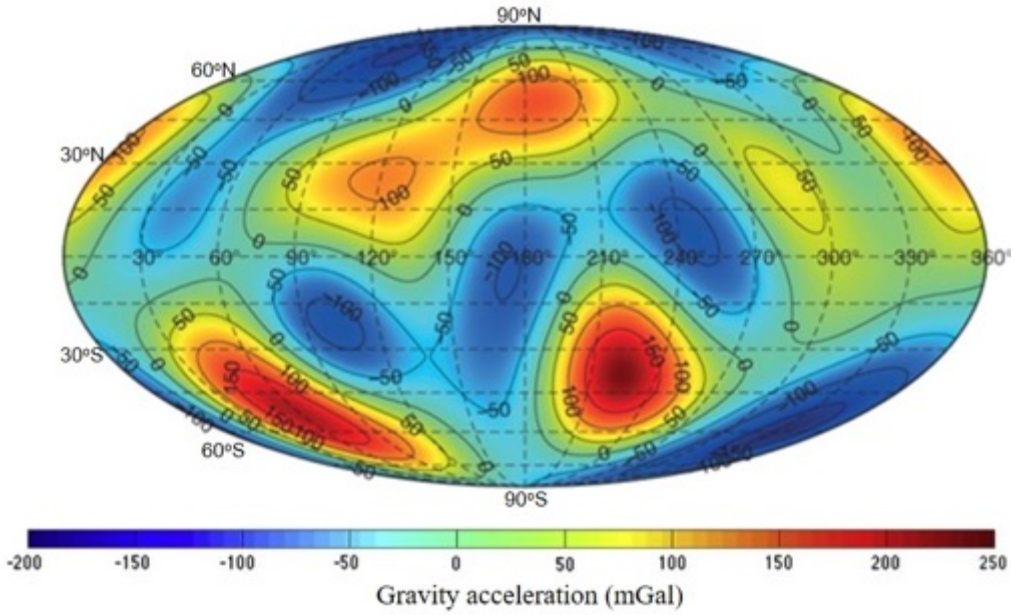

Figure 2.17 Bouguer anomaly gravity map of Ceres. The map is prepared onto 482 × 482 × 446 km ellipsoid through harmonic degree 5-14 (from Park et al., 2016, Copyright 2016, Macmillan Publishers Limited, part of Springer Nature). 1 m·Gal = 0.01 $m \cdot s^{-2}$. Bouguer anomaly is inverse relation with surface topography and is ranging from -250 m·Gal to 250 m·Gal (Park et al., 2016; Ermakov et al., 2018). Note the highest positive anomaly is within the Urvara crater (lower right) and a relatively low anomaly occur in the Hanami Planum region between 15˚N, 240˚E (in the center). The map is in Mollweide projection (equal area projection).

3. GEOLOGICAL BACKGROUND

3.1 Volatile related morphology

The exploration of asteroid surfaces in the past decade has revealed some exotic and peculiar surface features which are closely related to volatile activities. It is essential to understand the volatile distribution in the solar system due to its capability for sustaining life and the potential to produce rocket fuels for future planetary mission. The surface of Vesta and Ceres exhibits unique and unexpected geological characteristics due to the rheology of ice and sources of volatiles. Both Vesta and Ceres are airless bodies, therefore it is challenging to observe direct evidence related to volatiles without spectral information due to its ability to manifest surface and near surface composition. Besides, given the large difference in surface temperature and pressure, volatiles cannot survive in their pure nature when encounter the harsh environment of space. However, while mixed with regolith and other impurities, they are stable for relative longer time and leave behind the tail of geomorphological expressions which help to trace their presence within planetary objects.

Initial observations with earth-based telescopes suggested presence of volatiles and water-ice on the surface of Vesta and Ceres. In fact, it was one of the driving factors which lead the planning and execution of the Dawn mission (Russell et al., 2006). The instruments, on board the spacecraft acquired high resolution surface features which includes the geomorphological characteristics (such as relaxed crater, central pit craters, large domes, mounds, mass wasting deposits, pitted materials, curvilinear gullies, pit chains fractures, and smooth depressions and scarps) with potential relevance to volatiles (Sizemore et al., 2019a and reference therein). Overall, Vesta and Ceres has experienced volatile related erosional and resurfacing process at a global and localized scale which has altered the regolith layer (Hiesinger et al., 2016; Jaumann et al., 2012). The erosional process includes, (i) infilling of existing depressions by the emplacement of voluminous ejecta melts and dry regolith (Parekh et al., 2021b; Williams et al., 2014a), produced from the constant bombardment and (ii) compression and dispersion of material (induced by the large temperature difference) which give rise to coherent network of fractures and linear structures (Buczkowski et al., 2018b; Scully et al., 2018) and (iii) widespread long-run out mass wasting deposition (Schmidt et al., 2017; Hughson et al., 2019) which affects the surface elevation and exposes fresh bright subsurface substances (Parekh et al., 2021a). The analysis of these landforms suggested that Vesta has a relatively low concentration of localized volatiles (Denevi et al., 2012; Scully et al., 2015, Parekh et al., 2021b) whereas, Ceres is wet body with heterogenous distribution of subsurface ice and other volatiles in the upper ~10 km of the crust (Sizemore et al., 2019; Bland et al., 2016; Otto et al., 2019; Hiesinger et al., 2016). Each of these erosional processes involves regolith mobility and deposition which depends on the amount and distribution of the volatile substances. Thus, in this thesis, I focused onto the independent study related to production of smooth regolith deposits, pit chains and mass wasting to (i) establish potential relation between volatiles and surface regolith and further (ii) evaluate and compare the abundance and distribution of volatiles on Vesta and Ceres.

3.2 Ponded deposits

In order to understand localized volatile distribution on Vesta, the unusual pond deposits were analyzed (Chapter **5**). In general, they are also present on airless bodies such as Eros, Itokawa and the Moon. On Eros and Itokawa, they are formed by the transportation and accumulation of granular regolith and are known as 'dust ponds' (Robinson et al., 2001; Robinson et al., 2002; Sears et al., 2015; Fujiwara et al., 2006; Saito et al., 2006; Hawke & Head, 1977a; b; 1979). Grainy regolith is mobilized and deposited on regions of lower gravitation which then experience the sorting mechanism (Robinson et al., 2001; Veverka et al., 2001a; Cheng et al., 2002). During the sieving process, the coarser grains are liberated from the fine particles producing smooth pond-like impressions (Cheng et al., 2002; Robinson et al., 2001; Thomas et al., 2002; Veverka et al., 2001a). On the contrary, pond deposits on the Moon are produced from the confinement and/or emplacement of impact melts (Hawke & Head, 1977a; b; 1979). As a part of the ponding process, the temperature drops and the solidification of melt deposits creates smooth pond surfaces which are known as 'melt pools' (Hawke & Head, 1977a; b; 1979; Plescia & Cintala, 2012; Stopar et al., 2014). There are few common characteristics between dust ponds of Eros, Itokawa and melt ponds of the Moon such as: identified on low topographic location, smooth and levelled surface, often the deposit surface has low slopes, usually confined at the bottom of crater floors and embayed by a strong boundary between the deposit and the carter walls (Parekh et al., 2021b). However, this does not mean that there are no obvious differences between Eros, Itokawa and the lunar ponded deposits. The key difference is that on Eros and Itokawa granular ponded features are mostly present either in the equator region or they are observed within low gravitational zones whereas on the Moon, smooth deposits are not correlated with gravity and/or location (Stopar et al., 2014; Hawke & Head, 1977a; b; Plescia & Cintala, 2012). Figure **3.1** shows the example of ponded deposits identified on Eros and the Moon.

Pond deposits observed near the equator region on Vesta, shows similar characteristics as dust ponds of Eros, Itokawa and also melt pools of the Moon. From the Dawn data, it was clear that Vesta has overall dry surface compounds (Jaumann et al., 2012) but there are also localized evidences (flow lobes, striations) supporting the involvement of wet regolith movements (Williams et al., 2014a; Scully et al., 2015; Denevi et al., 2012). Based on the variation in the distribution and morphology of pond deposits, it is reasonable to suspect the influence of multiple mechanisms in transportation and accumulation of regolith material to justify the dichotomy of pond deposits on Vesta. So far, (i) seismic shaking (Robinson et al., 2001; Fujiwara et al., 2006), (ii) electrostatic levitation of dust particles (Lee, 1996; Roberts et al., 2014; Robinson et al., 2001; Veverka et al., 2001a), (iii) kinetic sieving (Robinson et al., 2001; Thomas et al., 2002; Veverka et al., 2001a; Fujiwara et al., 2006; Saito et al., 2006), (iv) disintegration of boulders (Dombard et al., 2010), (v) violent outgassing of volatiles from the subsurface (Sears et al., 2015) and (vi) emplacement of melt due to impact might be responsible (Hawke & Head, 1977a; b; Plescia & Cintala, 2012; Stopar et al., 2014) for the transition and further accretion of the surface material on Eros, Itokawa and the Moon. Given the regolith conditions and morphological features of ponds deposits on Vesta, seismic shaking, segregation and volatile outgassing is possibly involved in production of dust

deposits whereas downslope movement of impact melt suggests production of melt pond deposits (Parekh et al., 2021b). Hence the following discussion is focused onto these three mechanisms.

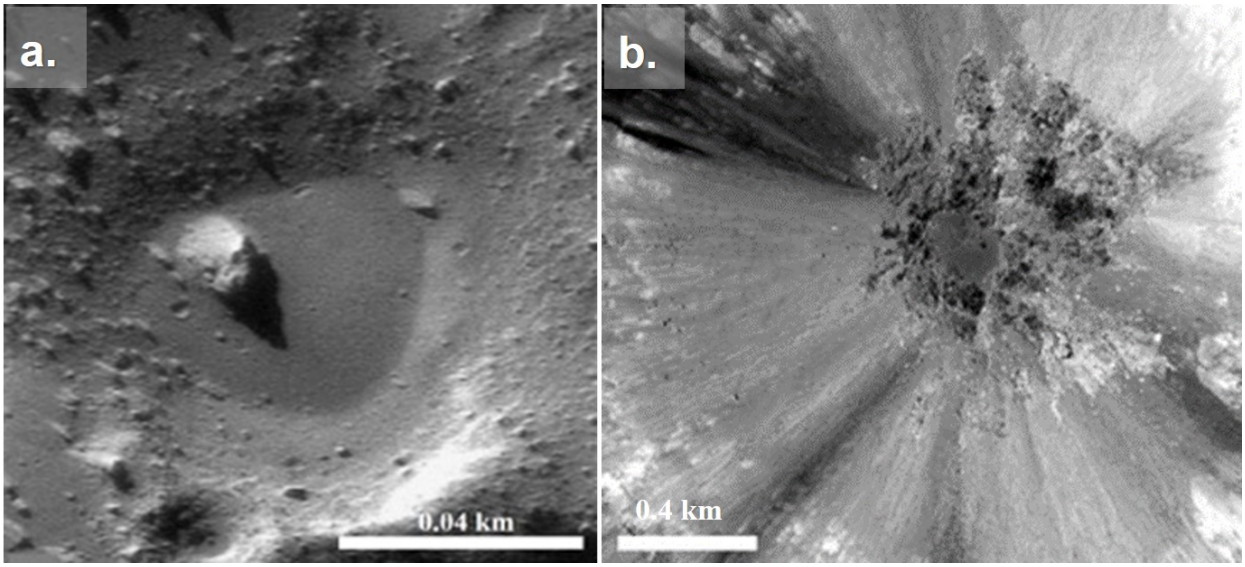

Figure 3.1 Examples of ponded deposits. (a.) dust deposits at crater floor on Eros (lat.: 179.04°W, long.: 2.42°S, and (b.) melt pool at the crater floor of the moon (lat.: 8.6°W, long.: 1.48°S).

3.2.1 Transportation and segregation of granular regolith

Likewise, Eros and Itokawa, the overall surface of Vesta has a granular regolith (Jaumann et al, 2012). Such material is mixture of various size and shape of particles which have the ability to retain any shape of the vessel containing them and thus shows fluid like characteristics (Richard et al., 2005; Jaeger et al., 1996). Nevertheless, they are not considered as fluid due to their potential to pile-up (Murdoch et al., 2015). The discussed mechanisms below involve mobility of dry granular medium is present.

Seismic shaking: Formation of fresh impact carters and excavation of old ejecta are common outcome resulting from an impact on the asteroid surfaces (Richardson et al., 2005). Post-impact, the surface regolith is severely shaken due to the attenuation of the seismic waves and often disturb the equilibrium state of the asteroid surface, inducing mobility of the material (Murdoch et al., 2015). The seismic diffusion weakens as it dispersed over long distances but has significant consequences on small asteroid surfaces (Richardson et al., 2020). Thomas & Robinson (2005) observed removal of 40% surface features (craters <0.5 km in dia.) as a consequence of production of >7.6 km diameter crater on Eros. Thus, attenuation of seismic energy is crucial in the case of dry granular regolith. Richardson (2005) developed numerical model for seismic diffusivity and infer that the size of the asteroid is an important factor to determine surface acceleration of material against gravity. On the surface of smaller planetary objects (≤50 km; Richardson et al., 2020), even small sale impactor produces relatively unusual vibrations within regolith particles at a global scale (Murdoch et al., 2015; Richardson et al., 2020). Given the location and size of Vesta, it is evident that the surface is exposed to multiple simultaneous impacts which has capacity to generate high frequency seismic energy (Williams et al., 2014a). The reverberations of seismic energy may also

cause some other localized disturbances (like rapid release of heat and cooling) due to which the surface experiences contraction and expansion of materials. When the asteroid surface undergoes this cycle frequently, it eventually shows the displacement and mobility of material (Murdoch et al., 2005).

***Regolith segregation*:** Segregation of granular particle is one of the prominent processes via which the pond deposits are able to achieve the typical smooth nearly flat surface (Veverka et al., 2001a; Fujiwara et al., 2006; Cheng et al., 2002; Thomas et al., 2002; Robinson et al., 2002). As the granular material falls downslope, the smaller particles fit efficiently into the open space (Veverka et al., 2001a). Thus, the smaller particles are drained in and concentrated at the lower regions whereas the larger grains are push towards the surface (Gray & Chugunov, 2006) and degrade or erase the morphology (Veverka et al., 2001a). This phenomenon requires the granular regolith material and is strongly dependent on the surface gravitational acceleration (Thornton, 2005; Murdoch et al., 2013c).

Volatile outgassing: Most of the proposed mechanisms involve the transportation of granular regolith material on the surface. However, Kareev (2002) and Haseltine (2006) conducted an experiment that showed the dust deposition from the subsurface via volatile outgassing. In addition, when experiment conducted under microgravity condition, it showed similar effect of granular fluidization (Franzen et al., 2002; Moore et al., 2003). In this experiment, the sample of loose unconsolidated surface material is covered with relatively large size pebbles (cm size). Later, the sample was placed within the chamber and water vapor was passed through the bottom of the sample. During degassing, the granular material beneath the pebbles was lifted with vapor and the churning continued until the supply of water vapor exhausted. At the end, a depression of fine granular material was formed around the outgassing region of the vapor whereas relatively large pebbles were concentrated at the outer rim of the depression creating a crater-like impression (Sears et al., 2015). The process of the experiment is illustrated in Figure **3.2**. During initial condition of the experiment, larger pebbles were present at the surface but at the end, they were partially buried at the outer rim. Additionally, the displacement of regolith also produced depression which is not a typical impact crater but has circular shape with relatively shallow floor and is covered by granular material. During the experiment, the vapor was produced due to the sublimation of ground ice and water, hence presence of volatiles plays a pivotal role. To follow this phenomenon, the surface requires volatile substances within the regolith material. On Vesta too pitted terrain and gully formation implied the low amount of volatile presence which potentially induced degassing and fluidization activity (Denevi et al., 2012; Scully et al., 2015). Thus, the proposed mechanism hold potential to produce dust pond deposits also on the Vesta.

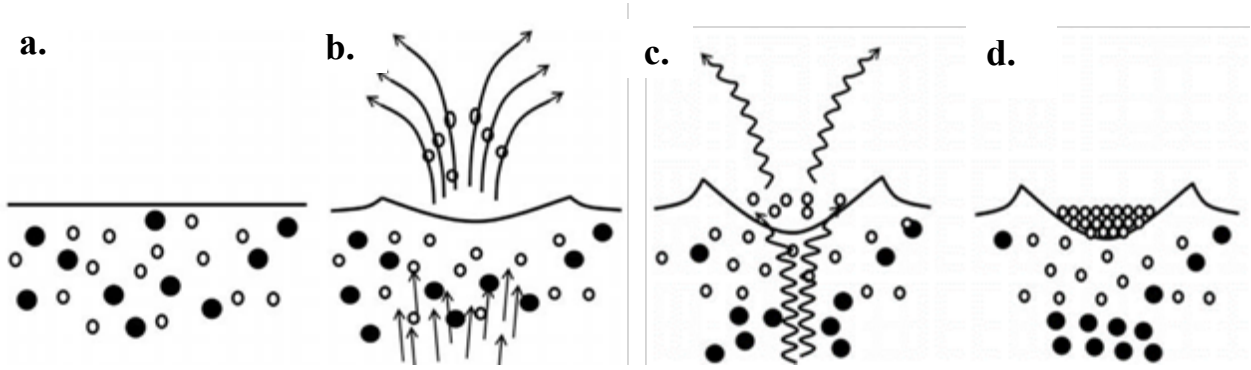

Figure 3.2 Schematic illustration volatile degassing. (a.) A mixture of fine and coarse material experiences devolatization (b.) from the bottom. Consequently, the fine particles were lifted from the subsurface and resettle near the venting region. (c.) The fine particles undergo lifting and resettling cycles until the vapor is too weak to levitate dust. (d.) During the resting stage, a cone-shaped depression is created where fine particles are mobilized at the lowest region. (Sketch is form Sears et al., 2015, reused with permission from Elsevier Inc., Copyright 2015).

3.2.2 Emplacement of impact ejecta melt

On Vesta, melt pond are observed which has similar characteristics to the impact melt ponds of the Moon (Chapter 5). On the moon, the production of a melt pool is attributed to the emplacement of impact melt produced via cratering process as a result of shock (Gault, 1968; Osinski & Pierazzo, 2013). Because of high velocity impact, the temperature of surface rises above 1000˚C (Stöffler, 1971; Ahrens & O'Keefe, 1972; Hörz & Cintala, 1997; French, 1998) causing melting of surface material (Stopar et al., 2014). The shock energy available to produce impact melt is correlated to the velocity and size of the impactor, volatile content of the surface material and porosity (Grieve et al., 1977; Wilhelms et al, 1987; Melosh, 1989; Hörz, 1991; Cintala & Grieve, 1998; Osinski et al., 2011; Collins et al., 2012; Osinski & Pierazzo, 2013).

The produced impact melt plays an important role in the production of melt pools which has similar characteristics as melt ponds on Vesta. During the impact, large portion of material occupies the lower part of the craters whereas a portion of melt is also mixed with ejecta and emplaced within exterior of the crater. After the excavation process, crater undergoes a modification during which some of the melt and wall debris were dragged downslope under the influence of gravity (Hawke & Head, 1979; Melosh, 1989; Cintala & Grieve, 1998; Melosh & Ivanov, 1999; Bray et al., 2010). Within the crater floor, the melt intermixes with brittle material and breccias which later solidifies as temperature goes down, forming a pond of impact melt (Howard & Wilshire, 1975; Hawke & Head, 1979; Melosh,1989; Stopar et al., 2014). The melt ponds identified on the moon are usually associated with larger craters (e.g. Giordano Bruno, dia.: ~22 km; King crater, dia.: ~77 km; Copernicus crater, dia.: ~93 km) which have capacity to produce voluminous impact melt (Howard & Wilshire, 1975; Bray et al., 2010; Ashley et al., 2012; Wagner & Robinson, 2014). Further, ejecta mixed melt is emplaced in the neighboring regions of the craters following the topographic slops and depressions, which potentially result into pond and/or flow lobes (Howard

& Wilshire, 1975; Hawke & Head, 1977b; Denevi et al., 2012). In addition, the angle of impactor also plays an important role in the distribution of melt around the crater (Shoemaker et al., 1968; Howard & Wilshire, 1975). Near vertical impactors confine impact melt within the crater floor whereas azimuth impacts allow melt to escape by excavating material from the floor (Hawke & Head, 1977; Neish et al., 2014).

Observed melt ponds are present within the exterior of Marcia impact crater. Due to its location within inner asteroid belt, it is hypothesized that Vesta might have experience infrequent high velocity impactor. Moreover, there are only few large craters (≥10 km in dia.; Liu et al., 2018) present on the surface of Vesta which can produce voluminous impact melts (Williams et al., 2014a) hence the melt ponds are not observed at global scale (Parekh et al., 2021b). Based on the surface topography and the close association of pond deposit with large carters, a possible emplacement of impact melt might be responsible for the production of melt pond on the Vesta (Section **5.6**).

3.3 Pit chains and troughs

In an analogy to understand influence and regional distribution of volatiles on Ceres, localized analysis of pit chains is carried out. Overall, pit chains are produced due to the drainage of weaker material into the deeper inlet beneath (Horstman & Melosh, 1989). Gradually they are muted together, forming partially adjoined chains of circular to semicircular pits which are widen up further and known as troughs (Wyrick et al., 2004).

In general, the weaker material falls into the underlying void until the space is completely stocked up and is not able to accommodate any further substances (Hardy, 2021). The fully developed linear troughs are relatively wider and often has deep u-shaped bowl geometries. Pit chains have been studied across the surface of Earth, Mars, Venus, Phobos, Enceladus and many asteroids (e.g. Gaspra, Ida, Eros, Steins, Lutetia, Vesta, Ceres [Chapter **6**], MU69; e.g., Thomas et al., 1978; Solomon et al., 1992; Veverka et al., 1994; Sullivan et al., 1996; Prockter et al., 2002; Ferrill et al., 2004; 2011; Wyrick et al., 2004; Keller et al., 2010; Thomas et al., 2012; Davey et al., 2013; Buczkowski et al., 2014; Scully et al., 2017; Whitten & Martin, 2019; Schenk et al., 2020) and are formed via different subsurface deformation activities (Wyrick et al., 2004; 2010). Pit chains documented on northern Iceland are formed from the faulting caused by the basaltic lava intrusion (Whitten & Martin, 2019; Figure **3.3a**). On small objects like Eros, they are clustered within relatively thick regolith areas (Buczkowski et al., 2008; Figure **3.3b**). Group of parallel pit chains across Enceladus supports the hypothesis of dilatational faulting (Martin et al., 2016; 2017; Figure **3.3c**). Martian pit chains are clustered in the region which has experienced surface extension and are associated with graben and volcanic edifices (Ferrill et al., 2014; Wyrick et al., 2004; 2010; Figure **3.3d**). Therefore, analysis of pit chains not only exposes the layered regolith heterogeneity but also offer insight into subsurface mechanisms which often otherwise can only be understood by in-situ measurements (Wyrick et al., 2010). Other than the above theories, few more hypotheses are postulated such as: dike swarms possibly associated with collapsed magma chambers (Mège et al., 2000; 2002; 2003); karst dissolution (Spencer & Fanale, 1990); fissuring beneath loose material

(Tanaka & Golombek, 1989; Banerdt et al., 1992; Tanaka, 1997); and dilational faulting (Ferrill & Morris, 2003; Ferrill et al., 2004; Sims et al., 2003; Wyrick et al., 2004) as a controlling theories for the production and distribution of pit chains on planetary bodies. On Ceres, small scale pit chains with varying pattern is observed which are associated with cryovolanic instruison and extension of brecciate fractures (Section **6.6**). These phenomena are also commonly observed on Earth, Moon, Mars (Xiao et al., 2010; Jozwiak et al., 2015) and discussed as following.

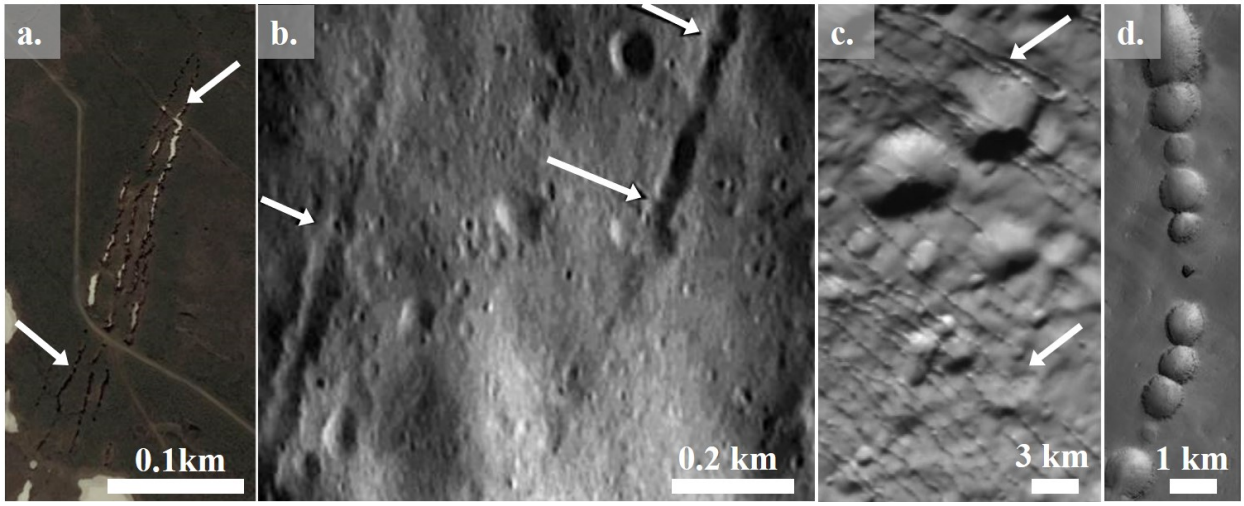

Figure 3.3 Example of pit chains observed on various planetary bodies. (a.) Linear group of pit chains observed in Iceland (Digital Globe; 0.5 m·pixel^{-1}); (b.) Circular to semi-circular pit chains observed on Eros (Buczkowski et al., 2008; Image: 135344864); (c.) Partially adjoined dense pit chains on Enceladus (Martin et al., 2017; Image: N1500061010; 134 m·pixel^{-1}); (d.) Circular pits observed on the southeast flank of Alba Patera on Mars (Ferrill et al., 2004; Image: PIA02874). Image (a.) is from Martin & Whitten, 2019 (Copyright 2019 with permission from American Geophysical Union) and (b.-d.) is from Martin et al., 2017 (Copyright 2017 with permission from Elsevier Ltd.)

Dikes: Dikes are subsurface vertical tube-like structures associated with the propagation of lava intrusion from a deep chamber. The vertical intrusion of lava carried out until it reached to the low density brecciate region. Due to neutral buoyancy, the propagation continues laterally producing strains within existing fractures and deforms the underlying region resulting into the sink holes. The Tharsis region on Mars has radial clusters of pit chains which are formed due to subsurface dike propagation (Mège & Masson, 1996, 1997; Liu & Wilson, 1998; Mège, 1999a, b; Montési, 1999; Mège et al., 2000; Scott et al., 2000, 2002; Gibbons et al., 2001; Wilson & Head, 2001, 2002). Often, the dike propagation is controlled by: (i) presence of permafrost or ground water which introduce vapor or water due to changing temperature. The pressurized vapor create dike like opening into which the overlying rock collapses. Often dike is in direct contact with the groundwater reservoir producing violent, phreatomagmatic eruption (Mège & Masson, 1996, 1997; Mège, 1999a; Montési, 1999), (ii) concentration of volatiles at the tip of dike pressurize the drainage opening (Liu & Wilson, 1998; Scott & Wilson, 2002; Wilson & Head, 2001; 2002) and

(iii) large Plinian eruption[4] causing the void underneath, producing huge pit chains (Scott et al., 2000; 2002; Gibbons et al., 2001; Scott & Wilson, 2002; Figure **3.4a-c**). On planetary bodies often, direct evidence for a subsurface dike is impossible to detect, thus, in such instances dike related expressions such as presence of volcanic features, evidences of fissure eruption and lava flows propagation within surrounding region is considered (Wyrick et al., 2004).

Collapsed magma chamber: The reservoirs of magma chamber are connected to dikes. When the reservoir deflates by magma migration or subsequent eruption, the overburden pressure of surface material sinks into the void within magma chamber causing pit chains (Figure **3.4d**). The interpretation of this phenomena would be similar to dike injection. (Mège et al., 2002; 2003).

Extension fractures: Multiple studies suggested that the expansion of fractures can also be attributed for the formation of pit chains (Tanaka & Golombek, 1989; Banerdt et al., 1992; Tanaka, 1997). Horizontal expansion can cause the extension and reactivation of fractures to produce graben. Further extension can lead to crumble the faults into small fissure opening at the basement (Tanaka & Golombek, 1989; Figure **3.4e**). Pit chains formed by extension fractures may have graben structures within their vicinity (Ferrill et al., 2014). Active tectonic events and possibly evidences of hydrological cycle is required here (Wyrick et al., 2004).

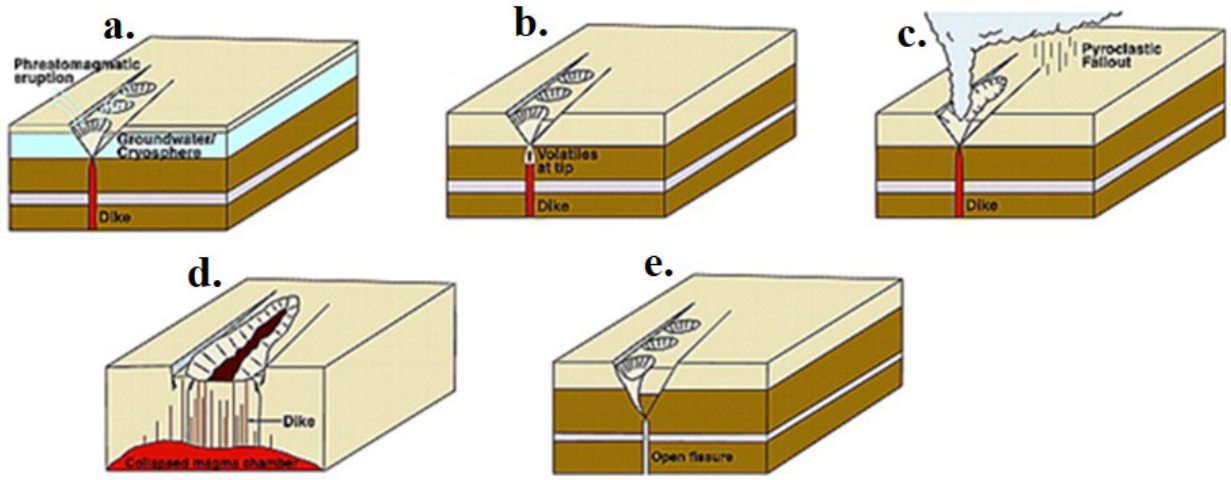

Figure 3.4 Illustration proposed mechanisms for pit chains. (a.) Dike formation via hydrospheric/cryovolcanic activity; (b.) Propagation due to accumulation of volatiles at the tip; (c.) Dike formation and opening via pressurized Plinian eruption; (d.) Collapse of magma chamber deforms the surface regolith; (e.) Extension fractures causes sinkholes for within subsurface layer (Sketch is from Wyrick et al., 2004; Copyright 2004 with permission from Wiley & Sons Ltd).

[4] Explosive eruption of fragmented magma and magmatic gas characterized by large volumes of tephra and tall eruption columns (Wyrick et al., 2004)

3.4 Mass wasting process

After impact cratering, mass wasting is one of the most studied geomorphological phenomena which strongly influence the evolution of planetary landscapes. Typically, it is defined as "*downward and outward movement of slope-forming materials composed of natural rock, soils, artificial fills, -or combinations of these material*" (Varnes, 1978). Mass wasting processes are related to the material properties, physical and atmospheric conditions which provoke the subaerial or flow-like mass movements or the transitioning deposit emplacement in between (Crosta et al., 2018a). During the initial phase, the material on terrain is under equilibrium condition where the cohesion force between the particles holds the mass against gravity forces. Due to slope failure, the stable condition is interrupted, the mass of material is detached, move downwards under the influence of gravity and tend to terminate up to the point where it counteracted by a shear resistance. As a result, a relatively steep slope at the highest parts of the failed mass (De Blasio, 2011) and large amounts of the ruptured deposits at the resting position is observed (Bulmer, 2012).

The emplacement style of mass deposits varies largely which lead to develop a classification system that efficiently reflect and highlight the typical geomorphological characteristics of each mass movement class. Varnes (1978) was the first one to develop the classification system which was later refined by Dikau (1996) as: fall, topple, slides, slump, lateral spreading, flow-like distribution and complex movements. The categorization is based on the terrestrial mass movements which is also adopted to study and interpret the mass wasting processes on other planets and asteroids. Out of above-mentioned categories, slides, slumps and flow-like features are observed at global scale on Vesta and Ceres (Chapter 7). Various type of mass movements, their geomorphological features, deposit conditions and transportation attributed to the physical and chemical characteristics of surface material and environmental condition on Vesta and Ceres (Section 7.2). Further, this phenomenon has the ability to expose fresh regolith underneath which are often not well explored due to lack of direct access. Thus, it is vital to understand the differences in various type of mass wasting processes in order to understand the geological history of planetary objects.

Slumps: In this type, large chunk of rocks and/or fine material (Ritter et al., 2006) travels relatively short distances (Varnes, 1978), usually have large volume (Xiao et al., 2013) and the detached deposit do not deform but remain as a chunk (De Blasio, 2011). Often material is ruptured from faults or joints and move concave upward exposing the underlying fresh surfaces. In a classic slump blocks multiple failure surfaces were observed which makes a step-like topographic profile. The multiple failure surface can be produced either during a single event of collapse or multiple occasional episodes of collapse. If the detached piece of mass has travel far from the crown, the overlaying mass has not sufficient support which trigger the new successive failures or scarps at the upper part of the mass which produce step-like structure (Varnes, 1978; Figure **3.5a**).

Slides: This type of movement takes place on shear plan surfaces (De Blasio, 2011) and the displacement occur along with one or multiple sliding areas (Varnes, 1978). It is a slow but progressive movement in which the detached mass is propagated from an area of local failure

(Varnes, 1978). In such a case, the ruptured block slides, travel beyond the original surface and rest on the ground surface. The efficiency of sliding depends on the shear strength of the surface material. (Figure **3.5b**).

Flow-like movements: Here the unconsolidated material mimic the flow which is either dry or wet. In flow-like movements, a high amount water or other volatiles are present within the deposits (Varnes, 1978). The cohesion between the particles is completely lost and each of them has their own mobility within the moving mass (Dikau, 1996). During the progression of mass, they encounter all types of material on their way including, large boulders, debris, organic matter, fine grains and rocks which get dragged along the flow. The material usually follows the downhill topography and often producing half bowl-shaped truncations. (Figure **3.5c**).

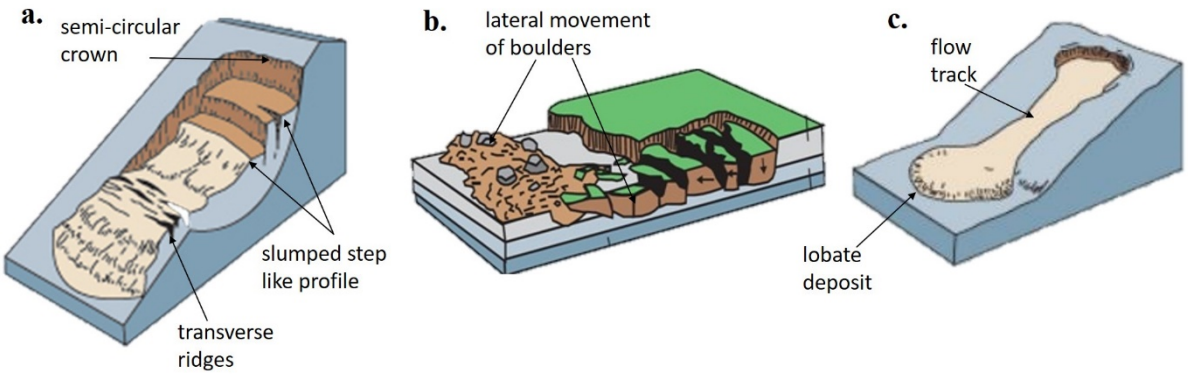

Figure 3.5 Illustration of various types of mass movements. The sketch is from Maina-Gichaba et al., (2013). Copyright 2013, with permission from Elsevier Ltd. and edited according to formate. Geomorphological features identified on (a.) slump; (b.) slide and (c.) flow-like movements. Note that the illustration is not upto the scale.

3.4.1 Mass wasting on other icy planetary bodies

Mass motion is a common phenomenon on the surfaces of Mars, the Martian moons of Phobos and Deimos, Ganymede, Callisto, and Europa orbiting Jupiter, Iapetus orbiting Saturn, and the asteroids of 4 Vesta, 1 Ceres, 433 Eros, 253 Mathilde, 951 Gaspra, 243 Ida, and 25143 Itokawa (Bulmer, 2012). This process has been also documented on the low temperature surfaces which have substantial elevation contrast and steep inclination (Moore et al., 1999). Overall, the dislocated mass mobile downwards under the influence of gravity and deposited on the lowest gravity regions (Greeley, 1998). Typically, movements are identified at the bottom of ridges, crater rims and groove floors (Stephan et al., 2010). In comparison to Earth, the study of extraterrestrial mass wasting process is limited by the availability of the extensive ground-based database. Thus, the analysis is often based on the surface geomorphology and geological interpretation (Bulmer, 2012).

In the past two decades, high-resolution images enabled in-depth analysis of mass wasting features which successfully enhanced our understanding related to regolith nature and further surface revolution of a planetary body. Quantitative measures of mass wasting on Iapetus and Rhea

(Saturn's moon) suggested reduced friction due to shear heating of ice layers present within upper few meters of regolith (Singer et al., 2012; Figure **3.6a, b**). On Charon, ammoniated impurities mixed with ice, decreased the internal friction of particles (Beddingfield et al., 2020; Figure **3.6c**). Iapetus, Rhea and Charon has similar gravitational condition as of Vesta and Ceres but differences in their surface composition plays a major role in material emplacement and mobility.

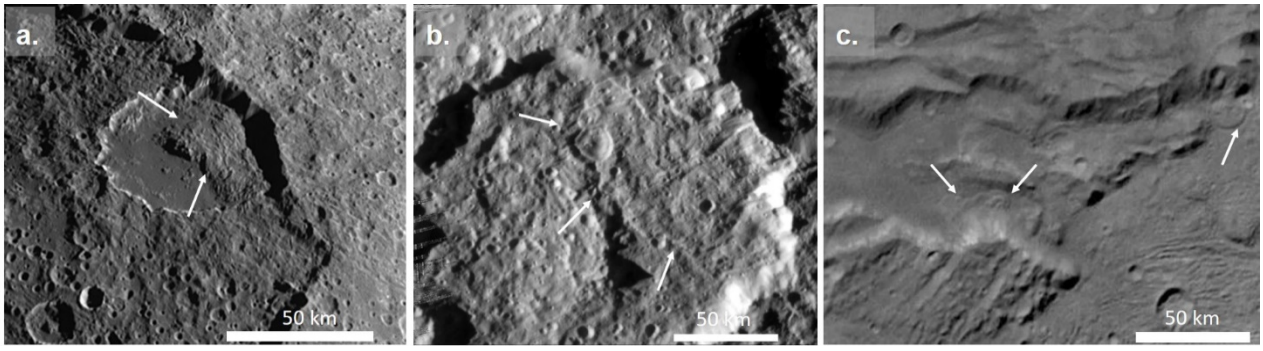

Figure 3.6 Examples of various mass wasting on icy planetary bodies. (a.) From the inner wall of Malun crater (lat.: 41.3˚W, long.: 5.9˚N; dia.: ~121 km) to the center of the crater, large blocky deposit has ~10^5 km^3 volume (Singer et al., 2012) on Iapetus. (b.) At the interior of Nishanu crater (lat.: 129˚W, long.: 9˚S; dia.: ~103.4 km) two slides were observed, one has a relatively larger deposit spreaded on the crater floor, the other is relatively small in scale which has a lobate deposit originated from NE rim (Parekh et al., 2016). (c.) Two mass movements (located at lat.: 9˚N, long.: 17˚W; lat.: 19˚N, long.: 21˚W) originated from the cliff (~7 km in height) with multiple lobate tongue like mass deposit present on the surface of Charon (Beddingfield et al., 2020). White arrows indicate the mass deposit.

3.4.2 Acoustic fluidization and friction of mass wasting deposits

The theory of acoustic fluidization was coined by Melosh (1979) to describe the temporary fluid state of a target mass. According to the theory, the surface rheology is disturbed by seismic waves which generates strong shaking and vibrations across the surface. The vibration has the ability to propagate within the surface due to close packed environment. Often the vibration is sufficiently strong to release the overburden pressure, separating fragments and allow the mass failure.

The average overburden pressure (ρ_o) increases with the depth (h) below the surface which can be estimated by $\rho_o = \rho g h$, where ρ is the density of planetary body and g is gravitation acceleration (here Vesta and Ceres). Under non-fluidized condition the ρ_o may exceed the threshold for sliding (ρ_t) which is defined as $\rho_t = \tau/\mu$, a ratio between τ (applied shear stress) and μ (coefficient of friction). During fluidization the viscosity (η) of the moving material and effective coefficient of friction (μ) is different than for the undisturbed material (Melosh & Ivanov, 1999; Melosh, 1989). While moving, the fluidized material behaves as Newtonian fluids[5] with an effective viscosity of:

$$\eta \approx \frac{\rho \lambda c_s^2}{2 c_p} \qquad (3.1)$$

[5] Fluid in which shear stress is linearly corelated to shear rate.

Where, ρ = bulk density of debris,

λ = wavelength of acoustic vibrations,

c_s = shear wave speed,

c_p = wave velocity (Collins & Melosh, 2003).

Alternatively, the viscosity of the Newtonian fluid on an inclined surface is estimated by the Jeffrey equation as:

$$\eta \approx \frac{g\rho \sin(\alpha) d^2}{3\vartheta} \qquad (3.2)$$

Where, g = surface acceleration,

α = angle of inclined surface,

d = thickness of deposit,

ϑ = velocity of viscous material (De Blasio, 2011).

Figure **3.7** illustrate the model of mobile mass and change in the physical characteristics in relation with effective coefficient of friction (μ) and is defined as the ratio between friction force (a_{fr}) and normal force (F_N) (Bowden & Leben, 1940; Bowden et al., 1943). In the absence of friction (a_{fr}), the moving mass will slide down with an acceleration of $a_{ff} = g \cdot sin(\alpha)$. Here g is gravity on a planetary object and α is inclination angle of a mass. Nevertheless, the acceleration (a_{ff}) is reduced due to apparent friction (a_{fr}) therefore total acceleration (a) will be $a_{ff} - a_{fr}$. Thus, the estimated effective coefficient of friction is:

$$\mu = \frac{F}{F_N} = \frac{a_{fr}}{g\cos(\alpha)} = \frac{a_{ff} - a}{g\cos(\alpha)} \qquad (3.3)$$

Besides, the coefficient of friction can also be estimated by measuring the fall height (H) and run-out length (L) of a sliding mass (McEwen, 1989; Collins & Melosh, 2003; De Blasio, 2011). The reduced friction of mobile mass is estimated by using the equation below, also known as Heim's ratio (Heim, 1932):

$$\mu = \frac{H}{L} \qquad (3.4)$$

Note that both the equation 3.3 and 3.4 are equivalent to estimate reduced coefficient of friction for mass wasting deposits. In general, for the estimation of the drop height (H), the top of the avalanche and for the run-out length (L), the margin of the deposit is considered (Figure **3.7**; Figure **B: 1**). In case of terrestrial mass movements, the run-out length is 40 times higher than the drop height (Beddingfield et al., 2020) and similar types of long-run mass wasting has been also observed on icy planetary bodies such as Iapetus, Rhea (Singer et al., 2012) and Ceres (Schmidt et al., 2017). Various mechanisms are responsible in triggering long-run out mass movements such as: riding a cushion of trapped air (Shreve, 1966; 1968); lubrication by release due to volatile materials (Lucchitta, 1979; 1987; Legros, 2002); aqueous pore pressure support (Johnson, 1978;

Harrison & Grimm, 2003); slipping on ice (De Blasio, 2011) or frictionally generated basal melt layers (Erismann, 1979; De Blasio and Elverhøi, 2008; Weidinger & Korup, 2009); sliding on evaporitic salt (De Blasio, 2011); lubrication by rock (Hsu, 1975; Han et al., 2011); mechanical fluidization (Davis, 1982; Campbell et al., 1995); fluidization by acoustic waves (Melosh, 1979; 1986; Collins & Melosh, 2003). On Iapetus and Rhea, localized friction reduction was caused at the base of mass movements which release energy during motion (Singer et al., 2012). The reduced effective coefficient of friction provokes the material to travel a longer distance (up to ~ 80 km and ~18.5 km on Iapetus and Rhea, respectively) away from the source, achieving a *H/L* ratio of ~0.1-0.3 and 0.07-0.4 on Iapetus and Rhea, respectively (Singer et al., 2013). Whereas, on Charon a similar range of reduced friction (0.1-0.3 with length up to 24.6 km) is not influenced by the release of the energy but probably due to the melt of ammonia hydrate present within the regolith (Beddingfield et al., 2020). Overall, terrestrial rock avalanches have *H/L* >0.3 whereas majority of wet debris flows are <0.1 (Siebert, 1984; McEwen, 1989). Thus, by estimating the *H/L* ratio of different mass movements, it is possible to delineate their mobility trend.

On Vesta, dislocated mass travel average up to ~4.5 km to reach the lowest elevated region of craters from a height of ~2 km, whereas on Ceres, mass is mobile up to average ~11.2 km which is detached from ~1.5 km height. This yields an average reduced coefficient of friction of 0.3-1.6 and 0.02-1.6 for Vesta and Ceres, respectively (Section **7.5.3**) and is considered as large landslides by the definition of Legros (2002). Nevertheless, frequently the run-out length is limit by the topographic restrictions and the effective coefficient of friction values does not reflect the absolute estimation but is considered as a rough approximation to understand the deposit mobility.

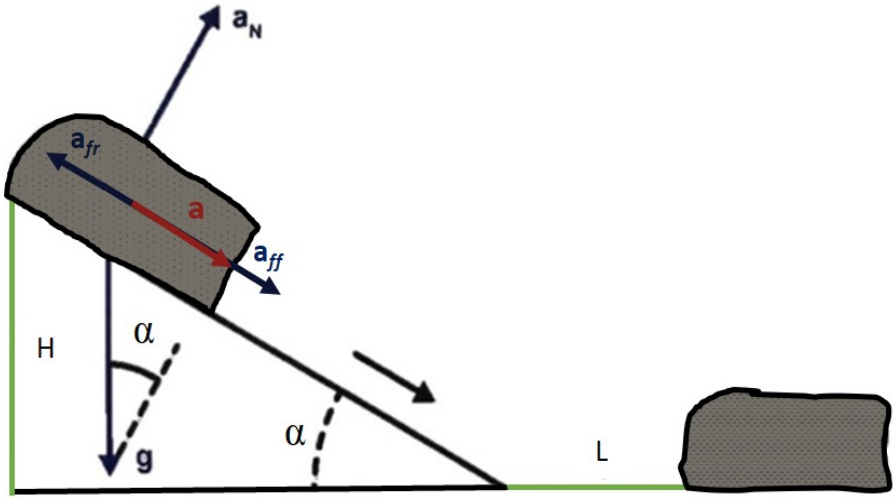

Figure 3.7 Sketch illustrating the geometry of a moving mass. A slab is accelerated downward from at an angle α from height *H*. The total acceleration (a_N) and the friction free sliding (a_{fr}) can be estimated from the magnitude of the gravity and inclination of the plane. Thus, the total acceleration down the plan (α) is from a_{ff} and a_{fr}. The slab is dropped from the height *H* and is mobile up to a length *L*. Image credit: K. Otto (DLR).

4. DATA AND METHODS

In this thesis, for geomorphological and topographic analysis the surface mosaics and stereopairs from the Framing Camera (HAMO, LAMO, extended mission cycle) from the Dawn spacecraft are utilized (Sierks et al., 2011). Table **4.1** summarizes the data utilized in this study and their resolution.

Table 4.1 Summary of data and their resolution utilized on this thesis

Data	Vesta [m·pixel^{-1}]	Ceres [m·pixel^{-1}]
LAMO	20	35
HAMO	70	140
DTM (LAMO)	-	32.5
DTM(HAMO)	92(±5m)	135(±10m)
XM02(extended mission)	-	2.5

4.1 Digital Terrain Model (DTM)

The elevation information was extracted from a HAMO DTM for both Vesta and Ceres. In general, the construction of a DTM is based on the stereophotogrammetric (SPG) mapping by considering the surface imaging data as well as the spacecraft and camera position. The information related to the spacecraft and camera position is available as of SPICE kernels (http://naif.jpl.nasa.gov/). Images of five different viewing angles are used to build a DTM. HAMO clear filer images are constrained based on the stereo requirements described in Table **4.2**. After pre-rectification, a common set of control points were defined to find mutual points within multiple images. The interaction of the line of sight from the FC to the multiple points determined the three-dimension position which are then interpolated into a global scale (Preusker et al., 2012a, 2016; Raymond et al., 2011).

For Vesta, during the cycle of HAMO1 and HAMO2 orbit, the FC instrument was able to map almost the entire surface (~99%; Russell et al., 2013). Hence, both the orbit data was utilized to produce a DTM which has ~90 m·pixel^{-1} resolution along with vertical accuracy of ~5 m (Preusker et al., 2012). The elevation of a DTM was referred on a best-fit ellipsoid body which has an axis of 286.3 × 278.6 × 223.2 km (Preusker et al., 2012; Roatsch et al., 2013).

Similarly, for Ceres, images acquired during the HAMO cycle (~98% of surface coverage; Preusker et al., 2016) were utilized to build global scale DTM. The final produced DTM has ~135 m·pixel^{-1} resolution and a mean ray intersection error of 16 m which translate to vertical accuracy of ~10 m·pixel^{-1}. Additionally, in this thesis LAMO DTM of Occator (Jaumann et al., 2017) is considered to analyse the crater floor. A best-fit ellipsoid of 482.8 × 480.6 × 445.0 km is used as a reference body to relate the elevation information (Preusker et al, 2016).

Table 4.2 Requirements for stereopairs for Vesta and Ceres. (Preusker et al., 2012; 2016)

Parameters [˚]	Vesta	Ceres
Illumination difference	<10	<10
Incident angle	0-60	10-90
Stereo angle	15-50	15-55
Emission angle	0-60	0-55
Phase angle	5-160	10-180

4.2 Mosaic

The images were converted into VICAR format and calibrated followed by orthorectifying into a cartographic map projection (Section **4.3**). This step was conducted by considering the detailed shape models produced from the DTM (Preusker et al., 2012; Jaumann et al., 2012). After rectification, each image was referred to the DTM and were stitched together producing a mosaic. The common overlapping regions within images were averaged out to avoid any information loss. At the end, the mosaics were projected onto a sphere (with mean radius of 255 km for Vesta and 470 km for Ceres; Roatsch et al., 2012; 2016a) to improve the evaluation and scientific analysis. Using the above-mentioned methodology, mosaics were prepared from images acquired during the HAMO and LAMO cycles.

In the case of Vesta, LAMO covers ~66% of the surface region (Russell et al., 2013) which includes southern and mid latitudes. The missing data regions were covered by relatively low resolution HAMO data. However, the northern latitude was under shadow during the time of the HAMO1 cycle and thus data could not be acquired. Nevertheless, most of the surface was covered under the high resolution LAMO cycle and the missing north pole region did not obstruct the scientific analysis.

For Ceres, both the HAMO and LAMO cycles successfully covered almost the entire surface with few shadow regions at both poles due to the rotational axis of the asteroid. Further, the extended mission covered only Occator crater and immediate regions at the highest resolution (~2.5 $m \cdot pixel^{-1}$) with low periapsis (20-50 km; Prettyman et al., 2021). This mission was specifically designed due to the scientific significance of Occator crater (Prettyman et al., 2019).

4.3 Co-ordinate system and map projection

The data used in this thesis has utilized the 'planetographic' system which has positive 0˚-360˚ East latitude (Archinal, 2013). For Vesta and Ceres, the longitudinal system was defined by a crater named Claudia (located at 356˚E; dia.: 0.57 km) and Kait (located at 0˚; dia.: 0.4 km) respectively (Russell et al., 2012; 2016). When HST mapped the surface of Ceres the longitudinal system was based on a Feature #1 (represents zero-longitude meridian; Archinal et al., 2011; Li et al., 2006), but the Dawn team could not clearly identify this feature in the newly generated data, thus, they

narrowed down to a new reference crater named Kait (Roatsch et al., 2017) which was approved by IAU WGCCRE[6].

The mosaic used in this study, has a cylindric equidistant map projection and are presented in Mollweide projection. For a cylindrical projection, a system is developed as rectangular map in which the surface area is divided into the grid of equally distant lines, each defined by latitude and longitude. In this projection, both the poles are stretched to a same line as the equator thus, polar surface features appeared to be distorted (Figure **4.1**).

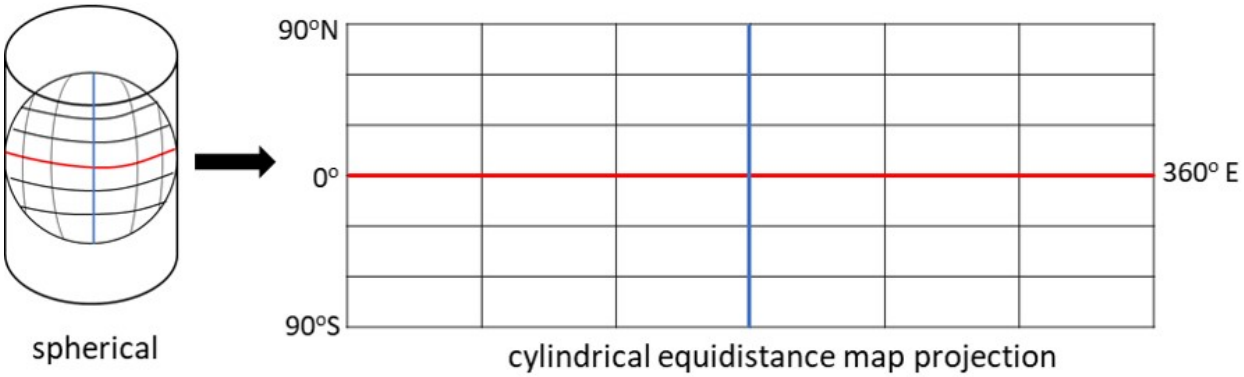

Figure 4.1 Schematic to illustrate a cylindrical equidistant projection. The blue line is a central meridian and red line suggest the equator on the planetary body which then transferred into flat 2-dimension equidistant map projection.

To produce a map the projected latitude (*x)* is coincide with the spherical equator which increases easterly and longitude *(y)* follows the central meridian which either increases (when its moving towards north) or decreases (when its moving towards south). Below is the equation to convert the spherical body into rectangular two-dimension cylindrical equidistance map co-ordinates.

$$x = R(\lambda - \lambda_0)\, cos\, \phi \qquad (4.1)$$

$$y = R\phi \qquad (4.2)$$

Where, R = radius of the sphere (Vesta: 262.7 km, Ceres: 470 km),

λ_0 = latitude of the central meridian of sphere,

λ = longitude of the central meridian of the sphere,

ϕ = geographic latitude (north [+] and south [-])

While representing small-scale maps, often a Mollweide projection is used to illustrate the overall area characteristics. A Mollweide projection is an equal-are pseudo cylindrical map projection in which the planetary bodies are presented in the form of an ellipse with axes in a 2:1 ratio (Snyder, 1987). However, in this projection the accuracy of shapes, angle and distance are compromised and distortion increased moving away from the equator.

[6] Working Group on Cartographic Coordinates and Rotational Elements

4.4 Chronological estimation

The estimation of a planetary surface age is based on the frequency and the size of the impact craters. It is a rudimentary technique which have been used to derive the relative ages of objects beyond Earth to understand their relative chronology since the acquisition of first remote sensing planetary surface data (Öpik, 1960; Shoemaker et al., 1961; Baldwin, 1964; Hartmann, 1965). The samples returned from the surface of the Moon during the Apollo mission helped to estimate their age via radiometric analysis which further lead to establish the absolute age of the lunar surface and to calibrate crater statistics (Shoemaker et al., 1970a; b; Baldwin, 1971; Neukum, 1971; 1977; Hartmann, 1973; Soderblom et al., 1974; Neukum & Wise, 1976). Since then, the lunar chronological model is used as a base to retrieve the relative ages of other planetary surfaces including asteroids present within inner solar system (Neukum et al., 2001a; Ivanov, 2001; Hartmann & Neukum, 2001a). Usually, older planetary surfaces are exposed to the space for longer time resulting in a higher density of impact carter in comparison to younger surfaces (McEwen & Bierhaus, 2006). Based on this idea, the planetary chronological model was developed. In the lunar chronology model the Size-Frequency Distribution (SFD) of impact craters was also measured in the same region from which the samples were collected (Neukum & Wise, 1976). The combination of SFD and the absolute age of samples determined frequencies of impact craters which are ≥1km in diameter. It was used as a function of lunar surface age from which the cratering chronology model was established using the below equation given by Neukum (1983) and values for each constant is provided by Schmedemann (2014; 2015):

$$logN(D \geq 1) = A \times (e^{B \times t} - 1) + C \times t \qquad (4.3)$$

Where, $N\ (D \geq 1)$ = cumulative impact crater frequency per km^2 for craters ≥1 km in diameter,
A = exponential term is scaled to the lunar value by taking ratio between planetary body and the moon, $C_{asteroid}\ /C_{moon}$ (C_{Vesta}: 1.2×10^{-12}; C_{Ceres}: 1.5×10^{-12}; C_{moon}: 5.4×10^{-14})
B = decay constant of exponential decay (Vesta, Ceres: 6.93)
C =rate of collisions ([Gyr$^{-1}\cdot$km^{-2}]; Vesta: 0.01979; Ceres: 0.0224)
t = time [Gyr]

The lunar model describes the cratering rate on the Moon as a function of time. The chronology function describes cumulative crater frequency (N) as a function of crater diameter (D). The production function is derived as a least square-fit of the normalized crater size and calculated using below equation (Shoemaker et al., 1970b; Hartmann & Wood, 1971; Chapman & Haefner, 1967; Neukum et al., 1975; Neukum & Wise, 1976; König, 1977; Neukum, 1983):

$$log\ N = \sum_{j=0}^{11} a_j\ (log\ D)^j \qquad (4.4)$$

Where, N =cumulative crater size frequency,
a_j = production function coefficient,
D = crater diameter [km]

To derive the specific surface age of any planetary object, first the frequency of craters with diameter larger than a threshold (dependent on resolution) measured. It is then modeled based on gravity, impactor distribution and referred to the lunar absolute age (Schmedemann et al., 2014). In general, multiple geological units were observed to extract the accurate age (Neukum et al., 2001a). In this thesis, the relative ages of Occator, Azacca and Urvara craters on Ceres were utilized to understand the evolution process (Section **6.5**). In Figure **4.2**, an example of relative age of one of the geological units with the Occator carter (Neesemann et al., 2018; Nathues et al., 2020) is illustrated. Based on their morphology and association with surrounding units, it was suspected that they were formed during different time scale on Ceres (Neesemann et al., 2018; Nathues et al., 2020). Using a chronological model, various units of the Occator crater (in total 25 units) were included to retrieve the frequency and diameter of impact craters which was used to estimate the relative age. This analysis concluded that the Occator region was active from ~19±2 Myr until recent time (Nathues et al., 2020).

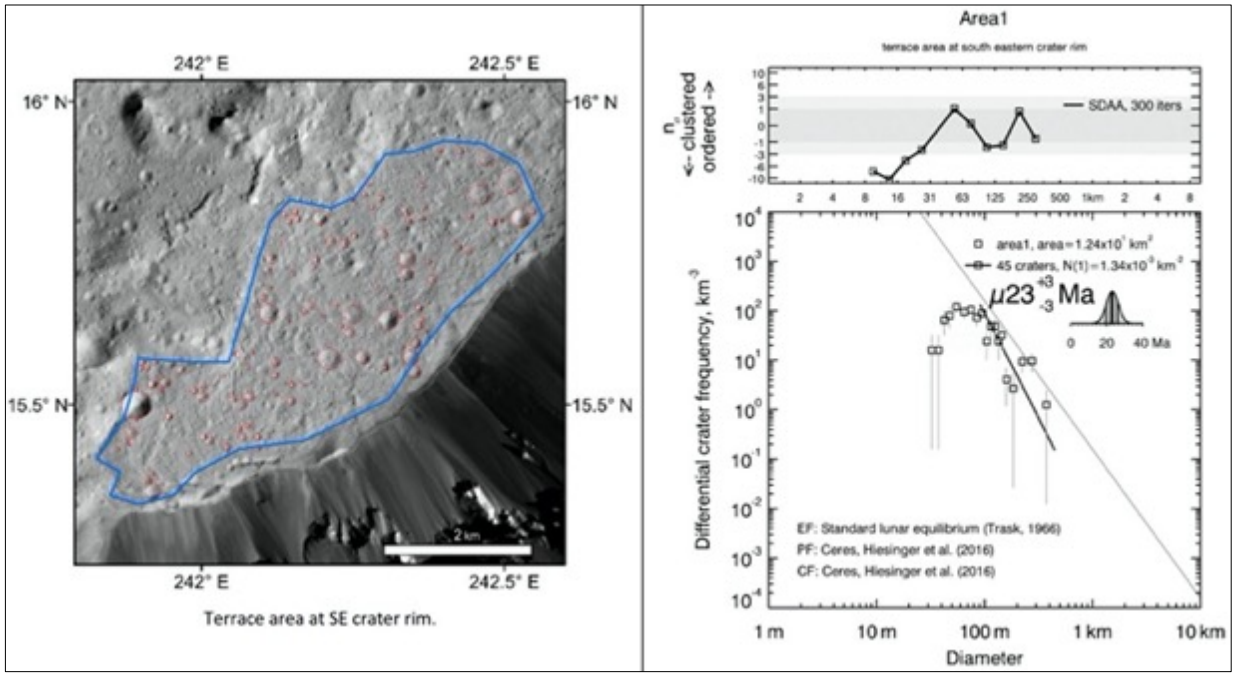

Figure 4.2 CSFD extracted from the southeast region of Occator crater and its relative age. On left, the blue line confined the area (~12.4 km^2) where the size and frequency of impact craters (in red circle) are identified and counted. On right side, the above graph denotes a randomness analysis and the below graph is of crater count. The age of surface is ~23±3 Myr estimated based on 45 craters (Nathues et al., 2020; Copyright 2020 with permission from Springer Nature.

5. FORMATION OF EJECTA AND DUST POND DEPOSITS ON ASTEROID VESTA

An edited version of following sections has been published as: **Parekh, R**., Otto, K.A., Jaumann, R., Matz, K. D., Roatsch, T., Kersten, E., Elgner, S., Raymond, C.A. (2021). Formation of ejecta and dust pond deposits on asteroid Vesta. *Journal of Geophysical Research: Planets,* volume 126, issue 11, page 1-17, article number e2021JE006873. doi: https://doi.org/10.1029/2021JE006873. The author contribution is explained in the Section **1.2**.

5.1 Abstract

Dust and melt ponds have been studied on planetary bodies including Eros, Itokawa and the Moon. However, depending on the nature of the regolith material properties and the location of the planetary body, the formation mechanism of the ponded features varies. On Eros and Itokawa, ponded features are formed from dry regolith materials whereas on the Moon similar features are thought to be produced by ejecta melt. On the surface of Vesta, we have identified type 1, ejecta ponds and type 2, dust ponds. On Vesta type 1 ponds are located in the vicinity of ejecta melt of large impact craters. The material is uniformly distributed across the crater floor producing smooth pond surfaces which have a constant slope and shallow depth. The hosting crater of melt-like ponds has a low raised rim and is located on relatively low elevated regions. Whereas, the type 2 ponds on Vesta reveal an undulating surface that is frequently displaced from the crater center or extends towards the crater wall with an abruptly changing slope. We suggested that for the production of the type 2 ponds, localized seismic diffusion and volatile-induced fluidization may be responsible on Vesta. Due to Vesta's large size (in comparison to Eros and Itokawa), the surface may have experienced local-scale rare high-amplitude seismic diffusion which was sufficient to drift fine material. Similarly, short-lived volatile activities were capable to transfer dusty material on to the surface. Segregation and smoothing of transferred material lack further surface activities, hindering formation of smooth morphology.

Key points:

- We identified ejecta and dust pond crater candidates on Vesta within 0˚-30˚ N/S.
- Ejecta ponds are smooth deposits and located within ejecta melt of large craters.
- Dust ponds are produced via local-scale seismic shaking and/or volatile fluidization.

5.2 Introduction

Ponded deposits widely receive attention due to their unusual characteristics on asteroid Eros as revealed by the NEAR Shoemaker mission (Robinson et al., 2001; 2002; Sears et al., 2015). Usually ponded features are identified within craters. However, there are also a few examples in which ponded features are observed in moderately large regions (Miyamoto, 2014) of a planetary body, for example the Sagamihara and Muses-Sea regions (Fujiwara et al., 2006; Saito et al., 2006) on asteroid Itokawa. Due to their smooth appearance, they are called 'ponds'. Typically, ponded

regions consist of a smooth layer of fine-grained material (less than cm size) (Robinson et al., 2001), partially covering the topography of a crater floor along with boulders of varying sizes or unconsolidated material (Sears et al., 2015) leaving behind a sharp edge of deposition at the walls of a crater depression (Robinson et al., 2001; Veverka et al., 2001a). Further, they form a nearly flat or low slope terrain (usually ~≤10° on Eros; Cheng et al., 2002) and often have apparent variations with sharp boundaries in albedo relative to the surrounding plains (Robinson et al., 2001). The smooth material is distributed either at the crater floor center and/or is often slightly offset from the geometric center (Robinson et al., 2001; Figure **5.1a-c**). The variation in albedo can be due to mineral heterogeneity (Robinson et al., 2001), space weathering (Heldmann et al., 2010; Robinson et al., 2001; Sears et al., 2015), or the difference in grain size between the pond regolith and the surrounding region (Heldmann et al., 2010; Robinson et al., 2001). Some of these characteristics of the pond deposits are found not only on Eros but are also identified within large regions (Sagamihara, Muses-Sea) of Itokawa (Fujiwara et al., 2006; Miyamoto et al., 2007; Saito et al., 2006; Yano et al., 2006; Figure **5.1d-f**) and small craters on the Moon (Figure **5.1g-i**) (Hawke and Head, 1977b;1979; Plescia and Cintala, 2012; Stopar et al., 2012). Overall, ponded regions are noted on planetary bodies with dry brittle regolith and/or low volatile content (Miyamoto et al., 2007; Robinson et al., 2001). However, based on the weathering process, impacts and regolith material properties of the different planetary bodies, these geomorphologic appearances may vary and are not necessarily identical in all the identified ponded regions.

Depending on the material properties and identified pond impressions, various geological processes have been suggested as mechanisms to produce ponds on Eros, Itokawa and the Moon. On Eros, electrostatic levitation and seismic shaking were proposed earlier as a possible formation mechanism for the dust ponds (Robinson et al., 2001; Veverka et al., 2001a; Cheng et al., 2002). Electrostatic levitation was proved to be responsible for the mobility of charged particles (Lee, 1996; Roberts et al., 2014; Robinson et al., 2001; Veverka et al., 2001a) whereas seismic waves induced the segregation to sort grains and produce smooth featureless pond deposits (Cheng et al., 2002; Robinson et al., 2001; Thomas et al., 2002; Veverka et al., 2001a). However, both theories fail to explain the distinct distribution of ponds and significant color variation identified within ponded material (Dombard et al., 2010). Later on, Dombard et al (2010) proposed the boulder disintegration due to space weathering based on the close proximity of large size boulders (up to ~30m) with pond deposits. Recent laboratory simulations also suggest the involvement of volatile outgassing as a possible production mechanism for the formation of ponded features on Eros via (i) exogenic volatile rich meteor impacts or (ii) endogenic substances present within subsurface regolith (Sears et al., 2015). Moreover, Eros is a class-S asteroid resembling ordinary chondrites (Bell et al., 2002) with the presence of hydrated minerals within chondrites (Hutchinson et al., 1987; Grossman et al., 2000). Even though none of the images show direct involvement or geological features of volatile outgassing activity (such as pitted terrains or cracks) on Eros, a possible involvement cannot be excluded.

Similarly, on Itokawa, the Muse-Sea and Sagamihara regions are composed of unconsolidated granular material that were rearranged post-accumulation (Miyamoto, 2014). As on Eros, it is assumed that the surface of Itokawa experiences similar process of particle segregation (Saito et

al., 2006). Given the small size of Itokawa (Table **5.1**), seismic energy generated through impacts can cause global surface vibrations within the regolith (Miyamoto, 2014) which may result in the rearrangement of unconsolidated material. The smooth ponded regions of Itokawa present within the low gravitational potential (Fujiwara et al., 2006) point towards gravitational movement of fine particles. Similar to Eros, volatile activity is also suspected as one of the potential mechanisms for the pond formation on Itokawa. The assumption was based on the (i) isotope studies of the Hayabusa returned samples which proved that dehydration occurred during the early history of Itokawa within the region of Muse-Sea (Jin and Bose, 2019), (ii) prediction models developed by considering the thermal diffusivity and collision history of Itokawa and the anticipated loss of water within Itokawa regolith at depths of 10 m to 1 km during its early history (Jin and Bose, 2019) and (iii) the presence of circular depression like geologic features (Saito et al., 2006; Table **5.1d-f**, highlighted in red) which resemble laboratory generated depressions formed due to volatile fluidization (Sears et al., 2015).

Table 5.1 Physical characteristics of the planetary objects discussed in this study (Murdoch et al., 2015)

Planetary body	**Size [km]**	**Bulk density [kg·m^{-3}]**	**Surface acceleration [m·s^{-2}]**
Eros	34.4x 11.2x 11.2	2700	0.0023-0.0056
Itokawa	0.535x 0.294x 0.209	1900	0.000024-0.000086
Moon (dia.)	3474.8	3344	1.62
Vesta	572.6x 557.2x 446.4	3500	0.25

Unlike Eros and Itokawa, the ponded features identified within craters of the Moon are known as 'melt pools' and majority of them are formed from the melting of impact materials (Hawke & Head, 1977a; b; 1979). Cintala & Grieve (1998) derived a model which predicted that high velocity impactors (~40 km·s^{-1}) are capable producing large volumes of melt that form thin layers in their neighboring regions (Hawke & Head, 1977a; b; Howard & Wilshire, 1975). The ejected melt will then flow to lower elevated regions, forming lobate-like bulge features (Howard & Wilshire, 1975). In such cases, the pre-existing topography conditions such as lower height downslope rim crest and evidence of flow margins is required. Nevertheless, only a small percentage of craters (~6%) reveal lobate flow margins and very few craters have low elevated rim crests allowing such drainage (23 out of 69; Stopar et al., 2014). Thus, the emplacement of melt material requires certain pre-existing surface conditions for the transport of the impact melts which are not always observed. Other than high velocity, near vertical impact velocity models (Cintala & Grieve, 1998; Pierazzo & Melosh, 2000; Plescia & Cintala, 2012) suggest an alternative explanation which does not require any topographic conditions. According to these models, near vertical impactors produce melt that does not spread outside the crater floor but allows the melt to remain within the crater which later creates smooth flat pond surfaces as the temperature decreases (Plescia & Cintala, 2012). The majority of studies focus on melt formation as a possible mechanism to produce ponds on the lunar surface (Hawke & Head, 1977a; b; Plescia & Cintala, 2012; Stopar et al., 2014), however, given the dusty regolith of the Moon, the formation of ponds via particle levitation cannot be overlooked. Nevertheless, particle levitation requires a higher degree of electric charging to lift and mobilize

dust particles on the Moon (Stopar et al., 2014) compared to smaller bodies like Eros due to the larger gravitational pull (Table **5.1**; Thomas et al., 2002). Furthermore, recent data from the Lunar Atmosphere Dust and Environment Explorer (LADEE) do not show any evidence of a dense dust cloud near the lunar surface (Horányi et al., 2015; Szalay and Horányi, 2015). Thus, impact melt

production appears to be the most feasible mechanism to explain the formation of ponded features on the surface of the Moon at a global scale.

In a nutshell, multiple mechanisms including electrostatic levitation (Lee, 1996; Robinson et al., 2001), seismic shaking (Robinson et al., 2001), boulder comminution (Dombard et al.,2010),

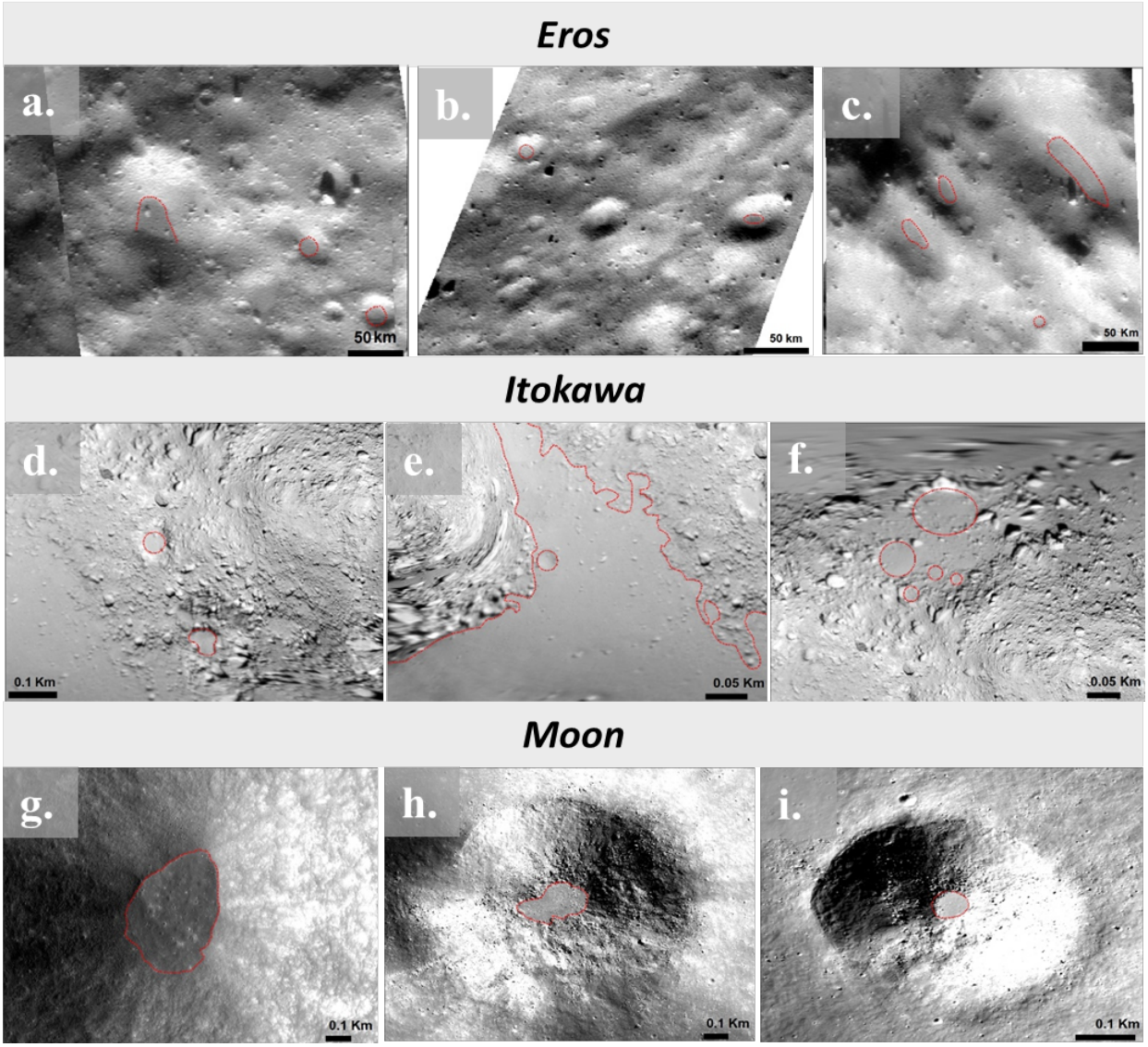

Figure 5.1 Examples of pond impressions on Eros (a.-c.), Itokawa (d.-f.) and the Moon (g.-i.). The ponded regions are highlighted by red dotted lines. The location of the shown ponds are as follows: (a.) lat.: 1.61˚S; long.: 175.7˚E (b.) lat.: 5.48˚S, long.: 6.56˚E ; (c.) lat.: 3.64˚S, long.: 165.28˚E on Eros; (a.) evenly distributed fine material at the crater floor, (b.) and (c.) identify ponded material at the steepening surface of the crater wall; (d.) Komaba crater (lat.: 10˚S, long.: 102˚E) and an unnamed flat region; (e.) crater like depression present within the large smooth region of Muses Sea and (f.) five small circular smooth features located within Uchinoura (lat.: 90˚S, long.: 40˚E) on Itokawa. Melt pool exhibiting a smooth surface at the bottom of the crater located at (g.) lat.: 2.36˚N, long.: 97.5˚E (h.) lat.: 32.02˚S, long.: 81.70˚E (i.) lat.: 40.6˚S, long.: 235.71˚E on the Moon. The presence of boulders is evident near the ponds' rims in (h.) and (i.).

fluidized impact ejecta (Hawke & Head, 1977b) and volatile outgassing (Sears et al., 2015) are possibly responsible for the formation of pond deposits on Eros, Itokawa and the Moon.

The asteroid Vesta is a dry planetary object (Jaumann et al., 2012) that was rigorously explored by the Dawn mission. Through this mission a large number of high-resolution data were collected which enabled us to study and understand the surface of Vesta closely. Vesta's surface consists of a low volatile content regolith with a few morphological exceptions such as pitted terrain (Denevi et al., 2012), gully-like features (Scully et al., 2015) and fluidized impact ejecta (Williams et al., 2014a; b) of large craters such as Marcia (~58 km in diameter). Vesta's regolith provides an ideal condition for the formation of ponds, which on Eros and Itokawa required a dry environment. In this study, our objective is to identify and characterize the ponded features on the surface of Vesta, including the material properties and surface conditions under which the ponds form. Further, we compare them with numerous possible material migration and regolith sorting mechanisms identified on Eros, Itokawa and the Moon to understand their formation and explore the detailed morphology of ponded features.

5.3 Methods

5.3.1 Data

For comparison we adopted the data from previous studies. For Eros, we have used the images collected by the NEAR-Shoemaker spacecraft (Multi-Spectral Imager and Near-Earth Asteroid Rendezvous lander) which has a spatial resolution of ~0.3–0.7 m·pixel^{-1}. For pond detection, we used geospatial point shapefile data from Robinson et al. (2002). In the case of Itokawa, we used the 0.3 m/pixel imaging mosaic derived from the Gaskell shape model prepared from the Asteroid Multiband Imaging Camera (AMICA) on the Hayabusa mission (Saito et al., 2006). Lastly, for the Moon, the mapped melt pool details are available from Plescia and Cintala (2012). Based on the shared latitude and longitude information, we gathered LROC (Lunar Reconnaissance Orbiter Camera) imaging data of the Moon. The image data has a spatial resolution ranging from 0.1-0.9 m/pixel.

For Vesta, we used mosaics from the Low Altitude Mapping Orbit (LAMO) from the Dawn mission's framing camera (Sierks et al., 2011) which has a spatial resolution of ~20 m·pixel^{-1} (Roatsch et al., 2013). For the topographic information, we overlaid a High-Altitude Mapping Orbit (HAMO) digital terrain model (DTM) with 92 m·pixel^{-1} lateral spatial resolution (Preusker et al., 2012). The DTM's spatial resolution is coarser than the image resolution, however given that our smallest craters are 1.4 km in diameter, this is the best available DTM suitable for our analysis. The HAMO DTM is referenced to a best-fit ellipsoid of 286.3 × 278.6 × 223.2 km (Preusker et al., 2012). On the Moon, melt-like ponds are visible in 25 m·pixel^{-1} image (Plescia and Cintala, 2012) whereas on Eros smooth ponded features can be identified at 0.5 m·pixel^{-1} (Robinson et al., 2001) and on Itokawa they are visible at the 50 m scale in images which have resolutions from 0.3-0.7 m·pixel^{-1} (Hirata et al., 2009). With similar dry regolith present on Vesta, the high resolution of surface data has successfully enabled us to identify pond deposits.

5.3.2 Criteria for identification of pond and method to measure pond depth

Distinguishing between different types of pond-like landforms can be an arduous task due to their morphologic similarities, especially while using remotely sensed data where confirmation via ground truth is impossible. In such instances, researchers need to rely on the geological context present within the datasets. In our study, we considered neighboring geological conditions and previous studies of ponded features on Eros, Itokawa and the Moon (Roberts et al., 2014; Robinson et al., 2001; Stopar et al., 2014) to understand the contrast in various morphological characteristics of ponded deposits. In general, dust pond deposits on Eros, Itokawa and melt-pools on the Moon have the following common characteristics, but they are not necessarily present in all the ponded candidates: often both types of deposits (i) have superimposed boulders and loose materials; (ii) are in general identified in small carters (<1 km in diameter); (iii) have a sharp boundary between the ponded deposit and the crater wall and (iv) are equipotentially distributed within the crater floor resulting in a smooth surface (Fujiwara et al., 2006; Roberts et al., 2014; Robinson et al., 2001). However, a key difference between both type of ponds is that the dust deposits on Eros and Itokawa comprise fine dry regolith (with grain sizes of mm to cm on Itokawa and <2 cm on Eros), preferentially present near the equator (observed on Eros) and the majority of them are identified in low gravity regions (Cheng et al., 2002; Fujiwara et al., 2006; Robinson et al., 2001; Saito et al., 2006; Thomas & Robinson, 2005; Veverka et al., 2001a). In contrast, the ejecta ponds are not correlated with latitude, longitude or gravitational regions (Plescia & Cintala, 2012; Stopar et al., 2014) and are formed from the fluidized impact ejecta and/or impact melt of a neighboring crater. In Table **5.2**, we list the observed morphological characteristics of ponded features on Eros, Itokawa and the Moon. While conducting the survey of ponded candidates on Vesta, we consider the characteristics mentioned in Table **5.2** as a key for identification and further classify them into two categories namely: type 1 and type 2 pond deposits.

Next, we estimate the approximate depth of the ponded material. For this we use the DTM and derived the current shape of the crater. We then add a least square fit of a power function (polynomial fit) to the crater walls and estimate the original crater depth (d). Previously, the polynomial fit method has been used to best estimate the depth of sedimentary infilling within simple bowl-shaped craters on Mars (Savage et al., 2018). The difference between the measured shape from the DTM and the fitted original depth is the ponded material depth.

Ponded characteristics on Vesta	Eros	Itokawa	Moon

Type 1 pond deposit			
Fluidized impact ejecta material	✗	✗	✓
Smooth, nearly flat crater floors	✓	✓	✓
Shallow pond depth	✓	✓	✓
Distributed equipotentially within crater floors	✓	✓	✓
Relatively shallow slope	✓	-	✓
Type 2 pond deposit			
Dry fine-grained material	✓	✓	✗
Uneven ponded surface	✗	✓	✗
Material distributed either within crater floors and/or partially extending to the wall	✓	✗	✗
Increase in slope	✓	✓	✓
Pit like impressions	✗	✗	✗
Relatively deep ponds	✗	✗	✗

Table 5.2 Summary of ponded impressions identified on Vesta, Eros, Itokawa, and the Moon

5.4 Observations and interpretations

The following sections focus on distinct characteristics of type 1 and type 2 pond deposits on Vesta with concentration to their distribution and morphological evidence. The identified host craters are located within central latitudes (0°-30° N and 0°-25° S) of Vesta. In total, we have identified 10 craters on Vesta which show one or more pond characteristics mentioned in Table 2. These craters have relatively small diameter (≤ 11 km) and half of them (5 out of 10) of them are scattered in the southern region of the Marcia (average ~75.3±32 km distance from rim) and northern part of Cornelia crater (2 out of 10 at the average distance of ~21.6±1 km form the rim) (Figure **5.2**). The derived original depth (*d*) to diameter (*D*) ratio of the crater (*d/D*) is ~0.60 (by assuming simple bowl-shaped fresh craters). This estimation represents the upper limit of d/D ratio of host craters in which ponded features are observed, because most of the craters have experienced some degree of degradation but not all the craters show ponded characteristics. Schenk et al. (2021) measured the current *d/D* ratio of simple bowl-shaped craters on the Vesta which is ~0.22. The difference in *d/D* ratio of original and current craters can be due to resurfacing events that have been taking place in the past. Note that this is an approximate estimation to understand the variation in pond depth within identified crater candidates.

We characterized ponded crater candidates into two categories depending upon their morphology and their position within the craters. Among the identified ponded craters, a few deposits show a shallow slope throughout (≤15°), have a smooth surface with pond material evenly distributed covering the crater floor, the host craters of these pond deposits are located on relatively low elevated regions (blue dots in Figure **5.2**) and in general present within the vicinity of impact ejecta spread (type 1). Such ponds are shallow in depth (average 0.04 km). So far, we identified 4 craters which exhibit the above-mentioned morphology (Figure **5.3a-c**). Based on the topographic profiles, we understand that the material infills the lowest region on the crater interior and gradually builds up towards the crater wall, producing a smooth surface. Similar smooth surfaces also appear outside in the vicinity of these carters (Figure **5.3a-c**). We notice smooth surfaces in the vicinity

(v-shaped cuspate toes and furrows highlighted in Figure 5.3a, b), partially broken low-raised rims and a downslope topography (~2.5 km relief difference) within the host craters' region (Figure 5.2). Based on this evidence we assume that the material creating the ponds and the neighboring smooth terrain must have originated from the same source. The identified craters in this category are present within the ejecta blanket of nearby larger impact craters (Figure 5.2). There are a few more small craters observed within ejecta blankets with similar morphology, however, they are not easy to delineate due to lack of strong morphological impressions unlike the above-mentioned examples. Due to the close proximity of ejecta ponds within Marcia, Calpurnia, Minucia and Cornelia crater, the combination of impact ejecta and impact melt deposits (Williams et al., 2014b) may be the putative source for the ponded deposit producing smooth and flat pond surfaces. These pond deposits show all the morphological characteristics similar to 'melt-pools' present on the Moon (Table 5.2).

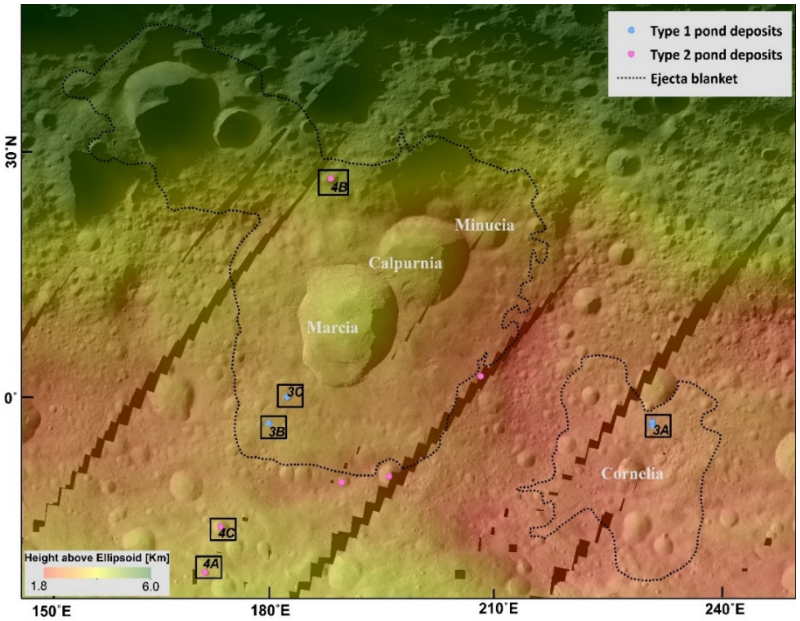

Figure 5.2 Map of ponded crater identified on the surface of Vesta. Black dotted line represents the ejecta blanket of the nearby large craters, derived from the geological map of Vesta by Williams et al., 2014b. All type 1 and type 2 pond deposits are obsereved in and around ejecta blankets. The black boxes indicate location of areas displayed in Figure 5.3 and Figure 5.4. The ponded craters are mapped on a LAMO global mosaic and on HAMO mosaic (only where high resolution data is not available) on which a HAMO DTM is superimposed (equidistant projection) to understand the surface elevation.

Additionally, we found a few ponded features with some different morphological impressions. The ponded deposits within these craters are distributed more heterogeneously, forming an irregular surface with an undulating slope (type 2). In this type, the loose ponded material is located at the base of the crater wall or partially extending towards the walls from the floor with a gradually increasing slope and/or is unevenly distributed on the crater floor (Figure 5.4a-c). These ponded features appear to not have experienced sufficient leveling mechanism to make entirely smooth surfaces, however, the features still possess the main characteristics of ponds mentioned in prior studies (such as pools of fine-grained regolith, partially extending towards crater walls with a sharp boundary with reference to Table 5.2; Robinson et al., 2001; Roberts et al., 2014; Robinson et al., 2001). In general, these ponds are identified inside relatively large craters (5.90-10.05 km) with estimated average pond depths of ~0.21 km. For this group of ponds, the feasible source of ponded material is the migration of loose surface material via seismic shaking and/or emplacement of fine

regolith from the subsurface via volatile outgassing. Our identified type 2 ponds on Vesta show some resemblance to ponded craters on Eros and Itokawa (Table **5.2**). Both type 1 and type 2 pond deposits have some different and some overlapping impressions which are summarized in Table **5.3**.

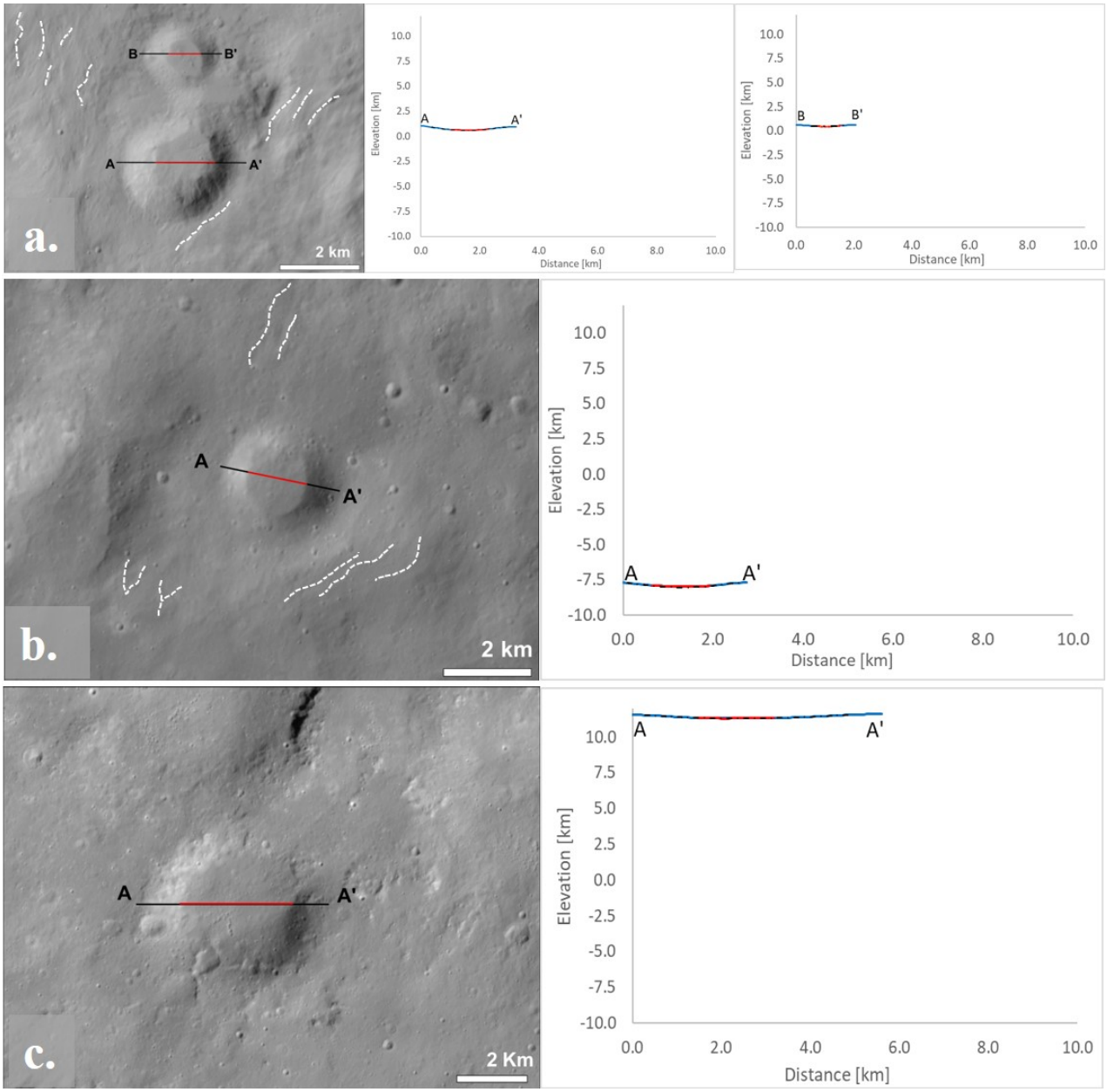

Figure 5.3 Example of type 1 pond deposit on Vesta. (a.) two unnamed craters located at south of Cornelia crater with their corresponding surface profile (A-A' and B-B'). The ponded deposit is sharply constrained by the pre-existing crater walls. (b.) and (c.) are two unnamed ejecta pond hosting craters and their corresponding elevation profile. The craters are located south west of Marcia crater at a distance of ~38.3 km and ~20 km from Marcia's crater wall. In the profiles, the blue line denotes the crater shape, red corresponds to the ponded deposit and the black white-doted line indicates original shape of the crater. In the images (a.) and (b.) white dashed lines highlight furrows and v-shaped cuspate flow-like impact melt. North is up in all the images.

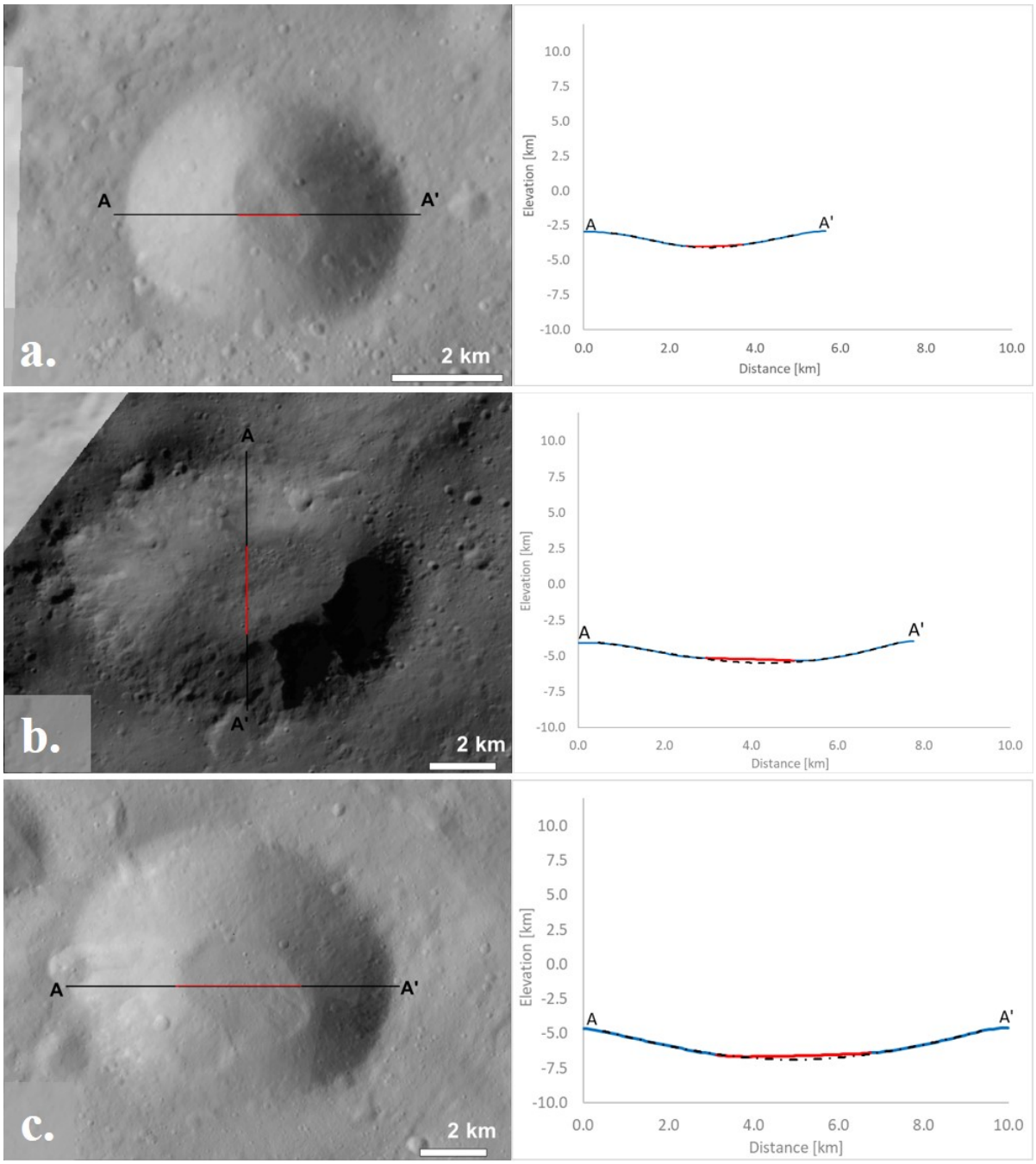

Figure 5.4 Example of type 2 ponds on Vesta. Craters (a., b., c.) and their corresponding elevation profile (right) in which the pond is partially extended at the steep wall of crater. (b.) Based on the topographic information, it is evident that the slope in the central region is not flat indicating that the deposit is not (yet) equipotentially distributed. (c.) Surface of ponded material identified within an unnamed crater and its topographic information shows a gradual increase in elevation. In all elevation examples, the current crater profile is shown in blue, the pond deposit is highlighted in red and the estimated original crater profile is shown as a black dashed-dotted line. North is up in all the images.

Table 5.3 Characteristics of ponded material on Vesta.

Pond Id	Lat.	Long.	Floor appearance	Crater floor to wall transition	Slope of ponded material	Pond depth (km)	Distinct change in slope from floor to wall	Surface profile direction	Notes
Type 1: Smooth, featureless deposits evenly distributed at the crater floor, shallow slope within deposit material, host craters located at low elevated regions with low relief topography, shallow pond depth, formed from fluidized impact melt.									
(1)	3.77˚S	228.34˚ E	flat and smooth	gradual	≤15°	0.02	no	W-E	smooth in-flow layer distributed equipotentially at the surface, deep bowl-shaped, following crater topography (Figure **5.3a**, bottom)
(2)	3.20˚S	228.34˚ E	flat and smooth	gradual	≤15°	--	no	W-E	partially covering crater floor in simple bowl shape crater with smooth texture (Figure **5.3a**, top)
(3)	3.24˚ S	179.40˚ E	flat and smooth	sharp	≤15°	0.05	no	NW-SE	melt material drained from north east and distributed within lower elevated regions of crater, the prominent striation flow patterns are visible in surrounding regions (Figure **5.3b**)
(4)	0.20˚ S	181.80˚ E	flat and smooth	sharp	≤15°	0.10	no	W-E	located nearby Marcia impact crater, the low-raised crater rim from north east provide channel to molten material which covers the entire crater floor (Figure **5.3c**)
Type 2: uneven deposit surface infilled with fine grained material, variation in slope within deposit terrain, pond material is partially extended off form the crater floor and often extended up to crater walls, depth of ponded material is higher.									
(5)	10.61˚ S	189.2˚ E	flat	sharp	≤15°	0.31	no	NW-SE	material at the floor is flat but the slope increases towards the crater wall
(6)	10.04˚ S	194.91˚ E	uneven	sharp	0°-31°	0.2	yes	N-S	partially infilling the crater floor, spread in E-S direction
(7)	2.53˚ N	206.51˚ E	uneven	sharp	0°-31°	0.1	yes	N-S	uneven distribution of pond material elevated towards the crater wall in SE direction
(8)	26.5˚ N	187.68˚ E	uneven	sharp	≤15°	0.19	no	N-S	irregular pond surface partially covering floor with possible pits (Figure **5.4b**)
(9)	16.1˚ S	173.30˚ E	uneven	sharp	≤15°	0.23	no	W-E	two ponded deposits are observed;(i) at the bottom of the cater floor, (ii)at the lower flank of SE crater wall (Figure **5.4c**)
(10)	21.59˚ S	171.29˚ E	uneven	sharp	0°-31°	0.23	no	W-E	oval shaped pond deposit emplaced at crater floor (Figure **5.4a**)

5.5 Comparison of Vesta ponds with those on Eros, Itokawa and the Moon

On Vesta, type 1 and type 2 ponds show various degrees of resemblance with ponded deposits on Eros, Itokawa and the Moon (Table **5.2**). However, ponded features on Eros and Itokawa are produced from fine dust substances whereas similar features are formed from molten and fluidized impact melt material on the surface of the Moon.

On Eros, 334 ponded deposits were identified, but due to limitations in data resolution only a minority of them (in this case 55) were analyzed in detail (Robinson et al., 2002). In terms of morphology, there are a few similarities between ponded features of Eros and Vesta, but differences are observed within their geometrical assessments. On Vesta, the majority of ponded craters are identified within similar latitudes as on Eros (0˚-30˚S/N). According to Roberts et al. (2014) out of 55, only 12 ponds have a flat smooth surface (≤10˚ slope) with an equipotential distribution of fine material at the crater floor (Figure **5.1a**) and a shallow depth similar to ejecta ponds on Vesta. On Eros, there are no ejecta ponds. However, in visual interpretation, the smooth surface of dust ponds on Eros appears similar to the smooth surface of ejecta ponds on Vesta. The remaining 43 ponds are identified on steep crater walls or are partially elongated (Figure **5.1b, c**), resembling dust ponds on Vesta. Nevertheless, the main difference is the size of the ponds and the potential source of ponded material. In general, the lower limit of the pond diameter is >30 m and is present within craters of <1 km diameter on Eros (Robinson et al., 2001). Further, the ponded deposits infill only a few meters of the original depth of the crater (Robinson et al., 2001) on Eros. Whereas on Vesta, the diameters of ponds range from 0.9-6.4 km within larger craters (~2-10 km). The overall pond depth is ~0.2 km on Vesta and covers a maximum of up to ~10% of the crater depth. The smaller size of ponded craters on Eros might be due to the significant size difference and consequently gravitational force between Eros and Vesta. Moreover, the majority of the ponds are present within low gravitational regions on Eros (Robinson et al., 2001; 2002), however Vesta's gravitational field is comparatively even.

On Itokawa, the surface also shows smooth flat pond regions and depressions. These smooth regions were described as featureless and consist of a fine regolith layer (Fujiwara et al., 2006; Miyamoto et al., 2007; Saito et al., 2006; Yano et al., 2006). So far 28 craters (out of 38; Hirata et al., 2009) show a morphology which has similar characteristics to dust and ejecta ponds of Vesta. The typical ponded feature on Itokawa includes smooth featureless fully or partially covered crater floors with low raised, brighter rims (Saito et al., 2006) and fine infilling material (~6 cm particle size) (Figure **5.1d-f**). On Vesta similar characteristics are present within both the category of ponded deposits (such as flat smooth surface within type 1 and fine-grained infilling material within type 2). The identified pond features on Itokawa are more abundant in small craters (0.002-0.134 km in diameter; Hirata et al., 2009). A strong correlation between color and albedo variation was observed and is possibly sensitive towards the grain sizes within regolith material (Saito et al., 2006). Other than the craters, the Sagamihara and Muses Sea regions also shows smooth featureless ponded deposits (Fujiwara et al., 2006; Figure **5.1e**) and occupy ~20% of the total asteroid surface (Hirata et al., 2009; Yano et al., 2006). Nevertheless, unlike Vesta, Itokawa reveals no obvious evidence of type 1 ponds. The overall generation of smooth pond-like impressions involves

migration of dry regolith (Fujiwara et al., 2006; Miyamoto et al., 2007; Saito et al., 2006) on Itokawa.

Characteristics of ponded materials were also identified within craters on the Moon (Hawke &Head, 1977a; b; Howard &Wilshire, 1975; Plescia &Cintala, 2012). Previous studies by Howard & Wilshire (1975) reported on the presence of flat featureless ponded material within small craters (dia. of 1-5 km). Fluidized ejecta melt for the production of ejecta ponds was proposed by Hawke and Head (1977a, b). They noted that craters with less than a certain diameter (<5 km) do not possess ponded deposits. However, this study was conducted in relatively low-resolution data. Later on, Plescia & Cintala (2012), used the LROC data set to conduct a global survey of small craters (up to 0.12 km in dia.) and catalogued features as 'melt pools'. Stopar (2014) observed similar smooth deposits outside crater rims and concluded that they must be produced from the fluidized ejecta melt. The molten material exhibits flat-floors with smooth texture, a sharp increase in slope from floor to wall, a heterogeneous distribution of boulders at the rim of the pond and infilling of the deepest region of the crater floors with molten substances (Figure **5.1g-i**). We identified similar features as type 1 ponds on Vesta. Depending upon the thickness of pool deposits, boulders and hummocky material can also be seen partially buried within the melted region on the Moon (Figure **5.1h-i**). The identified host craters with ponds on the Moon have diameters from 0.12-30 km and pool diameters of 0.007-6 km (Plescia & Cintala, 2012). In comparison to Vesta, the impact melt on the Moon is much more prevalent due to higher impactor energies caused by higher velocities of the impactors (40 $km \cdot s^{-1}$), derived via theoretical models (French, B., 1998). So far, the literature predominantly suggests the presence of melt pools on the Moon.

5.6 Hypothesized processes for the production of type 1 and type 2 ponds on Vesta

Both the pond deposits on Vesta reveal partially overlapping features with the ponded morphology noted on Eros, Itokawa and the Moon. However, their formation mechanism and material properties are different. Based on our observation and comparison with ponded characteristics on other planetary objects, we understand that both types of ponds on Vesta must have undergone different formation mechanisms.

Type 1 pond deposits show a flat smooth homogenous distribution of the flow-like impact melt material (Figure **5.3**) within the crater floor which is commonly identified on the surface of the Moon. The melt materials are well preserved in and around the vicinity of the impact craters. The craters hosting the ejecta ponds on Vesta are underneath the sheet of ejecta blanket. They are typically shallow and located within relatively small craters producing a smooth lens-like surface at the bottom of the crater cavity. Similar to ejecta ponds on the Moon, craters hosting type 1 ponds on Vesta too have low raised rims (average ~0.04 km in height) and are located on the lower elevated region which provide ideal topographic conditions for the downslope movements of melts. According to the stratigraphy and age models of the Marcia crater region, the northernmost Minucia crater must be the oldest crater followed by the Calpurnia crater and Marcia (Williams et al., 2014b). Geological and spectral evidence gathered from the Dawn data also suggests that the ejecta melt in this region is composed of the impact ejecta of Minucia, Calpurnia and Marcia (McCord et al., 2012; Williams et al., 2014b). Thus, based on the apparent age and the

morphological evidence of melt material, we hypothesize that given the close proximity of the ponds to the region that has been identified as melt-rich, the ponds are melt from Marcia, Calpurnia and Minucia that gathered in pre-existing craters. A similar impact melt infilling process may apply to the ponds identified on the north of Cornelia crater (Figure **5.2**, Figure **5.3a**). Additionally, the pond hosting craters are located in lower elevated regions in comparison to Cornelia which makes a possible downslope movement of flow-like impact melt material likely. Due to the similar characteristics of the melt pools of the Moon and type 1 pond deposits on Vesta we name them as 'ejecta ponds'. We illustrate the formation mechanism of ejecta ponds with a graphical sketch in Figure **5.5**. Other than the impact melt infilling process, we also consider the near vertical high velocity impact theory proposed for melt pool formation on the Moon. However, given the location of Vesta within the asteroid belt and the comparatively low velocities within the asteroid belt, Vesta has experienced relatively slow impacts (~8-10 $km \cdot s^{-1}$; O'Brien and Sykes, 2011; Williams et al., 2014a) in comparison to the lunar surface. Thus, direct melt pool formation in near-vertical high-speed impacts as suggested on the Moon is unlikely for Vesta. Additionally, if this mechanism was dominant on Vesta, there should be more ponded craters present on the surface of Vesta at a global scale, but that is not the case.

Type 2 shows (Figure **5.4**) resemblance with dust deposits of Eros and Itokawa, however, they are often less flat and smooth. Based on the surface morphology and multi-step seismic model results, it was demonstrated that seismic reverberation on Eros and Itokawa is able to destabilize the slope, cause the regolith to move downslope and formed pond deposits (Veverka et al., 2001a; Richardson et al., 2004; 2005). Thus, we suspect similar process may account for type 2 pond formation on Vesta. Due to seismic shaking the fine material may drift from parts of the rim and/or the crater wall and serve as source for the type 2 pond deposit. Once the deposits are transported downslope, the next step is segregation of fine-grained material. However, unlike type 1 pond deposits, type 2 do not show smooth nearly flat pond deposits at the center of the crater floors. Thus, we suggest that after moving downslope, the dusty material did not undergo a sorting process to form smooth deposits. To support this hypothesis, we compare the process of Vesta with dusty regolith bearing asteroids. On Eros too, few dust pond candidates (approximately 20%) lack the smooth morphology (Roberts et al., 2014). The absence of a smooth pond morphology is possible either due to an insufficient amplitude of seismic shaking and/or the duration of the shaking that might have lasted only to transport the dusty material downslope (Roberts et al., 2014) but not smoothen it. Thus, to understand diffusivity of the impact-induced seismic shaking, series of numerical shake-table experiments were conducted (Richardson & Kedar, 2013; Richardson et al., 2020). According to the results, the small size impactors (dia. of 4 m to 500 m for Eros and 0.07 m to 0.5 m for Itokawa) are capable of producing global scale seismic shaking which then diffuses (at the average peak rate of ~0.5±0.2 $km^2 \cdot s^{-1}$ and ~0.002±0.001 $km^2 \cdot s^{-1}$) maximum up to the distance of 20 km and 0.62 km on Eros and Itokawa, respectively. Nevertheless, the derived diffusion rate is still of inadequate amplitude to generate a flat floored pond deposit morphology at a global scale on Eros (Roberts et al., 2014). Given the size of Minucia, Calpurnia and Marcia craters on Vesta, rare but relatively large-scale impactors (de Elía & Di Sisto, 2011) with similar velocity are expected to generate higher seismic shaking and diffusivity locally. Post-impact the

seismic energy dispersion may have possibly disturbed the stable conditions and induced the downslope movements of dust. However, to achieve the smooth morphology, separation of grains via segregation would require seismic diffusion for relatively longer time. Since only 6% of total impactor has velocity of ~8 $km \cdot s^{-1}$ (Williams et al., 2014a), frequent repetition of high amplitude seismic dispersion is not expected on Vesta. Moreover, the global scale seismic diffusion is applicable to the asteroids with ≤50 km in diameter, on larger asteroids only local seismic shaking and diffusion is expected (Richardson et al., 2020). Thus, large impacts on the surface of Vesta are not capable of diffusing seismic energy at global scale. From the above arguments, it is clear that smaller asteroids' surfaces (such as Eros, Itokawa) vibrate more significantly than the larger asteroids (Richardson et al. 2004; 2005; Murdoch et al., 2015; Marchi et al., 2015) for a given impactor size. Additionally, the Small Body Cratered Terrain Evolution Model (SBCTEM) also suggested that at given seismic diffusivity (~0.5±0.2 $km^2 \cdot s^{-1}$), 0.04 km diameter crater experiences a gradual infilling process and requires energy diffusion for ~10 Myr to produce smooth pond morphology on Eros (Richardson & Abramov, 2020). On Vesta, our observed host craters have significantly higher diameters (5.90 km-10.05 km) which will require even more time along with higher attenuation of seismic diffusivity. Considering the massive size of Vesta and large diameter of pond hosting craters, we suspect rare high-amplitude seismic diffusivity at localized scale might be adequate to transport the material downslope but not able to develop smooth, nearly flat pond deposits due to infrequent large impactors. Another potential mechanism for regolith transport on Vesta is the volatile-induced outgassing of the material from the subsurface (Sears et al., 2015). This process expected only on planetary bodies which has volatile bearing regolith (Benoit et al., 2003). The volatile-induced fluidization process can be triggered either by the impact that produced the host crater excavating volatile-rich material which subsequently degasses and fluidizes the regolith grains (Sears et al., 2015) or by the implantation of thermal energy via impact that may release mineral-bound hydroxyl groups (and/or other volatiles). Under laboratory conditions, it has been proven that fluidization by gas flow at subsurface scale lifts the individual grains, resettles them on the surface and produce fine-grained dust ponds on asteroids (Benoit et al., 2003; Sears et al. 2015). Based on the morphological evidences, small amount of localized volatile presence is strongly suggested on Vesta (Denevi et al., 2012; Scully et al.,2015). However, they cannot survive for longer time (Scully et al., 2021). Therefore, type 2 pond formation on Vesta may also be possible via one or more of the above described mechanisms. Both cases are likely to be relatively quick and the pond material might not experience severe sorting or segregation post-accumulation. This may also lead to a not well-established equipotential alignment of dry pond material. The dry brittle regolith condition of Vesta also provides favorable conditions for electrostatic particle levitation (Lee, 1996; Roberts et al., 2014; Robinson et al., 2001; Veverka et al., 2001a) and boulder disintegration (Dombard et al., 2010) which are suggested as potential mechanism for the formation of dust ponds on Eros. Given the higher gravity, larger size (Table **5.1**; Russell et al., 2012) and high escape velocity (~363$m \cdot s^{-1}$; Veverka et al., 2000) of Vesta, the particle levitation and their segregation is not possible. Next, our mapped type 2 ponds do not reveal any large differences in their surface area and lack the presence of boulders within their depressions at given resolution. Thus, the boulder disintegration mechanism may not be applied in the case of Vesta. The available

data has different spatial resolution for Vesta, Eros and Itokawa which may have hindered the analysis and make a direct comparison difficult. It is totally possible that there are Eros and Itokawa like ponds on Vesta, but we simply do not see them. Nevertheless, we can still make a comparison to discuss the different processes. The ponded material of this particular group of craters consists of loose fragmented dust-like dry particles and are closely related to pond deposits on Eros and Itokawa, thus we name them as 'dust ponds'.

Both type 1, ejecta pond and type 2, dust ponds are identified within a similar region on Vesta's surface. However, we comprehend that both of them were produced via different mechanisms. Ejecta ponds show flattened surfaces and are evenly distributed within crater floors whereas dust ponds are unlevelled and present on steep regions of the crater hosting the pond. We interpret that ejecta ponds must have formed via infilling of ejecta from the neighboring large craters (Minucia, Calpurnia, Marcia and Cornelia) which later solidified as part of the crater evolution process (Figure **5.5**). Whereas for the production of the dust ponds, rare high-amplitude localized seismic diffusion and/or volatile-induced fluidization may be responsible for the transportation of granular material downslope (Figure **5.6**). Nevertheless, given Vesta's size, the transported dust material may not have experienced enough seismic shaking allowing the grainy regolith to remain unlevelled and only partially distributed across the crater floor. As a consequence, the typical smooth surface as observed on Eros or Itokawa may not be achieved in dust ponds on Vesta. In Table **5.4** we have summarized all possible pond formation mechanisms discussed so far on Vesta, Eros, Itokawa and the Moon.

Table 5.4 Summary of possible geological processes responsible for the production of ponds on Vesta, Eros, Itokawa and the Moon. The colors represent the likelihood with which the geologic processes occur: Green: possible, Orange: may or may not be possible and red: highly unlikely.

Geological Process	Vesta	Eros	Itokawa	Moon
Dust pond deposit via volatile outgassing	Likely (this work, e.g. nearby pitted terrains)	Possible, hypothesized under laboratory conditions (Sears et al., 2015), but Eros is a dry S-type asteroid and so far, no direct morphological evidences for volatiles are found	Possible, but unbound volatiles are not present, as this process has been suggested to work for Eros, it should work for Itokawa too	Possible, because volatiles are present in the lunar regolith (Basilevsky et al., 2012), but not reported in literature in relation to ponds
Migration of dust via seismic shaking	Since the surface of Vesta has been heavily bombarded, seismic shaking is possible	Eros' regolith has experienced impacts, due to its small size, seismic waves may propagate through the entire body (Robinson et al., 2001;2004)	Due to seismic shaking granular material may have fallen from higher elevated regions into depressions (Fujiwara et al., 2006).	The surface of the Moon has experienced impacts which have the capacity to generate seismic waves (Plescia & Cintala, 2012)
Material segregation via seismic shaking	Unlikely due to the large size of the body, this phenomenon might not be observable due to limitation in the resolution of the data	Possible (Cheng et al., 2002; Robinson et al., 2001; 2004 ; Thomas et al., 2002; Veverka et al., 2001a)	Smooth terrains likely involve processes for grain-size sorting via seismic shaking initiated by impacts (Fujiwara et al., 2006; Saito et al., 2006)	No evidence of dust sorting mechanism noted using current data.
Material segregation via electrostatic forces	Unlikely due to large distances to be travelled and the topography that would need to be overcome electrostatic charging has not been suggested to be a dominant process either	Pond deposits follow underlying topography because of the low gravity and this mechanism is possible for ponds which are not leveled or flatten (Lee, 1996; Roberts et al., 2014; Robinson et al., 2001; Veverka et al., 2001a)	As this mechanism is possible for Eros, it should also be possible for Itokawa. The fine material may have been levitated but high escape velocity (10-20 $cm \cdot s^{-1}$) restrict the particle rearrangement (Miyamoto et al., 2007)	Unlikely due to the high gravitational pull and a lack of evidence for a dust cloud near the lunar surface (Horányi et al., 2015; Stopar et al., 2014; Szalay and Horányi, 2015)
Boulder disintegration	Unlikely because there are not enough large boulders to fill an entire crater pond	Thermally disaggregated boulders have been proposed (Dombard et al., 2010)	This mechanism has not been suggested, but given that it is possible on Eros, it should also be possible on Itokawa	Unlikely because there are not enough large boulders to fill an entire crater pond
Ejecta pond infilling via fluidized ejecta (melt and/or volatiles)	Likely, since impact melt has been observed near ponded craters (Williams et al., 2014b)	Unlikely because melt does not occur in impact craters	Unlikely because melt does not occur in impact craters	Likely, impact melt has been observed near ponded craters (Hawke and Head, 1977a; b; Plescia and Cintala, 2012; Stopar et al., 2014)

5.7 Conclusion

In analogy to investigation on asteroids Eros, Itokawa and the Moon, we have identified two types of ponded features in craters on Vesta which show some different and some overlapping geomorphologic characteristics. These ponded deposits have experienced different formation mechanisms. Type 1 are ejecta ponds which has smooth and flat surface with a constant slope and shallow infilling deposits (average ~0.04 km). They retain the original shape of the crater and the material is evenly distributed within the crater floor. Crater hosting ejecta ponds are possibly formed by the distribution of impact ejecta of nearby craters (Minucia, Calpurnia, Marcia and Cornelia) on Vesta. They are similar to the melt pools identified on the Moon. The pre-existing topography (e.g. low raised rims and location of host crater in low elevated regions) plays a vital role in channelizing and downslope movement of the melt material. Type 2 are dust ponds which have a few different characteristics (in comparison to type 1 ponds) such as granular pond material, pond deposits with undulating surfaces, often relatively greater depth (average ~0.2 km) and sometimes an abrupt change in slope. The type 2 ponded material on Vesta either moved downwards from parts of crater walls via seismic shaking or may have been transferred on to the surface through volatile outgassing. In case of seismic activity, the energy diffusion is restricted to local scale due to large size of Vesta. Additionally, the surface has not experienced large scale impactors frequently. Thus, rare high-amplitude of seismic diffusivity is not capable to conduct particle segregation and produce smooth morphology in relatively huge host craters. Similarly, the presence of volatiles on Vesta is observed at regional scale (Denevi et al., 2012; Scully et al., 2015) but they might have survived for shorter time (Scully et al., 2021). Therefore, we interpret that type 2 pond material was transported downslope via seismic diffusivity and/or volatile outgassing. However, the transported material might not experience severe sorting or segregation post-accumulation due to rare high amplitude seismic diffusivity and a short span of volatile activity, thus failing to produce the smooth featureless ponded surfaces as observed on Eros and Itokawa.

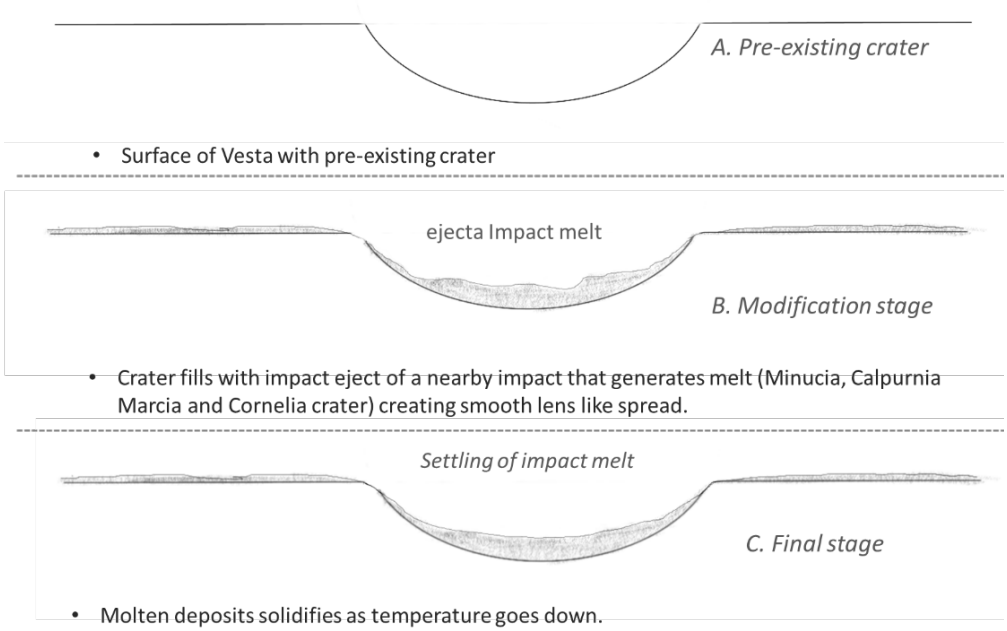

Figure 5.5 Illustration of production of type 1 ponds via emplacement of impact melt. The ejecta ponds on Vesta can be formed via downslope movement of ejecta melt material from neighboring impact crater ejecta. The ejecta infills the lower cavity of the crater and later solidifies.

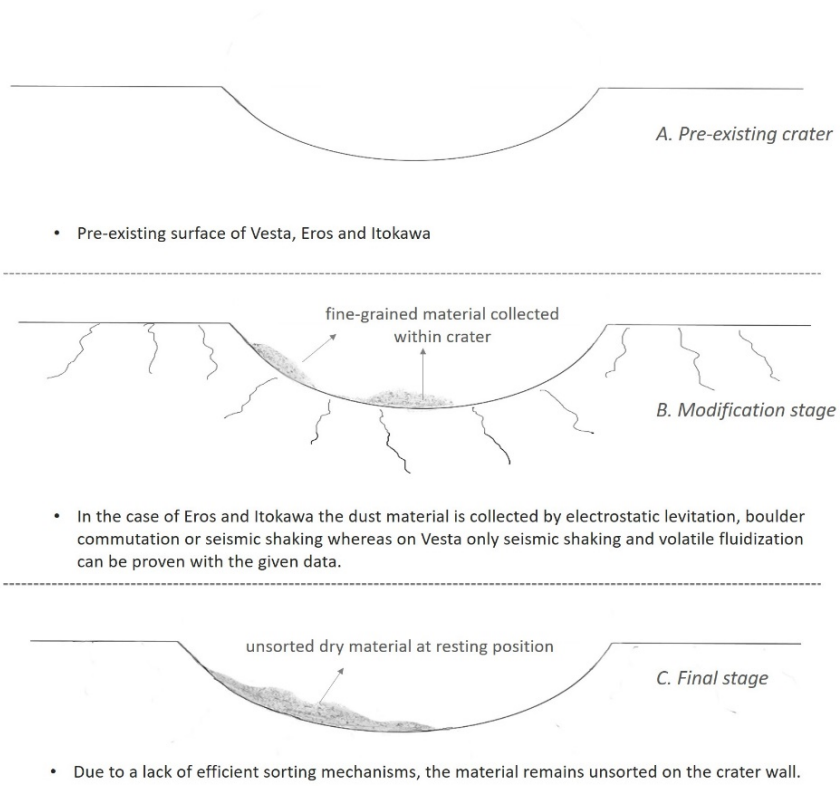

Figure 5.6 Illustration of production type 2 ponds via seismic shaking. Two possible mechanisms may be responsible for the production of dust ponds, depending upon the environment of the planetary body. Previous studies explain the involvement of all 3 mechanisms (electrostatic levitation, seismic shaking or boulder commutation) on the surface of Eros (Robinson et al., 2001; Thomas and Robinson, 2005; Veverka et al., 2001a; Cheng et al., 2002) and Itokawa (Saito et al., 2006; Fujiwara et al., 2006). But in the case of Vesta a low degree of seismic shaking and volatile- induced outgassing (illustrated by Sears et al., 2015) is probably responsible for the mobility of fine-grained material into the crater.

5.8 Acknowledgments

The authors acknowledge the Dawn team for providing data and support. This work is part of the research project "The Physics of Volatile Related Morphologies on Asteroids and Comets". RP and KO would like to gratefully acknowledge the financial support and endorsement from the German Academic Exchange Service (under DLR- DAAD PhD Fellowship) and the DLR Management Board Young Research Group Leader Program by the Executive Board Member for Space Research and Technology. A portion of the work was carried out at the Jet Propulsion Laboratory under contract with NASA.

Data Availability Statement

Raw images used in this work for Eros (Robinson & Carcich, 2001), Itokawa (Stooke, P., 2015) and calibrated data from Dawn at Vesta (Nathues et al., 2011) are available at Small Bodies Node of Planetary Data System (PDS). Additionally, we also utilized the pond catalogue of Eros (Roberts, J., 2021) available at PDS. Derived data products are available via Figshare: Parekh, R. (2021): Formation of ejecta and dust pond deposits on asteroid Vesta (https://doi.org/10.6084/m9.figshare.16863478.v2).

6. SMALL-SCALE PIT CHAINS ON CERES AND THEIR RELATION WITH SURFACE REGOLITH

The following has been under review as **Parekh, R.**, Otto, K. A., Jaumann, R., Hauber, E., Russell, C.T. and Raymond, C.A., Small-scale pit chains on Ceres and their relation with surface regolith. Submitted to *Icarus*. The author contribution is explained in the Section **1.2**.

6.1 Abstract

High-resolution XM02 data provided the opportunity to carry out the mapping and analysis of small-scale pit chains within crater floors of Occator, Azacca and Urvara. As a result, 557 pit chains and 284 trough features were mapped. The observed pit chains are often present as isolated pits which later produce semicircular partially adjoined chains and further developed as wider troughs. Within Occator, pit chains are of smaller scale and has pristine nature relatively, however their scale increases moving towards Azacca and Urvara. The diverse distribution patterns of pit chains are associated with different endogenic activities. Radial distribution of pit chains at Cerealia Faculae and south west zone of Occator favors laccolith formation underneath whereas linear distribution at Vinalia Faculae is potentially produced by a network of fractures connected to deep reservoir (~35 km). Linear clusters of pit chains within Azacca and Urvara are related to the compression-contraction of ice pockets. Nevertheless, the ice pocket within Azacca is present at relatively deeper depths (10-20 km; Sizemore et al., 2019) in comparison to Urvara (<1 m; Bland et al., 2016) where ice is mixed with a large amount of mechanically weaker materials. In general, when the loose upper surface regolith material falls into the subsurface stronger base, it produces sinkholes which subsequently develop as a sequence of muted pit chains. Hence, the pit depth is often considered as a proxy to estimate the thickness of surface regolith. We derived the minimum average thickness of surface regolith within Occator (30 m), Azacca (200 m) and Urvara (800 m) based on the pit chains depth. However, the Azacca estimation may precisely represent the equatorial-scale surface regolith thickness whereas Occator and Urvara estimation constitute for the regolith thickness of crater floor due to their distinct subsurface and surficial conditions.

6.2 Introduction

Pit chains are type of linear structure comprise of circular to semi-circular collapsed pit rims (Martin & Kattenhorn, 2013; Martin et al., 2017; Nahm & Kattenhorn, 2015; Whitten & Martin, 2019; Wyrick et al., 2004) which are partially or fully fused together to produce scalloped-edged steeply dipping troughs. Isolated pits in an alignment are considered as an initial phase of the linear structure which gradually transit into a wider trough structure (Horstman and Melosh, 1989). On Earth, Icelandic pit chains are widely considered as an analogue for the surface of planetary objects including Mars (Wyrick et al., 2004), Venus (Bleamaster & Hansen, 2004), Moon (Head & Wilson, 1993), Phobos (Horstman & Melosh, 1989), Vesta (Cheng & Klimczak, 2020), Ceres (Buczkowski et al., 2018b; Scully et al., 2017), Enceladus (Martin et al., 2017) and Arrokoth (aka 2014 MU69) (Schenk et al., 2021). Depending upon the planetary bodies, multiple mechanisms (Wyrick et al., 2004) have been hypothesized to form pit chains via sinking of the surface regolith material into

subsurface void caused by the extension of pre-existing fractures (Buczkowski et al., 2014; Ferrill et al., 2004; Martin et al., 2017; Prockter et al., 2002; Scully et al., 2017; Sullivan et al., 1996; Thomas et al., 1978; Veverka et al., 1994; Wyrick et al., 2004). All the proposed mechanisms involve endogenic subsurface activities depending upon the conditions of the planetary bodies.

On Ceres too, subsurface endogenic processes are suspected for producing various features such as grooves, floor fractures and large-scale pit craters (Buczkowski et al., 2016; 2018a; b; Scully et al., 2017). The pit craters of Samhain Catenae region (0˚– 30˚S) are influenced by subsurface convection and based on their spacing the derived localized thickness of the crustal layer of Ceres is ~≥58 km (Scully et al., 2017). Buczkowski (2018a) studied fractures within vicinity of Occator crater (19.8˚N) and suspected compaction of the volatile rich material as controlling mechanism. Crater floor-fractures associated with Yalode (42˚S) and Urvara (45˚S) are attributed to the upwelling of low-density mobilized material (Buczkowski et al., 2016; Scully et al., 2017). Lastly, computation modeling of floor fractures of Azacca (6.7˚S), Ikapati (33.8°N) and Occator suggested that the fractures are related to the low viscosity ice rich volatile layer and thus are present only within the crater which match as such criteria (Otto et al., 2019). In a nutshell, different large-scale fracturing processes analyzed by previous research noted the influence of endogenic activities on Ceres.

Previous investigations carried out using LAMO data sets which limit the small-scale regional analysis due to resolution restrictions. This limitation can be bypassed using the Dawn extended mission (XM02) datasets. The Dawn spacecraft explored Occator and nearby regions during its second phase of the mission from 2017 to 2018 (Castillo-Rogez & Rayman, 2020). During its extended mission, spacecraft acquired relatively higher spatial resolution (up to ~3.3 $m \cdot pixel^{-1}$) in an elliptical orbit at the altitude of ~35 km (Castillo-Rogez & Rayman, 2020). The key motivation for the extended mission is to enhance the understanding of volatile sources within Occator by acquiring better surface and spectral data (Castillo-Rogez & Rayman, 2020). Hence, by using the XM02 data, we aim to conduct regional analysis of pit chains with a key motivation to establish relationship between surface pit chains, subsurface fracturing and intrusion of magmatic material as well as derive quantitative information to understand the distribution of regolith. In addition, we anticipate amplifying near-surface crustal properties of Ceres by examining the questions below:

- Is it possible that pit chains may have been formed by the diverse physiological activities on Ceres?
- If so, what are the possible endogenic subsurface events responsible and what factors account for presence or absence of these events?
- What inferences related to surface conditions can be drawn based on the presence of pit chains?

With this in mind, we (i) mapped small-scale pit chains, (ii) conducted detailed morphological analysis and estimated diverse morphometrical parameters (depth, length, dimeter, pit spacing), (iii) establish potential links between surface pit chains and subsurface endogenic events and (iv) derived the thickness of loose surface regolith material.

6.3 Methodology

6.3.1 Identification and classification of pit chains

The identification and classification of pit chains is conducted based on the morphological identifiers described in previous studies (Buczkowski et al., 2016; Martin et al., 2017; Scully et al., 2017; Wyrick et al., 2004). Typically pit chains are a series of circular to elongated or irregular shaped depressions (Martin et al., 2017; Wyrick et al., 2004). In general, they have low-raised rims and manifest absence of an ejecta blanket, frequently reveal gullies features, often show evidence of downslope regolith movements and color heterogeneity on their walls (Wyrick et al., 2004). The pit chains experience erosion at the walls and transit into wider collinear troughs (Horstman & Melosh, 1989). Depending upon their formation mechanisms they are either v-shaped (during initial stage of formation) or flat/bowl shaped floor as trough (Wyrick et al., 2004).

6.3.2 Mapping survey and imaging data

Previous studies presented the mapping of large-scale pit chains using relatively low-resolution LAMO mosaic on global scale (Scully et al., 2017). In our study, we focused on small-scale pit chains which were not observed earlier due to resolution limitations. For the mapping survey, we utilized surface mosaic from the extended mission (XM02) data which has resolution of ~5 m/pixel. The mapping was done using a geospatial environment in ArcMap for detailed viewing and further classification is conducted based on the morphological identifiers (Section **6.3.1**). For an efficient survey we produced a grid of 50×50 km and tagged the completed area.

6.3.3 Estimation of physical parameters

To understand scaling variation and its association with surface regolith, it is essential to consider physical properties such as length, diameter, depth and distance between individual pits. Multiple studies have assumed a geometrical relationship between pit diameter and angle of repose (30˚) to estimate the depth of pit chains (Prockter et al., 2002; Sullivan et al., 1996; Veverka et al., 1994). Rather than assuming the angle of repose, a more reliable method was proposed by Wyrick (2004). In this approach, pit slope is considered as an angle of repose for stable surface regolith.

$$d = \frac{1}{2} D \times tan\theta \qquad (6.1)$$

Here d is pit depth, D is pit diameter and θ will be slope of pit chains (Martin & Kattenhorn, 2003). In our study area, often pit chains were too small to estimate the slope at a given resolution. Thus, we considered slope of crater walls to represent the angle of repose. Further, the depth of pit chains is used as proxy to approximate the surface regolith thickness. This approach assumes that depth of a pit chain is identical to the surface regolith (Wyrick et al., 2004; Martin & Kattenhorn, 2003).

6.4 Observations

To understand the pit chains morphology, three craters namely, Occator, Azacca and Urvara have been chosen in this study. There are multiple reasons why we focused down to these craters: (i) the location of the chosen craters: Occator is at mid-northern latitude of Ceres, Azacca at equator and Urvara located near south pole of the Ceres, (ii) The relative ages of various geological units of these craters goes back to 490 Ma (Crown et al., 2018), representing one of the oldest regions of Ceres, which has significant effect on the morphology of various features, (iii) The restricted coverage of high resolution XM02 images captured certain regions of Ceres.

6.4.1 Distribution and morphological facies of pit chains

In addition to the linear feature maps from Otto (2019) and Scully (2020), we mapped 472 candidates of fractures. In total, we present 1355 linear features which includes mapping candidates from Scully (2020; 527 linear features), Otto (2019; 356 linear features) and our mapping campaign (472). From 1355 features, 557 are classified as pit chains, 284 as troughs and the rest were tagged as 'unknown' due to inadequate illumination conditions. While mapping the pit chains, we observed diversity within their morphology which helped to assert their evolution sequence into troughs (Section **6.4.2**).

Occator crater is located at 19.8°N and 239.3°E on Ceres with a diameter of ~92 km while the inner floor is ~73 km. The southern part of the floor is relatively smooth while the rest of the regions are blanketed with brines (Schenk et al., 2020) with varying thickness (Scully et al., 2020). Pit chains are located at the floor of Occator and within circumference up to the maximum distance of ~91.8 km from the center of the crater. The pit chains developed in the crater floors are extended from the SW to center and western area (Figure **6.1a**). Most of them are densely populated in the hummocky surface of the SW region and at the center of the elevated region of Cerealia Faculae whereas very few are located within Vinalia Faculae (Figure **6.1a**). Pit chains identified within Occator are not always extended straight, those present at SW region and around the central dome have radial and polygonal distribution whereas isolated chains nearby Vinalia faculae have linear orientation (Figure **6.1a**). Most of the pit chains appeared in groups and some crossed each other with common conjunction points (Figure **6.1b**). Pit chains have different morphologies within Occator. Often, they are shallow, isolated, evenly spaced with visible rims and partially muted (Figure **6.1c**). In such examples, identification of individual pits are possible. We understand that this must be the early phase of pit chain development and such candidates are rare. Few pit chains are fully coalesced into semicircular to elliptical shapes with multiple low elevated regions, separated by a partially low standing rim of the original pit forming long chain features (Figure **6.1d**). Besides, there are various dome features closely associated with pit chains (Figure **6.1b, f, g**). The pit chains are either developed at the elevated regions of domes (Figure **6.1f**) or cut through by the domical features (Figure **6.1g**). We also observed significant color heterogeneity within the walls of the pit chains (Figure **6.1e**). A group of pit chains and fully developed troughs nearby Cerealia Faculae shows color heterogeneity from the upper flank to the bottom of the wall and the downslope mass movements revealing unconsolidated materials (such as boulders) at the floor

(Figure **6.1e**). At Vinalia Faculae pit chains are relatively small in number and are complexly covered by the bright dense material (Nathues et al., 2020) implying their close association with excavation of volatiles and/or brine. We also observed individual pit chains overlapping lobate floor units in western zone of Cerealia Faculae (Figure **6.1g**). In contrast, the pit chains present in SW region rarely have any strong color heterogeneity and are populated with fully developed troughs with relatively narrower section (max up to ~0.4 km), higher depth (avg. 0.1 km depth) and linear rims. The outline of the troughs is often semicircular, similar to coalesced pit chains except that the troughs are relatively wider. Hence, it is challenging to distinguish them from the coalesced pit chains. In total we observed 440 pit chains and 264 troughs. The mapped pit chains have a variety of preserved morphology (including fragile surface albedo), hence we suspected them as one of the most recently developed surface features within Occator. Other than pit chains, we also observed cracks at the crater bottom of the crater walls with varying scale. Scully et al., 2020 published a detailed map which describes various other features including cracks.

Azacca crater is located (lat.: 6.7°S; long.: 218.4°E) at the mid latitude of the Cerean surface. The crater has ~50 km diameter while the inner crater floor is ~40km wide. Pit chains are also noted near the central peak of Azacca crater and north west part of the rim (Figure **6.2a**) only. In total, we observed 11 pit chains and 13 troughs. The identified pit chains are relatively mature with limited morphological impressions. Few pit chains exhibit scalloped troughs which suggest the possibility of further collapse and formation of fully developed trough features (Figure **6.2b**). The number of pit chains is relatively lower within Azacca. Unlike Occator, we did not observe any individual pits on the crater floor nor any of the domical features identified at given resolution. Pit chains are clustered in two groups, one present beyond the crater rim (majority spreading radially from south to north) and rest clustered at the floor near the central peak. Here the pit chain features are more ambiguous and relatively degraded (at a given resolution).

Urvara crater is located (lat.: 45˚S, long.: 250˚E) near the southern pole with an average diameter of ~170 km and floor width of ~139 km. Majority of the floor is blanketed by smooth intermixed impact ejecta from Urvara and Yalode crater (Crown et al., 2018). The interior of the crater is characterized by a central peak, hummocky floor near the western rim and south east zones (Figure **6.3a**). We identified three complex networks of pit chains (i) at the Eastern side of central peak, (ii) at NW zone near the hummocky terrain and (iii) down near the southern rim (Figure **6.3a**) on the floors of Urvara. Unlike Occator, pit chains within crater floors are of small scale. However, we identified mounds and domes of various shapes, sizes and few of them are closely related to pit chains. At the NW zone, the pit chains are relatively low in number and are scattered without any specific orientation (Figure **6.3d**). Pit chains are present within close vicinity to domes with few more examples of albedo dichotomy at the steep walls of chains (Figure **6.3c**). The group of pit chains are passing by the base of the large dome and few are also developed at the summit (Figure **6.3c**). The pit chains at the summits are smaller than the ones observed at the base and isolated pits are distinguished. One of them also shows significant color variation at the steep of the pit chain (Figure **6.3c**). The pit chains here are closely packed and few showed coalesced pit chains (Figure **6.3c**). Most of the pit chains in this zone are directed in NW-SE however, a group of fractures in

the south is a cross-cutting pit chain cluster (Figure **6.3a**). Lastly, a cluster of pit chains is also present near the southern rim area which are crossing a relatively smooth zone and extending on the rough floor (Figure **6.3b**). In total the number of pit chains and troughs are 106 and 7 respectively. The pit chains morphology of Urvara is degraded in comparison to those present at Occator but are relatively more pristine than the Azacca ones.

Eventually, the pit chains distribution, their morphology, close relation with smooth floor and dome features are some of the common impressions observed both on Occator and Urvara. Considering the case of Azacca, we did not observe strong morphological characteristics with multiple examples of pit chains.

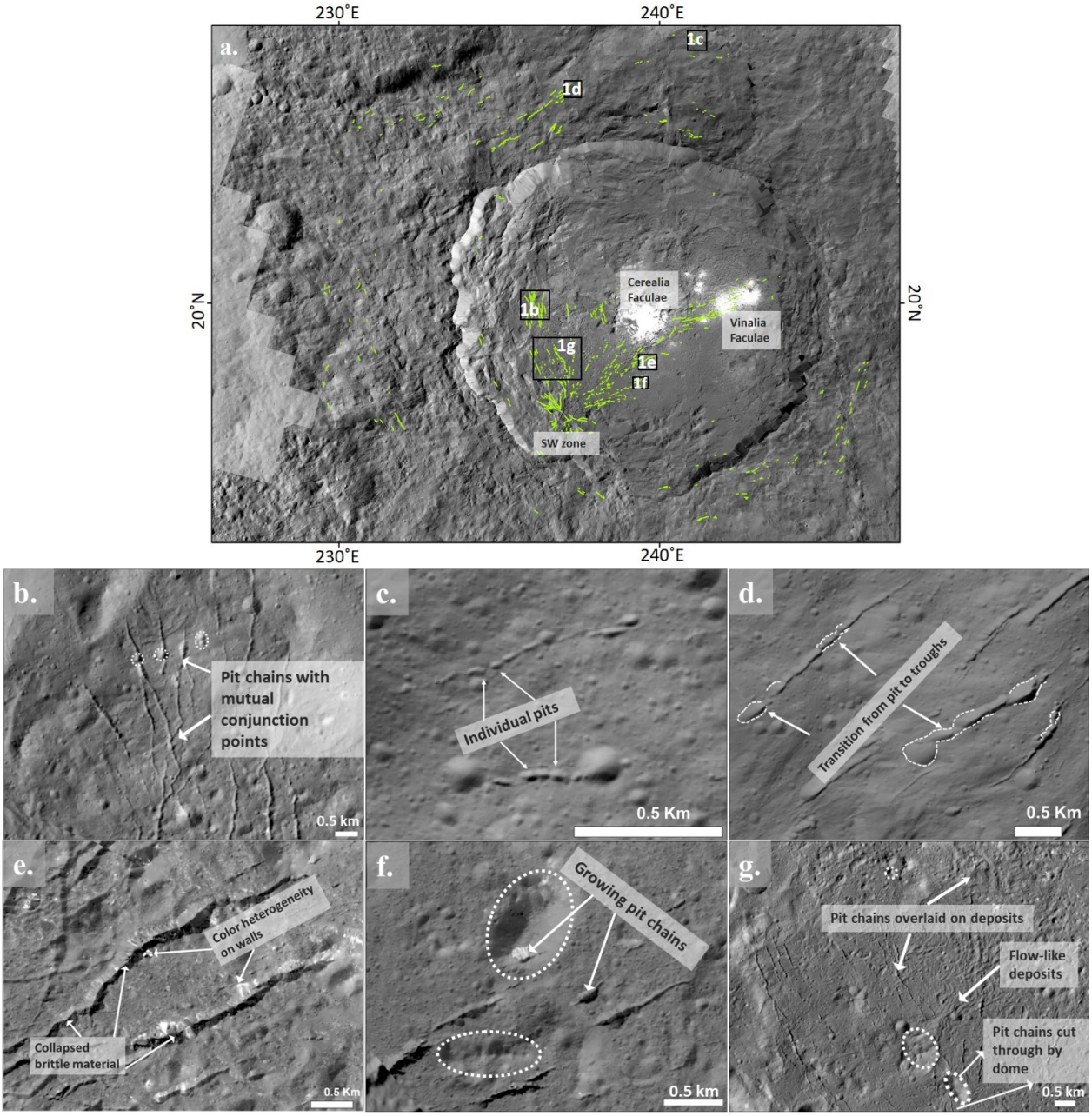

Figure 6.1 Distribution of pit chains and their morphological facies within Occator crater. (a.) Map of pit chains (green lines) identified within Occator. (b.) Close clusters of pit chains, some of them are adjoined via mutual points. (c.) Initial stage of pit formation, where the circular head of the rims can be seen. (d.) As the erosion develops, the rim walls of the pits collapse and adjoined with each other producing scalloped troughs, highlighted in white dash lines. (e.) Examples of mutated pit chains reveal significant surface brightness between their wall and the floor. (f.) & (g.) Close relation of pit chains with domes features. Often pit chains are either passing by or partially buried beneath the domes. (g.) Examples of growing pit chains on the smooth floors of Occator. In image b., f., g. domical features are highlighted with white dotted circle. The data of dome features was retrieved from Schmidt et al., 2020.

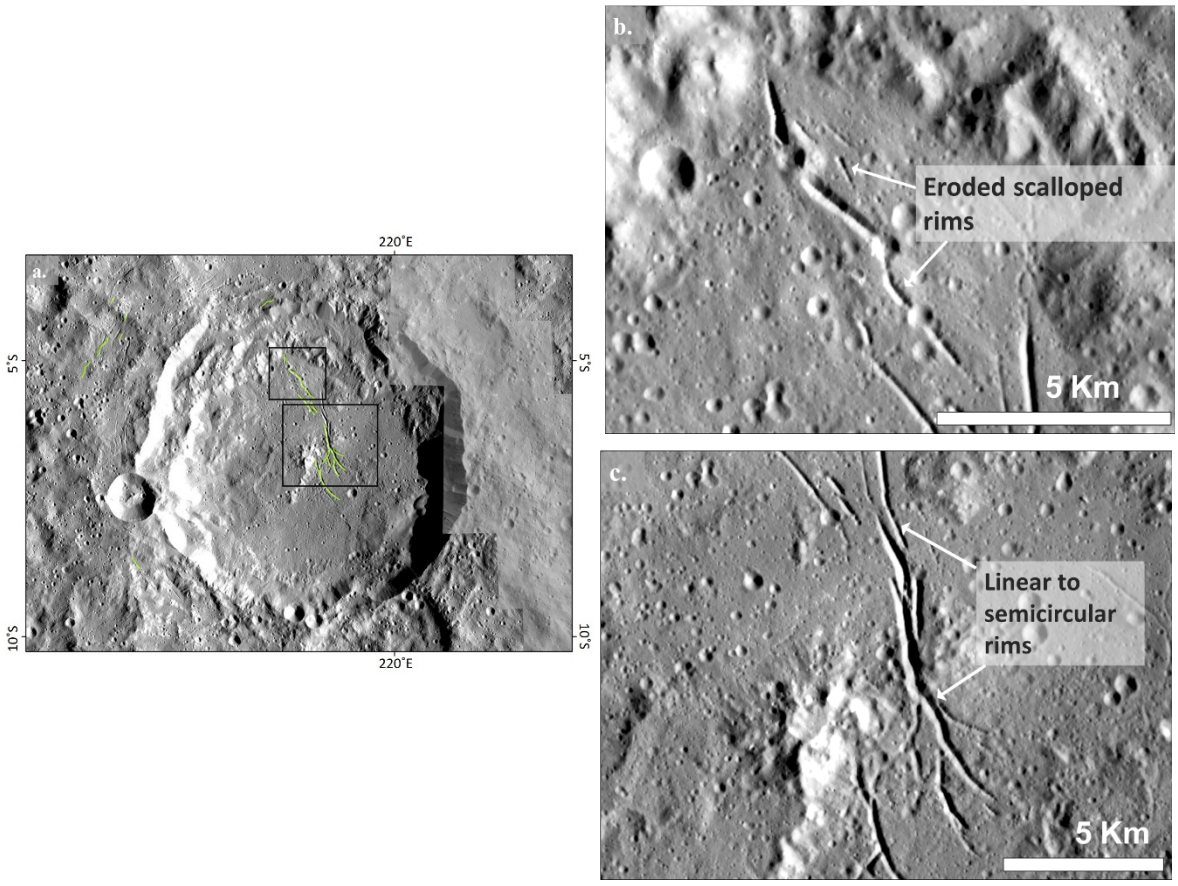

Figure 6.2 Distribution of pit chains and their morphological facies within Azacca crater. (a.) Map of pit chains (green lines) identified within Azacca. (b.) and (c.) shows scalloped to linear rims of fully developed troughs within lower elevation of Azacca crater floor. Likewise, Occator, we did not find various morphological facies of pit chains, probably most of them are already in the last stage of development.

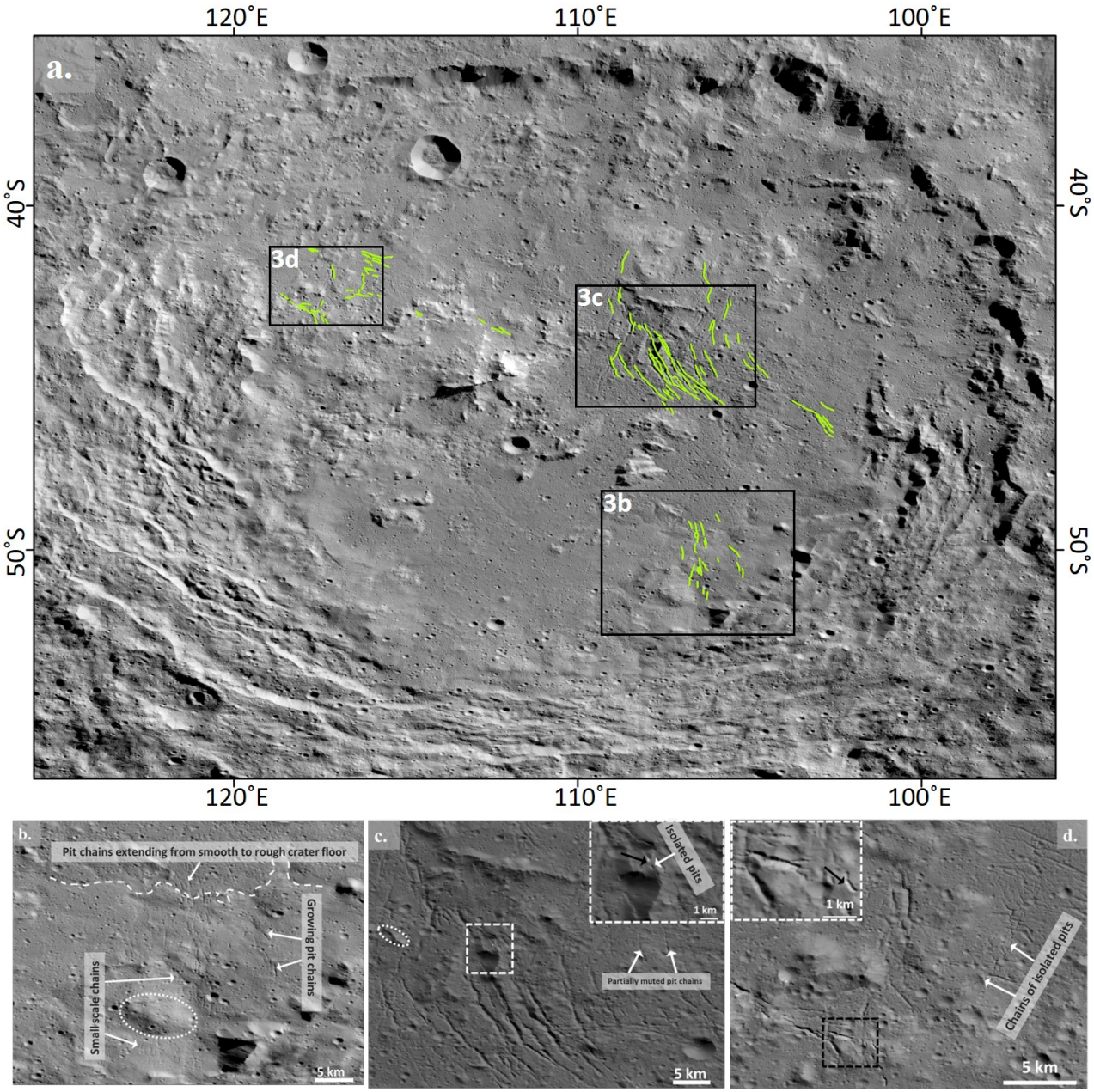

Figure 6.3 Distribution of pit chains and their morphological facies within Urvara crater. (a.) Map of pit chains (green lines) identified within Urvara. (b.) Group of pit chains are growing from the smooth region and extending onto the rough, older zone of the crater floor. (c.) A closely packed pit chains and troughs are aligned parallel and perpendicular to each other. The white dashed region is further zoomed in the upper right corner. We observed isolated pits (with color heterogeneity at the pit wall highlighted with black arrow) at the summit of the dome which are of smaller scale than those present at the bottom. (d.) Randomly distributed group of growing pit chains with albedo variation at the steep walls of coalesced pit chains (highlighted with black arrow in expanded version upper left).

6.4.2 Evolution sequence of pit chains

Overall, we identified multiple examples of pit chains which denote different evolution stages starting from the development of individual pits to linear, wider troughs formation. During the initial stage, isolated pits are developed in an alignment (Figure **6.4a**) and as the pits grew, they are muted together forming linear to curvilinear alignments of circular to elliptical shape which gradually transit into scalloped (Figure **6.4b**) to fully developed troughs (Figure **6.4c**). While these evolution stages cannot provide quantitative information on the surface age, they are helpful to understand the localized chronology of regolith modification (Section **Aa**).

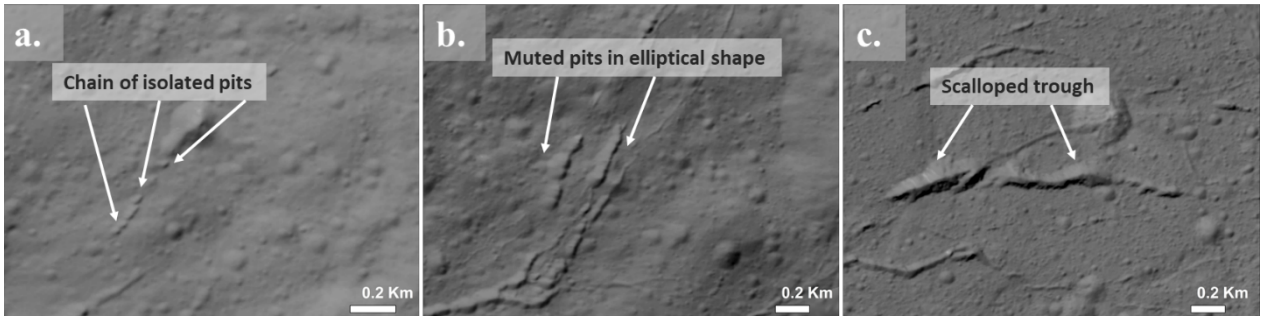

Figure 6.4 Transition sequence from isolated pit chain (a.) to trough (c.). (a.) Primary stage: individual, conical shape pits are aligned, (b.) Developing stage: as the pits began to grow, they have multiple low elevated regions and are muted with each other having elliptical to uneven shape forming long chain like orientation; (c.) Terminating stage: with further collapse the pit chains evolve into scalloped to straight rims and flat floored structures which are then termed as *troughs*.

6.4.3 Structural analysis of pit chains

We estimated length, diameters, depth and spacing of pit chains located at Occator, Azacca and Urvara summarized on Table **6.1**. The average length of pit chains is 1.05 km, 1.6 km and 3.8 km on Occator, Azacca and Urvara respectively. Similar to the length, the average diameter (0.14 km, 0.2 km, 0.8 km) and depth (0.03 km, 0.2 km, 0.8 km) increases from central to low latitudes. The spacing between individual pits are relatively less at the Occator floor (~0.10 km) and the distance increases moving downwards from Azacca (~0.26 km) to Urvara (~0.39 km). Overall, the pit chains observed within the vicinity of Occator are smaller, shallower and their scale increases from equator to poles. However, the number of observed pit chains within Azacca and Urvara is relatively smaller. Thus, we suspect smaller numbers may have influence on the average estimation of the population. Since pit chains subsequently develop into troughs, a similar pattern of structural evolution is observed in troughs from Occator to Azacca down to Urvara (Table **A: 1**).

Table 6.1 Dimensions of pit chains observed within three craters

Craters [slope˚]	Lat.	Long.	*n* of pit chains mapped	*n* of pit chains for the estimation	Length [km]	Diameter [km]	Av. depth [km]	Av. distance btw pits [km]
Occator (35˚)	19.82	239.33	440	200	0.1-7.1	0.02-0.8	0.03±0.02	0.10±0.1
Azacca (32˚)	-6.66	218.4	11	4	1.1-2.2	0.2-0.37	0.2±0.06	0.26±0.1
Urvara (36.5 ˚)	-45.66	249.24	106	53	0.5-11.4	0.05-0.5	0.8±0.5	0.39±0.1

6.5 Relative ages of pit chains

The observed pit chains are distributed within the vicinity of Occator, Azacca and Urvara crater. However, based on their distribution pattern and varying morphology it is reasonable to depict that they must have formed during a different time scale which can be confirmed based on the relative age of the surface. Beginning from the Occator, the Lunar derived model (LDM) attributes the age of the crater formation ~22 Myr (Neesemann et al., 2018). The morphological evidences suggested that the interior of the crater to be active for quite a long time due to unstable volatile extrusions (Nathues et al., 2020) and eruption activities (Raymond et al., 2020) in comparison to the ejecta distributed exterior surface which do not show sign of the young resurfacing activities. The chronological modeling and morphological evidences proved that both, crater floor and the ejecta surface of the Occator has experienced resurfacing activities (Neesemann et al, 2018; Nathues et al., 2020) and are formed under different time scale. Neesemann (2019) estimated age of the surrounding ejecta blanket surface and the smooth lobate material ~18.1±1.8 Myr. Thus, it is feasible to conclude that most of the superimposed pit chains present in this region have formed post-ejecta. In contrast, the interior floor of the Occator crater has experienced multiple resurfacing events within SW region (~19±2 Myr), Cerealia Faculae (~7.5 Myr), central dome (~≤2 Myr), Vinalia Faculae (~1.7-3.9 Myr; Nathues et al., 2020) and was one of the most active regions on the surface of Ceres. Based on the close association of pit chains with various Occator regions and LDM relative age models, we propose that the pit present within the ejecta surface must have formed first followed by the SW regions, Cerealia Faculae and lastly at the Vinalia Faculae.

While estimating the age for Azacca, Schmedemann (2016) focused on the northern exterior of the crater. This region is superimposed by the subsurface impact material and impact ejecta of the Azacca (Schmedemann et al., 2016) and is the best reliable unit to detect the age of the crater. The LCM estimated the age of the Azacca and the smooth ejecta material is ~75±15 Myr (Schmedemann et al., 2016; Sizemore et al., 2017). Most of the pit chains are observed at the center of the crater, near the central pits. Thus, based on the chronological models it is viable to conclude that the pit chains at Azacca are younger than ~75±15 Myr.

In the case of Urvara, pit chains and troughs are distributed within a smooth crater floor. The geological mapping and crater counting age model implies that the interior floor of Urvara has been

covered by two types of material; (i) Yalode/Urvara smooth material (covering most of the northern region of the crater floor and north to east terrain of exterior surface), has ~420±70 Myr age and (ii) Urvara floor smooth material (covering southern region of the crater floor) has estimated age ~190±20 Myr (Crown et al., 2018). Our observed pit chains are present in 3 units out of which two of them are present in the central region of the Urvara basin and one in the southern region which is one of the youngest regions of Urvara basin. Thus, it is reasonable to depict that the northern pit chains and troughs are younger than ~420 Myr and the central ones are ~190 Myr or younger.

Thus, formation of the pit chain took place during long time on the surface of Ceres. The oldest group of pit chains are present on the floor of Urvara with minimum 420 Myr age, followed by the development of pits at Azacca sometime during 75 Myr and lastly the youngest clusters of pit chains are produced at the floor of Occator which are 20 Myr (Nathues et al., 2020) or younger. Hence, it is reasonable to depict that the pit chains at Urvara are mature due to their exposure to erosion for a longer time whereas those present within the vicinity of Occator are still in a developing stage and exposed to less erosion activities.

6.6 Physical mechanism for the development of pit chains

Based on the mapping and size variation of pit chains we suspect involvement of diverse mechanisms and surface material, therefore, we briefly discuss the likelihood of possible mechanisms in the context of Ceres and their influence on the scale of pit chains.

6.6.1 Occator

Considering the morphology, distribution and floor conditions of Occator, we suspect the intrusion of volatile rich brine emplacement from a deeper, pre-existing reservoir (Scully et al., 2020; Schenk et al., 2020, Buczkowski et al., 2018b) plays a crucial role in destabilizing grounds over which the pit chains are formed.

The giant impactor produced Occator ~ 20 Myr which may have developed brecciated layer of faults and fractures (Nathues et al., 2017; 2020; Scully et al., 2020) beneath the crater floor (Buczkowski et al., 2018a). Based on the crater counting model, it has been concluded that the SW is one of the oldest regions of Occator (Neesemann et al., 2018). Given the radial distribution of pit chains, we suspect localized laccolith formation beneath SW zone (Buczkowski et al., 2016; 2018b). On the Moon and Mars, similar mechanisms have been hypothesized for silicate magma intrusion (Jozwiak et al., 2015). Laccolith formation is common during the outbreak magmatic events which is being fed by the deeper reservoir (Figure **6.5a**). Given the history of Ceres, it is likely that the ancient subsurface ocean would have frozen which served as intrusive material from the reservoir of volatile rich brine material (Castillo-Rogez & McCord, 2010; Castillo-Rogez et al., 2019; Fu et al., 2017; Ruesch et al., 2016). Buczkowski (2018b) proposed magmatic intrusion within subsurface of craters on Ceres as for the formation of fractures. We suspect a similar mechanism could be applicable for pit chains formation. According to the mechanism, the cryomagmatic material propagate towards the crater surface from the deep-rooted brine reservoir and reaches the breccia layer. As soon as it reaches the low-density brecciate layer, the upward

propagation ceased and magmatic material was distributed laterally (Buczkowski et al., 2018b; Figure 5b). In our case, lateral distribution of the material would divert in the direction of western rim and Cerealia Faculae causing expansion of existing faults (Buczkowski et al., 2018b). Any further lateral distribution might not be possible due to higher overburden pressure of the thick rim layer. Meanwhile, constant infilling of magmatic material would have formed swelling like laccolith beneath and the uplift of localized region. This would result into the bending of localized stress causing extension of faults. The expansion of fractures due to surface uplift would create void, leaving the upper grounds baseless, followed by the sinking of surface regolith and producing circular or oval pits along the strikes (Figure **6.5c**). Further driving force would have then caused violent outgassing of the magmatic material. However, we did not observe any evidences which supports the involvement of an outgassing event with the SW zone. We suspect post-laccolith further developments might have ceased due to depletion of magmatic intrusion collapsing the surface floor (Figure **A: 2**).

Similar, geological phenomena could be applicable for radial pit chains in Cerealia Faculae. Nevertheless, the theory of subsurface laccolith (also known as brine pocket, melt chamber) has been well established using hydrocode modeling, elevation information and localized geology within Cerealia Faculae (Castillo-Rogez et al., 2010, 2019; Fu et al., 2017, Scully et al., 2020; Raymond et al., 2020). However, unlike the SW zone, post-laccolith activities might be continued for a relatively longer time (Scully et al., 2020). Additionally, strong color heterogeneity is observed at the walls of pit chains of Cerealia Faculae (Figure **6.1 e, f**) implying volatile outgassing. We suggest that during the formation of pit chains, the melt chamber might be actively fed by the deep-rooted brine reservoir. Hence, the moment pits are connected with the fractures beneath, it created a conduit like structure and as a result, violent outgassing of volatile rich material took place, causing significant volume loss (Schenk et al., 2020) from the subsurface in Cerealia Faculae zone (Nathues et al., 2020; Scully et al., 2020; Schenk et al., 2020). Evidence of volatile outgassing has been strongly proposed based on the preserved morphology (such as pingos, lobate flows and sheets, carbonate deposits; Schenk et al., 2020; Nathues et al., 2020) and VIR observation (De Sanctis et al., 2020). Meanwhile, the small domes associated within close vicinity of pit chains are suggested as open-system pingos, produced from the freezing of brine fluid, acquiring localized uplift (Schmidt et al., 2020). Thus, within Cerealia Faculae production of pit chains is possibly attributed to the long-survived subsurface laccolith formation and they served as a channel for volatile outgassing or desiccation onto the surface.

Considering the morphology and distribution pattern of pit chains in Vinalia Faculae, we suspect a different working theory for their formation. The pit chains at Vinalia Faculae are located on relatively thinner (2-3 m) hummock deposits (Scully et al., 2020). Hence, relatively lower driving pressure and energy (in comparison to SW zones and Cerealia Faculae) should be required to destabilize the breccia layer and develop sinkholes. Hydrocode modeling implied that the Cerealia Faculae laccolith is unlikely to be the feeder for Vinalia Faculae due to its distance (~30 km apart) and its dimensions (~20 km wide) (Bowling et al., 2019; Hesse & Castillo-Rogez, 2019; Raymond et al., 2020; Scully et al., 2020). Further, the pit chains at Vinalia Faculae are distributed

linearly and not radially. The latter pattern would be expected in case of column and laccolith pocket formation. Instead, we suspect the connection to deep rooted brine reservoir (Castillo-Rogez et al., 2019; Quick et al., 2019; Raymond et al., 2020; Bowling et al., 2019; Hesse & Castillo-Rogez, 2018) via complex network of subsurface fractures and faults (Scully et al., 2020). If so, intruding brines will require constant high pressure from the deep reservoir (≥35 km; Scully et al., 2020) for a longer time to reach near to the crater floor, reactivate fractures, destabilize brecciated grounds and create the sinkholes for the pit. Therefore, the mobility of brines will be relatively slow at the depth and will take prolonged time to reach the brecciated layers (due to the distance).

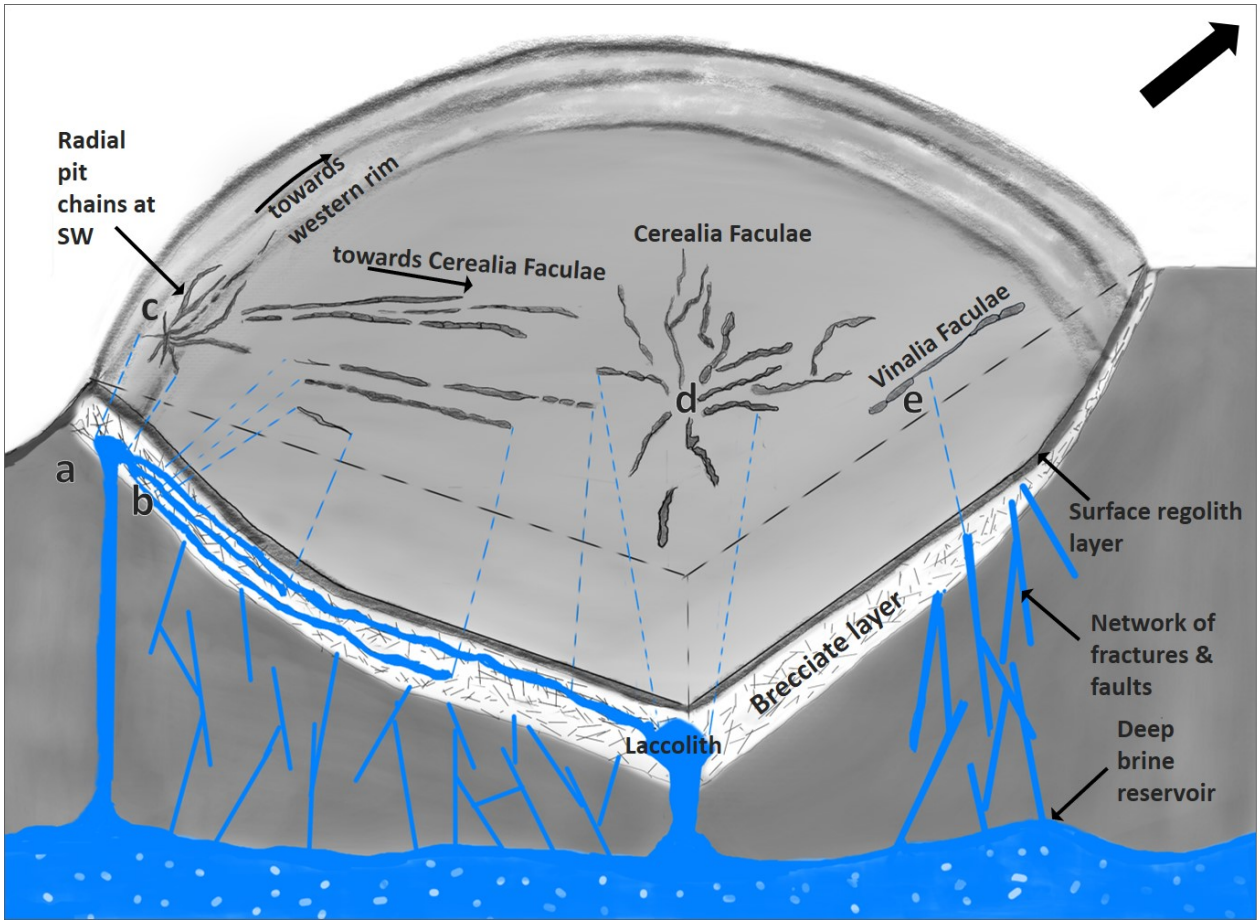

Figure 6.5 Illustration of the formation of pit chains in the floor of Occator crater. The blue color represents cryovolcanic intrusion along the faults and fractures. The radial pit chain distribution is observed near SW rim and at the Cerealia Faculae zone. (a.) The column of intruding material is stalled as soon as it reaches a low-density brecciated layer. (b.) Since upward motion is stalled, the driving pressure of infilling magmatic material causes bending of localized stress which results in the lateral spreading. Due to low elevation the material is mobile downwards in the western and central region underneath (Figure **6.1b,e,f**). (c.) The swelling of the laccolith bends the local pressure and reactivates fractures in the brecciated layer resulting in the radial to polygonal the pit chains in SW zone (Figure **A: 2**). (d.) At the center, Cerealia faculae pit chains must have formed due to laccolith swelling beneath (Scully et al., 2020, Raymond et al., 2020; Castillo-Rogez et al., 2018). (e.) Lastly, at Vinalia faculae the pit chains are connected to the deep volatile reservoir via a network of faults and fractures. Sketch is not to the scale and a few features are exaggerated for visibility.

As a consequence, the pit formation process will be moderate (even though it requires lower driving pressure) at Vinalia Faculae contributing towards a low number of pit chains.

In summary, the formation of pit chains within the vicinity of SW zone is attributed to the short-lived laccolith formation whereas those at Cerealia Faculae are possible via prolonged laccolith uplift and are further associated with volatile outgassing/desiccation. We reckon that sometime between 20 Myr (SW zone age) and 7.5 Myr (Cerealia Faculae age), geological evolution may have invoked brine material to stay active for relatively prolonged time. Lastly, at Vinalia Faculae a deep-rooted (at ≥35 km) brine reservoir is potentially responsible for the formation of pit chains.

6.6.2 Azacca

The pit chains at Azacca are present near the central peak and very few were spotted beyond the rim. We propose an expansion and compression cycle of the ice layer might be responsible for the pit formation. Unlike the lower region, at the equator an ice layer is not present near to the surface and has a heterogenous distribution (Sizemore et al., 2019). Multiple lines of evidences (such as distribution of type 2 landslides, global scale dome topography and floor fractures of craters) supported ice layer depth is ≤20 km (Buczkowski et al., 2018b; Bland et al., 2019; Chilton et al., 2019; Schörghofer et al., 2016b; Otto et al., 2019). Additionally, the equator regions may have experienced rapid temperature change due to Ceres' low obliquity (Hayne & Aharonson, 2015) which would result in stress and thermal fatigue. Otto (2019) predicted the stress production by considering the low-viscosity ice layer at various depths (upto 10 km) and interpreted least stress magnitude at the upper surface. Thus, it is possible that ice within Azacca subsurface (at the depth of 10-20 km; Otto et al., 2019; Sizemore et al., 2019) may introduce low magnitude of stress. As a consequence, only a handful of pit chains were developed which were further expanded due to weathering. Sizemore et al. (2019) also observed, lowest density of expansion resultant features (such as fractures, grooves, channels, troughs) near equator at LAMO resolution (~20 $m \cdot pixel^{-1}$).

6.6.3 Urvara

The Urvara surface is one of the oldest geological units on Ceres (Crown et al., 2018). Most of the pit chains are developed at the center and western site but small-scale pit chains are also developed at the south (Figure **6.3**). Unlike Occator, pit chains here are parallel to each other and randomly distributed on the crater surface. Similar to Azacca, a parallel distribution of fractures within Urvara may be attributed to the contraction and expansion of the ice layer (Krohn et al., 2020) which caused the sinking of the upper regolith material. In general, the ice layer is suspected near to the surface (≤1 m; Bland et al., 2016; Prettyman et al., 2017; 2021); and is mixed with a high portion of phyllosilicates (ammoniated, Mg-, Na-bearing), carbonates (De Sanctis et al., 2015; 2016; Castillo-Rogez & McCord, 2010; Combe et al., 2019; Park et al., 2016), both of them has brittle nature (Krohn et al., 2020). Such material is mechanically weaker (Schröder et al., 2021) and is susceptible to thermal fatigue. Thermal fatigue is caused by the vast surface temperature gradient (dT/dt) within a shorter time span (Molaro & Byrne, 2012). On Ceres, during the time of sunset sunrise the surface temperature near the pole is ~110 K and ~140 K respectively (Hayne & Aharson, 2015). Thus, on a rapidly rotating body like Ceres (rotation period 9.07 hrs; Schröder et

al., 2021), rapid temperature changes are likely to cause thermal fatigue. Additionally, during the high obliquity period (>5˚) of Ceres, the orbital eccentricity may have also influenced the variation in temperature cycles seasonally (Hayne & Aharson, 2015). At the moment, Ceres has ~4˚ obliquity, however over the past 20 Ma years it varied from 2˚ to 20˚ (Ermakov et al., 2017; Vaillant et al., 2019). Given the age of the Urvara basin we argue that during high obliquity of Ceres near-surface, volatile-rich, mechanically-weaker material may have produced new fractures or expanded the pre-existing ones. As a result, an unstable brecciated region would create a void for the upper material to sink in and develop isolated pits. The pit chains observed at central and western zones are of relatively larger scale than the southern cluster. A supporting argument for this diversity could be either (a) difference in their age and/or (b) the viscosity of the surface material. The geological mapping of Urvara suggested that the majority of the northern crater floor is blanketed by the intermixed impact old material of Urvara and Yalode whereas the southern zone is covered by relatively younger Urvara material (Crown et al., 2018; Figure **A: 3**). We suspect either one or both of the above-mentioned theories may have influence on the scaling of pit chains. In summary, presence of brittle susceptible material near the Urvara floor is possibly responsible for the pit chains formation and the scaling differentiation is related to the chronology and/or material viscosity. However, our proposed mechanism does not address the potential reasoning behind clusters of pit chains within certain sites and not all over the crater floor.

6.7 Implication for surface regolith thickness

The diversity in distribution and scale variation within pit chains observed near the equator to low latitudes on Ceres suggests that the regolith thickness is widely dispersed across the surface. Despite our limited candidates, we interpret that the small-scale pits chains have strong correlation with surface regolith. However, the absence of pit chains within plains does not necessarily imply the absence of loose surface regolith. Perhaps, lack of their presence may suggest the absence of potential deformation which destabilizes the surface regolith or pit chains have not been preserved in a particular region (Whitten & Martin, 2019). Eventually, the presence of pit chains within these craters indicates the presence of loose surface regolith.

A first-order estimation of surface regolith thickness (not including the mega-regolith of the crust) can be derived from the depth of the pit chains by assuming their conical shape (Wyrick et al., 2004). In this approach, depth is calculated based on a geometric relation between pit chain diameter and angle of repose (Section **6.3.3**). This is a similar method which was utilized for the studies of pit chains on Ida (Sullivan et al., 1996), Gaspra (Veverka et al., 1994), Eros (Prockter et al., 2002) and Enceladus (Whitten & Martin, 2019). The resulting depth of the pit chain can be considered as a proxy to represent a minimum depth of the surface regolith of a planetary body (Whitten & Martin, 2019) in which it forms. On Ceres, the diameter range and angle of repose (Table **6.1**) of pit chains corresponds to average surface regolith depth of 30 m, 200 m and 800 m within Occator, Azacca and Urvara respectively. Note that not all pits will penetrate through and reach the basement of the regolith. Thus, we cannot derive the maximum thickness of surface regolith. The above-mentioned values represent the minimum average surface regolith thickness.

Based on the estimation, it is reasonable to depict that surface regolith thickness is least near the mid north poles and it increases towards the pole.

The production of pit chains requires drainage of low cohesive loose surface grounds to fall into an underlying void with a strong base (Hardy, 2021; Wyrick et al., 2004). Thus, we suggest that the upper plains of Ceres must have abundant loose regolith which is covered over the relatively stronger base material. The break-down and further distribution of the loose regolith material on Ceres is likely to come from impact gardening (Buczkowski et al., 2016; Hiesinger et al., 2016), a global scale process capable of producing ejecta deposits. Ceres is located at the center of the asteroid belt (Russell & Raymond, 2011) which makes it likely to experience greater flux of impacts. The crater mapping by Gou (2018) suggested the highest density (≥1 km dia.) within the equator. Thus, the production, dispersion and thickness of impact-induced surface regolith within Azacca (near the equator) is expected to be higher. Moving up to the Occator region (mid northern latitudes), the crater density outcome implies relatively thinner surface regolith (Gou et al., 2018). Further, the presence of subsurface brine intrusion also supports the thinner regolith distribution (Scully et al., 2020; Schenk et al., 2020). Morphological studies observed thin flow fronts within the Occator floor and suspected them of mud flows (Nathues et al., 2020; Schenk et al., 2020; Scully et al., 2020). If the regolith would be very thick, flow features might not be preserved. Lastly, given the fact that the interior of Occator is very young (~19 Myr; Nathues et al., 2020), presence of a thin regolith layer is expected. Hence, based on the distinct interior characteristics, we depict that the Occator pit chains represent the localized surface regolith thickness and not the latitude scale. Lastly, within low latitudes crater density is relatively less (Gou et al., 2018) but a higher number of larger impact craters are observed (Hiesinger et al, 2016). Geological mapping suggested that Urvara crater floor was blanketed by impact induced material from Yalode and Urvara (Crown et al., 2018) which may have contributed to relatively thicker surface regolith with Urvara floor.

Thus, our proposed estimation represents localized average surface regolith thickness within Occator and Urvara floor whereas in the case of Azacca, derived estimation may represent equatorial regolith thickness.

6.8 Conclusion

We have mapped and carried out morphological analysis of pit chains within Occator, Azacca and Urvara impact craters using high resolution XM02 data on Ceres. Various stages of pit chains development and its relation with surface regolith suggests that they belong to different timescales throughout Ceres. The scale of pit chains is increasing from Occator to Azacca down to Urvara. Additionally, the population of pit chains is relatively lower within Azacca in comparison to Occator and Urvara. Beginning from isolated pits to forming assemblages of parallel and radial orientation sets, pit chains represent diverse physical formation mechanisms. The radial distribution of pit chains within the vicinity of SW zone and Cerealia Faculae is attributed the laccolith formation. However, underneath SW region post-uplift the depletion of magmatic material may have ceased the further eruption activities causing the subsidence of the center part

(elevation difference is min ~0.2 km). Additionally, there were no obvious evidence of violent outgassing observed within SW zone via pit chains. Linear group of pit chains at Vinalia Facula was potentially produced by a deep-rooted reservoir connected via a network of fractures. Within Azacca and Urvara, pit chains are the result of the expansion and compression cycle of the ice layer. Nevertheless, at Azacca the presence of ice at the transition depth (deeper than the poles; 10-20 km; Sizemore et al., 2019) and distribution heterogeneity possibly failed to produce significant pressure to develop substantial size sinkholes. In contrast, within Urvara ice at shallower depths (Prettyman et al., 2017; 2021) is mixed with a large amount of mechanically weaker materials (Schröder et al., 2021) which may have played a significant role in clustered development of pit chains. The formation of pit chains requires coating of loose surface regolith within which pits are formed as regolith drains down into a subsurface layer. Based on pit chains depth, the estimated minimum average surface regolith thickness is 30 m, 200 m and 800 m within Occator, Azacca and Urvara respectively. The depth estimation at Occator and Urvara represents the localized thickness whereas Azacca measurements potentially represents the thickness of the regolith within the equatorial belt. Hence, our analysis related to morphology, distribution and physical estimations of pit chains not only provide direct evidence of the diverse subsurface conditions but also reveal the thickness heterogeneity of the surface regolith layer at a regional scale on Ceres.

6.9 Acknowledgments

The authors acknowledge the Dawn team for providing data and support. We would like to extend our gratitude to Hanna Sizemore (PSI) and Danielle Wyrick (SwRI) for discussion. We also thank Jennifer Scully for sharing the geological map of Occator. Image and topographic data used in this work are available at the Planetary Data System (https://pds.nasa.gov/ds-view/pds/viewDataset.jsp?dsid=DAWN-A-FC1-2-EDR-CERES-IMAGES-V1.0). This work is part of the research project "The Physics of Volatile Related Morphologies on Asteroids and Comets". RP and KO would like to gratefully acknowledge the financial support and endorsement from the German Academic Exchange Service (under DLR- DAAD Phd Fellowship) and the DLR Management Board Young Research Group Leader Program by the Executive Board Member for Space Research and Technology. A portion of the work was carried out at the Jet Propulsion Laboratory under contract with NASA.

7. INFLUENCE OF VOLATILES ON MASS WASTING PROCESSES ON VESTA AND CERES

An edited version of following sections has been published as: **Parekh, R**., Otto, K.A., Jaumann, R., Matz, K. D., Roatsch, T., Kersten, E., Elgner, S., Raymond, C.A. (2021). *Influence of Volatiles on Mass Wasting Processes on Vesta and Ceres*. *Journal of Geophysical Research: Planets*, volume 126, issue 3, page 1-19, article number e2020JE006573. doi: https://doi.org/10.1029/2020JE006573. The author contribution is explained in the Section **1.2**.

7.1 Abstract

We have analyzed mass wasting features, their distribution and deposit geometry on the two largest main asteroid belt objects – protoplanet Vesta and dwarf planet Ceres – and compared their geomorphology and mobility. Both asteroids have similar surface accelerations, but different surface compositions. Based on our observations and previous studies, we categorized three distinct morphological mass wasting classes: slumps, slides, and flow-like movements. We conclude that Ceres has abundant features of flow-like mass movements. Further, sliding and flow-like characteristics are identified in craters within mid latitudes which supports the possibility of the presence of water ice in the near subsurface of Ceres. Vesta predominantly shows characteristics of dry granular-like slide features which are distributed homogenously across the surface. By plotting the ratio between fall height (H) and run-out length (L) (effective coefficient of friction, H/L) against the run-out length and spreading width (W), we demonstrate that deposits on Vesta terminate on shorter distances whereas on Ceres they travel longer distances. The deposit geometry and the similar surface gravity on both asteroids suggest that the material composition and volatile component have a significant effect on deposit emplacement. However, both bodies' mass movements have similar effective coefficients of friction, even though Vesta's regolith is comparatively dry whereas Ceres is rich in water ice. This leads to the conclusion that volatile content alone cannot be responsible for low effective coefficients of friction, and that more than one geological process is needed to explain the mass motion behavior and morphology.

Key points:

- We classified and estimated the effective coefficient of friction of mass movements to investigate the mechanisms of deposition on Vesta and Ceres**.**
- Vesta has dry granular like slides as dominant mass wasting feature whereas Ceres has abundant features of flow-like mass movements.
- The mass wasting deposit mobility is influenced by the material composition and volatile content on Vesta and Ceres.

7.2 Introduction

The Dawn mission was designed to understand the conditions and processes that shaped the formation and evolution of two large planetesimals from the initial stages of planetary accretion

(Russell & Raymond, 2011), and was the first mission to visit and orbit two planetary bodies located in main asteroid belt. Both Vesta and Ceres are terrestrial protoplanets with Vesta being a dry rocky body and Ceres a volatile-rich body (Russell & Raymond, 2011). They have provided the opportunity to enhance our understanding of planetary formation related to the existence of volatiles (Buczkowski et al., 2016; Chilton et al., 2019; Combe et al., 2016; De Sanctis et al., 2012; 2013; Jaumann et al., 2012; Sizemore et al., 2019). As a result of the Gamma Ray and Neutron Detector (GRaND) and Visible and Infrared Mapping Spectrometer (VIR) observations, the connection between the HED meteorites and Vesta has been confirmed. Vesta has experienced significant heating and dehydration (Formisano et al., 2013; Toplis et al., 2013) whereas Ceres appears to be rich in water ice, which appears to exert control on short-wavelength surface morphology (Otto et al., 2019; Schmidt et al., 2017; Sizemore et al., 2019; 2019a).

As a result of high-resolution surface images acquired by the Dawn rendezvous mission, Vesta and Ceres have been of particular interest for studies of their surface morphology and geology. The internal and external conditions that shaped the surface of Vesta and Ceres can be studied with the data returned by the mission, including detailed shape models (Preusker et al., 2016) and geological maps (Jaumann et al., 2012; Krohn et al., 2014; Roatsch et al., 2012; 2017; 2015; 2016; Williams et al., 2014a). Both Vesta and Ceres have undergone critical erosional processes, including impact cratering, that gradually changed their chemical and physical composition, playing a significant role in their evolution (Russell et al., 2004, 2012; Russell & Raymond, 2011; Toplis et al., 2013). The high-resolution images gathered by the Framing Camera (FC) of the Dawn mission (Sierks et al., 2011) have provided visual evidence of geologic processes including landslides (Otto et al., 2013; 2019; Schmidt et al., 2017; Sizemore et al., 2019), impact cratering, and huge impact basins (Rheasilvia and Veneneia) on the southern latitudes of Vesta (Marchi et al., 2012; Otto et al., 2013; Schenk et al., 2012). Similarly, the FC data has also improved our understanding related to cryovolcanic processes (Nathues et al., 2020; Ruesch et al., 2016; Sori et al., 2018), large scale mass wasting features and the existence of subsurface water ice on Ceres (Bland et al., 2016; Buczkowski et al., 2016; Chilton et al., 2019; Duarte et al., 2019; Reddy et al., 2012; Schmidt et al., 2017; Sizemore et al., 2019). The VIR instrument also found ammoniated phyllosilicates (De Sanctis et al., 2017) on Ceres which are proposed to be linked to geomorphologic features such as flow-like mass wasting features (Chilton et al., 2019; Otto et al., 2013). Overall, landslides are one of the most prominently studied geological features on Vesta and Ceres due to their ability to expose fresh regolith material (Otto et al., 2013; Schmidt et al., 2017). In fact, mass wasting analyses provided clues of granular-like material behavior on Vesta (Krohn et al., 2014; Otto et al., 2013) and the possible existence of subsurface volatiles that may have triggered lubricated mass wasting processes on Ceres (Schmidt et al., 2017).

On Vesta, the classification of mass wasting features was conducted based on morphological characteristics which include intra-crater mass wasting, flow-like and creep-like features, slumps, slides and curvilinear features within the Rheasilvia basin (Otto et al., 2013). Considering the varying morphological characteristics throughout the southern latitudes on Vesta, it is thought to be the most geologically active region of the asteroid (Schenk et al., 2012). This region is also rich

in ejected materials which cover the original surface of the Rheasilvia and Veneneia basins (Otto et al., 2013; Reddy et al., 2012). Another detailed study of a prominent slumping block at the Matronalia Rupes scarp suggests that forces like friction and cohesion affect slump formation (Krohn et al., 2014). Furthermore, gully formation on Vesta suggests a granular-like brittle regolith (Krohn et al., 2014; Scully et al., 2015; Williams et al., 2014b) with characteristics similar to dry gullies on Mars (Crosta et al., 2018a; b). On Vesta, only very few morphologic features, including pitted terrains (Denevi et al., 2012) and inter-connected curvilinear gullies (Scully et al., 2015) suggest the presence of volatiles in the regolith, which may have been delivered via impacts.

Previous investigations of landslides on Ceres focused on morphological appearance and spatial distribution (Chilton et al., 2019; Schmidt et al., 2017). Various flow-like mass movement features were identified and were classified in three categories: deposits with thick frontal lobes, dominating latitudes $\geq 50^{o}$ (type 1), deposits with broad sheet-like spreading, travelling on longer distances (type 2) and platy lobate sheets with cuspate toes (type 3; Schmidt et al., 2017). Most of the landslides were identified proximal to crater rims. The morphology, spatial distribution of mass movements and variation in the geometry of the deposits suggest the presence of subsurface ice on a global scale on Ceres (Schmidt et al., 2017; Sizemore et al., 2017; 2019). In addition, the low effective coefficient of friction, defined as the ratio of the fall height (H) and the run-out length (L) of a mass wasting feature, point towards low shear strength which is attributed to icy material in the upper subsurface of Ceres (Chilton et al., 2019). Recently, Duarte (2019) provided a more detailed investigation of Cerean flows based on intermediate flow features. The morphological characteristics of these flows agree with the previously described classification by Schmidt (2017). However, type 2 flows are prominently identified in relatively shallow craters near the polar regions (Duarte et al., 2019), which supports the hypothesis of a shallow subsurface ice layer in the polar latitudes on Ceres, a conclusion also reached by analysis of GRaND data (Prettyman et al., 2017; Schörghofer 2008, 2016a, b). This ice layer is thought to be stable for millions of years (Chilton et al., 2019) due to low surface temperatures (Hayne & Aharonson, 2015) and sublimation rates. Further, an extended study conducted by Hughson (2019) showed that type 3 flows resemble fluidized ejecta and they suggest the presence of an ice-rich subsurface with a low coefficient of friction within upper surface material. In a nutshell, the morphology on Ceres is consistent with the ice-rich composition.

Landslides are also commonly studied geological features on other planetary bodies, such as the icy satellites of Jupiter and Saturn including Iapetus, Rhea (Singer et al., 2012) and Callisto (Moore et al., 1999), Pluto's largest satellite Charon, (Beddingfield et al., 2020), Mars (Crosta et al., 2018a; Quantin et al., 2004) and the Moon (Brunetti et al., 2015). Previous studies conducted on Iapetus, Rhea and Charon provided quantitative measurements of the effective coefficient of friction and demonstrated that landslides on these planetary bodies exhibit unusual long run-out length. The reduction in friction supports the theory of shear heating within icy surfaces (Singer et al., 2012). On Charon, mixtures of H_2O and ammonia hydrates reduce the melting temperature of the ice, decreasing the internal friction without the necessity of large amounts of energy to melt the ice (Beddingfield et al., 2020). Martian landslides have occurred throughout its history and provide

a window into its erosional and environmental evolution (Crosta et al., 2018b). On the Moon, landslides, including slumping features, appear as fragmented deposits probably triggered by meteorite impacts and the associated impact shock wave propagation (Scaioni et al., 2017; Xiao et al., 2013).

Landslide run-out length, morphological characteristics (such as hummocky surfaces, brittle deposits, wide alcoves, blocky or lobate frontal margins) and deposit spreading depend on the material and environmental conditions during the time of formation, the presence of ice, water or other volatiles and impurities as well as mass wasting triggering factors (e.g. meteorite impacts, shock wave propagation). Depending on the planetary bodies, the influence of these parameters on landslide formation, appearance and morphology may vary.

On Ceres, previous investigations of mass movements focused on their flow behavior (Chilton et al., 2019; Combe et al., 2019; Duarte et al., 2019; Schmidt et al., 2017) whereas on Vesta the analysis was limited to the mid latitudes (Marcia, Calpurnia carter and its neighboring regions) and southern regions (Krohn et al., 2014; Otto et al., 2013; 2016; Williams et al., 2014a). Using these investigations as a base, we extend existing findings by classifying and comparing three different types of mass wasting processes under similar gravitational conditions but compositionally different environments as present on Vesta and Ceres. Our aim is to classify landslides based on morphology and highlight the similarities and differences. Next, we quantify the mobility of landslide depositions by estimating the effective coefficient of friction and the spreading efficiency on Vesta and Ceres. Our interpretation is based on the analysis of morphological characteristics and geometrical estimations to constrain the effect of volatiles on the morphology of Vesta and Ceres.

7.3 Data

To identify mass movement features on Vesta and Ceres, we used mosaics of the Low Altitude Mapping Orbit (LAMO) and High-Altitude Mapping Orbit (HAMO) (Roatsch et al., 2012; 2016; 2017) of the Dawn mission's framing camera (Sierks et al., 2011). The Dawn HAMO mosaics have a spatial resolution of ~70 m·pixel^{-1} for Vesta and 140 m·pixel^{-1} for Ceres and LAMO mosaics have a spatial resolution of ~20 m·pixel^{-1} for Vesta and ~35 m·pixel^{-1} for Ceres (Roatsch et al., 2012; 2016; 2016a; 2017). For regions largely shadowed in the mosaics (e.g. the northern hemisphere of Vesta and the polar regions on Ceres), we additionally used individual images (where available) for identification of mass wasting features. Unfortunately, the northern regions of Vesta (≥60^{o} N) were mainly in shadow due to the northern winter during the LAMO phase of Dawn and thus, we had to exclude this particular region in our analysis. The measurements of drop height (H), run-out length (L) and spreading width (W) of deposits was carried out by taking surface profiles using digital terrain model (DTM) mosaics with ~135 m·pixel^{-1} resolution (with ~10 m vertical accuracy) on Ceres and 92 m·pixel^{-1} resolution (with ~5 m vertical accuracy) on Vesta, (Preusker et al., 2016) derived from stereo pairs. All data used in this work on Vesta and Ceres can be downloaded from the Planetary Data System (PDS) at http://tiny.cc/Vestadata and http://tiny.cc/Ceresdata respectively.

7.4 Materials and Method

7.4.1 Global mass movement feature classification, identification and mapping

Our mass movement classification is based on the system developed by Dikau et al. (1996). This method categorizes 6 different mass movement processes namely; falls, topples, slides, lateral spreads, flows and complex mechanisms. Each category reveals various modes of morphological features, material properties and surface conditions. For example, falls are found on surfaces with steep slopes, topples are recognized in rocky materials, slides are commonly found within dry granular-like materials, lateral spread is prominent in fine grain materials with shallow topography and flow-like movements are common within water rich surfaces (Varnes, 1978). On Vesta and Ceres, based on morphological indicators (Table **7.1**), three common morphological types were noted: slides associated with granular-like behavior (Otto et al., 2013); a wide spread of unconsolidated material, slumps (or rotational slides) exhibiting transverse ridges at lateral margins on large cohesive blocks of material; and, flow-like movements correlated with lobate tongue-like spreading and/or thin sheet-like (Schmidt et al., 2017) large fans with rippled deposition. Each category shows distinct morphological signatures (Table **7.1**) and using this as an identification tool, we mapped and updated the list of mass movement features on Vesta and Ceres. To understand the behavior of mass wasting processes comprehensively, previously identified landslides (Chilton et al., 2019; Duarte et al., 2019; Krohn et al., 2014; Otto et al., 2013; Schmidt et al., 2017) were also included and are marked accordingly in our global maps (Figure **7.4**, Figure **7.5**).

On Vesta, earlier mapping analyses classified mass wasting features based on geological appearance (Krohn et al., 2014; Otto et al., 2013) in the southern latitudes (30°- 60°). These studies either focused on certain regions of the bodies that were of particular interest (e.g. the southern impact basins on Vesta) or concentrated on features of particular interest (e.g. lobate and alcove fan-like flows on Ceres). In our study, the characterization was conducted globally based on multiple morphological impressions of the mass wasting features. To be able to compare the observations on both bodies, we chose the three versatile classes mentioned above (slides, slumps and flow-like movements; Table **7.1**) which were commonly recognized on both bodies. This classification covers all types of mass wasting features identified at global scale.

In our global mapping campaign on Vesta and Ceres, each of the three mass wasting classes is displayed in a separate color and the symbol geometry is designated to the different mapping surveys. Landslides have been identified and marked by using geomorphological indicators as listed in table 1. The mapping was conducted at the scale of 1:125,000 and 1:200,000 in ArcGIS 10.3™ on Vesta and Ceres respectively, and catalogued in a GIS geodatabase. For a consistent mapping, a fishnet of 150 × 150 m for Vesta and 250 × 250 m for Ceres was evaluated systematically and a minimum feature size of 0.02 km^2 and 0.03 km^2 was defined on Vesta and Ceres, respectively.

Table 7.1 Key indicators taken into consideration for the identification and classification of mass movements. The indicators were adapted from the classification system developed by Dikau et al., 1996.

Characteristics	Slump	Slide	Flow
Deformation during wasting process	very little	yes	yes
Exposed scar	partly exposed	yes	covered
Transverse features/striations	possible, but not observed on Vesta and Ceres	no	yes
Lobate trunks	no	possible but rare	yes
Sheet like wide fans	no	no	yes
Boulders and spur/gullies	rare	common	rare
Albedo variations	no	common	rare

7.4.2 Landslide Geometry

One of the most rudimentary methods to estimate the efficiency of landslide deposit mobility is to analyze the effective coefficient of friction represented as the ratio of fall height and run-out length of a mass wasting feature (*H/L*) (McEwen, 1989), also known as Heim's ratio (Heim, 1932). The ratio *H/L* reflects the capacity of material to travel in the direction of movement, whereas the spreading width (*W*) denotes the material spreading efficiency perpendicular to the direction of motion. Another technique known as center of mass estimation (Cruden, 1980; De Blasio, 2011) uses the center of the scarp and deposit to estimate the values. However, it shows a high level of inaccuracy due to the irregular topography of Vesta and Ceres (Chilton et al., 2019) and thus, we avoided using this method.

To measure the length and width of a landslide, we first identified the boundaries of deposited materials of all possible mass wasting sites. The horizontal run-out length (*L*) of the deposit was estimated by taking five profiles (evenly distributed within the boundary of the deposit) in the direction of the movement and averaging it. The boundaries at the top of the deposit and the toe of the deposit were considered as starting and end points for these measurements. Similarly, the spread width (*W*) was estimated by taking five evenly distributed profiles perpendicular to the direction of movement and the average value was considered. Next, the drop height (*H*) was measured from the top of the scarp to the tip of the deposit (Figure **B: 1**). However, in a few regions, due to erosion, the scarp was not clearly identifiable. In such cases, the height of the crater rim or ridge from which the mass wasting feature originated was considered as the highest dropping point. This is common practice for the estimation of vertical fall height when using topography alone (Singer et al., 2012). For each possible landslide site, five profiles were taken for all parameters (*H, L,* and *W*).

Out of our marked mass wasting sites, the estimation of all three parameters (*H, L* and *W*) was feasible only for 85 sites on Vesta and 34 on Ceres. The limited number of measurements is due to restrictions in image or DTM resolutions, blurred deposit boundaries or inadequate illumination conditions (e.g. shadowed features), on both bodies. Other than our measurements, we also adapted

previous measurements of *H* and *L* from Duarte (2019) and Schmidt (2017) of Ceres landslides. After determining the parameters, we compared the material mobility on Vesta and Ceres.

7.5 Results

The identified mass-wasting features on Vesta and Ceres show significant similarities and differences in terms of geomorphological signatures (Table **7.2**). In this section, we first present details of morphological classes followed by measurements of the deposit geometry.

Table 7.2 Summary of mass wasting related geomorphological features identified on Vesta and Ceres

Mass-Wasting Features	Vesta	Ceres
Slump	Rough, transverse ridges, single and/or multiple heads, located inside craters and along large basin rims	Hummocky, single and/or multiple heads, identified inside large craters
Slide	Overlapping deposits, spur and gullies at crest, boulders on crater floor	Overlapping deposits, spur and gullies, boulders at rim and floor
Flow	Small scale single frontal lobes, gullies or spur at the rim	Multiple lobate tongues with furrows, thin sheet-like wide fan spreading

7.5.1 Morphological identification of landslides on Vesta and Ceres

7.5.1.1 Slumps (rotational slides)

Rotational slides are commonly identified on terrains with extensive slopes and cohesive materials (De Blasio, 2011). A chunk of material detaches from its host surface due to the gravitational pull often triggered via a shock wave propagation (e.g. from a nearby impact) (Shingareva & Kuzmin, 2001), creating a spoon-like circular or semicircular surface of failure (De Blasio, 2011). Cohesion within the sliding mass prevents extensive spreading and the mass maintains most of its original shape along the surface of rupture (Otto et al., 2013), causing a step-like topographic profile with one or multiple scarps (Krohn et al., 2014). At the rest position, the detached material partly exposes the steep surface of rupture and is comparatively flat at the frontal margins (Figure **3.5a**). In a few cases, the frontal deposit exhibits transverse ridges or cracks as a result of the material deformation.

Octavia crater (Figure **7.1a**) located at -15.47, 168.48 on Vesta is an examples of a single step rotational slump. The crater is ~60 km in diameter and ~9 km deep. The slump head appears on the crater wall with a fall height of ~4.5 km. The slump deposit covers about 208.9 km^2 of the crater floor. The slump major and minor scarp and the exposed slope are seen in Figure **7.1**. The slump block moved downwards from the crown region and the top surface of the detached material leans backwards towards the crater wall. However, even though Octavia's landslide possesses most attributes defining a rotational slide, it appears to have formed in granular material leaving a relatively small head compared to the scarp. Nevertheless, we defined it as slump as it shares

predominantly slump attributes. More unambiguous rotational slumps are evident in the basins at the southern latitudes of Vesta including the one on the eastern side of Matronalia Rupes (Krohn et al., 2014) where a huge slumping mass covers approximate 600 km^2 with multiple ridges and minor scarps. Similar features have also been identified on Ceres, e.g. in the crater of Toharu (Figure **7.1c**). The crater is ~150 km in diameter and ~3.5 km in depth, located at -48.32, 155.95. We have identified two slump regions at the western and eastern rim of this crater. The detached slump material slipped along the direction of the slope, exposing a steep scarp. Multiple heads are evident which locally have given rise to subsequent failure, generating multiple steps-like surface features (Figure **7.1d** and Figure **7.1e**). Similar to Vesta, Ceres also has single step slumping features (Figure **B: 2f**). Transverse ridges are also evident within some slumping bodies (Figure **B: 2**).

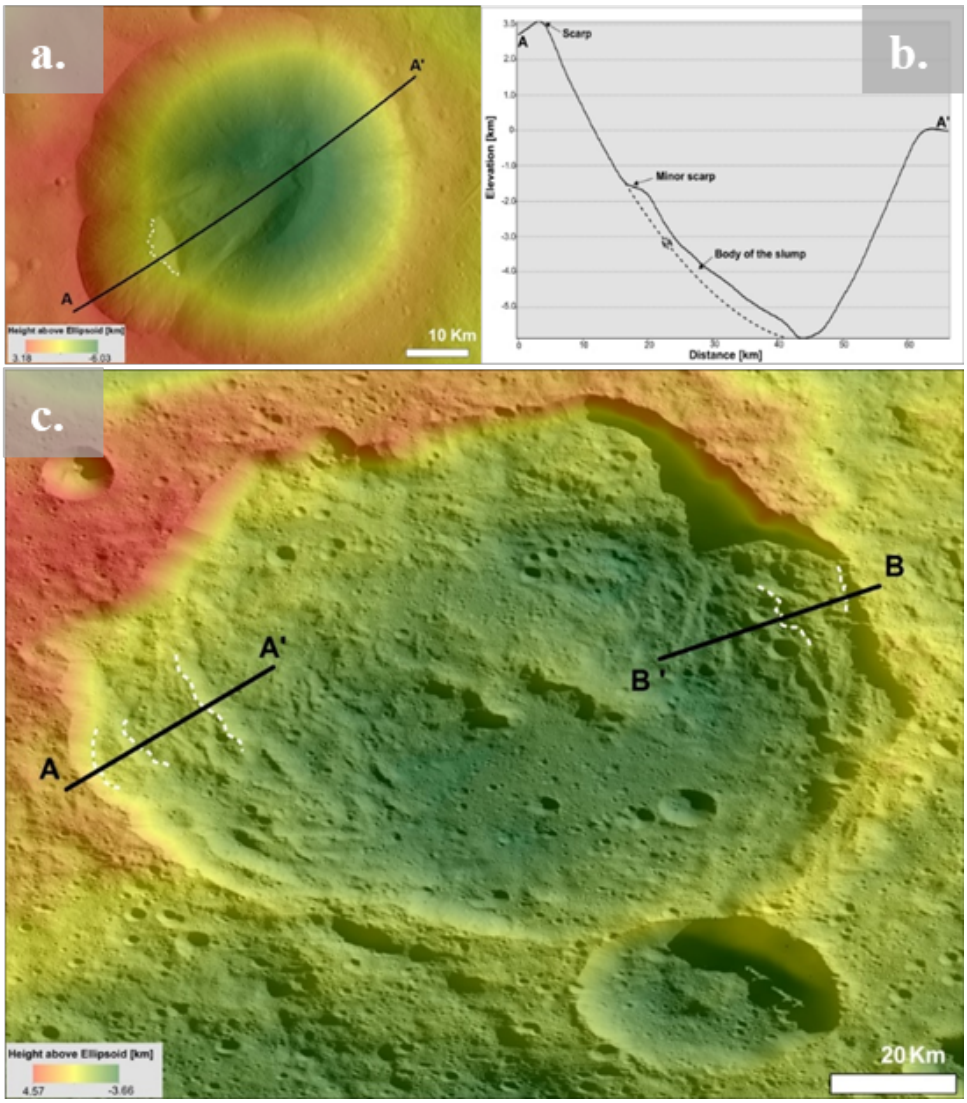

continue

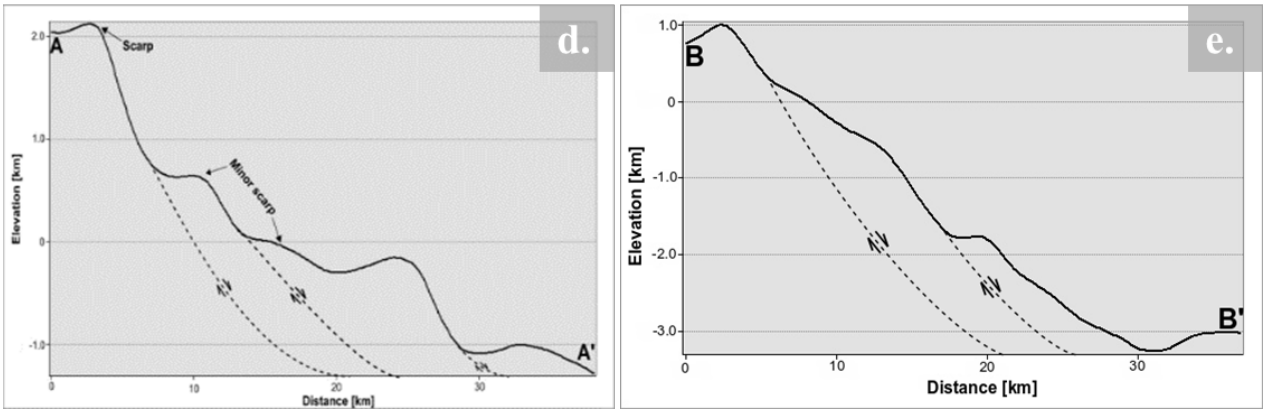

Figure 7.1 Example of slumps of Vesta and Ceres. (a.) A slump observed in Octavia crater on Vesta with its topographic profile (b.). (c.) Multiple slump examples observed along Toharu crater's wall on Ceres. The slumps show a step-like profile (in d and e) with multiple minor scarps (white dotted line in c.) and deposits covering an area of ~1000 km^2 and ~800 km^2, respectively. There is ~1.1 km elevation difference between the western and eastern rim of the crater. Black dotted lines in the topographic profiles (b., d., e.) represent the presumed subsurface of rupture joining the scarp outlined in image a. and c.

Overall, on Vesta and Ceres we noted two types of slump events: (i) slumping areas with multiple deposit blocks and transverse ridges. They are specifically observed within the largest crater on Vesta (e.g. the Rheasilvia crater covering Vesta's southern hemisphere) and within multiple craters on Ceres (Sintana, Toharu, Urvara, Occator, Tupo craters), and (ii) single slumping block features. However, we find handful of candidates which have a single slumping block on both, Vesta (only within Octavia) and Ceres (at the north west rim of Dantu and within an unnamed crater located at 43.57, 34.94).

7.5.1.2 Slides

Slides move along a planar shear surface potentially exposing the upper area of the shear surface after coming to a rest (De Blasio, 2011). The foot of the material may undergo disaggregation and the slide material experiences some degree of deformation such as lateral spreading (Otto et al., 2013).

An example of such a slide is seen in Pinaria crater (lat.: -29.54, long.:181.63) on Vesta (Figure **7.2a**). Here, we identify multiple areas of slide material deposition on the crater floor. Slides moved downwards from the crater rim, covering the crater floor and exposing the surface of failure at the northern crater rim. The occurrence and preservation of fragile spur features at the crater rim where the slides originated indicate that Pinaria's slides are relatively young. The slide material travelled on a surface with decreasing slope from 40°- 20°. The process continued until the deposit reached a slope flat enough to hold the material. Similar to Pinaria, an unnamed crater located in the southern part of Ceres (lat.: 22°S, long: 80°W), shows layered piles of slide material on the crater floor (Figure **7.2b**) with spurs and boulders near the crater rim. The boulders' sizes are ≥50 m and indicate that parts of the wasted material are composed of brittle substances.

In general, on both bodies, slide features involve the disintegration and spreading of the sliding material (Figure **B: 3**). Usually within this type of mass wasting feature it is challenging to constrain the deposit boundaries as material originating from various crater wall locations often intermix leaving no particular boundary or spreading margins.

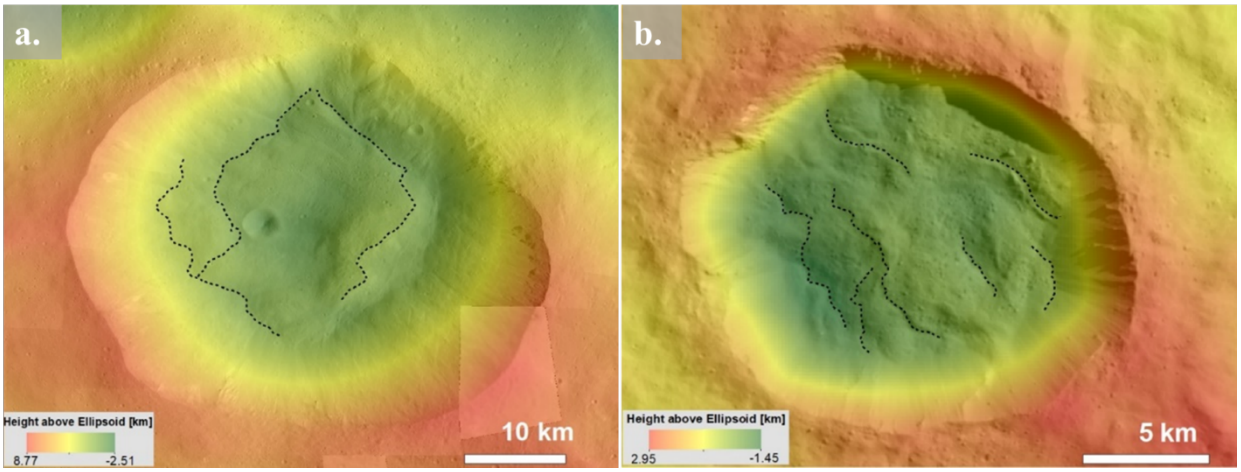

Figure 7.2 Examples of slides on Vesta and Ceres. Slides emanating from the rim of Pinaria crater on (a.) Vesta. (b.) Overlapping slide deposits covering an unnamed crater floor on Ceres. Spurs along the crater rim and some larger boulders are evident. The black dotted lines highlight topographic boundaries within the slide material.

7.5.1.3 Flow-like movements

Large scale flow-like movements occur when the cohesion between individual wasting particles is limited, the particles travel independently within a moving mass (De Blasio, 2011) and material starts behaving like a fluid. Fluidized behavior can be caused by melting of volatiles within the material (Schmidt et al., 2017), saltation (De Blasio, 2011), acoustic fluidization (De Blasio, 2011; Melosh, 1986) or the presence of trapped air bubbles within the material (Shreve, 1966; 1968). While travelling, the moving fragments (granular material and/or other consolidated particles) within the material collide with each other and due to friction, form multiple striations in the direction of travel on the surface. Upon rest, the deposit morphology appears either in the form of a thin sheet (Schmidt et al., 2017) or multiple lobate tongues at the motion's front depending on the volume of the mass and its spreading efficiency. The striations are the main morphological difference to the slides and slumps described in the sections above.

On Vesta, for example, a flow-like movement originates from the south east rim of Rufillia crater (~15 km in dia.) and travels towards the crater floor at a slope of ~20° generating two frontal lobes (Figure **7.3a**). The flow-like movement was probably generated by the impact of a younger crater, potentially the one in southeast of the flow feature. The well-preserved morphology of the flow-like feature suggests that it is relatively young. On Ceres, similarly well-defined multiple lobate flow units are evident within and outside of the Haulani crater (Krohn et al., 2017). The units include surface characteristics such as high albedo, fine grained material, multiple flow units, and streak-like or swirled patterns (Krohn et al., 2017). Other than Haulani, there are examples in craters such as Juling, Kupalo and Urvara (Duarte et al., 2019) also displaying similar mass wasting

morphologies (Krohn et al., 2017; Schmidt et al., 2017; Scully et al., 2015). In addition to lobate flow-like features, Ceres also shows prominent impressions of sheet like fans around Xevioso (lat.: 0.7, long.: 310.6) and an unnamed crater (lat.:1.92, long.:309.68), covering ~127 km^2 and ~102 km^2 area respectively, masking the surrounding terrain and suggesting it to be related to impact ejecta (Figure **7.3b**). A detailed analysis of morphological characteristics of ejecta related flows can also be found in Hughson (2019). Fluidized impact ejecta does not necessarily follow the topography (Schmidt et al., 2017) but covers the original landscape. Overall on Ceres flow-like features are generally identified in the regions surrounding craters (Chilton et al., 2019; Combe et al., 2019; Duarte et al., 2019; Hughson et al., 2019; Schmidt et al., 2017).

Usually this type of mass movement travels longer distances than the other two described, suggesting a lower internal friction and/or higher momentum involved in the motion. But there are morphological differences in flow-like movements on both targeted bodies. On Vesta the majority of flow-like features appears as small elongated features with lobate shaped fronts (Figure **B: 4a-c**) whereas on Ceres a large number of sheet-like features expressed as wide fans with multiple lobes at the flow front (Figure **B: 4d-e**) are present.

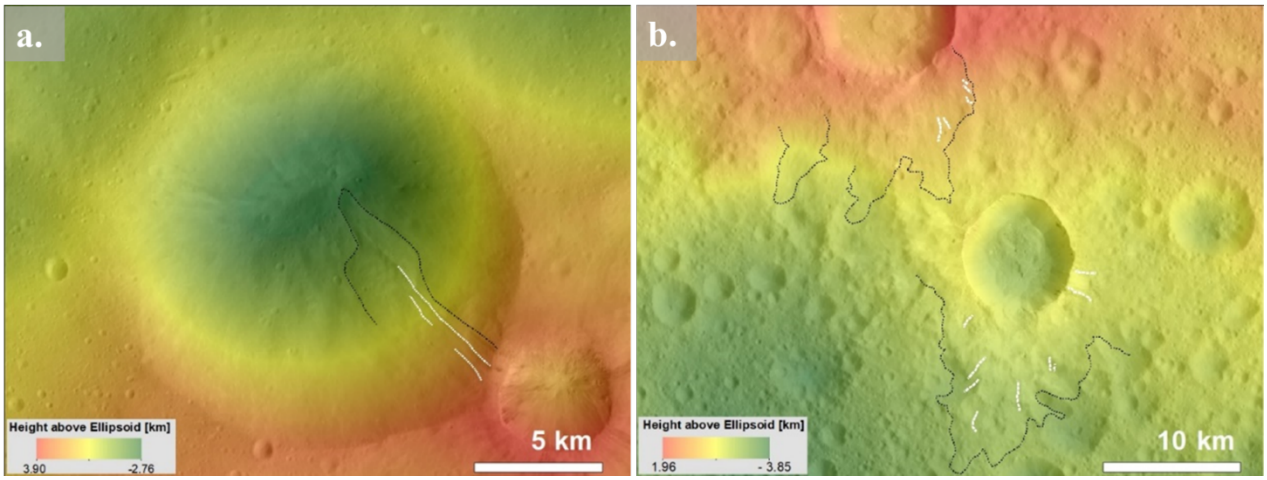

Figure 7.3 Flow-like movements observed on Vesta and Ceres. (a.) A tongue-like flow in Rufillia crater on Vesta and (b.) A thin sheet-like flow nearby Xevioso (center crater in which surroundings are highlighted with black dotted lines) and an unnamed (partially visible in the upper center of (b.) crater on Ceres. The sheet-like flow appearance is common on Ceres and possibly related to ejecta depositions and regolith volatile content (Hughson et al., 2019; Schmidt et al., 2017). The black dotted lines indicate the extent to which material has traveled. The white dotted lines highlight super imposing furrows.

7.5.2 Global distribution of mass wasting features on Vesta and Ceres

We identified a large number of mass-wasting features within the vicinity of craters, basin walls or on cliffs. In addition, to the previously identified mass wasting features (29 on Vesta by Krohn et al., 2014; Otto et al., 2013), we identified 159 further mass-wasting features out of which 74 are slides, 84 flow-like movements and 1 slump feature (in total 188 mass wasting features) located at mid latitudes on Vesta. In addition to our inventory, there are a few more slump blocks distributed frequently within Rheasilvia and Veneneia in the southern region of Vesta (Otto et al., 2013)

(Figure 7.4). The strong elevation difference (up to ~20 km high basin walls) makes these regions most favorable for slumping processes. Overall, slumping blocks are the largest mass wasting features on Vesta. Nevertheless, the large number of slides on Vesta suggests a prominently dry granular behavior noted at a global scale. Both slides and flow-like movements are correlated with craters of diameters ranging between ~2.6 km - 53 km (average of 14.88 km).

On Ceres, previous studies reported 150 mass movement features as flow-like movements (Chilton et al., 2019; Duarte et al., 2019; Schmidt et al., 2017). Besides these, we identified an additional 35 flow-like features, 12 slides and 13 rotational slump (in total 210) features (Figure 7.5). Flow-like movements are the dominant mass wasting process. Overall, the flow-like mass movements are homogenously distributed on Ceres. However, the other two mass wasting features, slump and sliding features, are not present in Ceres' polar regions and confined within 0°-60° latitude. Further, slides and flow-like impressions are noted in or around craters which have diameters from ~5.1 km to ~77.8 km (with an average of 26.5 km). Similar to Vesta, slumping blocks are also present on Ceres within large craters (average size ~61.4 km). Usually the flow-like morphologies are evident within crater floors and along/around crater rims.

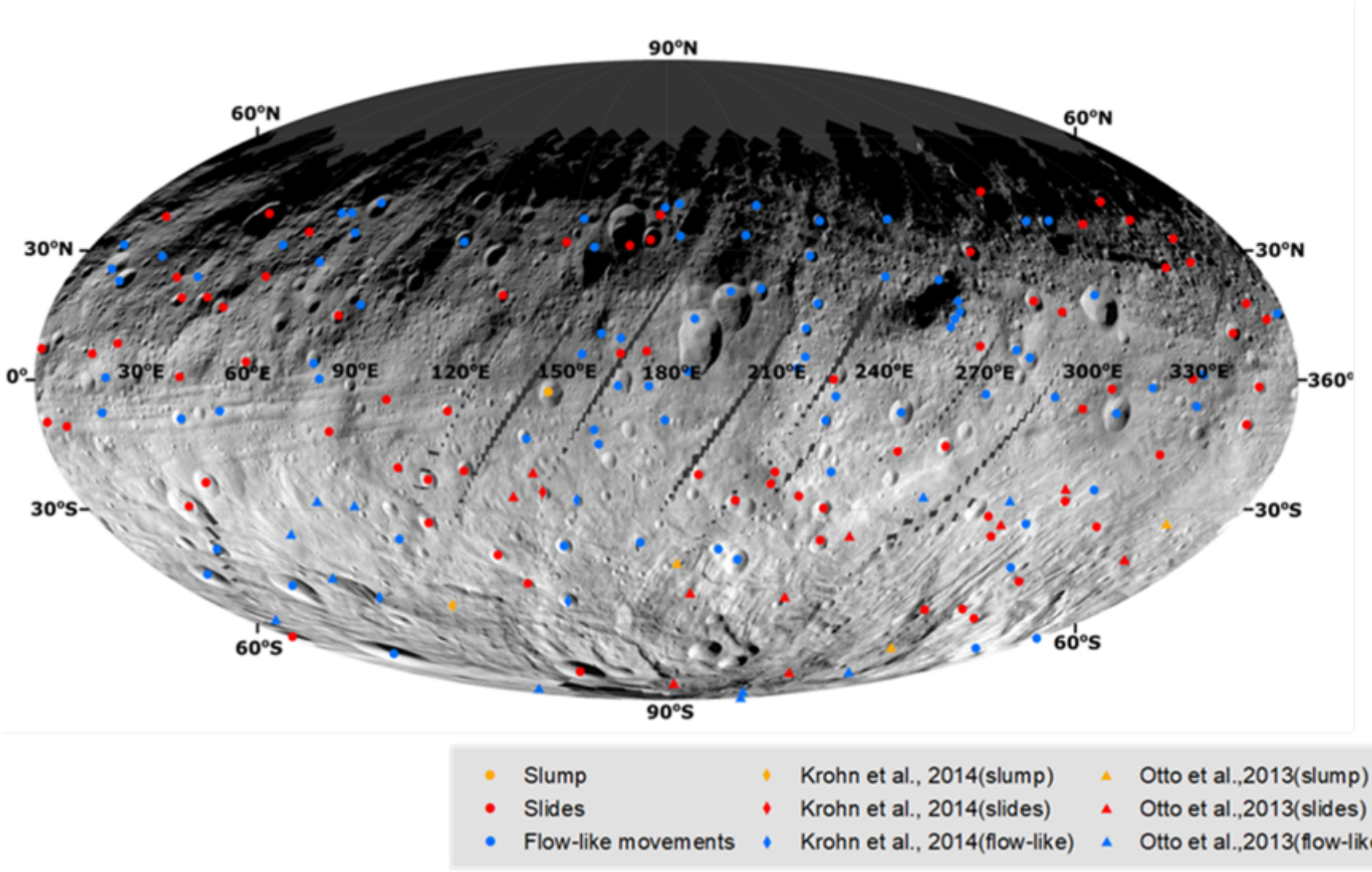

Figure 7.4 Global distribution of classified mass wasting features on Vesta. For a comprehensive analysis, we have also included and categorized mass wasting features identified by Krohn et al. (2014) and Otto et al. (2013) in the southern region. Additional features found and analyzed in this work are marked as dots. The classification map was prepared using a LAMO mosaic in Mollweide projection.

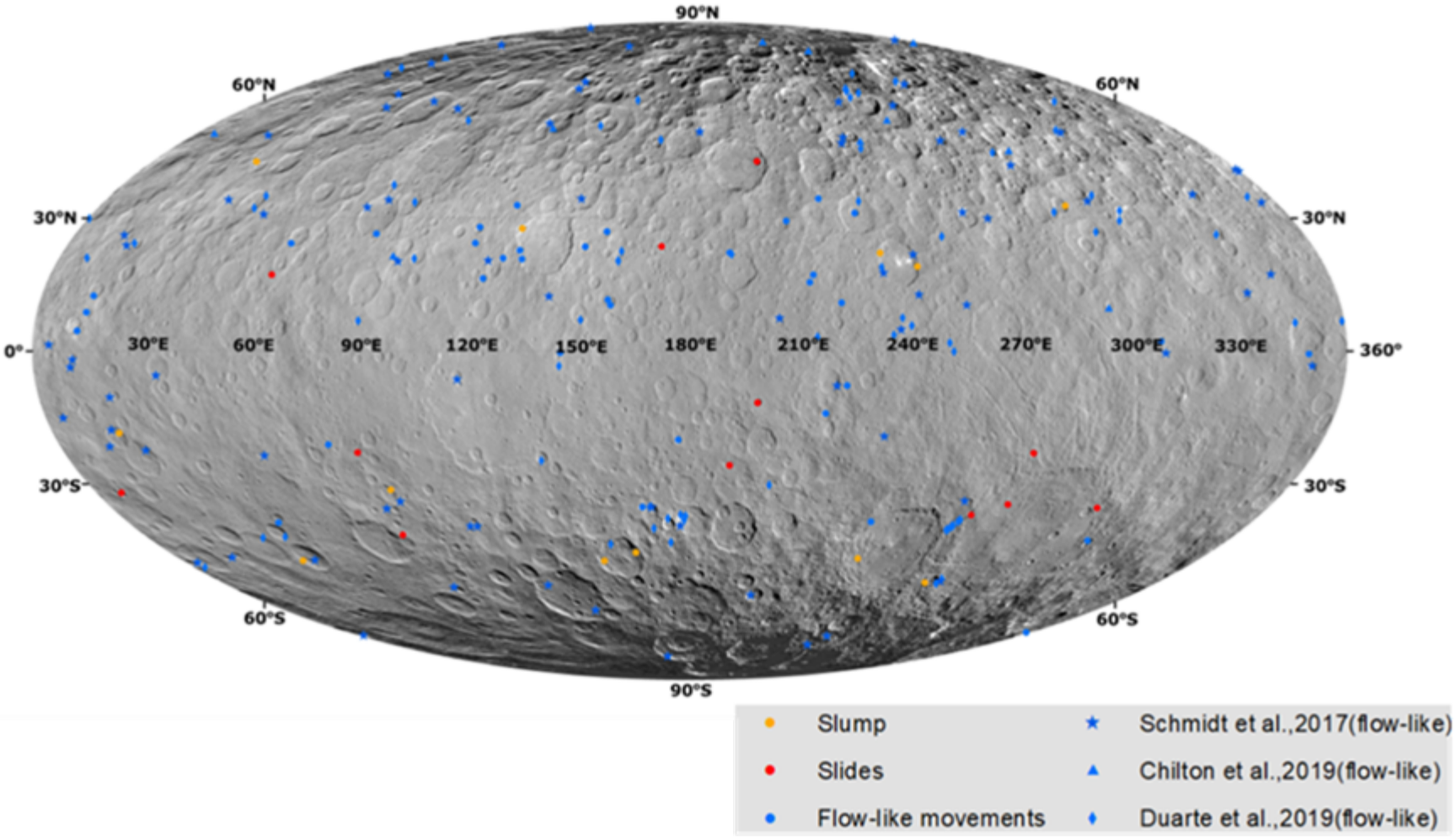

Figure 7.5 Global distribution of classified mass wasting features on Ceres. In earlier studies, mass wasting features were exclusively classified as flows (Chilton et al., 2019; Schmidt et al., 2017; Duarte et al., 2019). The classification map was prepared using a LAMO mosaic in Mollweide projection.

7.5.3 Geomorphologic measurements

7.5.3.1 Effective coefficient of friction

The friction between the wasting particles has a significant influence on the travelling distance of the material. A common way to describe the friction within a mass movement is to analyze the effective coefficient of friction (*H/L*). We plot the effective coefficient of friction of the different types of mass wasting features identified on Vesta and Ceres against their run-out length (*L*) which can be assumed as a proxy for a mass movement's volume (Figure 7.6). Here we compare *H/L* and run-out length (*L*) and additionally show the drop-height (*H*), indicated by the size of the data point. In Figure 7.7, we compare the effective coefficient of friction (*H/L*) with spreading width (*W*) on Vesta and Ceres. From Figure 7.6 and Figure 7.7, we observe the following trends: (i) the effective coefficient of friction (*H/L*) of landslides on both Vesta and Ceres follows an approximate linear decrease with run out length (*L*) in a double logarithmic plot; (ii) for a given run-out length, there is no strong relation between run-out length and the friction coefficient on Vesta and Ceres (e.g. a range of values is observed for each value of *L*); (iii) the drop height (*H*) is lower on Ceres than on Vesta possibly due to the higher topographic relief on Vesta (~40 km elevation difference overall on Vesta compared to 14.5 km on Ceres); and (iv) material travelling ≥10 km is more common on Ceres compared to Vesta with the longest travel distance being ~66.4 km on Ceres and ~60.6 km on Vesta, despite Ceres' smaller topographic range. On Vesta the southern hemisphere has a prominent difference in elevation due to the large impact basins Veneneia and Rheasilvia which cause high drop heights for wasting materials.

The range of *H/L* for each of the three categories on Vesta and Ceres is provided in Table 7.3. Slides and flow-like movements evenly cover the entire range of measured run-out lengths (*L*) 0.57 – 23 km on Vesta (Figure 7.6). Slumps appear to have larger run-out length (10-60 km) possibly due to their comparatively large size. The slope of the least square fit of a power function to the data (linear in log-log plot) of each morphological class was estimated. To understand the relation between two parameters (here *H/L* with *L*) in quantitative manner we derived the slope of least-square fit. The slope in these diagrams shows how strongly the effective coefficient of friction

Table 7.3 Summary of *H/L* range and their fitted slope for all types of mass wasting movements identified on Vesta and Ceres.

Mass-Wasting Features	Vesta		Ceres	
	H/L range	Fitted slope	H/L range	Fitted slope
Slump	0.05-0.15 (mean 0.13±0.06)	0.69±1.15	0.05-1.54 (mean 0.31±0.59)	0.82±2.80
Slide	0.04-0.61 (mean 0.30±0.29)	-0.40±0.12	0.02-0.92 (mean 0.43±0.25)	-0.22±0.09
Flow	0.03-1.02 (mean 0.30±0.22)	-0.33±0.15	0.06-1.67 (mean 0.13±0.17)	-0.08±0.06

changes when the run-out length increases. A steep slope means that the effective coefficient of friction decreases with run-out length at a higher rate compared to a less steep slope in these diagrams. This rate of decreasing effective coefficient of friction may hint at the different processes which could also be caused by different materials such as volatiles acting within the moving masses. On Vesta the slope is as follows; slump: -0.69±1.15, slides: -0.40±0.12, and flow-like movements: -0.33±0.15 (Table **7.3**, Figure **7.6a**). All three categories are consistent by having a negative slope which means that the effective friction of coefficient (*H/L*) tends to decrease with increasing run-out length (*L*), which can be assumed as a proxy for the mass movement's volume; however, looking at the large error to the fits, the trend is not strong. Likewise, the fitted slope of all types of mass movements on Ceres is as follows; slump: 0.82±2.80, slides: -0.22±0.09, and flow-like moments: -0.08±0.06 (Table **7.3**, Figure **7.6b**). Similar to Vesta, on Ceres slide and flow-like features have negative correlations between their effective coefficient of friction and run-out length. On both planetary bodies, the slumping fit shows a relatively high value of error which may be influenced by the small number of data points. In the case of Mars and Earth, the H/L values range from 0.1 to 0.3 for rock avalanches and 0.01 to 0.1 for saturated terrestrial submarine landslides (Quantin et al., 2004). The slides and flow-like movements on Vesta and Ceres appears less confined and cover a wider range of H/L values. Furthermore, the different gravitational pull and atmospheric condition on the planets and the asteroids makes a direct comparison unreasonable.

There is a prominent distinction between slides and flow-like features in terms of mobility on Ceres; slides terminate at shorter distances (average: ~3.3±0.07 km) whereas flow-like movements have maximum extent up to ~66.4 km (average: ~11.05±10.2 km) on Ceres. This is not observed for Vesta (maximum deposits extend ~16.1 km with avg. 4.98±3.61 km). However, the range of *H/L* values is similar on Vesta and Ceres (Vesta: 0.03-1.61, Ceres: 0.02-1.67) regardless of their length.

In addition, we have also analyzed the relationship between the deposit width (*W*) and friction coefficient (*H/L*) of mass-wasting features (Figure **7.7**). This provides information about the spreading efficiency of the wasting material perpendicular to the direction of movement. When determining the least square power fit to the *H/L* versus *W* plot in double logarithmic scale, it was observed that for Vesta the slope is -0.10±0.13 and in the case of Ceres the slope is 0.38±0.21, but the correlation is not strong. By plotting the coefficient of friction (*H/L*) against the width (*W*) of the deposit, we can demonstrate that mass movement features on Vesta generally do not spread as much as on Ceres, where width up to ~7.5 km on average is commonly measured. This implies that the deposits on Ceres are more mobile in terms of lateral disintegration compared to Vesta. These conditions may be favorable for generating multiple lobate features or sheet like fluidized spreads which are one of the most prominent features on Ceres.

7.6 Discussion

The global distribution of the identified classes of mass movements illustrates that both Vesta and Ceres have a diverse range of materials at the surface and in their subsurface, resulting in three

different mass wasting types. The mass wasting features are present on both bodies but show some similarities (transverse ridges, overlapping slide deposits, boulders and spurs/gullies, brittle material in deposit, lobate tongue-like flow features, single/multiple step like slump, albedo variations) and differences in their morphologies (conglomerate lobate features, hummocky surfaces, sheet-like wide fans). Comparing the global mapping of Vesta and Ceres, slides are the most commonly identified mass wasting type on Vesta whereas flow-like movements are dominant on Ceres. This is consistent with the fact that Vesta is a dry brittle body (Jaumann et al., 2012) and Ceres is rich in water ice (Schmidt et al., 2017, Prettyman et al., 2017).

7.6.1 Role of physical and chemical conditions of surface material

On Vesta most of the slumping blocks are identified within the southern latitudes (Krohn et al., 2014; Otto et al., 2013). The high elevation difference and steep slope (~40°-10°; Jaumann et al., 2012) in this region is thought to be favorable for slump formation on Vesta. Slumping behavior is also common within cohesive materials that have the tendency to collapse when reaching a critical abundance of water or has critical slope (angle of repose) on Earth or Mars (Varnes, 1978). Usually a block of slumping material includes cohesive substances like clay, lithic clasts, igneous rocks, organic minerals and materials enriched in water (Varnes, 1978). In the case of Ceres, VIR observations identified carbonates, phyllosilicates and ammoniated clays with OH and/or H_2O mixed within the surface materials possibly explaining the occurrence of slumping on Ceres (Ammannito et al., 2016; Chilton et al., 2019; De Sanctis et al., 2017; Rivkin et al., 2006). Various processes can affect the cohesion between particles of the surface material by weakening bonds. On Ceres, a putative process reducing the material's cohesive strength involves the formation of fracture networks generated either by impact shock wave or from the occasional heating cycle during Ceres' history (Chilton et al., 2019). Most slumping blocks on Ceres are in the mid latitudes where ice rich materials are possibly present at several meters' depth (Chilton et al., 2019; Prettyman et al., 2017; Schmidt et al., 2017; Bland et al., 2016). This may influence the cohesion within the wasting material allowing slumps to occur more frequently in this region. Overall, on Vesta the slumping blocks are correlated with terrain conditions (high altitude, steep slope) whereas on Ceres slumping features are best explained by the surface composition (presence of clays, water ice; Ammannito et al., 2016; Chilton et al., 2019).

Slides are a form of mass movements involving brittle and granular-like behavior. Such materials are common on dry Vesta (Otto et al., 2013) and subsequently they are the most abundant mass wasting features on Vesta. The Vestan mineralogy data collected by visible and infrared spectra shows that the majority of the crust consists of dry eucritic basalts and pyroxene (De Sanctis et al., 2012; Prettyman et al., 2013) which has brittle composition. In the case of Ceres, we have identified craters with granular-like slide behavior near the mid latitudes. The slide behavior is identified inside craters which have depth from ~0.7 to 1.8 km within ±60˚ latitude. A possible explanation for the high concentration of slides in the mid latitudes of Ceres is the lower abundance of water ice within the regolith in these regions (Prettyman et al., 2017). GRaND has detected the ice layer within 1m of the depth at equator and near to surface at poles on Ceres (Prettyman et al., 2017). The lower ice table depth in the lower latitudes may have caused the upper material layer

(which is involved in mass wasting processes) to be drier and thus less cohesive, preferentially generating slides rather than flow-like or slumping features. Thus, distribution of fragmented slides within the mid-latitude points to a relatively brittle ice-rock rich regolith on Ceres, assuming that the depth of the ice layer along with presence of brittle material is the main cause for slides on Ceres, whereas global presence of eucrite and pyroxene dry regolith can be the potential cause for slide on Vesta.

Lastly, on both, Vesta and Ceres, the majority of the flow-like features are located within the vicinity of crater ejecta and/or crater rims. When correlated to impact ejecta, the flow-like features are present at a global scale on both asteroids. Usually, flow-like movements follow the downhill direction however; this movement can sometimes be diverted due to the high mobility of materials affected by the impact. Earlier studies of impact related melt production on Vesta (Williams et al., 2014b) suggest that lobate flows are impact-derived and associated with melt displacement of high velocity impacts (8-10 $km \cdot s^{-1}$). Another study finds that the presence of highly shocked and fractured material correlates with the presence of flow-like features within the Rheasilvia basin in the southern hemisphere of Vesta (Otto et al., 2013). Moreover, impact flow movements are also present on much smaller and dry asteroids including (433) Eros (*H/L*: ~0.03 – 0.1) (Cheng et al., 2002; Sullivan et al., 2002) and (21) Lutetia (*H/L*: ~0.4; Elbeshausen et al., 2012; Massironi et al.,

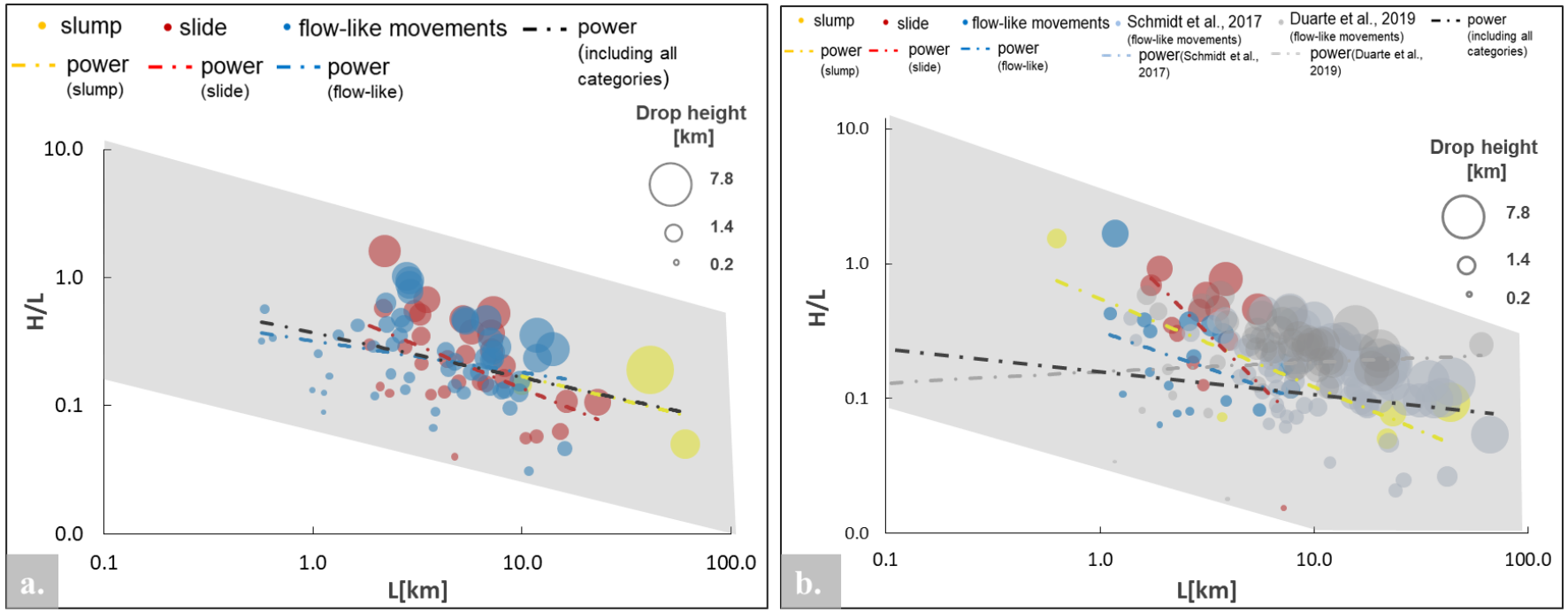

Figure 7.6 Landslide mobility on (a.) Vesta and (b.) Ceres. Shown is the measurement of the friction coefficient (*H/L*) versus the run-out length (*L*) of the three different types of mass movements. (a.) For each category the least squares power law fit between *H/L* and *L* yields a slope as follows on Vesta: slump: −0.69 ± 1.15 (yellow dashed-dotted line), slide: −0.40 ± 0.12(red dashed-dotted line), flow-like movements: −0.33 ± 0.15 (blue dashed-dotted line). The combined slope including all types is −0.44 ± 0.11 (black dashed-dotted line). (b.) Similarly, the slopes on Ceres are: slump: 0.82 ± 2.80 (yellow dashed-dotted line), slide: −0.22 ± 0.09 (red dashed-dotted line), flow-like movements: −0.08 ± 0.06 (blue dashed-dotted line). In addition to our measurements we also included data from Duarte (2019) and Schmidt (2017). Their slopes are 0.31 ± 0.27 and 0.0 ± 0.14, respectively. On Ceres the slope of *H/L* versus *L* for all type of landslides combined is −0.03 ± 0.05. The gray shaded area is to highlight the range of *H/L* values for a given *L* and is for orientation only. The size of the dots corresponds to the drop height. x and y axis are in logarithmic scale. Measurements adopted from earlier studies are highlighted in a lighter shade.

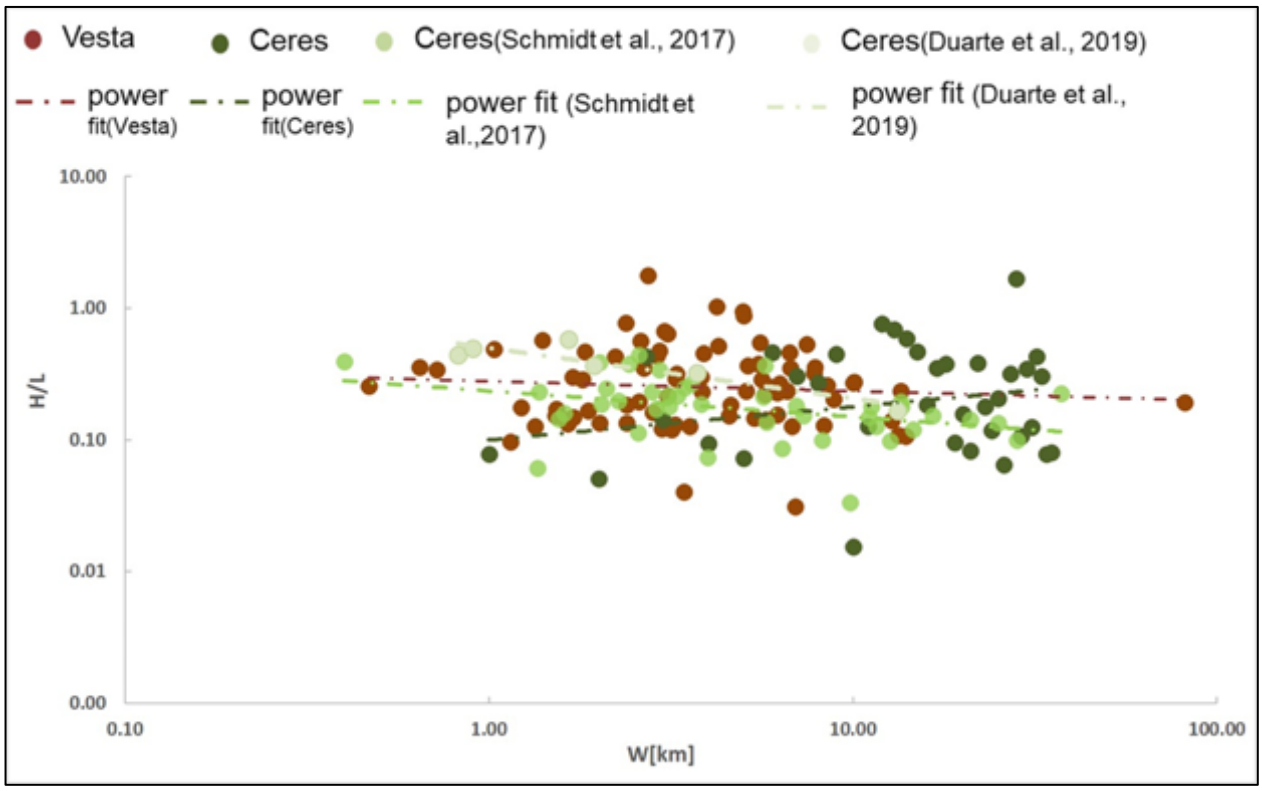

Figure 7.7 Deposit width versus landslide mobility. Illustrated is the friction coefficient versus the deposit width. Earlier measurements of the friction coefficient (Duarte et al., 2019; Schmidt et al., 2017) are added. The least squares power fit between *H/L* with *W* yields slopes as follow: Vesta: −0.10 ± 0.13, Ceres: 0.38 ± 0.21, data from Schmidt (2017): −0.68 ± 0.27 and Duarte (2019): −0.48 ± 0.14. The deposit width was measured from the supporting information provided in the mentioned publications. Note, both axes are in logarithmic scale.

2012). Whereas sheet-like spreading is more commonly identified on Ceres and associated with the presence of water ice in the subsurface (Chilton et al., 2019; Combe et al., 2019; Schmidt et al., 2017). According to GRaND's observations, the presence of shallow subsurface ice (Prettyman et al., 2017) at mid latitudes and above (~≥ 50°) correlates with the abundance of flow features (Schmidt et al., 2017). Further, hydrodynamic models suggest low velocity impactors within the asteroid belt (average ~5 km·s^{-1} velocity; Marchi et al., 2013). At this velocity, impact melts on Vesta may achieve temperatures >1000 K (Marchi et al., 2013) and melt the regolith whereas on Ceres these impactors may only generate ~300 K which can melt crystalline ice or liberate OH present within the regolith (Marchi et al., 2016; Bowling et al., 2019). Thus, the contrast in the morphology of flow-like mass wasting movements on Vesta and Ceres may be due to the difference in rheology within this two-temperature regime. Flow-like mass wasting behavior can be associated with both impact melt and impact-driven mobility as well as post-impact surface temperature and volatile regolith content on Vesta and Ceres.

Both slides and flow-like movements are identified within craters of diameters ranging from ~2.6 km to ~53 km on Vesta and ~5.1 km to 77.8 km on Ceres. However, considering their average value (14.9±10.6 km on Vesta and 26.5±23.2 km on Ceres), it is evident that the majority of these

features occur within smaller craters which are naturally more abundant (Liu et al., 2018; Gou et al., 2018; Hiesinger et al., 2016) on both asteroid surfaces. There does not seem to be a correlation between crater size and mass-wasting feature abundance. One thing that is interesting though is that the mass wasting features occur in comparatively larger craters on Ceres than on Vesta. The difference in the size of craters might be due to the fact that (i) large impact craters might have been blanketed by the ejecta of the Rheasilvia and Venetia impact basins (Otto et al., 2013; Reddy et al., 2012; Marchi et al., 2012) and thus are not present on the surface and/or; (ii) due to the lower resolution LAMO data available for the analysis of Ceres (a factor of ~3 less than on Vesta) that may disguise small-scale features.

7.6.2 Landslide effective coefficient of friction

The contrast in the morphology of mass movements on Vesta and Ceres may be quantified statistically by comparing properties of landslide mobility. The effective friction coefficient can be correlated to rheological properties. A previous measurement of friction coefficients (Schmidt et al., 2017) suggests similar behavior of Cerean flows to flows on Saturn's icy moon Iapetus. The large range of friction coefficients at a given run-out length is explained by the presence of slippery ice at the surface of motion on Iapetus (Singer et al., 2012). Our investigation shows that a large range of friction coefficients is present on Vesta as well as Ceres (Figure **7.6**). Given that Vesta's regolith is dry, slippery ice theory cannot be the only explanation for a wide range of friction coefficients. Instead, a complex combination of various geological processes is probably involved in planetary mass wasting processes.

To explore the theory of slippery ice on Ceres, we test whether the amount of energy released during the mass movements would be sufficient to create melt. The required energy to melt a kilogram of ice is calculated using the (Turnbull, 2011) equation,

$$E_m = C_p\left(T_f - T_a\right) + \zeta \qquad (7.1)$$

Where, C_p = specific heat capacity of ice at constant pressure (2.108 kJ·kg^{-1}·K^{-1}),
T_f = freezing temperature of ice (273.15 K),
T_a = surface temperature on Ceres (150 K; Bland et al., 2016), and
ζ = latent heat of fusion (334 kJ·kg^{-1}; Turnbull, 2011)

We estimate the specific energy released during the mass movements using the drop height (H= 0.11- 4.60 km) and the gravitational force on Ceres (g= 0.27 m·s^{-2}),

$$E_r = gH \qquad (7.2)$$

This estimate assumes that the entire energy stored in the gravitational potential will be converted into heat and is thus an upper limit to the real values. Our estimations of E_r for all movements on Ceres range between 0.03-1.24 kJ·kg^{-1}. The specific energy required for melting pure ice is ~594 kJ·kg^{-1}, which is significantly higher than the estimated energy released during mass wasting processes on Ceres. It is therefore unlikely that substantial amounts of ice melted during mass wasting processes on Ceres, however, it is possible that higher temperatures are

reached along the landslide bases (Beddingfield et al., 2020). In addition, the presence of carbonates within the material may also reduce the melting temperature of the mixture (Chilton et al., 2019). Thus, the melting of water ice cannot be excluded as possible cause for fluidized movements, but it is probably a minor effect considering the difference in required and provided energy. Nevertheless, note that the above explained calculation does not include the energy released due to the impact. Similar ideas of ice melting cannot be applied to Vesta's flow-like movements as it lacks substantial amounts of volatile materials in the regolith (Jaumann et al., 2012).

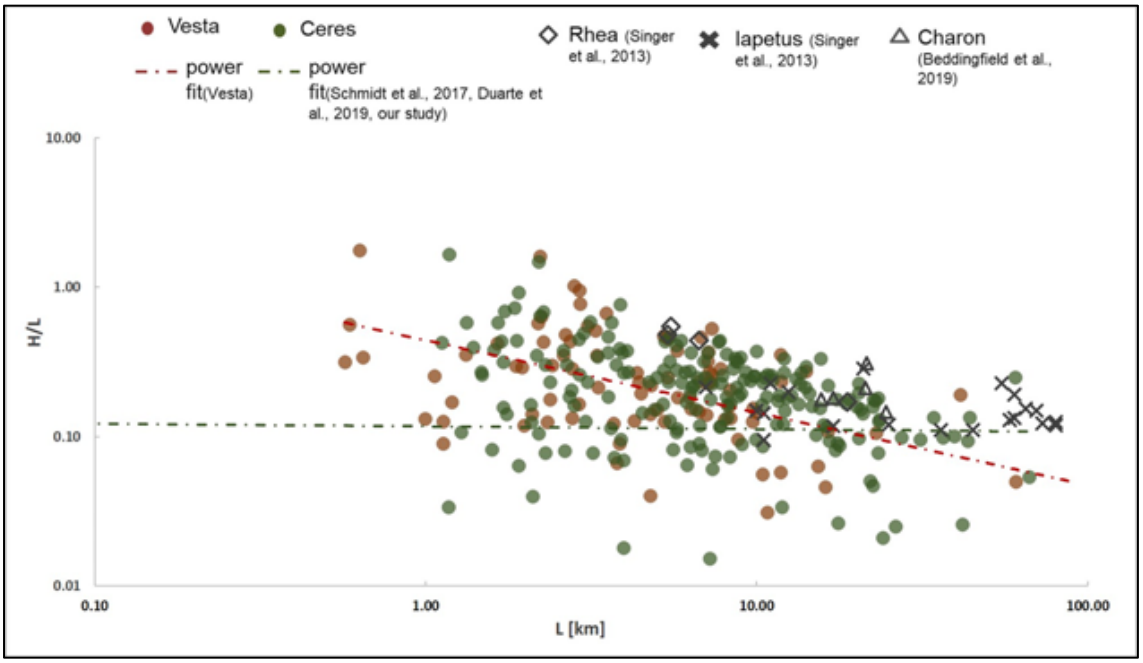

Figure 7.8 Comparison of landslide mobility on planetary bodies with similar surface accelerations. The identified mass wasting features on Vesta and Ceres are compared with lobate blocky landslides on Iapetus, intra-crater slides on Rhea (Singer et al., 2012), and long run-out slides on Charon (Beddingfield et al., 2020). Small Vesta landslides exhibit similar friction coefficients as the rest of the ice rich planetary bodies. Note that different image resolutions lead to differences in the ranges of measured H and L values.

We also compared the friction coefficient of mass wasting features of Vesta and Ceres to other icy planetary bodies (Figure 7.8, Figure 7.9). Previous studies (Schmidt et al., 2017; Singer et al., 2012) have compared the effective coefficient of friction of mass wasting flows with Mars and Earth, however, these bodies have significantly larger gravitational acceleration (g). To examine the role of volatiles in the regolith, we compare the H/L range of Vesta and Ceres mass movements with those of planetary bodies of similar g including Iapetus (0.22 $m \cdot s^{-2}$), Rhea (0.29 $m \cdot s^{-2}$) and Charon (0.27 $m \cdot s^{-2}$) in Figure 7.8. To provide a better visual perspective, we have also plotted the data shown in Figure 7.8 individually for Vesta and Ceres in Figure 7.9 highlighting each mass wasting category on Vesta and Ceres individually. The icy bodies are much colder than Vesta and Ceres and consist predominantly of volatiles. Even though Vesta is a comparatively dry asteroid, the effective coefficients of friction fall within a similar range as the other icy bodies which have

substantial amounts of volatiles and comparatively lower surface temperatures (Figure 7.8, Figure 7.9). We show that flow-like and sliding movements on Vesta have a similar range in *H/L* values, but are shorter in comparison to landslides on Rhea, Iapetus and Charon (Figure 7.9). Whereas on Ceres, the flow-like mobility is similar to the other planetary bodies, the slides also terminate at shorter distances. It should be noted that the lower limit of *L* values of the icy bodies is likely influenced by the generally lower image resolution available for these bodies.

We conclude that the presence of volatiles cannot be the single mechanism in the reduction of the effective coefficient of friction, because we did not observe lower values for the icy bodies and Ceres compared to dry Vesta. Instead, mass wasting measurements follow a common trend with degreasing *H/L* values for increasing *L*. Although the low number of landslides detected on some of the icy bodies may bias this observation, the icy bodies appear to have comparatively high *H/L* values (towards the upper end of the range at a given run-out length). This may hint at the temperature having a more significant influence on landslide mobility than previously thought.

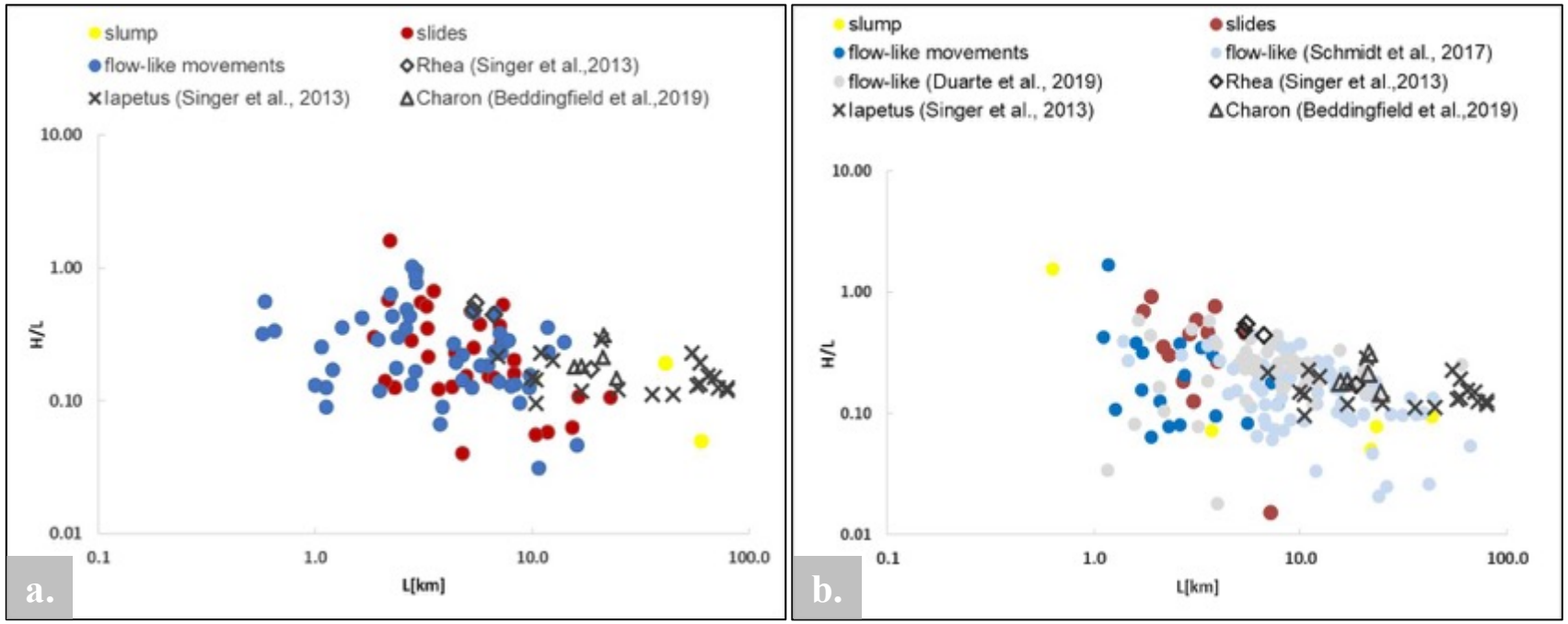

Figure 7.9 Comparison of landslides classes with other planetary bodies. (a) On Vesta, slides and flow-like movements behave similar to the lobate flows of Iapetus and Charon. However, both the movements on Vesta show shorter run-out lengths. (b) On Ceres, flow-like movements behave similar to the rest of the icy bodies however, slides terminate on shorter distances compared with Iapetus, Rhea, and Charon.

7.7 Summary

- We have mapped, analyzed and classified landslides on Vesta and Ceres to derive a relationship between landslide morphology, coefficient of friction and mobility. By choosing two bodies with similar surface accelerations, we were able to focus on the regolith volatile content on affecting these parameters.
- We have identified three common types of mass wasting features on Vesta and Ceres: slumps, slides and fluidized movements. There are some similarities (overlapping deposit pile, transverse ridges, multiple head slumping features, striations, lobate bulges), and differences (abundance of steps like slump deposits, conglomerate lobes, furrows, alcove like sheets), which we attribute primarily to a varying degree of volatile content on Vesta and Ceres. Further, we also mapped these features at a global scale on both asteroids. In total, the mapping database includes 188 mass wasting features on Vesta and 210 on Ceres.
- Various types of mass wasting process carved some of distinct geological impressions which have reshaped the surface of Vesta and Ceres. Huge slumps have distorted the crater rims due to collapse of material, and has significant influence on the surface elevation, contributing towards geologically chaotic terrain. Sliding material has produced spur/gully like fragile features at the crater walls and given rise to an albedo dichotomy which can be easily detectable on Vesta even today. Large-scale alcove fan-like deposition has been wrapped in and around Cerean craters, concealing the original topography and average slope of the neighboring regions on Ceres.
- The identified mass wasting features occur on slopes including in or around craters, basin walls or on cliffs. On Vesta, slide and fluidized features are located nearby smaller craters (average 14.8 km) whereas on Ceres the majority of these characteristics are identified within relatively larger crater (average 26.5 km). Slump characteristics are generally associated with larger craters on both bodies. On Ceres, the pole regions do not show any obvious evidence of slumps and slides but they are evident within mid latitudes, supporting the speculation of vertical variations of ice in the outer shell. Vesta has predominantly dry granular-like slides whereas on Ceres fluidized mass wasting behavior is dominant.
- Based on the comparison of run out length (L) and spread width (W) on Vesta and Ceres, we show that mass wasting features on Vesta become immobile on shorter distances and spread less whereas Cerean mass movements are voluminous, extend up to longer distance and cover larger areas. We suggest that the deposit emplacement is influenced by the difference in impact-induced surface temperature achieved due to contrast in material composition and volatile content. Compared to this, terrain conditions seem to have no significant effect on these values.
- The effective coefficient of friction varies significantly for a given run-out length or width on both bodies. A general decrease in friction coefficient is observed for larger L values as expected from observations from other planetary mass wasting features. Both bodies have a similar range of friction coefficients (even though Vesta is dry and Ceres is rich in water ice). Thus, the determination of H/L alone may not be sufficient to identify volatile content in mass wasting material. A combined analysis with geomorphologic characteristics is required.

- Comparing the friction coefficient of Vesta and Ceres with cold ice-rich planetary bodies of similar gravitational acceleration (Iapetus, Charon, Rhea), we find similar *H/L* values regardless of the volatile content of the regolith involved and deduce that the temperature, which is much lower on the other ice rich planetary bodies compared to main belt asteroids Vesta and Ceres, may have a more significant influence on *H/L* on the ice rich planetary bodies than the volatile content.

7.8 Acknowledgments

We would like to thank two anonymous reviewers for their constructive and helpful comments that greatly improved this work. The authors acknowledge the Dawn team for providing data and support. We would like to extend our gratitude to Chloe Beddingfield and Gou Sheng for sharing their data. We are also thankful to Stefan Schröder for helpful discussions. Image and topographic data used in this work are available at the Small Bodies Node of the Planetary Data System (for link refer Section **7.3**). Derived data products are available via Figshare: Parekh, Rutu (2020) Data for 'Influence of Volatiles on Mass Wasting Processes on Vesta and Ceres'.7z. (https://doi.org/10.6084/m9.figshare.13466642.v1). Measurement results are listed in the supporting information. This work is part of the research project "The Physics of Volatile Related Morphologies on Asteroids and Comets". RP and KO would like to gratefully acknowledge the financial support and endorsement from the German Academic Exchange Service (under DLR-DAAD PhD Fellowship) and the DLR Management Board Young Research Group Leader Program by the Executive Board Member for Space Research and Technology. A portion of the work was carried out at the Jet Propulsion Laboratory under contract with NASA.

8. SUMMARY & CONCLUSION

8.1 Summary

The overall objective of this thesis is to (i) establish potential relation between volatiles and surface regolith and (ii) evaluate and compare the abundance of volatiles by analyzing the regional and global scale morphological characteristics of various landforms on Vesta and Ceres. These two asteroids were chosen due to their similar surface acceleration (Vesta: 0.25 $m \cdot s^{-1}$, Ceres: 0.27 $m \cdot s^{-1}$) but different regolith composition and nature. For this study, I utilized surface mosaics (90 $m \cdot pixel^{-1}$ to 5 $m \cdot pixel^{-1}$) and processed elevation data (135 $m \cdot pixel^{-1}$ to 32 $m \cdot pixel^{-1}$) with varying resolutions obtained by the Dawn mission. Additionally, I used surface mosaics and measurements of physiological characteristics of other bodies (including Rhea, Iapetus, Charon, Eros, Itokawa, Moon) for the comparative analysis. To address the first objective, I scaled down to regional geological characteristics such as ponded features of Vesta and small-scale pit chains of Ceres. Whereas for comprehensive analysis, mass wasting features were studied on global scale (commonly observed on both objects) and was able to address the second objective.

Chapter **5**, focuses on the investigation of pond morphologies distributed within the vicinity of rare large impact craters such as Marcia and Cornelia on Vesta. In total, 10 host craters were observed, which resemble melt pools as of the Moon and dust pond deposits as of Eros and Itokawa (Table **5.2**). The type 1, ejecta ponds have smooth surface, the deposit is distributed evenly within the crater floor and consists of relatively shallow pond depth (<100 m) with a constant slope (Figure **5.3**). They are proposed to produce from the downslope movement of fluidized ejecta of large craters on Vesta (i.e. Marcia, Cornelia). In contrast, the type 2, dust pond candidates have a rough surface, increasing slope within the ponded terrain, are deeper (~200 m) and the deposited material extends from the crater floor towards the crater walls (Figure **5.4**). The dust pond deposits on Vesta are produced from the transportation of dusty regolith material. Given the size of Vesta (dia.: 525.4 km; Russell & Raymond, 2011), rare high-amplitude seismic diffusion is expected to transport the dusty granular material locally. Alternatively, subsurface volatile outgassing could also be responsible for the mobility of granular media on the surface. However, unlike Eros and Itokawa, on Vesta the dust particles, it did not undergo segregation to attain a smooth morphology. The lack of segregation is either due to infrequent large impactors (responsible for seismic attenuation) or insufficient amount of volatiles within local regolith (accountable for the short-lived outgassing activity). Therefore, the analysis and existence of diverse pond deposits indicates localized presence of volatiles within regolith of Vesta.

Chapter **6** describes the morphological analysis of small-scale pit chains observed within the vicinity of Occator, Azacca and Urvara craters on Ceres. The analysis conducted using high resolution mosaics prepared from the extended Dawn mission (XM02). For the pit chain survey, data from previous studies have been utilised (Scully et al., 2018; Otto et al., 2019) which were reprocessed and updated using XM02 mosaic. By definition, pit chains are series of circular to elongated collapse sinkholes that are eventually fused together and develop relatively larger steep

wall troughs (Martin et al., 2017; Martin and Kattenhorn, 2013; Nahm & Kattenhorn, 2012; Wyrick et al., 2004; Whitten & Martin, 2019; Martin et al., 2017). On Ceres, the observed pit chains show various stages of development and based on the surface chronology, we suspect that they are produced during different time-scale. Additionally, their distribution pattern favors the influence of multiple endogenic activities, for instance, within Occator, laccolith formation suspected to produces radial to polygonal pit chains in the southwest and the Cerealia Faculae region, whereas within Vinalia Faculae the subsurface complex fractures network connected to deep cryomagmatic reservoir may be responsible to form linear pit chains (Section **6.6.1**, Figure **6.5**). Moving on to Azacca and Urvara crater, the linear groups of pit chains are possibly the result of expansion-compression cycle of ice pockets present within the subsurface (Section **6.6.2**, Section **6.6.3**). However, in the case of Azacca (near equator) the ice layer is present at deeper depths (~10-20 km; Otto et al., 2019) in comparison to Urvara (near low-latitudes) where large amount of mechanically weaker volatiles (mixed with ice) are present near the surface (≤1 m; Bland et al., 2016). In total, the geologic map demonstrates 557 pit chains and 284 troughs features (Figure **6.1,** Figure **6.2**, Figure **6.3**). The physical parameters of pit chains (such as length, width, depth) suggest an increase in their dimension from mid- to low-latitudes on Ceres. By considering the pit chain depth as a proxy for surface regolith thickness, the minimum average thickness of surface regolith is 30 m, 200 m and 800 m within Occator, Azacca and Urvara craters, respectively (Section **6.7**). Nevertheless, the Azacca estimation accurately represents equatorial-scale surface regolith thickness. In contrast, within Occator and Urvara, the proposed estimation constrains the regolith thickness of the crater floor due to distinct subsurface conditions of Occator and thicker ejecta material blanket within Urvara.

In Chapter **7**, the comparative study of mass-wasting features on Vesta and Ceres evaluate the influence of volatiles and their concentration within the surface regolith on a global scale. Three common categories of mass wasting are identified: slumps, slides and flow-like movements (Section **7.5.1**). The observed mass movements show partial similarities and differences in their characteristics (Table **7.2**) which are related to the volatile content within the regolith on both Vesta and Ceres. The global scale mapping yield 188 mass wasting features on Vesta (Figure **7.4**) and 210 on Ceres (Figure **7.5**) which were not addressed in prior studies. On Vesta, a sliding type of granular mass movement is distributed homogeneously across the surface (Figure **7.4**). On Ceres, slump and slide movements are confined within mid-latitudes whereas flow-like mass movements are present at all latitudes (Figure **7.5**). The apparent difference in distribution is attributed to the relatively dry regolith nature of Vesta and wet subsurface conditions on Ceres. Most of the mass wasting features are observed within smaller impact craters (~14.8 km) on Vesta in comparison to Ceres (~26.5 km). The estimated physiological parameters of mass wasting features (such as height, length, effective coefficient of friction, spreading width) suggest that deposits on Vesta terminates at shorter distances in comparison to Ceres (Section **7.5.3**). Both Vesta and Ceres have similar range of coefficient of friction (*H/L*) implying that *H/L* might not be sufficient tool to identify influence of volatiles (Figure **7.6**). Further, the comparative analysis of the *H/L* of the inner asteroid belt objects (Vesta, Ceres) with cold ice-rich outer solar belt bodies (Rhea, Iapetus, Charon

which have similar acceleration; Figure 7.8) suggests that temperature may dominate the *H/L* on ice-rich bodies.

8.2 Conclusion

Understanding the location, distribution and burial depth of volatiles within the asteroid belt has become a key interest for the scientific community due to its potential to harbor life and proving targets for future landing missions. Therefore, a comprehensive analysis of geomorphological features which has direct or possible association with volatiles near the surface of Vesta and Ceres is performed in this thesis. The study includes multi-scale analysis of three surface features related to volatiles using data from the Dawn spacecrafts' primary and extended mission. In addition, a comparative examination enables the opportunity to investigate the relation between the volatile content and the surface regolith. The multi-scale features analysis includes (i) localized pond deposits associated with a mobility of the regolith on Vesta, (ii) regional pit chains indicative of endogenic activities on Ceres and (iii) diverse range of mass wasting features of varying impressions across the surface of Vesta and Ceres. The independent analysis of above-mentioned features demonstrates the existence of volatiles in the regolith and provides verification related to the volatile distribution heterogeneity.

A. Regional scale analysis of features*:*

- **Vesta**: Smooth surface features are categorized as type 1, ejecta ponds representing devolatilization of water-bearing regolith forming fluidized ejecta whereas rough, unsorted type 2, dust deposits support the transportation of dusty regolith via rare high-amplitude of seismic diffusion and/or short-lived subsurface outgassing activity. Based on the analysis, the presence of a relatively low amount of localized volatiles within the Vesta regolith is reasonable.
- **Ceres**: The diverse pattern and clustered distribution of pit chains is linked to laccolith intrusion of volatile rich material and diurnal thermal contraction of ice present at varying depths. The estimated depth of the pit chains indicates relatively thin coating of loose dusty surface regolith at mid latitudes. The analyses of pit chains morphological features and their dimensions implies a vertical heterogeneity in the ice distribution on Ceres from the equator to south pole.

B. Global scale analysis of features*:*

- **Vesta:** The dominant distribution of granular-like slide features implies the presence of relatively dry regolith across the surface.
- **Ceres:** The dominant distribution of flow-like movements on Ceres suggests the presence of volatiles on a global scale, whereas the confined characteristic of slides and slumping features indicate the lateral hemisphere-scale difference in the ice content and support ice-rock fractionation.

C. Comparative analysis*:*

- The study related to the geometry of mass wasting deposit demonstrated that on Vesta, mass mobility is limited in comparison to Ceres where extensive deposit emplacements are observed.

The difference is attributed to the apparent contrast in the volatile content at global scale on both the asteroids.

- Similar range of effective coefficient of friction (*H/L*) for mass mobility on Vesta and Ceres might suggests that *H/L* alone might not be reliable tool to derive the volatile influence.
- While comparing the (*H/L*) of Vesta and Ceres with ice-rich outer planetary bodies such as Rhea, Iapetus, Charon, the results suggest that on colder surface (50-80 K), temperature influence the friction of masses.

This study summarizes the feature analysis, their physical estimations and provide multiple lines of evidence supporting the existence of volatiles and heterogeneity within their distribution on Vesta and Ceres. The GRaND and VIR observations were able to characterized the volatiles which are present on and near the surface (Sizemore et al., 2019). However, the features analysis carried out in this thesis help to characterized the volatiles (e.g. ~0.05 vol% and ~20 vol.% volatiles required for average distance of ~4.5 km ~11.2 km mobility on Vesta and Ceres, respectively; Reddy et al., 2012a; Sizemore et al., 2019; Parekh et al., 2021a) present at intermediate depths, where direct observation via any other medium is not possible. In addition, comparative study emphasizes a unique spectrum of how the contrast in the volatile content can directly shape the surface rheology and produce distinct geological impressions under similar gravitational conditions as observed on Vesta and Ceres. Moreover, the global maps are prepared using the highest possible resolution data and review the locations which can serve as a target for future missions for in-situ investigation and acquire better resolution data to constrain deeper understanding of the asteroids' crust. Lastly, this work also provides basis for future laboratory analogues studies and computational modeling by presenting morphological estimations to attain insights into volatile sublimation and outgassing processes.

The results from this thesis created backdrop for two important objectives; (i) derive the volatile loss rate via surface features and (ii) investigate possible causes that reactivated subsurface volatiles on Vesta and Ceres. In a nutshell, this work not only amplifies science related to volatile distribution and their concentration within asteroid belt objects but also demonstrates the potential of volatile driven surface processes with the ability to influence the crustal evolution.

REFERENCES

Adams, J. B. (1974). Visible and near-infrared diffuse reflectance spectra of pyroxenes as applied to remote sensing of solid objects in the solar system. *Journal of Geophysical Research, 79*(32), 4829-4836. doi:https://doi.org/10.1029/JB079i032p04829

Ahrens, T. J., & O'Keefe, J. D. (1972). Shock melting and vaporization of lunar rocks and minerals. *The moon, 4*(1), 214-249. doi:10.1007/BF00562927

Ammannito, E., De Sanctis, M. C., Capaccioni, F., Teresa Capria, M., Carraro, F., Combe, J.-P., et al. (2013). Vestan lithologies mapped by the visual and infrared spectrometer on Dawn. *Meteoritics & Planetary Science, 48*(11), 2185-2198. doi:10.1111/maps.12192

Ammannito, E., De Sanctis, M. C., Ciarniello, M., Frigeri, A., Carrozzo, F. G., Combe, J.-P., et al. (2016). Distribution of phyllosilicates on the surface of Ceres. *Science, 353*, aaf4279. doi:10.1126/science.aaf4279

Archinal, B. A., A'Hearn, M. F., Bowell, E., Conrad, A., Consolmagno, G. J., Courtin, R., et al. (2011). Report of the IAU working group on cartographic coordinates and rotational elements: 2009. *Celestial mechanics dynamical astronomy, 109*(2), 101-135. doi:10.1007/s10569-010-9320-4

Ashley, J. W., Robinson, M. S., Hawke, B. R., Van der Bogert, C. H., Hiesinger, H., Sato, H., et al. (2012). Geology of the King crater region: New insights into impact melt dynamics on the Moon. *Journal of Geophysical Research: Planets, 117*(E12). doi:10.1029/2011JE003990|

Baldwin, R. B. (1964). Lunar crater counts. *The Astronomical Journal, 69*, 377.

Baldwin, R. B. (1971). On the history of lunar impact cratering: The absolute time scale and the origin of planetesimals. *Icarus, 14*(1), 36-52. doi:10.1016/0019-1035(71)90100-X

Banerdt, W. B., Golombek, M. P., & Tanaka, K. L. (1992). Stress and tectonics on Mars. *The Mars*, 249-297.

Basilevsky, A., Abdrakhimov, A., Dorofeeva, V. (2012). Water and other volatiles on the Moon: a review. *Solar system research*. 46, 89-107. doi:10.1134/S0038094612010017

Basu, A., & Molinaroli, E. (2001). Sediments Of The Moon And Earth As End-Members For Comparative Planetology. *Earth, Moon and Planets, 85*, 25-43. https://ui.adsabs.harvard.edu/abs/2001EM&P...85...25B

Beddingfield, C. B., Beyer, R. A., Singer, K. N., McKinnon, W. B., Runyon, K., Grundy, W., et al. (2020). Landslides on Charon. *Icarus, 335*. doi:10.1016/j.icarus.2019.07.017

Benoit, P., Hagedorn, N., Kracher, A., Sears, D.W.G., White, J. (2003). Grain size and density sepration on asteroids:composition of seismic shaking. LPSC XXXIV.

Bell, J. F.III, et al., Near-IR reflectance spectroscopy of 433 Eros from the NIS instrument on the NEAR mission. Low phase angle observations, *Icarus*, 155, 119–144, 2002.

Binzel, R., Rivkin, A., Bus, S., & Tokunaga, A. (2004). *Near-Infrared Spectral Properties of Near-Earth Objects: Results for Space Weathering Trends.* Paper presented at the AAS/Division for Planetary Sciences Meeting Abstracts# 36.

Binzel, R. P., Gaffey, M. J., Thomas, P. C., Zellner, B. H., Storrs, A. D., & Wells, E. N. (1997). Geologic mapping of Vesta from 1994 Hubble space telescope images. *Icarus, 128*(1), 95-103. doi:10.1006/icar.1997.5734

Bland, M. T. (2013). Predicted crater morphologies on Ceres: Probing internal structure and evolution. *Icarus, 226*, 510. doi:10.1016/j.icarus.2013.05.037

Bland, M. T., Raymond, C. A., Schenk, P. M., Fu, R. R., Kneissl, T., Pasckert, J. H., et al. (2016). Composition and structure of the shallow subsurface of Ceres revealed by crater morphology. *Nature Geoscience, 9*(7), 538-542. doi:10.1038/ngeo2743

Bland, M. T., Buczkowski, D., Sizemore, H., Ermakov, A., King, S. D., Sori, M., et al. (2019). Dome formation on Ceres by solid-state flow analogous to terrestrial salt tectonics. *Nature Geoscience, 12*(10), 797-801.

Bleamaster, L. F., & Hansen, V. L. (2004). Effects of crustal heterogeneity on the morphology of chasmata, Venus. *Journal of Geophysical Research: Planets, 109*(E2).

Bottke, W. F., Jedicke, R., Morbidelli, A., Petit, J.-M., & Gladman, B. (2000). Understanding the Distribution of Near-Earth Asteroids. *Science, 288*, 2190. doi:10.1126/science.288.5474.2190

Bottke, W. F., Vokrouhlický, D., Minton, D., Nesvorný, D., Morbidelli, A., Brasser, R., et al. (2012). An Archaean heavy bombardment from a destabilized extension of the asteroid belt. *Nature, 485*(7396), 78-81. doi:10.1038/nature10967

Bowden, F., & Leben, L. (1940). The friction of lubricated metals. *Philosophical Transactions of the Royal Society of London. Series A, Mathematical, 239*(799), 1-27. doi:10.1098/rsta.1940.0007

Bowden, F., Moore, A. J. W., & Tabor, D. (1943). The ploughing and adhesion of sliding metals. *Journal of Applied Physics, 14*(2), 80-91. doi:10.1063/1.1714954

Bowling, T. J., Ciesla, F. J., Davison, T. M., Scully, J. E., Castillo-Rogez, J. C., Marchi, S., & Johnson, B. C. (2019). Post-impact thermal structure and cooling timescales of Occator crater on asteroid 1 Ceres. *Icarus, 320*, 110-118.

Bray, V. J., Tornabene, L. L., Keszthelyi, L. P., McEwen, A. S., Hawke, B. R., Giguere, T. A., et al. (2010). New insight into lunar impact melt mobility from the LRO camera. *Geophysical Research Letters, 37*(21). doi:10.1029/2010GL044666|

Britt, D. T., Colsolmagno, B. G., & Lebofsky, L. (2007). Main-Belt Asteroids. In *Encyclopedia of the solar system- second edition* (pp. 349).

Brunetti, M. T., Xiao, Z., Komatsu, G., Peruccacci, S., & Guzzetti, F. (2015). Large rock slides in impact craters on the Moon and Mercury. Icarus, 260, 289-300

Brunetto, R., Loeffler, M. J., Nesvorný, D., Sasaki, S., & Strazzulla, G. J. A. I. (2015). Asteroid Surface Alteration by Space Weathering Processes. In *Asteroids IV* (pp. 597). Tucson, Arizona, USA: University of Arizona press.

Buczkowski, D., Barnouin-Jha, O. S., & Prockter, L. M. J. I. (2008). 433 Eros lineaments: Global mapping and analysis. *Icarus, 193*(1), 39-52.

Buczkowski, D., Wyrick, D. Y., Iyer, K. A., Kahn, E. G., Scully, J. E. C., Nathues, A., et al. (2012). Large-scale troughs on Vesta: A signature of planetary tectonics. *Geophys Research Letters, 39*, L18205. doi:10.1029/2012gl052959

Buczkowski, D., Wyrick, D., Toplis, M., Yingst, R., Williams, D., Garry, W., et al. (2014). The unique geomorphology and physical properties of the Vestalia Terra plateau. *Icarus, 244*, 89-103.

Buczkowski, D., Schmidt, B. E., Williams, D. A., Mest, S. C., Scully, J. E. C., Ermakov, A. I., et al. (2016). The geomorphology of Ceres. *Science, 353*(6303), aaf4332. doi:doi:10.1126/science.aaf4332

Buczkowski, D., Williams, D., Scully, J., Mest, S., Crown, D., Schenk, P., et al. (2018a). The geology of the Occator quadrangle of dwarf planet Ceres: floor-fractured craters and other geomorphic evidence of cryomagmatism. *Icarus, 316*, 128-139.

Buczkowski, D., Sizemore, H. G., Bland, M. T., Scully, J. E. C., Quick, L. C., Hughson, K. H. G., et al. (2018b). Floor-Fractured Craters on Ceres and Implications for Interior Processes. *Journal of Geophysical Research, 123*, 3188. doi:10.1029/2018je005632

Bulmer, M. (2012). Landslides on other planets. In John J. Clague & D. Stead (Eds.), *Landslides: types, mechanisms and modeling* (pp. 393). Cambridge, UK: Cambridge university press.

Burbine, T. H., McCoy, T. J., Meibom, A., Gladman, B., & Keil, K. (2002). Meteoritic parent bodies: Their number and identification. In *Asteroids III* (pp. 653-667). Tucson, Arizona, USA: Universit of Arizona press.

Bus, S. J., & Binzel, R. P. (2002a). Phase II of the Small Main-Belt Asteroid Spectroscopic Survey. A Feature-Based Taxonomy. *158*, 146. doi:10.1006/icar.2002.6856

Bus, S. J., & Binzel, R. P. (2002b). Phase II of the Small Main-Belt Asteroid Spectroscopic Survey. The Observations. *158*, 106. doi:10.1006/icar.2002.6857

Bus, S. J., Vilas, F., & Barucci, M. A. (2002). Visible-Wavelength Spectroscopy of Asteroids. In *Asteroids III* (pp. 169-182). Tucson, Arizona, USA: University of Arizona press.

Campbell, C. S., Cleary, P. W., & Hopkins, M. (1995). Large-scale landslide simulations: Global deformation, velocities and basal friction. *Journal of Geophysical Research: Solid Earth, 100*(B5), 8267-8283. doi:10.1029/94JB00937|

Carrozzo, F. G., De Sanctis, M. C., Raponi, A., Ammannito, E., Castillo-Rogez, J., Ehlmann, B. L., et al. (2018). Nature, formation, and distribution of carbonates on Ceres. *Science Advances, 4*(3), e1701645. doi:10.1126/sciadv.1701645

Castillo-Rogez, J. C., & McCord, T. B. (2010). Ceres' evolution and present state constrained by shape data. *Icarus, 205*(2), 443-459.

Castillo-Rogez, J. C., Hesse, M., Formisano, M., Sizemore, H., Bland, M., Ermakov, A., & Fu, R. (2019). Conditions for the long-term preservation of a deep brine reservoir in Ceres. *Journal of Geophysical Research, 46*(4), 1963-1972. doi:10.1029/2018GL081473

Castillo-Rogez, C., & Rayman, M. D. (2020). A bountiful harvest on Ceres. *Nature Astronomy, 4*(8), 807-807.

Cellino, A (2020). Reference Module in Earth Systems and Environmental Science, Asteroids. doi:10.1016/B978-0-12-409548-9.11842-1

Chapman, C. R., & Haefner, R. R. (1967). A critique of methods for analysis of the diameter-frequency relation for craters with special application to the Moon. *Journal of Geophysical Research, 72*(2), 549-557. doi:10.1029/JZ072i002p00549

Chapman, C. R., Morrison, D., & Zellner, B. (1975). Surface Properties of Asteroids: A Synthesis of Polarimetry, Radiometry, and Spectrophotometry. *Icarus, 25*, 104. doi:10.1016/0019-1035(75)90191-8

Cheng, A. F., Izenberg, N., Chapman, C. R., & Zuber, M. T. (2002). Ponded deposits on asteroid 433 Eros. *Meteoritics & Planetary Science, 37*, 1095. doi:10.1111/j.1945-5100.2002.tb00880.x

Cheng, H. C. J., & Klimczak, C. (2020). The large-scale troughs on Asteroid 4 Vesta are opening-mode fractures. *Journal of Geophyscial:Research.* doi: 10.31223/X51G6T

Chilton, H. T., Schmidt, B. E., Duarte, K., Ferrier, K. L., Hughson, K. H. G., Scully, J. E. C., et al. (2019). Landslides on Ceres: Inferences Into Ice Content and Layering in the Upper Crust. *Journal of Geophysical Research: Planets*. doi:10.1029/2018je005634

Cintala, M. J., & Grieve, R. A. F. (1998). Scaling impact-melt and crater dimensions: Implications for the lunar cratering record. *Meteoritics & Planetary Science, 33*, 889. doi:10.1111/j.1945-5100.1998.tb01695.x

Clarke, J. D. (2009). Extraterrestrial regolith. In *Regolith science* (pp. 377-400). Melborne, Austrailia

Cloutis, E. A., Binzel, R. P., & Gaffey, M. J. (2014). Establishing asteroid–meteorite links. *Elements, 10*(1), 25-30. doi:10.2113/gselements.10.1.25

Collins, G. S., & Melosh, H. J. (2003). Acoustic fluidization and the extraordinary mobility of sturzstroms. *Journal of Geophysical Research: Solid Earth, 108*(B10). doi:10.1029/2003JB002465|

Collins, G. S., Melosh, H. J., & Osinski, G. R. (2012). The impact-cratering process. *Elements, 8*(1), 25-30. doi:10.2113/gselements.8.1.25

Combe, J. P., McCord, T. B., Tosi, F., Ammannito, E., Carrozzo, F. G., De Sanctis, M. C., et al. (2016). Detection of local H2O exposed at the surface of Ceres. *Science, 353*(6303). doi:10.1126/science.aaf3010

Combe, J.-P., Raponi, A., Tosi, F., De Sanctis, M. C., Carrozzo, F. G., Zambon, F., et al. (2019). Exposed H2O-rich areas detected on Ceres with the dawn visible and infrared mapping spectrometer. *Icarus, 318*, 22. https://ui.adsabs.harvard.edu/abs/2019Icar..318...22C

Crosta, G. B., De Blasio, F. V., & Frattini, P. (2018a). Introducing a New Inventory of Large Martian Landslides. *Journal of Geophysical Research: Planets, 5*, 89-119. doi:10.1002/2017je005398

Crosta, G. B., Frattini, P., Valbuzzi, E., & De Blasio, F. V. (2018b). Global Scale Analysis of Martian Landslide Mobility and Paleoenvironmental Clues. Journal of Geophysical Research: Planets, 123(4), 872-891.

Crown, D. A., Sizemore, H. G., Yingst, R. A., Mest, S. C., Platz, T., Berman, D. C., et al. (2018). Geologic mapping of the Urvara and Yalode Quadrangles of Ceres. *Icarus, 316*, 167. doi:10.1016/j.icarus.2017.08.004

Cyr, K. E., Sears, W. D., & Lunine, J. I. (1998). Distribution and evolution of water ice in the solar nebula: Implications for solar system body formation. *Icarus, 135*(2), 537-548. doi:10.1006/icar.1998.5959

Cruden, D. M. (1980). The anatomy of landslides. Canadian Geotechnical Journal, 17(2), 295-300.

Davey, S., Ernst, R. E., Samson, C., & Grosfils, E. (2013). Hierarchical clustering of pit crater chains on Venus. *Canadian Journal of Earth Sciences, 50*(1), 109-126. doi:10.1139/cjes-2012-0054

Davis, R. H., Herbolzhiemer, E., & Acrivos, A. (1982). The sedimentation of polydisperse suspensions in vessels having inclined walls. *International Journal of Multiphase Flow, 8*(6), 571-585. doi:10.1016/0301-9322(82)90064-7

De Blasio, F. V., & Elverhøi, A. (2008). A model for frictional melt production beneath large rock avalanches. *Journal of Geophysical Research: Earth Surface, 113*(F2). doi:10.1029/2007JF000867

De Blasio, F. V. (2011). *Introduction to the physics of landslides: lecture notes on the dynamics of mass wasting*: Springer Science & Business Media.

De Sanctis, M., Coradini, A., Ammannito, E., Filacchione, G., Capria, M., Fonte, S., et al. (2011). The VIR spectrometer. In R. C. T & R. C. A (Eds.), *The Dawn mission to minor planets 4 Vesta and 1 Ceres* (pp. 329-369). New York, USA: Springer.

De Sanctis, M. C., Combe, J. P., Ammannito, E., Palomba, E., Longobardo, A., McCord, T. B., et al. (2012). Detection of Widespread Hydrated Materials on Vesta by the VIR Imaging Spectrometer on Board the Dawn mission. *The Astrophysical Journal, 758*(2). doi:10.1088/2041-8205/758/2/l36

De Sanctis, M. C., Ammannito, E., Capria, M. T., Capaccioni, F., Combe, J.-P., Frigeri, A., et al. (2013). Vesta's mineralogical composition as revealed by the visible and infrared spectrometer on Dawn. *Meteoritics & Planetary Science, 48*(11), 2166-2184. doi:10.1111/maps.12138

De Sanctis, M. C., Ammannito, E., McSween, H. Y., Raponi, A., Marchi, S., Capaccioni, F., et al. (2017). Localized aliphatic organic material on the surface of Ceres. Science, 355(6326), 719-722. https://science.sciencemag.org/content/sci/355/6326/719.full.pdf

De Sanctis, M. C., Ammannito, E., Carrozzo, F. G., Ciarniello, M., Giardino, M., Frigeri, A., et al. (2018). Ceres's global and localized mineralogical composition determined by Dawn's Visible and Infrared

Spectrometer (VIR). *Meteoritics Planetary Science Journal, 53*(9), 1844-1865. doi:10.1111/maps.13104

De Sanctis, M. C., Ammannito, E., Raponi, A., Marchi, S., Ciarniello, M., McSween , H. Y., et al. (2015b). *Ammonia Bearing Species on Ceres: Implication on Origin and Evolution.* Paper presented at the AGU Fall Meeting Abstracts.

De Sanctis, M. C., Ammannito, E., Raponi, A., Marchi, S., McCord, T. B., McSween, H., et al. (2015a). Ammoniated phyllosilicates with a likely outer Solar System origin on (1) Ceres. *Nature, 528*(7581), 241-244. doi:10.1038/nature16172

De Sanctis, M. C., Raponi, A., Ammannito, E., Ciarniello, M., Toplis, M., McSween, H., et al. (2016). Bright carbonate deposits as evidence of aqueous alteration on (1) Ceres. *Nature, 536*(7614), 54-57.

De Elía, G. and Di Sisto, R. (2011). Impactor flux and cratering on Ceres and Vesta: Implecations for early solar system. *Astronomy & Astrophysics*, 534, A129. doi: 10.1051/0004-6361/201117543

Denevi, B. W., Blewett, D. T., Buczkowski, D. L., Capaccioni, F., Capria, M. T., De Sanctis, M. C., et al. (2012). Pitted terrain on Vesta and implications for the presence of volatiles. *Science, 338*(6104), 246-249. doi:10.1126/science.1225374

Dikau, R., Brunsden, D., Schrott, L., & Ibsen, M.-L. (1996b). *Landslide recognition: Identification, movement, and causes.* (Vol. 21): Wiley

Dikau, R., Brunsden, D., Schrott, L., & Ibsen, M.-L. (1996). Book Review: Landslide recognition: Identification, movement, and causes. (Vol. 21): Wiley and Sons, New York.

Dombard, A. J., Barnouin, O. S., Prockter, L. M., & Thomas, P. C. (2010). Boulders and ponds on the Asteroid 433 Eros. *Icarus, 210*, 713. doi:10.1016/j.icarus.2010.07.006

Duarte, K. D., Schmidt, B. E., Chilton, H. T., Hughson, K. H. G., Sizemore, H. G., Ferrier, K. L., et al. (2019). Landslides on Ceres: Diversity and Geologic Context. *Journal of Geophysical Research: Planets*. doi:10.1029/2018je005673

Duke, M. B., & Silver, L. T. (1967). Petrology of eucrites, howardites and mesosiderites. *Geochimica et Cosmochimica Acta, 31*(10), 1637-1665. doi:10.1016/0016-7037(67)90112-3

Eggleton, R A (ed) (2001) The regolith glossary. Cooperative Research Centre for Landscape Evolution and Mineral Exploration, Canberra.

Elbeshausen, D., Wünnemann, K., Sierks, H., Vincent, J. B., & Oklay, N. (2012). Landslides triggered by impacts on asteroid (21) Lutetia? Paper presented at the European Planetary Science Congress 2012.

Emery, J. P., Marzari, F., Morbidelli, A., French, L. M., & Grav, T. J. A. I. (2015). The Complex History of Trojan Asteroids. In *Asteroids IV* (pp. 203).

Erismann, T. H. (1979). Mechanisms of large landslides. *Rock Mechanics, 12*(1), 15-46. doi:10.1007/BF01241087

Ermakov, A. I., Zuber, M. T., Smith, D. E., Raymond, C. A., Balmino, G., Fu, R. R., & Ivanov, B. A. (2014). Constraints on Vesta's interior structure using gravity and shape models from the Dawn mission. *Icarus, 240*, 146-160. doi:10.1016/j.icarus.2014.05.015

Ermakov, A., Fu, R., Castillo-Rogez, J., Raymond, C., Park, R., Preusker, F., et al. (2017). Constraints on Ceres' internal structure and evolution from its shape and gravity measured by the Dawn spacecraft. *Journal of Geophysical Research: Planets, 122*(11), 2267-2293.

Ferrill, D. A., & Morris, A. P. (2003). Dilational normal faults. *Journal of structural geology, 25*(2), 183-196. doi:10.1016/S0191-8141(02)00029-9

Ferrill, D. A., Wyrick, D. Y., Morris, A. P., Sims, D. W., & Franklin, N. M. (2004). Dilational fault slip and pit chain formation on Mars. *Geological Society of America, 14*(10), 4-12.

Foderà Serio, G., Manara, A., Sicoli, P., & Bottke, W. F. (2002). Giuseppe Piazzi and the discovery of Ceres. In *Asteroids III* (pp. 17-24). Tucson, Arizona, USA: University of Arizona Press.

Formisano, M., Federico, C., Turrini, D., Coradini, A., Capaccioni, F., De Sanctis, M.C. and Pauselli, C. (2013), The heating history of Vesta and the onset of differentiation. Meteorit Planet Sci, 48: 2316-2332. doi:10.1111/maps.12134

Fornasier, S., Lantz, C., Barucci, M., & Lazzarin, M. (2014). Aqueous alteration on main belt primitive asteroids: Results from visible spectroscopy. *Icarus, 233*, 163-178. doi:10.1016/j.icarus.2014.01.040

Franzen, M., Nichols, S., Bogdon, K., White, C., Godsey, R., Napieralski, N., et al. (2003). The origin of chondrites: metal–silicate separation experiments under microgravity conditions–I. *Geophysical Research Letters, 30*(14), 4. doi:10.1029/2003GL017659

French, B. M. (1998). *Traces of Catastrophe: A Handbook of Shock-Metamorphic Effects in Terrestrial Meteorite Impact Structures*. Houston: LPI Contributor no. 954.

Frigeri, A., Schmedemann, N., Williams, D. A., Chemin, Y., Mirino, M., Nass, A., et al. (2018). The geology of the Nawish quadrangle of Ceres: The rim of an ancient basin. *Icarus, 316*, 114-127. doi:10.1016/j.icarus.2018.08.015

Fu, R. R., Ermakov, A. I., Marchi, S., Castillo-Rogez, J. C., Raymond, C. A., Hager, B. H., et al. (2017). The interior structure of Ceres as revealed by surface topography. *Earth and Planetary Science Letters, 476*, 153-164.

Fujiwara, A., Kawaguchi, J., Yeomans, D. K., Abe, M., Mukai, T., Okada, T., et al. (2006). The Rubble-Pile Asteroid Itokawa as Observed by Hayabusa. *Science, 312*, 1330. doi:10.1126/science.1125841

Gaffey, M. J. (1976). Spectral reflectance characteristics of the meteorite classes. *Journal of Geophysical Research, 81*(5), 905-920. doi:10.1029/JB081i005p00905

Garlick, M. A. (1888). *The Asteroids; Or Minor Planets Between Mars and Jupiter*: Good Press.

Garlick, M. A. (2003). *The story of the Solar System*. Cambridge, UK: Cambridge university press.

Gault, D. E., L, Q. W., & R, O. V. (1968). Impact cratering mechanics and structures In: French BM, Short NM (eds) Shock Metamorphism of Natural Materials. In *Shock Metamorphism of Natural Materials*. Baltimore, USA: Mono book corp.

Gehrels, T. (1971). *Physical studies of minor planets* (Vol. 267): NASA Special Publication.

Gibbons, H. L., Scott, E., Wilson, L., & Head, J. (2001). *Inferred properties of giant radial dikes beneath graben in northern Tharsis.* Paper presented at the Proc. Lunar. Planet. Sci. Conf. 32nd.

Gou, S., Yue, Z., Di, K., & Liu, Z. (2018). A global catalogue of Ceres impact craters≥ 1 km and preliminary analysis. *Icarus, 302*, 296-307.

Gradie, J., & Tedesco, E. (1982). Compositional structure of the asteroid belt. *Science, 216*(4553), 1405-1407. doi:10.1126/science.216.4553.1405

Gray, J. M. N. T., Chugunov, V. A. (2006) Particle-size segregation and diffusive remixing in shallow granular avalanches. *Journal of Fluid Mechanics*, 569, 365–398

Greeley, R., Sullivan, R., Coon, M. D., Geissler, O. E., Tufts, B. R., Head III, J. W., et al. (1998). Terrestrial sea ice morphology: Considerations for Europa. *Icarus, 135*(1), 25-40. doi:10.1006/icar.1998.5977

Grieve, R. A. F., Dence, M. R., & Robertson, P. B. (1977). Cratering processes-As interpreted from the occurrence of impact melts. In *Impact and explosion cratering: Planetary and terrestrial implications* (pp. 791-814). New York: Pergamon press.

Grossman, J.N., Alexander, C.M.O.d., Wang, J., Brearley, A.J. (2000). Bleached chondrules: Evidence for widespread aqueous processes on the parent asteroids of ordinary chondrites. *Meteoritics and planetary science*. 35, 467. https://doi.org/10.1111/j.1945-5100.2000.tb01429.x

Gundlach, B., & Blum, J. (2013). A New Method to Determine the Grain Size of Planetary Regolith. *Icarus*, 1-19. doi:10.1016/j.icarus.2012.11.039

Han, R., Hirose, T., Shimamoto, T., Lee, Y., & Ando, J. (2011). Granular nanoparticles lubricate faults during seismic slip. *Geology, 39*(6), 599-602. doi:10.1130/G31842.1

Hardy, S. (2021). Discrete Element Modelling of Pit Crater Formation on Mars. *Geosciences*.

Harris, A. W., & D'Abramo, G. (2015). The population of near-Earth asteroids. *Icarus, 257*, 302-312. doi:10.1016/j.icarus.2015.05.004

Harrison, K. P., & Grimm, R. E. (2003). Rheological constraints on Martian landslides. *Icarus, 163*(2), 347-362.

Hartmann, W. K. (1965). Terrestrial and lunar flux of large meteorites in the last two billion years. *Icarus, 4*(2), 157-165. doi:10.1016/0019-1035(65)90057-6

Hartmann, W. K. (1973). Ancient lunar mega-regolith and subsurface structure. *Icarus, 18*(4), 634-636. doi:10.1016/0019-1035(73)90066-3

Hartmann, W. K., Anguita, J., de la Casa, M. A., Berman, D. C., & Ryan, E. V. (2001b). Martian Cratering 7: The Role of Impact Gardening. *Icarus, 149*, 37. doi:10.1006/icar.2000.6532

Hartmann, W. K., & Neukum, G. (2001a). Cratering chronology and the evolution of Mars. In Kallenbach R., Geiss J., & H. W.K. (Eds.), *Chronology and Evolution of Mars* (Vol. 12, pp. 165-194). Space Sciences Series of ISSI: Springer, Dordrecht.

Hartmann, W. K., & Wood, C. A. (1971). Moon: Origin and evolution of multi-ring basins. *The moon, 3*(1), 3-78. doi:10.1007/BF00620390

Haseltine, J. D., Franzen, M. A., & Sears, D. W. G. (2006). *Fluidization from continuous outgassing as a cause of geological structures on 433 Eros.* Paper presented at the 37th Lunar and Planetary Science Conference.

Hawke, B. R., & Head, J. W. (1977a). *Impact Melt in Lunar Crater Interiors*. http://articles.adsabs.harvard.edu/pdf/1977LPI.....8..415H

Hawke, B. R., & Head, J. W. (1977b). *Impact melt on lunar crater rims*. p. 815. https://ui.adsabs.harvard.edu/abs/1977iecp.symp..815H

Hawke, B. R., & Head, J. W. (1979). *Impact Melt Volumes Associated with Lunar Craters*. https://ui.adsabs.harvard.edu/abs/1979LPI....10..510H

Hayne, P. O., & Aharonson, O. (2015). Thermal stability of ice on Ceres with rough topography. *Journal of Geophysical Research: Planets, 120*, 1567.

Head, J. W., & Wilson, L. (1993). Lunar graben formation due to near-surface deformation accompanying dike emplacement. *Planetary and Space Science, 41*, 719.

Heim, A. (1932). Bergsturz und menschenleben. Fretz & Wasmuth

Heldmann, J.L., Conley, C.A., Brown, A.J., Fletcher, L., Bishop, J.L., McKay, C.P. (2010). Possible liquid water origin for Atacama Desert mudflow and recent gully deposits on Mars. *Icarus*. 206, 685. doi:10.1016/j.icarus.2009.09.013

Hesse, M. A., & Castillo-Rogez, J. C. (2019). Thermal evolution of the impact-induced cryomagma chamber beneath Occator crater on Ceres. *Geophysical Research Letters, 46*(3), 1213-1221. doi:10.1029/2018GL080327|

Hiesinger, H., Marchi, S., Schmedemann, N., Schenk, P., Pasckert, J., Neesemann, A., et al. (2016). Cratering on Ceres: Implications for its crust and evolution. *Science, 353*(6303).

Hirata, N., Barnouin-Jha, O.S., Honda, C., Nakamura, R., Miyamoto, H., Sasaki, S., Demura, H., Nakamura, A.M., Michikami, T., Gaskell, R.W., Saito, J., (2009). A survey of possible impact structures on 25143 Itokawa. *Icarus*. 200, 486. doi:10.1016/j.icarus.2008.10.027

Hiroi, T., Binzel, R., Sunshine, J., Pieters, C. M., & Takeda, H. (1995). Grain Sizes and Mineral Compositions of Surface Regoliths of Vesta-like Asteroids. *Icarus, 115*(2), 374-386.

Horányi, M., Szalay, J.R., Kempf, S., Schmidt, J., Grün, E., Srama, R., Sternovsky, Z., 2015. A permanent, asymmetric dust cloud around the Moon. *Nature*. 522, 324. doi:10.1038/nature14479

Horstman, K., & Melosh, H. (1989). Drainage pits in cohesionless materials: Implications for the surface of Phobos. *Journal of Geophysical Research: Solid Earth, 94*(B9), 12433-12441.

Hörz, F., & Cintala, M. (1997). The Barringer Award Address presented 1996 July 25, Berlin, Germany: Impact experiments related to the evolution of planetary regoliths. *Meteoritics Planetary Science Journal, 32*(2), 179-209. doi:10.1111/j.1945-5100.1997.tb01259.x|

Hörz, F., Grieve, R. A. F., Heiken, G., Spudis, P., & Binder, A. (1991). Lunar surface processes. In *Lunar source book* (pp. 61-120). New York, USA: Cambridge University Press.

Housen, K. R., & Wilkening, L. L. (1982). Regoliths on Small Bodies in the Solar System. *Annual review of earth planetary science, 10*, 355. doi:10.1146/annurev.ea.10.050182.002035

Howard, K. A., & Wilshire, H. G. (1975). Flows of impact melt at lunar craters. *Journal of research Of U.S. Geological Survey, 3*, 237. https://pubs.usgs.gov/journal/1975/vol3issue2/report.pdf

Hsu, K. J. (1975). Catastrophic debris streams (sturzstroms) generated by rockfalls. *Geological Society of America Bulletin, 86*(1), 129-140. doi:10.1130/0016-7606(1975)86<129:CDSSGB>2.0.CO;2

Hughson, K. H. G., Russell, C. T., Schmidt, B. E., Chilton, H. T., Sizemore, H. G., Schenk, P. M., & Raymond, C. A. (2019). Fluidized Appearing Ejecta on Ceres: Implications for the Mechanical Properties, Frictional Properties, and Composition of its Shallow Subsurface. *Journal of Geophysical Research (Planets), 124*, 1819. https://ui.adsabs.harvard.edu/abs/2019JGRE..124.1819H

Hutchison, R., Alexander, C.M.O., Barber, D.J., (1987). The Semarkona meteorite: first recorded occurrence of smectite in an ordinary chondrite, and its implications. *Geochim. Cosmochim. Acta* 51, 1875–1882. doi:10.1016/0016-7037(87)90178-5

Ivanov, B. A., Neukum, G., & Wagner, R. (2001). Size-frequency distributions of planetary impact craters and asteroids. In M. M.Y. & R. H (Eds.), *Collisional processes in the solar system* (Vol. 161, pp. 1-34). Astrophysics and Space Science Library: Springer, Dordrecht.

Jaeger, H. M., Nagel, S. R., & Behringer, R. P. (1996). Granular solids, liquids, and gases. *Reviews of modern physics, 68*(4), 1259. doi:10.1103/RevModPhys.68.1259

Jaumann, R., Williams, D. A., Buczkowski, D. L., Yingst, R. A., Preusker, F., Hiesinger, H., et al. (2012). Vesta's Shape and Morphology. *Science, 336*(6082), 687-690. doi:10.1126/science.1219122

Jaumann, R., Nass, A., Otto, K., Krohn, K., Stephan, K., McCord, T. B., et al. (2014). The geological nature of dark material on Vesta and implications for the subsurface structure. *Icarus, 240*, 3-19. doi:10.1016/j.icarus.2014.04.035

Jaumann, R., Preusker, F., Krohn, K., von der Gathen, I., Stephan, K., Matz, K.-D., et al. (2017). *Topography and geomorphology of the interior of Occator crater on Ceres.* Paper presented at the Lunar and Planetary Science Conference.

Jin, Z., Bose, M., (2019). New clues to ancient water on Itokawa. *Science Advances*. 5, 8106. doi:10.1126/sciadv.aav8106.

Johnson, B. (1978). Rockslides and Avalanches. 1. Natural Phenomena. *Elsevier Science*, 481-504.

Jozwiak, L. M., Head, J. W., & Wilson, L. (2015). Lunar floor-fractured craters as magmatic intrusions: Geometry, modes of emplacement, associated tectonic and volcanic features, and implications for gravity anomalies. *Icarus, 248*, 424-447.

Jutzi, M., Asphaug, E., Gillet, p., Barrat, J.-A., & Benz, W. (2013). The structure of the asteroid 4 Vesta as revealed by models of planet-scale collisions. *Nature, 494*(7436), 207-210. doi:10.1038/nature11892

Kareev, M. S., Sears, D. W. G., Benoit, P. H., Thompson, J., Jansma, P., & Mattioli, G. (2002). *Laboratory simulation experiments and the ponds on Asteroid 433 Eros.* Paper presented at the Lunar and Planetary Science Conference.

Keller, H. U., Barbieri, C., Koschny, D., Lamy, P., Rickman, H., Rodrigo, R., et al. (2010). E-type asteroid (2867) Steins as imaged by OSIRIS on board Rosetta. *Science, 327*(5962), 190-193. doi:10.1126/science.1179559

King, A., Schofield, P., Howard, K., & Russell, S. (2015a). Modal mineralogy of CI and CI-like chondrites by X-ray diffraction. *Geochimica et Cosmochimica Acta, 165*, 148-160. doi:10.1016/j.gca.2015.05.038

King, A. J., Solomon, J. R., Schofield, P. F., Russell, S. S. J. E., Planets, & Space. (2015b). Characterising the CI and CI-like carbonaceous chondrites using thermogravimetric analysis and infrared spectroscopy. *Earth, Planets & Space, 67*(1), 1-12. doi:10.1186/s40623-015-0370-4

Kleinhans, M. G., Markies, H., De Vet, S. J., & Postema, F. N. (2011). Static and dynamic angles of repose in loose granular materials under reduced gravity. *Journal of Geophysical Research: Planets, 116*(E11). doi:10.1029/2011JE003865|

König, B. (1977). *Investigations of primary and secondary impact structures on the Moon and laboratory experiments to study the ejecta of secondary particles.* AA SCITRAN, Inc (Santa Barbara, CA, USA).

Konopliv, A. S., Asmar, S. W., Park, R. S., Bills, B. G., Centinello, F., Chamberlin, A. B., et al. (2014). The Vesta gravity field, spin pole and rotation period, landmark positions, and ephemeris from the Dawn tracking and optical data. *Icarus, 240*, 103-117. doi:10.1016/j.icarus.2013.09.005

Konopliv, A. S., Park, R. S., Vaughan, A. T., Bills, B. G., Asmar, S. W., Ermakov, A. I., et al. (2018). The Ceres gravity field, spin pole, rotation period and orbit from the Dawn radiometric tracking and optical data. *Icarus, 299*, 411-429. doi:10.1016/j.icarus.2017.08.005

Küppers, M., Pain, C., Kereszturi, A., Hargitai, H. (2014). Regolith. Encyclopedia of planetary landforms, *Springer science*. doi: 10.1007/978-1-4614-9213-9_293-1

Krohn, K., Jaumann, R., Elbeshausen, D., Kneissl, T., Schmedemann, N., Wagner, R., et al. (2014a). Asymmetric craters on Vesta: Impact on sloping surfaces. *103*, 36. doi:10.1016/j.pss.2014.04.011

Krohn, K., Jaumann, R., Otto, K., Hoogenboom, T., Wagner, R., Buczkowski, D. L., et al. (2014b). Mass movement on Vesta at steep scarps and crater rims. *Icarus*, 244, 120-132

Krohn, K., Jaumann, R., Otto, K. A., Schulzeck, F., Neesemann, A., Nass, A., et al. (2017). The unique geomorphology and structural geology of the Haulani crater of dwarf planet Ceres as revealed by geological mapping of equatorial quadrangle Ac-6 Haulani. *Icarus*, 316, 84. https://ui.adsabs.harvard.edu/abs/2018Icar..316...84K.

Krohn, K., von der Gathen, I., Buczkowski, D., Jaumann, R., Wickhusen, K., Schulzeck, F., et al. (2020). Fracture geometry and statistics of Ceres' floor fractures. *Planetary and Space Science, 187*, 104955.

Lebofsky, L. A. (1978). Asteroid 1 Ceres: Evidence for water of hydration. *Monthly Notices of the Royal Astronomical Society, 182*(1), 17P-21P. doi:10.1093/mnras/182.1.17P

Lee, P. (1996). Dust levitation on asteroids. *Icarus, 124*(1), 181-194. doi:10.1006/icar.1996.0197

Legros, F. (2002). The mobility of long-runout landslides. *Engineering Geology, 63*(3-4), 301-331. doi:10.1016/S0013-7952(01)00090-4

Li, J.-Y., Le Corre, L., Schröder, S. E., Reddy, V., Denevi, B. W., Buratti, B. J., et al. (2012). Global photometric properties of asteroid (4) Vesta observed with Dawn framing camera. *Icarus, 226*(2), 1252-1274. doi:10.1016/j.icarus.2013.08.011

Li, J.-Y., McFadden, L. A., Parker, J. W., Young, E. F., Stern, S. A., Thomas, P. C., et al. (2006). Photometric analysis of 1 Ceres and surface mapping from HST observations. *Icarus, 182*(1), 143-160. doi:10.1016/j.icarus.2005.12.012

Liu, S., & Wilson, L. (1998). *Collapse pits due to gas release from shallow dikes on Mars.* Paper presented at the Lunar Planetary Science.

Liu, Z., Yue, Z., Michael, G., Gou, S., Di, K., Sun, S., & Liu, J. (2018). A global database and statistical analyses of (4) Vesta craters. *Icarus, 311*, 242-257. doi:10.1016/j.icarus.2018.04.006

Lucchitta, B. K. (1979). Landslides in Valles Marineris, Mars. *Journal of Geophysical Research, 84*(B14). doi:10.1029/JB084iB14p08097

Lucchitta, B. K. (1987). Valles Marineris, Mars: Wet debris flows and ground ice. *Icarus, 72*(2), 411-429. doi:10.1016/0019-1035(87)90183-7

Lumine, J and Reid, I. (2006). Astrobiology: a multidisciplinary approach. *Physics Today*, 59,58.

Luzzi, E., Rossi, A. P., Massironi, M., Pozzobon, R., Corti, G., Maestrelli, D (2021). Caldera Collapse as the Trigger of Chaos and Fractured Craters on the Moon and Mars. *Geophysical Research Letters*, 48, e2021GL092436. doi:10.1029/2021GL092436

Maina-Gichaba, C., Kipseba, E. K., & Masibo, M. (2013). Overview of landslide occurrences in Kenya: causes, mitigation, and challenges. In *Developments in earth surface processes* (Vol. 16, pp. 293-314): Elsevier.

Marchi, S., Delbo', M., Morbidelli, A., Paolicchi, P., & Lazzarin, M. (2009). Heating of near-Earth objects and meteoroids due to close approaches to the Sun. *Monthly Notices of the Royal Astronomical Society, 400*(1), 147-153. doi:10.1111/j.1365-2966.2009.15459.x

Marchi, S., Bottke, W. F., Cohen, B. A., Wünnemann, K., Kring, D. A., McSween, H. Y., de Sanctis, M. C.,O'Brien, D. P.,Schenk, P., Raymond, C. A., Russell, C. T.. (2013). High-velocity collisions from the lunar cataclysm recorded in asteroidal meteorites. *Nature Geoscience* 6: 411

Marchi, S., Chapman, C.R., Barnouin, O.S., Richardson, J.E., Vincent, J.B., (2015). Cratering on asteroids. In: Michel, P., DeMeo, F.E., Bottke, W.F. (Eds.), *Asteroids IV*. University of Arizona Press, Tucson, pp. 725–744. http://dx.doi.org/10.2458/azu_uapress_9780816532131-ch037

Marchi, S., Ermakov, A. I., Raymond, C. A., Fu, R. R., O'Brien, D. P., Bland, M. T., et al. (2016). The missing large impact craters on Ceres. *Nature Communication, 7*, 12257. doi:10.1038/ncomms12257

Martikainen, J., Penttilä, A., Gritsevich, M., Videen, G., & Muinonen, K. (2019). Absolute spectral modelling of asteroid (4) Vesta. *Monthly Notices of the Royal Astronomical Society, 483*(2), 1952-1956. doi:10.1093/mnras/sty3164

Martin, E. S., & Kattenhorn, S. A. (2013). *Probing Regolith Depths on Enceladus by Exploring a Pit Chain Proxy*. Paper presented at the LPSC.

Martin, E. S. (2016). The distribution and characterization of strike-slip faults on Enceladus. *Geophysical Research Letters, 43*(6), 2456-2464. doi:10.1002/2016GL067805|

Martin, E. S., Kattenhorn, S. A., Collins, G. C., Michaud, R. L., Pappalardo, R. T., & Wyrick, D. Y. (2017). Pit chains on Enceladus signal the recent tectonic dissection of the ancient cratered terrains. *Icarus, 294*, 209. doi:10.1016/j.icarus.2017.03.014

Massironi, M., Marchi, S., Pajola, M., Snodgrass, C., Thomas, N., Tubiana, C., et al. (2012). Geological map and stratigraphy of asteroid 21 Lutetia. *Planetary and Space Science*, 66(1), 125-136.

McCord, T. B., Adams, J. B., & Johnson, T. V. (1970). Asteroid Vesta: Spectral reflectivity and compositional implications. *Sceince, 168*(3938), 1445-1447. doi:10.1126/science.168.3938.1445

McCord, T. B., Li, J.-Y., Combe, J.-P., McSween, H. Y., Jaumann, R., Reddy, V., et al. (2012). Dark material on Vesta from the infall of carbonaceous volatile-rich material. *Nature, 491*, 83-86. doi:10.1038/nature11561

McEwen, A. S. (1989). Mobility of large rock avalanches: Evidence from Valles Marineris, Mars. *Grology, 17*(12), 1111-1114. doi:10.1130/0091-7613(1989)017

McEwen, A. S., & Bierhaus, E. B. (2006). The importance of secondary cratering to age constraints on planetary surfaces. *Annual Review of Earth & Planetary Sciences, 34*, 535-567. doi:10.1146/annurev.earth.34.031405.125018

McFadden, L. A., Tholen, D. J., Veeder, G. J. in *Asteroids II*, Univ. of Arizona Press, Tucson, 1979, pp. 442-467

McKay, D.S., Heiken, G., Basu, A., Blanford, G., Simon, S., Reedy, R., French, B.M. and Papike, J., 1991. The lunar regolith. *Lunar sourcebook, 567*, pp.285-356.

McSween, H. Y., Binzel, R. P., De Sanctis, M. C., Ammannito, E., Prettyman, T. H., Beck, A. W., et al. (2013b). Dawn; the Vesta-HED connection; and the geologic context for eucrites, diogenites, and howardites. *Meteoritics & Planetary Science, 48*(11), 2090-2104. doi:10.1111/maps.12108

McSween, H. Y., Mittlefehldt, D. W., Beck, A. W., Mayne, R. G., & McCoy, T. (2011). HED meteorites and their relationship to the geology of Vesta and the Dawn mission. In *The Dawn mission to minor planets 4 Vesta and 1 Ceres* (pp. 141-174). New York: Springer.

McSween, H. Y., Raymond, C. A., Prettyman, T. H., De Sanctis, M. C., Castillo-Rogez, J. C., & Russell, C. T. (2017). *Geology of Dwarf Planet Ceres and Meteorite Analogs.* Paper presented at the 80th Annual Meeting of the Meteoritical Society.

McSween , H. Y., Raymond, C. A., Stolper, E. M., Mittlefehldt, D. W., Baker, M. B., Lunning, N. G., et al. (2019). Differentiation and magmatic history of Vesta: Constraints from HED meteorites and Dawn spacecraft data. *Journal of Geochemistry, 79*(4), 125526. doi:10.1016/j.chemer.2019.07.008

McSween, H. Y., & Treiman, A. H. (2018a). Martian meteorites. *Planetary materials*, 953-1006. doi:10.1515/9781501508806-021

McSween Jr, H. Y., Emery, J. P., Rivkin, A. S., Toplis, M. J., C. Castillo-Rogez, J., Prettyman, T. H., et al. (2018b). Carbonaceous chondrites as analogs for the composition and alteration of Ceres. *Meteorite & planetary science, 53*(9), 1793-1804. doi:10.1111/maps.12947

Mège, D., & Masson, P. (1996). A plume tectonics model for the Tharsis province, Mars. *Planetary Space Science Reviews, 44*(12), 1499-1546. doi:10.1016/S0032-0633(96)00113-4

Mège, D., & Masson, P. (1997). Graben formation and dike emplacement on Earth and other planets. Paper presented at the Lunar and Planetary Science Conference.

Mège, D. (1999a). Graben morphology, dike emplacement, and tension fracturing in the Tharsis igneous province of Mars. Paper presented at the The Fifth International Conference on Mars.

Mège, D. (1999b). Dikes on Mars:(1) What to look for?(2) A first survey of possible dikes during the Mars Global Surveyor aerobreaking and science phasing orbits. Paper presented at the The Fifth International Conference on Mars.

Mège, D., Lagabrielle, Y., Garel, E., Cormier, M.-H., & Cook, A. (2000). Collapse features and narrow grabens on Mars and Venus: Dike emplacement and deflation of underlying magma chamber. Paper presented at the Lunar and Planetary Science Conference.

Mège, D., Cook, A., Garel, E., Lagabrielle, Y., & Cormier, M.-H. (2002). Surface collapse and volcanic rifting on Mars. Paper presented at the Lunar and Planetary Science Conference.

Mège, D., Cook, A. C., Garel, E., Lagabrielle, Y., & Cormier, M. H. (2003). Volcanic rifting at Martian grabens. *Journal of Geophysical Research: Planets, 108*(E5). doi:10.1029/2002JE001852|

Melosh, H. J. (1979). Acoustic fluidization: A new geologic process? *Journal of Geophysical Research: Solid Earth, 84*(B13), 7513-7520. doi:10.1029/JB084iB13p07513|

Melosh, H. J. (1986). The physics of very large landslides. *Acta Mechanica*, 64(1-2), 89-99

Melosh, H. J. (1989). *Impact cratering: A geologic process*. New York, USA: Oxford: Clarendon Press.

Melosh, H. J., & Ivanov, B. A. (1999). Impact crater collapse. *Annual Review of Earth & Planetary Sciences, 27*(1), 385-415.

Michel, P., DeMeo, F. E., & Bottke, W. F. (2015). Asteroids: recent advances and new perspectives. In *Asteroids IV* (Vol. 1, pp. 1). Tucson, Arizona, USA: University of Arizona press.

Miyamoto, H., 2014. Unconsolidated boulders on the surface of Itokawa. *Planetary and Space Science*. 95, 94. https://doi.org/10.1016/j.pss.2013.06.016.

Molaro, J., & Byrne, S. (2012). Rates of temperature change of airless landscapes and implications for thermal stress weathering. *Journal of Geophysical Research: Planets, 117*(E10).

Montési, L. G. J. (1999). *Concentric dike swarm and internal structure of Pavonis Mons (Mars).* Paper presented at the Lunar and Planetary Science Conference.

Moore, J. M., Asphaug, E., Morrison, D., Spencer, J. R., Chapman, C. R., Bierhaus, B., et al. (1999). Mass movement and landform degradation on the icy Galilean satellites: Results of the Galileo nominal mission. *Icarus, 140*(2), 294-312. doi:10.1006/icar.1999.6132

Moore, S. R., Franzen, M., Benoit, P. H., Sears, D. W. G., Holley, A., Meyer, M., et al. (2003). The origin of chondrites: Metal-silicate separation experiments under microgravity conditions-II. *Geophysical Research Letters, 30*(10). doi:10.1029/2002GL016860|

Morbidelli, A., Bottke, W. F., Jr., Froeschlé, C., & Michel, P. (2002). Origin and Evolution of Near-Earth Objects. In *Asteroids III* (pp. 409). Tucson, Arizona, USA: University of Arizona press.

Mousis, O., & Alibert, Y. (2005). On the composition of ices incorporated in Ceres. *Monthly Notices of the Royal Astronomical Society, 358*(1), 188-192. doi:10.1111/j.1365-2966.2005.08777.x

Mousis, O., Alibert, Y., Hestroffer, D., Marboeuf, U., Dumas, C., Carry, B., et al. (2008). Origin of volatiles in the main belt. *Monthly Notices of the Royal Astronomical Society, 383*(3), 1269-1280. doi:10.1111/j.1365-2966.2007.12653.x

Murdoch, N., Rozitis, B., Nordstrom, K., Green, S., Michel, P., de Lophem, T. L., & Losert, W. (2013c). Granular Convection in Microgravity. *Asteroids, Comets, Meteors, 1667*, 6278. doi:10.1103/PhysRevLett.110.018307

Murdoch, N., Sánchez, P., Schwartz, S. R., & Miyamoto, H. (2015). Asteroid Surface Geophysics. In *Asteroid IV* (pp. 767-792).

Nahm, A. L., & Kattenhorn, S. A. (2015). A unified nomenclature for tectonic structures on the surface of Enceladus. *258*, 67. https://ui.adsabs.harvard.edu/abs/2015Icar..258...67N

Nathues, A., Platz, T., Thangjam, G., Hoffmann, M., Mengel, K., Cloutis, E., et al. (2017). Evolution of Occator crater on (1) Ceres. *The Astrophysical Journal, 153*(3), 112.

Nathues, A., H. Sierks, P. Gutierrez-Marques, S. Schroeder, T. Maue, I. Buettner, M. Richards, U. Chistensen, U. Keller, DAWN FC2 CALIBRATED VESTA IMAGES V1.0, DAWN-A-FC2-3-RDR-VESTA-IMAGES-V1.0, NASA Planetary Data System, : https://sbn.psi.edu/pds/resource/dawn/dwnvfcL1.html 2011

Nathues, A., Schmedemann, N., Thangjam, G., Pasckert, J., Mengel, K., Castillo-Rogez, J., et al. (2020). Recent cryovolcanic activity at Occator crater on Ceres. *Nature, 4*(8), 794-801.

Neesemann, A., Van Gasselt, S., Schmedemann, N., Marchi, S., Walter, S., Preusker, F., et al. (2018). The various ages of Occator crater, Ceres: results of a comprehensive synthesis approach. *Icarus, 320*, 60-82.

Neish, C. D., Madden, J., Carter, L., Hawke, B., Giguere, T., Bray, V., et al. (2014). Global distribution of lunar impact melt flows. *Icarus, 239*, 105-117. doi:10.1016/j.icarus.2014.05.049

Neukum, G. (1971). *Untersuchungen über Einschlagskrater auf dem Mond.*

Neukum, G. (1977). Lunar cratering. *Royal Society of London Philosophical Transactions Seris A, 285*(1327), 267-272. doi:10.1098/rsta.1977.0064

Neukum, G. (1983). *Meteoritenbombardement und datierung planetarer oberflachen.* Ludwig-Maximilians-Univ., Munich, Germany.

Neukum, G., Ivanov, B. A., & Hartmann, W. K. (2001a). Cratering records in the inner solar system in relation to the lunar reference system. In *Chornology & evolution of Mars* (Vol. 12, pp. 55-86): Springer, Dordrecht.

Neukum, G., König, B., & Arkani-Hamed, J. (1975). A study of lunar impact crater size-distributions. *The moon, 12*(2), 201-229. doi:10.1007/BF00577878

Neukum, G., & Wise, D. U. (1976). Mars- A standard crater curve and possible new time scale. *Sceince, 194*(4272), 1381-1387.

Noguchi, T., Nakamura, T., Kimura, M., Zolensky, M., Tanaka, M., Hashimoto, T., et al. (2011). Incipient space weathering observed on the surface of Itokawa dust particles. *Science, 333*(6046), 1121-1125. doi:10.1126/science.1207794

O'Brien, D.P., Sykes, M.V., (2011). The origin and evolution of the asteroid belt—Implications for Vesta and Ceres. *Space Science Reviews*. 163, 41-61. doi:10.1007/s11214-011-9808-6

O'Brien, D. P., Marchi, S., Schenk, P., Russell, C., & Raymond, C. (2014). *The impact history of Vesta: Developing and testing an absolute cratering chronology.* Paper presented at the Lunar and Planetary Science Conference.

Öpik, E. J. (1960). The lunar surface as an impact counter. *Monthly Notices of the Royal Astronomical Society, 120*(5), 404-411.

Osinski, G.R., Pierazzo, E., (2013). Impact cratering: Processes and products. In: Osinski, G.R., Pierazzo, E. (Eds.), *Impact Cratering: Processes and Products*. Wiley-Blackwell, pp. 1–20.

Osinski, G. R., Tornabene, L. L., & Grieve, R. A. (2011). Impact ejecta emplacement on terrestrial planets. *Earth Planetary Science Letters, 310*(3-4), 167-181.

Otto, K., Jaumann, R., Krohn, K., Matz, K.-D., Preusker, F., Roatsch, T., et al. (2013). Mass-wasting features and processes in Vesta's south polar basin Rheasilvia. *Journal of Geophysical Research: Planets, 118*(11), 2279-2294. doi:10.1002/2013je004333

Otto, K., Jaumann, R., Krohn, K., Spahn, F., Raymond, C. A., & Russell, C. T. (2016). The Coriolis effect on mass wasting during the Rheasilvia impact on asteroid Vesta. *Geophysical Research Letters*, 43(24), 12,340-312,347.

Otto, K., Marchi, S., Trowbridge, A., Melosh, H. J., & Sizemore, H. G. (2019). Ceres Crater Degradation Inferred From Concentric Fracturing. *Journal of Geophysical Research (Planets), 124*, 1188. https://ui.adsabs.harvard.edu/abs/2019JGRE..124.1188O

Palomba, E., Longobardo, A., De Sanctis, M. C., Stein, N. T., Ehlmann, B., Galiano, A., et al. (2019). Compositional differences among Bright Spots on the Ceres surface. *Icarus, 320*, 202-212. doi:10.1016/j.icarus.2017.09.020

Parekh, R., Vijayan, S., Sivaramann, B., (2016). Landslide Phenomena on Saturn's Icy Moon: Rhea. Enceladus and the Icy Moons of Saturn, 3055.

Parekh, R., Otto, K. A., Jaumann, R., Matz, K. D., Roatsch, T., Kersten, E., et al. (2021a). Influence of volatiles on mass wasting processes on Vesta and Ceres. *Journal of Geophysical Research: Planets, 126*(3), e2020JE006573. doi:10.1029/2020JE006573.

Parekh, R., Otto, K., A., Matz, K. D., Jaumann, R., Krohn, K., Roatsch, t., Kertsten, E., Elgner, S. Russell, C.T. , Raymond, C., A., (2021b). Formation of ejecta and dust pond deposits on asteroid Vesta. . *Journal of Geophysical Research: Planets*. doi: 10.1029/2021JE006873.

Park, R., Konopliv, A., Bills, B., Rambaux, N., Castillo-Rogez, J., Raymond, C., et al. (2016). A partially differentiated interior for (1) Ceres deduced from its gravity field and shape. *Nature, 537*(7621), 515-517

Park, R. S., Konopliv, A., Bills, B., Castillo-Rogez, J., Asmar, S., Rambaux, N., et al. (2016a). *Gravity science investigation of Ceres from Dawn.* Paper presented at the EGU General Assembly Conference Abstracts.

Park, R. S., Konopliv, A. S., Ermakov, A. I., Castillo-Rogez, J. C., Fu, R., Hughson, K. H. G., et al. (2020). Evidence of non-uniform crust of Ceres from Dawn's high-resolution gravity data. *Nature Astronomy, 4*(8), 748-755. doi:10.1038/s41550-020-1019-1

Pieters, C. M., Ammannito, E., Blewett, D. T., Denevi, B. W., De Sanctis, M. C., Gaffey, M. J., et al. (2012). Distinctive space weathering on Vesta from regolith mixing processes. *Nature, 491*(7422), 79-82. doi:10.1038/nature11534

Pierazzo, E., Melosh, H.J., (2000). Melt Production in Oblique Impacts. *Icarus*. 145, 252. doi:10.1006/icar.1999.6332

Plescia, J. B., & Cintala, M. J. (2012). Impact melt in small lunar highland craters. *117*(E12). doi:https://doi.org/10.1029/2011JE003941

Prettyman, T. H., Feldman, W. C., McSween, H. Y., Dingler, R. D., Enemark, D. C., Patrick, D. E., et al. (2011). Dawn's gamma ray and neutron detector. In R. C. T. & R. C. A. (Eds.), *The Dawn Mission to Minor Planets 4 Vesta and 1 Ceres* (pp. 371-459).

Prettyman, T. H., Mittlefehldt, D. W., Yamashita, N., Lawrence, D. J., Beck, A. W., Feldman, W. C., et al. (2012). Elemental mapping by Dawn reveals exogenic H in Vesta's regolith. *Sceince, 338*(6104), 242-246. doi:10.1126/science.1225354

Prettyman, T. H., Mittlefehldt, D. W., Yamashita, N., Beck, A. W., Feldman, W. C., Hendricks, J. S., et al. (2013). Neutron absorption constraints on the composition of 4 Vesta. *Meteoritics and Planetary Science*, 48, 2211. https://ui.adsabs.harvard.edu/abs/2013M&PS...48.2211P

Prettyman, T. H., Yamashita, N., Toplis, M. J., McSween, H. Y., Schörghofer, N., Marchi, S., et al. (2017). Extensive water ice within Ceres' aqueously altered regolith: Evidence from nuclear spectroscopy. *Science, 355*(6320), 55-59. doi:10.1126/science.aah6765 %J Science

Prettyman, T. H., Yamashita, N., Ammannito, E., Ehlmann, B. L., McSween, H. Y., Mittlefehldt, D. W., et al. (2019b). Elemental composition and mineralogy of Vesta and Ceres: Distribution and origins of hydrogen-bearing species. *Icarus, 318*, 42-55. doi:10.1016/j.icarus.2018.04.032

Prettyman, T. H., Yamashita, N., Landis, M., Castillo-Rogez, J., Ehlmann, B., Mcsween, H., et al. (2019a). *DAWN'S GRAND FINALE: HIGH SPATIAL-RESOLUTION ELEMENTAL MEASUREMENTS REVEAL AN ANOMALY AT OCCATOR CRATER. T.* Paper presented at the Lunar and Planetary Science Conference.

Prettyman, T. H., Yamashita, N., Landis, M. E., Castillo-Rogez, J. C., Schörghofer, N., Pieters, C. M., et al. (2021). Replenishment of Near-Surface Water Ice by Impacts Into Ceres' Volatile-Rich Crust: Observations by Dawn's Gamma Ray and Neutron Detector. *Geophysical Research Letters, 48*(15), e2021GL094223. doi:10.1029/2021GL094223

Preusker, F., Scholten, F., Matz, K.-D., Roatsch, T., Jaumann, R., Raymond, C. A., & Russell, C. T. (2012). *Topography of Vesta from Dawn FC stereo images*. Lunar & Planetary Science conference, Houston.

Preusker, F., Scholten, F., Matz, K.-D., Elgner, S., Jaumann, R., Roatsch, T., et al. (2016). *Dawn at Ceres — Shape Model and Rotational State*. Paper presented at the Lunar and Planetary Science Conference. https://ui.adsabs.harvard.edu/abs/2016LPI....47.1954P

Prockter, L., Thomas, P., Robinson, M., Joseph, J., Milne, A., Bussey, B., et al. (2002). Surface expressions of structural features on Eros. *Icarus, 155*(1), 75-93.

Quantin, C., Allemand, P., & Delacourt, C. (2004). Morphology and geometry of Valles Marineris landslides. *Planetary and Space Science*, 52(11), 1011-1022.

Quick, L. C., Buczkowski, D. L., Ruesch, O., Scully, J. E., Castillo-Rogez, J., Raymond, C. A., et al. (2019). A possible brine reservoir beneath Occator crater: thermal and compositional evolution and formation of the Cerealia dome and Vinalia Faculae. *Icarus, 320*, 119-135.

Rabinowitz, D., Bowell, E., Shoemaker, E., & Muinonen, K. (1994). The population of Earth-crossing asteroids. *Hazards due to Comets, 285*, 312.

Raymond, C. A., Jaumann, R., Nathues, A., Sierks, H., Roatsch, T., Preusker, F., et al. (2011). The Dawn topography investigation. In C. T. Russel & C. A. Raymond (Eds.), *The Dawn Mission to Minor Planets 4 Vesta and 1 Ceres* (pp. 487-510). New York, USA: Springer.

Raymond, C. A., Park, R. S., Konopliv, A. S., Asmar, S. W., Jaumann, R., McSween, H. Y., et al. (2014a). *Geophysical constraints on the structure and evolution of Vestas crust and mantle.* Paper presented at the LPSC.

Raymond, C. A., Ermakov, A., Castillo-Rogez, J. C., Marchi, S., Johnson, B. C., Hesse, M. A., et al. (2020). Impact-driven mobilization of deep crustal brines on dwarf planet Ceres. *Nature Astronomy, 4*(8), 741-747.

Reddy, V., Nathues, A., Le Corre, L., Sierks, H., Li, J. Y., Gaskell, R., et al. (2012a). Color and albedo heterogeneity of Vesta from Dawn. *Science, 336*(6082), 700-704. doi:10.1126/science.1219088

Reddy, V., Le Corre, L., O'Brien, D. P., Nathues, A., Cloutis, E. A., Durda, D. D., et al. (2012b). Delivery of dark material to Vesta via carbonaceous chondritic impacts. *Icarus, 221*(2), 544-559. doi:10.1016/j.icarus.2012.08.011

Richardson, J. E., Melosh, H. J., Greenberg, R. J., & O'Brien, D. P. (2005). The global effects of impact-induced seismic activity on fractured asteroid surface morphology. *Icarus, 179*, 325. doi:10.1016/j.icarus.2005.07.005

Richardson, J.E., Kedar, S., (2013). An experimental investigation of the seismic signal produced by hypervelocity impacts. In: *Lunar and Planetary Science Conference*, Vol. 44. p. 2863

Richardson, J. E., Steckloff, J. K., & Minton, D. A. (2020). Impact-produced seismic shaking and regolith growth on asteroids 433 Eros, 2867 Šteins, and 25143 Itokawa. *Icarus, 347*, 113811. doi:10.1016/j.icarus.2020.113811

Ritter, D.F., Kochel, C.R., Miller, J.R., 2006. Process Geomorphology, fourth edition. Waveland Press, Long Grove, pp. 79–133

Rivkin, A. S., Volquardsen, E. L., & Clark, B. E. (2006). The surface composition of Ceres: Discovery of carbonates and iron-rich clays. *Icarus, 185*(2), 563-567. doi:10.1016/j.icarus.2006.08.022

Rivkin, A. S., Li, J.-Y., Milliken, R. E., Lim, L. F., Lovell, A. J., Schmidt, B. E., et al. (2011). The surface composition of Ceres. In *The Dawn Mission to Minor Planets 4 Vesta 1 Ceres* (pp. 95-116). New York: Springer.

Rivkin, A. S. (2012). The fraction of hydrated C-complex asteroids in the asteroid belt from SDSS data. *Icarus, 221*(2), 744-752. doi:10.1016/j.icarus.2012.08.042

Rivkin, A. S., Campins, H., Emery, J. P., Howell, E. S., Licandro, J., Takir, D., & Vilas, F. (2015). Astronomical observations of volatiles on asteroids. In *Asteroids IV* (pp. 65-87). Tucson, Arizona, USa: Univeristy of Arizona press.

Roatsch, T., Kersten, E., Matz, K.-D., Preusker, F., Scholten, F., Jaumann, R., et al. (2012). High resolution Vesta high altitude mapping orbit (HAMO) atlas derived from Dawn Framing Camera images. *Planetary Space Science Reviews, 73*(1), 283-286. doi:10.1016/j.pss.2012.08.021

Roatsch, T., Kersten, E., Matz, K.-D., Preusker, F., Scholten, F., Elgner, S., et al. (2013). High-resolution Vesta Low Altitude Mapping Orbit Atlas derived from Dawn Framing Camera images. *Planetary and Space Science, 85*, 293. doi:10.1016/j.pss.2013.06.024

Roatsch, T., Kersten, E., Matz, K.-D., Preusker, F., Scholten, F., Jaumann, R., et al. (2015). "Ceres Survey Atlas derived from Dawn Framing Camera images." Planetary and Space Science 121: 115-120.

Roatsch, T., Kersten, E., Matz, K. D., Preusker, F., Scholten, F., Jaumann, R., et al. (2016). Ceres Survey Atlas derived from Dawn Framing Camera images. Planetary and Space Science, 121, 115-120.

Roatsch, T., Kersten, E., Matz, K.-D., Preusker, F., Scholten, F., Elgner, S., et al. (2016a). Dawn FC2 Derived Ceres HAMO DTM SPG V1.0. *NASA Planetary Data System*, DAWN-A-FC2-5-CERESHAMODTMSPG-V1.0. https://ui.adsabs.harvard.edu/abs/2016PDSS..266.....R

Roatsch, T., Kersten, E., Matz, K.-D., Preusker, F., Scholten, F., Jaumann, R., et al. (2017). High-resolution Ceres Low Altitude Mapping Orbit Atlas derived from Dawn Framing Camera images. *Planetary and Space Science, 140*, 74. https://ui.adsabs.harvard.edu/abs/2017P&SS..140...74R

Roberts, J. H., Kahn, E. G., Barnouin, O. S., Ernst, C. M., Prockter, L. M., & Gaskell, R. W. (2014). Origin and flatness of ponds on asteroid 433 Eros. *Meteoritics and planetary science, 49*, 1735. doi:10.1111/maps.12348

Roberts, J., Roberts Eros Ponds Catalog V1.1. urn:nasa:pds:ast-eros.roberts.ponds-catalog::1.1. NASA Planetary Data System, 2021; doi: 10.26033/4dqc-8067

Robinson, M. S., Thomas, P. C., Veverka, J., Murchie, S., & Carcich, B. (2001). The nature of ponded deposits on Eros. *Nature, 413*, 396. doi:10.1038/35096518

Robinson M., B.T. Carcich, NEAR MSI DIM EROS GLOBAL BASEMAPS V1.0, NEAR-A-MSI-5-DIM-EROS/ORBIT-V1.0, NASA Planetary Data System, https://arcnav.psi.edu/urn:nasa:pds:context:target:asteroid.433_eros/data, 2001.

Robinson, M. S., Thomas, P. C., Veverka, J., Murchie, S. L., & Wilcox, B. B. (2002). The geology of 433 Eros. *Meteoritics & Planetary Sciences, 37*(12), 1651-1684. doi:10.1111/j.1945-5100.2002.tb01157.x

Ruesch, O., Hiesinger, H., Williams, D., Nathues, A., Prettyman, T., Tosi, F., et al. (2014a). *Marcia Crater, Vesta: Geology, Mineralogy, Composition and thermal Properties.* Paper presented at the Lunar and planetary science conference.

Ruesch, O., Hiesinger, H., Blewett, D. T., Williams, D. A., Buczkowski, D., Scully, J. E., et al. (2014b). Geologic map of the northern hemisphere of Vesta based on Dawn Framing Camera (FC) images. *Icarus, 244*, 41-59. doi:10.1016/j.icarus.2014.01.035

Ruesch, O., Platz, T., Schenk, P., McFadden, L., Castillo-Rogez, J., Quick, L., et al. (2016). *Cryovolcanism on ceres*. Paper presented at the Lunar and Planetary Science, Houston, USA.

Russell, C. T., Coradini, A., Christensen, U., De Sanctis, M. C., Feldman, W. C., Jaumann, R., et al. (2004). Dawn: A journey in space and time. *Planetary and Space Science, 52*, 465. https://ui.adsabs.harvard.edu/abs/2004P&SS...52..465R

Russell, C. T., Raymond, C., Fraschetti, T., Rayman, M., Polanskey, C., Schimmels, K., & Joy, S. (2005). Dawn mission and operations. *Proceedings of the International Astronomical Union, 1*(S229), 97-119. doi:10.1017/S1743921305006691

Russell, C. T., & Raymond, C. A. (2011). The Dawn Mission to Vesta and Ceres. *Space Science Reviews, 163*, 3. https://ui.adsabs.harvard.edu/abs/2011SSRv..163....3R

Russell, C. T., Raymond, C. A., Coradini, A., McSween, H. Y., Zuber, M. T., Nathues, A., et al. (2012). Dawn at Vesta: Testing the Protoplanetary Paradigm. *Science, 336*, 684. doi:10.1126/science.1219381

Russell, C. T., Raymond, C. A., Jaumann, R., McSween, H. Y., De Sanctis, M., Nathues, A., et al. (2013). Dawn completes its mission at 4 Vesta. *Meteoritics Planetary Science Journal, 48*(11), 2076-2089. doi:doi.org/10.1111/maps.12091

Russell, C. T., Raymond, C. A., Ammannito, E., Buczkowski, D. L., De Sanctis, M. C., Hiesinger, H., et al. (2016). Dawn arrives at Ceres: Exploration of a small, volatile-rich world. *Science, 353*(6303), 1008-1010. doi:10.1126/science.aaf4219

Saito, J., Miyamoto, H., Nakamura, R., Ishiguro, M., Michikami, T., Nakamura, A. M., et al. (2006). Detailed Images of Asteroid 25143 Itokawa from Hayabusa. *312*, 1341. doi:10.1126/science.1125722

Savage, R., Palafox, L., Morris, C.T., Rodriguez, J.J., Barnard, K., Byrne, S.,Hamilton, C., (2018). A Bayesian Approach to Subkilometer Crater Shape Analysis Using Individual HiRISE Images. *IEEE Transactions on Geoscience*. 56, 1-11. doi: 10.1109/tgrs.2018.2825608

Sarafian, A. R., Roden, M. F., & Patiño-Douce, A. E. (2013). The volatile content of Vesta: Clues from apatite in eucrites. *Meteoritics Planetary Science Journal, 48*(11), 2135-2154. doi:10.1111/maps.12124

SBAG (2020), Goals and Objectives for the Exploration and Investigation of the Solar System's Small Bodies. ver. 2.0.2020, 44 p., at http://www.lpi.usra.edu/sbag/goals/

Scaioni, M., Yordanov, V., Brunetti, M. T., Melis, M. T., Zinzi, A., Kang, Z., & Giommi, P. (2017). Recognition of landslides in lunar impact craters. European Journal of Remote Sensing, 51(1), 47-61.

Schenk, P., O'Brien, D. P., Marchi, S., Gaskell, R., Preusker, F., Roatsch, T., et al. (2012). The Geologically Recent Giant Impact Basins at Vesta's South Pole. *Science, 336*, 694. https://ui.adsabs.harvard.edu/abs/2012Sci...336..694S

Schenk, P., Sizemore, H., Schmidt, B., Castillo-Rogez, J., De Sanctis, M. C., Bowling, T., et al. (2018). The central pit and dome at Cerealia Facula bright deposit and floor deposits in Occator crater, Ceres: morphology, comparisons and formation. *Icarus, 320*, 159-187. doi:10.1016/j.icarus.2018.08.010

Schenk, P., Scully, J., Buczkowski, D., Sizemore, H., Schmidt, B., Pieters, C., et al. (2020). Impact heat driven volatile redistribution at Occator crater on Ceres as a comparative planetary process. *Nature Communication, 11*, 3679. https://ui.adsabs.harvard.edu/abs/2020NatCo..11.3679S

Schenk, P., Singer, K., Beyer, R., Beddingfield, C., Robbins, S. J., McKinnon, W. B., et al. (2021). Origins of pits and troughs and degradation on a small primitive planetesimal in the Kuiper Belt: high-resolution topography of (486958) Arrokoth (aka 2014 MU69) from New Horizons. *Icarus, 356*, 113834.

Schmedemann, N., Kneissl, T., Ivanov, B., Michael, G., Wagner, R., Neukum, G., et al. (2014). The cratering record, chronology and surface ages of (4) Vesta in comparison to smaller asteroids and the ages of HED meteorites. *Planetary Space Science Reviews, 103*, 104-130. doi:10.1016/j.pss.2014.04.004

Schmedemann, N., Michael, G., Ivanov, B., Kneissl, T., Neesemann, A., Hiesinger, H., et al. (2015). A preliminary chronology for Ceres.

Schmedemann, N., Kneissl, T., Neesemann, A., Stephan, K., Jaumann, R., Krohn, K., et al. (2016). Timing of optical maturation of recently exposed material on Ceres. *Geophysical Research Letters, 43*, 11,987. doi:10.1002/2016gl071143

Schmidt, B. E., Hughson, K. H. G., Chilton, H. T., Scully, J. E. C., Platz, T., Nathues, A., et al. (2017). Geomorphological evidence for ground ice on dwarf planet Ceres. *Nature Geoscience, 10*(5), 338-343. doi:10.1038/ngeo2936

Schmidt, B., Sizemore, H., Hughson, K., Duarte, K., Romero, V., Scully, J., et al. (2020). Post-impact cryo-hydrologic formation of small mounds and hills in Ceres's Occator crater. *Nature Geoscience, 13*(9), 605-610.

Schörghofer, N. (2008). The Lifetime of Ice on Main Belt Asteroids. *The Asterophysical Journal*, 682, 697. https://ui.adsabs.harvard.edu/abs/2008ApJ...682..697S.

Schörghofer, N. (2016a). Predictions of depth-to-ice on asteroids based on an asynchronous model of temperature, impact stirring, and ice loss. *Icarus*, 276, 88. doi:10.1016/j.icarus.2016.04.037

Schörghofer, N., Mazarico, E., Platz, T., Preusker, F., Schröder, S. E., Raymond, C. A., & Russell, C. T. (2016b). The permanently shadowed regions of dwarf planet Ceres. *Geophysical Research Letters, 43*, 6783. doi:10.1002/2016gl069368

Schröder, S. E., Mottola, S., Keller, H. U., Raymond, C. A., & Russell, C. T. (2014). Reprint: Resolved photometry of Vesta reveals physical properties of crater regolith. *Planetary and Space Science, 85*, 198-213. doi:10.1016/j.pss.2013.06.009

Schröder, S. E., Carsenty, U., Hauber, E., Raymond, C. A., & Russell, C. T. (2021). The brittle boulders of dwarf planet Ceres. *Planetary Science Journal, 2*(3), 111

Schultz, P.H. (1976). Floor-fractured lunar craters. The Moon 15, 241–273.

Scott, E. D., & Wilson, L. (2002). Plinian eruptions and passive collapse events as mechanisms of formation for Martian pit chain craters. *Journal of Geophysical Research: Planets, 107*(E4), 4-1-4-11. doi:10.1029/2000JE001432|

Scott, E. D., Wilson, L., & Head III, J. (2000). *Martian plinian eruptions and pit chain craters.* Paper presented at the Lunar and Planetary Science Conference.

Scully, J. E. C., Russell, C. T., Yin, A., Jaumann, R., Carey, E., Castillo-Rogez, J., et al. (2015). Geomorphological evidence for transient water flow on Vesta. *Earth and Planetary Science Letters, 411*, 151-163. doi:10.1016/j.epsl.2014.12.004

Scully, J. E. C., Buczkowski, D. L., Schmedemann, N., Raymond, C. A., Castillo-Rogez, J. C., King, S. D., et al. (2017). Evidence for the Interior Evolution of Ceres from Geologic Analysis of Fractures. *Geophys Research Letters, 44*, 9564. doi:10.1002/2017gl075086

Scully, J. E. C., Schenk, P., Castillo-Rogez, J., Buczkowski, D., Williams, D., Pasckert, J., et al. (2020). The varied sources of faculae-forming brines in Ceres' Occator crater emplaced via hydrothermal brine effusion. *Nature, 11*(1), 1-11.

Scully, J.E.C., Poston, M., Carey, E., Baker, S., Castillo-Rogez, J., Raymond, C., (2021). Testing the hypothesis that curvilinear gullies, lobate deposits and pitted terrain on Vesta and ceres were formed

by short-lived, debris-flow-like processes. *LPSC 2021*. 2548. https://www.hou.usra.edu/meetings/lpsc2021/pdf/1252.pdf

Sears, D. W. G., Tornabene, L. L., Osinski, G. R., Hughes, S. S., & Heldmann, J. L. (2015). Formation of the "ponds" on asteroid (433) Eros by fluidization. *Planetary and Space Science, 117*, 106. doi:10.1016/j.pss.2015.05.011

Shingareva, T. V., & Kuzmin, R. O. (2001). Mass-Wasting Processes on the Surface of Phobos. *Solar System Research*, 35, 431. https://ui.adsabs.harvard.edu/abs/2001SoSyR..35..431S

Shoemaker, E. M. (1961). Interplanetary correlation of geologic time. *AAPG Bulletin, 45*(1), 130-130.

Shoemaker, E. M., Batson, R. M., Holt, H. E., Morris, E. C., Rennilson, J. J., & Whitaker, E. A. (1968). *Television observations from Surveyor VII*.

Shoemaker, E. M., Batson, R. M., Bean, A. L., Conrad, J. C., Dahlem, D. H., Goddard, E. N., et al. (1970a). *Preliminary geologie investigation of the Apollo 12 landing site, part A*.

Shoemaker, E. M., Hait, M. H., Swann, G. A., Schleicher, D. L., Schaber, G. G., Sutton, R. L., et al. (1970b). Origin of the lunar regolith at Tranquillity Base. *Science, 1*, 2399. doi:10.1126/science.167.3918.452

Shoemaker, E S, Hait, M H (1971) The Bombardment of the Lunar Maria. *Lunar & Planetary Science Conference 2*:11, Houston

Shreve, R. L. (1966). Sherman landslide, Alaska. *Science, 154*(3757), 1639-1643.

Shreve, R. L. (1968). *The blackhawk landslide* (Vol. 108): Geological Society of America.

Siebert, L. (1984). Large volcanic debris avalanches: characteristics of source areas, deposits, and associated eruptions. *Journal of volcanology geothermal research, 22*(3-4), 163-197. doi:10.1016/0377-0273(84)90002-7

Sierks, H., Keller, H. U., Jaumann, R., Michalik, H., Behnke, T., Bubenhagen, F., et al. (2011). The Dawn Framing Camera. *Space Science Reviews, 163*, 263. doi:10.1007/s11214-011-9745-4

Sims, D. W., Morris, A. P., Ferrill, D. A., Wyrick, D. Y., & Colton, S. L. (2003). *Physical models of pit chain formation over dilational faults on Mars.* Paper presented at the Lunar and Planetary Science Conference.

Singer, K. N., McKinnon, W. B., Schenk, P. M., & Moore, J. M. (2012). Massive ice avalanches on Iapetus mobilized by friction reduction during flash heating. *Nature Geoscience, 5*(8), 574-578. doi:10.1038/ngeo1526

Sizemore, H., Platz, T., Schorghofer, N., Prettyman, T. H., De Sanctis, M. C., Crown, D. A., et al. (2017). Pitted terrains on (1) Ceres and implications for shallow subsurface volatile distribution. *Geophysical Research Letters, 44*(13), 6570-6578. doi:10.1002/2017gl073970

Sizemore, H., Schmidt, B. E., Buczkowski, D. A., Sori, M. M., Castillo-Rogez, J. C., Berman, D. C., et al. (2019). A Global Inventory of Ice-Related Morphological Features on Dwarf Planet Ceres: Implications for the Evolution and Current State of the Cryosphere. *Journal of Geophysical Research: Planets, 124*(7), 1650-1689. doi:10.1029/2018je005699

Sizemore, H., Schmidt, B. E., & Castillo-Rogez, J. (2019a). Introduction to the Special Issue: Ice on Ceres. *Journal of Geophysical Research: Planets*, 124(7), 1639-1649.

Snyder, J. P. (1987). *Map projections--A working manual* (0318235625).

Soderblom, L. A., Condit, C. D., West, R. A., Herman, B. M., & Kreidler, T. J. (1974). Martian planetwide crater distributions: Implications for geologic history and surface processes. *Icarus, 22*(3), 239-263. doi:10.1016/0019-1035(74)90175-4

Solomon, S. C., Smrekar, S. E., Bindschadler, D. L., Grimm, R. E., Kaula, W. M., McGill, G. E., et al. (1992). Venus tectonics: An overview of Magellan observations. *Journal of Geophysical Research: Planets, 97*(E8), 13199-13255. doi:10.1029/92JE01418|

Sori, M. M., Byrne, S., Bland, M. T., Bramson, A. M., Ermakov, A. I., Hamilton, C. W., et al. (2017). The vanishing cryovolcanoes of Ceres. *Geophysical Research Letters, 44*(3), 1243-1250. doi:10.1002/2016GL072319|

Sori, M. M., Sizemore, H. G., Byrne, S., Bramson, A. M., Bland, M. T., Stein, N. T., & Russell, C. T. (2018). Author Correction: Cryovolcanic rates on Ceres revealed by topography. *Nature Astronomy*, 2, 995

Sorter, S., (2007). Are Planetary Systems Filled to Capacity? *American Scientist. 95(5)*,414. doi: 10.1511/2007.67.414

Spencer, J. R., & Fanale, F. P. (1990). New models for the origin of Valles Marineris closed depressions. *Journal of Geophysical Research: Solid Earth, 95*(B9), 14301-14313. doi:10.1029/JB095iB09p14301|

Stephan, K., Jaumann, R., & Wagner, R. (2013). Geology of icy bodies. In M. Gudipathi & J. C. Castillo-Rogez (Eds.), *The Science of Solar System Ices* (pp. 279-367): Springer Science & Business Media.

Stöffler, D. (1971). Progressive metamorphism and classification of shocked and brecciated crystalline rocks at impact craters. *Journal of Geophysical Research, 76*(23), 5541-5551. doi:10.1029/JB076i023p05541

Stooke. P., Stooke Small Bodies Maps V3.0. MULTI-SA-MULTI-6-STOOKEMAPS-V3.0. NASA Planetary Data System, https://sbn.psi.edu/pds/resource/stookemaps.html, 2015.

Stopar, J., Hawke, B., Robinson, M., Denevi, B., Giguere, T., (2012). Distribution, Occurrence, and Degradation of Impact Melt Associated with Small Lunar Craters, *Lunar and Planetary Science Conference*, p. 1645. Available at: https://www.lpi.usra.edu/meetings/lpsc2012/pdf/1645.pdf

Stopar, J. D., Hawke, B. R., Robinson, M. S., Denevi, B. W., Giguere, T. A., & Koeber, S. D. (2014). Occurrence and mechanisms of impact melt emplacement at small lunar craters. *Icarus, 243*, 337. doi:10.1016/j.icarus.2014.08.011

Su, K. Y., Rieke, G. H., Malhotra, R., Stapelfeldt, K. R., Hughes, A. M., Bonsor, A., et al. (2013). Asteroid belts in debris disk twins: Vega and Fomalhaut. *The Astrophysical Journal, 763*(2), 118.

Sullivan, R., Greeley, R., Pappalardo, R., Asphaug, E., Moore, J., Morrison, D., et al. (1996). Geology of 243 Ida. *Icarus, 120*(1), 119-139.

Sullivan, R. J., Thomas, P. C., Murchie, S. L., & Robinson, M. S. (2002). Asteroid Geology from Galileo and NEAR Shoemaker Data. *In Asteroids III* (pp. 331).

Szalay, J.R., Horányi, M., (2015). The search for electrostatically lofted grains above the Moon with the Lunar Dust Experiment. *Journal of Geophysical Research Letters*. 42, 5141. doi:10.1002/2015gl064324

Tanaka, K. L. (1997). Origin of Valles Marineris and Noctis Labyrinthus, Mars, by structurally controlled collapse and erosion of crustal materials. Paper presented at the Lunar and Planetary Science Conference.

Tanaka, K. L., & Golombek, M. P. (1989). Martian tension fractures and the formation of grabens and collapse features at Valles Marineris. Paper presented at the Lunar and Planetary Science Conference Proceedings.

Thomas, P., Veverka, J., & Duxbury, T. (1978). Origin of the grooves on Phobos. *Nature, 273*(5660), 282-284.

Thomas, P. C., Binzel, R. P., Gaffey, M. J., Storrs, A. D., Wells, E. N., & Zellner, B. H. (1997). Impact excavation on asteroid 4 Vesta: Hubble space telescope results. *Science, 277*(5331), 1492-1495. doi:10.1126/science.277.5331.1492

Thomas, P. C., Prockter, L., Robinson, M., Joseph, J., & Veverka, J. (2002). Global structure of asteroid 433 Eros. *Journal of geophysical research letter, 29*, 1408. doi:10.1029/2001gl014599

Thomas, P. C., & Robinson, M. S. (2005). Seismic resurfacing by a single impact on the asteroid 433 Eros. *Nature, 436*, 366. doi:10.1038/nature03855

Thomas, N., Barbieri, C., Keller, H. U., Lamy, P., Rickman, H., Rodrigo, R., et al. (2012). The geomorphology of (21) Lutetia: Results from the OSIRIS imaging system onboard ESA's Rosetta spacecraft. *Planetary Space Science Reviews, 66*(1), 96-124. doi:10.1016/j.pss.2011.10.003

Thornton, A. R. (2005). *A study of segregation in granular gravity driven free surface flows.* (PhD), The University of Manchester UK.

Toplis, M. J., Mizzon, H., Monnereau, M., Forni, O., McSween, H. Y., Mittlefehldt, D. W., et al. (2013). Chondritic models of 4 Vesta: Implications for geochemical and geophysical properties. *Meteoritics Planetary Science Journal, 48*(11), 2300-2315. doi:10.1111/maps.12195|

Tosi, F., Carrozzo, F. G., Raponi, A., De Sanctis, M. C., Thangjam, G., Zambon, F., et al. (2018). Mineralogy and temperature of crater Haulani on Ceres. *Meteoritics Planetary Science Journal, 53*(9), 1902-1924. doi:10.1111/maps.13078|

Turnbull, B. (2011). Scaling Laws for Melting Ice Avalanches. *Physical Review Letters*, 107, 258001. https://ui.adsabs.harvard.edu/abs/2011PhRvL.107y8001T

Varnes, D. J. (1978). *Slope Movement Types and Processes*, R. L. Schuster & R. J. Krizek (Eds.) *Transportation Research Board of the National Academy of Sciences*.

Vaillant, T., Laskar, J., Rambaux, N., & Gastineau, M. (2019). Long-term orbital and rotational motions of Ceres and Vesta. *Astronomy & Astrophysics, 622*, A95.

Vernazza, P., & Beck, P. (2016). Composition of Solar System Small Bodies. In Planetesimals: Early Differentiation and Consequences for Planets (pp. arXiv:1611.08731). Retrieved from https://ui.adsabs.harvard.edu/abs/2016arXiv161108731V. https://ui.adsabs.harvard.edu/abs/2016arXiv161108731V

Veverka, J., Thomas, P., Simonelli, D., Belton, M., Carr, M., Chapman, C., et al. (1994). Discovery of grooves on Gaspra. *Icarus, 107*(1), 72-83.

Veverka, J., Robinson, M., Thomas, P., Murchie, S., Bell, J.F., Izenberg, N., Chapman, C., Harch, A., Bell, M., Carcich, B., Cheng, A., Clark, B., Domingue, D., Dunham, D., Farquhar, R., Gaffey, M.J., Hawkins, E., Joseph, J., Kirk, R., Li, H., Lucey, P., Malin, M., Martin, P., McFadden, L., Merline, W.J., Miller, J.K., Owen, W.M., Peterson, C., Prockter, L., Warren, J., Wellnitz, D., Williams, B.G., Yeomans, D.K., (2000). NEAR at Eros: Imaging and Spectral Results. *Science*. 289, 2088-2097. doi:10.1126/science.289.5487.2088

Veverka, J., Thomas, P. C., Robinson, M., Murchie, S., Chapman, C., Bell, M., et al. (2001a). Imaging of Small-Scale Features on 433 Eros from NEAR: Evidence for a Complex Regolith. *Science, 292*(5516), 484-488. doi:10.1126/science.1058651

Vilas, F., & Gaffey, M. J. (1989). Phyllosilicate Absorption Features in Main-Belt and Outer-Belt Asteroid Reflectance Spectra. *Sceince, 246*, 790. doi:10.1126/science.246.4931.790

Walsh, K. J., Morbidelli, A., Raymond, S. N., O'brien, D., & Mandell, A. (2012). Populating the asteroid belt from two parent source regions due to the migration of giant planets—"The Grand Tack". *Meteoritics & Planetary Science Journal, 47*(12), 1941-1947. doi:10.1111/j.1945-5100.2012.01418.x

Weidenschilling, S. (2000). Formation of planetesimals and accretion of the terrestrial planets. *Sapce Science Reviews, 92*(1), 295-310. doi:doi.org/10.1023/A:1005259615299

Weidinger, J. T., & Korup, O. (2009). Frictionite as evidence for a large Late Quaternary rockslide near Kanchenjunga, Sikkim Himalayas, India—Implications for extreme events in mountain relief destruction. *Geomorphology, 103*(1), 57-65. doi:10.1016/j.geomorph.2007.10.021

Whitten, J. L., & Martin, E. S. (2019). Icelandic Pit Chains as Planetary Analogs: Using Morphologic Measurements of Pit Chains to Determine Regolith Thickness. *Journal of Geophysical Research: Planets, 124*(11), 2983-2999. doi:https://doi.org/10.1029/2019JE006099

Whitten, J. L., & Martin, E. S. (2019). Icelandic Pit Chains as Planetary Analogs: Using Morphologic Measurements of Pit Chains to Determine Regolith Thickness. *Journal of Geophysical Research: Planets, 124*(11), 2983-2999. doi:10.1029/2019JE006099

Wilhelms, D. E., John, F., & Trask, N. J. (1987). The geologic history of the Moon (2330-7102). USGE Publication Warehouse. doi:10.3133/pp1348.

Williams, D. A., O'Brien, D. P., Schenk, P. M., Denevi, B. W., Carsenty, U., Marchi, S., et al. (2014a). Lobate and flow-like features on asteroid Vesta. *Planetary and Space Science, 103*, 24. doi:10.1016/j.pss.2013.06.017

Williams, D. A., Denevi, B. W., Mittlefehldt, D. W., Mest, S. C., Schenk, P. M., Yingst, R. A., et al. (2014b). The geology of the Marcia quadrangle of asteroid Vesta: Assessing the effects of large, young craters. *Icarus, 244*, 74. doi:10.1016/j.icarus.2014.01.033

Wilson, L., & Head III, J. (2001). Giant dike swarms and related graben systems in the Tharsis province of Mars. Paper presented at the *Lunar and Planetary Science Conference.*

Wilson, L., & Head III, J. W. (2002). Tharsis-radial graben systems as the surface manifestation of plume-related dike intrusion complexes: Models and implications. *Journal of Geophysical Research: Planets, 107*(E8), 1-1-1-24. doi:10.1029/2001JE001593.

Wyrick, D., Ferrill, D. A., Morris, A. P., Colton, S. L., & Sims, D. W. (2004). Distribution, morphology, and origins of Martian pit crater chains. *Journal of Geophysical Research: Planets, 109*(E6).

Wyrick, D. Y., Buczkowski, D. L., Bleamaster, L. F., & Collins, G. C. (2010). Pit crater chains across the Solar System. Paper presented at the *Lunar and Planetary Science Conference*.

Xiao, Z., Zeng, Z., Xiao, L., Fa, W., & Huang, Q. (2010). Origin of pit chains in the floor of lunar Copernican craters. *Physics, Mechanics, Astronomy & Astrophysics, 53*(12), 2145-2159. doi:10.1007/s11433-010-4174-z.

Xiao, Z., Zeng, Z., Ding, N., & Molaro, J. (2013). Mass wasting features on the Moon – how active is the lunar surface? *Earth and Planetary Science Letters, 376*, 1-11. doi:10.1016/j.epsl.2013.06.015

Yano, H., Kubota, T., Miyamoto, H., Okada, T., Scheeres, D., Takagi, Y., Yoshida, K., Abe, M., Abe, S., Barnouin-Jha, O., Fujiwara, A., Hasegawa, S., Hashimoto, T., Ishiguro, M., Kato, M., Kawaguchi, J., Mukai, T., Saito, J., Sasaki, S., Yoshikawa, M., (2006). Touchdown of the Hayabusa Spacecraft at the Muses Sea on Itokawa. *Science*. 312, 1350. doi:10.1126/science.1126164.

Yingst, R. A., Mest, S. C., Berman, D. C., Garry, W. B., Williams, D. A., Buczkowski, D., et al. (2014). Geologic mapping of Vesta. *Planetary Space Science Reviews, 103*, 2-23. doi:10.1016/j.pss.2013.12.014

Zellner, B. H., Albrecht, R., Binzel, R. P., Gaffey, M. J., Thomas, P. C., Storrs, A. D., & Wells, E. N. (1997). Hubble Space Telescope images of asteroid 4 Vesta in 1994. *Icarus, 128*(1), 83-87. doi:10.1006/icar.1997.5735

Zuber, M. T., McSween, H. Y., Binzel, R. P., Elkins-Tanton, L. T., Konopliv, A. S., Pieters, C. M., & Smith, D. E. (2011). Origin, internal structure and evolution of 4 Vesta. *Space Science Reviews, 163*(1), 77-93. doi:10.1007/s11214-011-9806-8

APPENDICES

This appendix contains the supporting information of the manuscript presented in Chapter 6, and Chapter 7.

A. Pit chains on Ceres

The supporting material presents additional information related to the analysis of pit chains on Ceres. The section shows detail information and analysis on troughs candidates (Section **Aa**). Additionally, the morphological comparison of pit chains with laboratory experiments (under Martian environment) is carried out along (Section **Ab**) with 3-dimension view of southern part of Urvara (Section **Ac**).

a. Trough analysis

In total we mapped 284 troughs out of which we could conduct estimation of 246 within Occator, Azacca and Urvara. Troughs are distinguished from the pit chains on the basis of morphological characteristics described in Section **6.3.1**. The development of trough is the end result of fully developed pit chains, hence it is expected to have sizable difference between them. Below Table **A: 1** summarizes the estimated length and width of troughs and their scale increases from Occator down to Urvara. In general, observed troughs have U-shaped floors and often shows presence of brittle material at the wall foot (Figure **A: 1**). We suspect the downward mobility and further dispersion of steep wall material might have infilled the floor of trough.

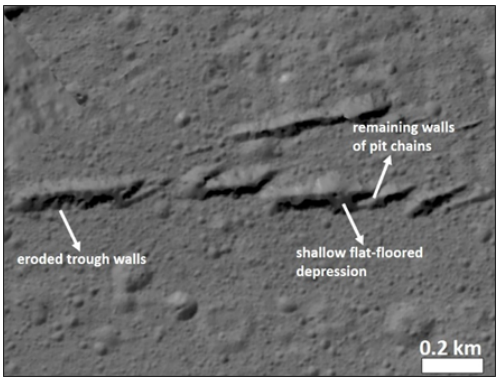

Figure A: 1 Example of fully developed trough. The shown trough is located at south of Cerealia Faculae. The rim is adjoined forming U-shaped trough. We observed remnants of eroded walls suggesting existence of pit chains. The trough has shallow floor which may be infilled with the material from the walls

Table A: 1 Dimensions of troughs observed within three craters

Craters	Latitude	Longitude	*n* of troughs utilized for estimation	Length [km]	Width [km]
Occator	19.82	239.33	230	0.2-6.2	0.04-9.4
Azacca	-6.66	218.4	9	1.54-7.8	0.7-1.2
Urvara	-45.66	249.24	7	0.9-8.8	0.1-2.4

b. Ceres and Mars

The presence of endogenic magma intrusion has been accepted as controlling theory for the formation pit chains on Mars (Mége et al., 2000; 2003; Tanaka, 1997). In general, the formation of laccolith causes the uplift of the surface material forming a dome (Schulz, 1976). However, the recent analogue experiment of magma intrusion does not produce similar feature. According to experiment result, during the initial stage of magma intrusion substantial surface uplift and dome feature was eminent within periphery of laccolith (Figure **A: 2b**). As soon as the magma flow was depleted from the reservoir, the bulge was collapsed (Figure **A: 2c**). At the end, there was no obvious evidence of dome existence and sever subsidence of the collapsed floor (elevation difference: 0.15 cm in lab represents ~3 km elevation difference on Mars) was noted (Luzzi et al., 2021). Considering the case of Ceres, similar characteristics were noted such as (i) the subdued region (Figure **A: 2a**; tagged as *'SW zone'*) located on relatively lower elevation (~0.25 km difference) suggesting the floor collapse, (ii) no obvious existence of dome-like positive relief and (iii) presence of radial to polygonal blocks extending towards center and western region of Occator. Therefore, we suspect relatively small-scale near surface laccolith formation deformed the brassica layer, produced radial chains which was then collapsed due to withdrawal of cryomagmatic material.

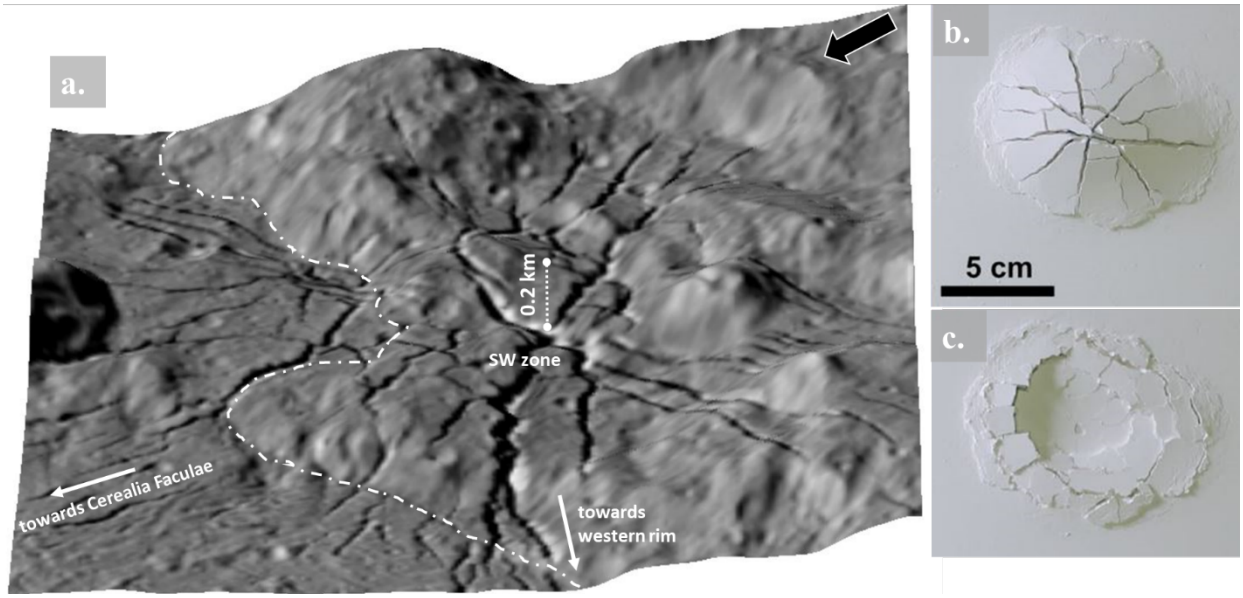

Figure A: 2 Comparison between SW zone in Occator and laboratory analogue results. (a.) The radial pattern in SW is extending towards western region and Cerealia Faculae. The white dotted-dash line highlights boundary between high and low elevated region. Some of the pit chains are extended from high relief to lower grounds in north direction of Cerealia Faculae and towards western region near the rim. LAMO DTM is overlaid (~32 m·pixel^{-1}) on the XM02 mosaic (~5 m·pixel^{-1}). For viewing purpose vertical exaggeration is a factor of 2. (b.) Initial result of first magma intrusion forming radial fractures extending from the center of the uplifted mound. (c.) Due to the withdrawal of magma intrusion, the void within subsurface laccolith cannot hold the overburden pressure causing the floor collapse. Image credit for b. & c.: Luzzi et al., 2021.

c. Urvara pit chains

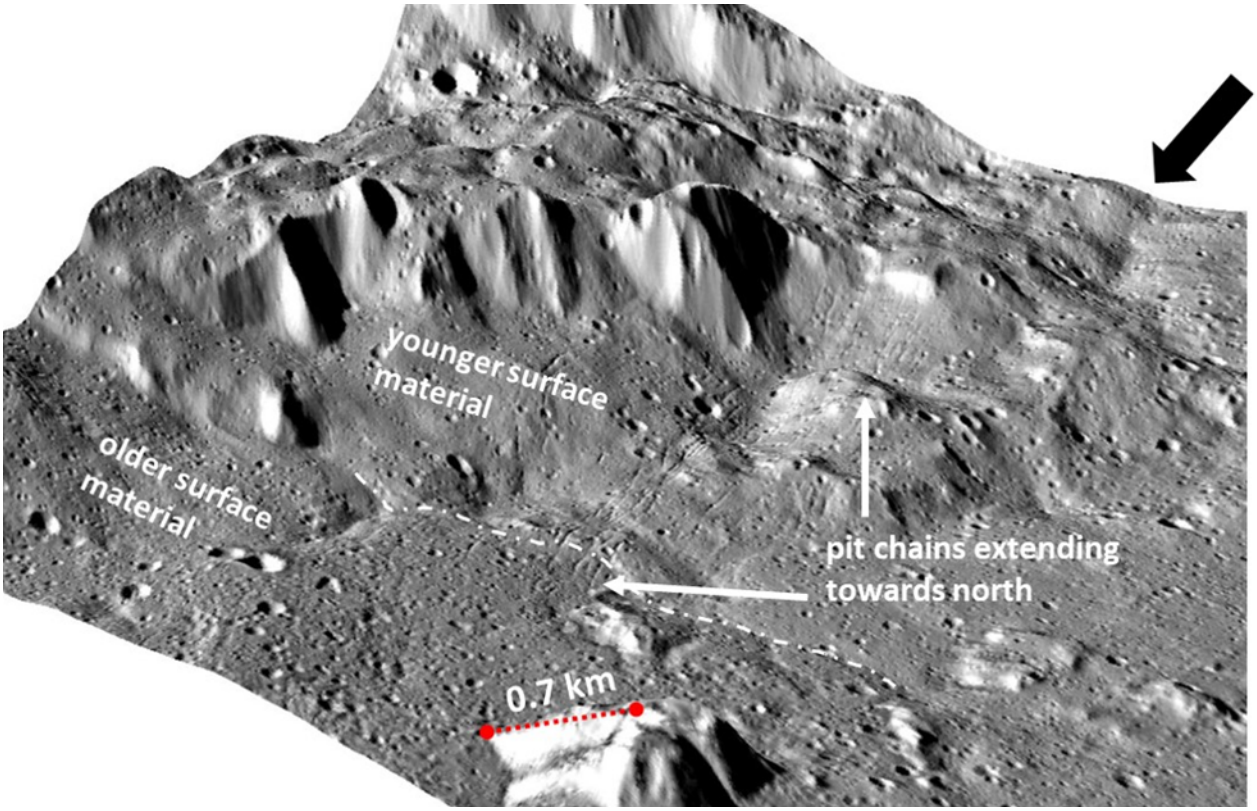

Figure A: 3 Urvara southern region in perspective view. The crater floor is divided into two plains: a southern younger zone and a northern older surface (Crown et al., 2018). Both the plains are highlighted with dotted-dash white boundary. It is suspected that southern younger material is from the rim collapse which infilled and erased existing morphological features, producing relatively smooth crater floor. A cluster of growing pit chain is extending from subdued crater walls up to older northern plains. Almost all the chain features are intermittent and very few are developed at the summit of dome. The suspected thickness of smooth material varies from tens to hundreds of meters. HAMO DTM (~135 m·pixel^{-1} resolution) is overlaid on the XM02 mosaic (~5 m·pixel^{-1}). For viewing purpose, vertical exaggeration of a factor of 2 used.

B. Landslides on Vesta and Ceres

This supporting information presents additional visual information regarding the mobility measurements of drop-out height (H), run-out length (L) and spread width (W) of identified deposits (Figure **B: 1**). Further, it includes examples of slides, slumps and flow-like movements identified on a global scale on Vesta and Ceres. For each mass movement category three examples from both planetary bodies are provided along with their geomorphological features highlighted.

a. Graphical example of *H/L* estimation

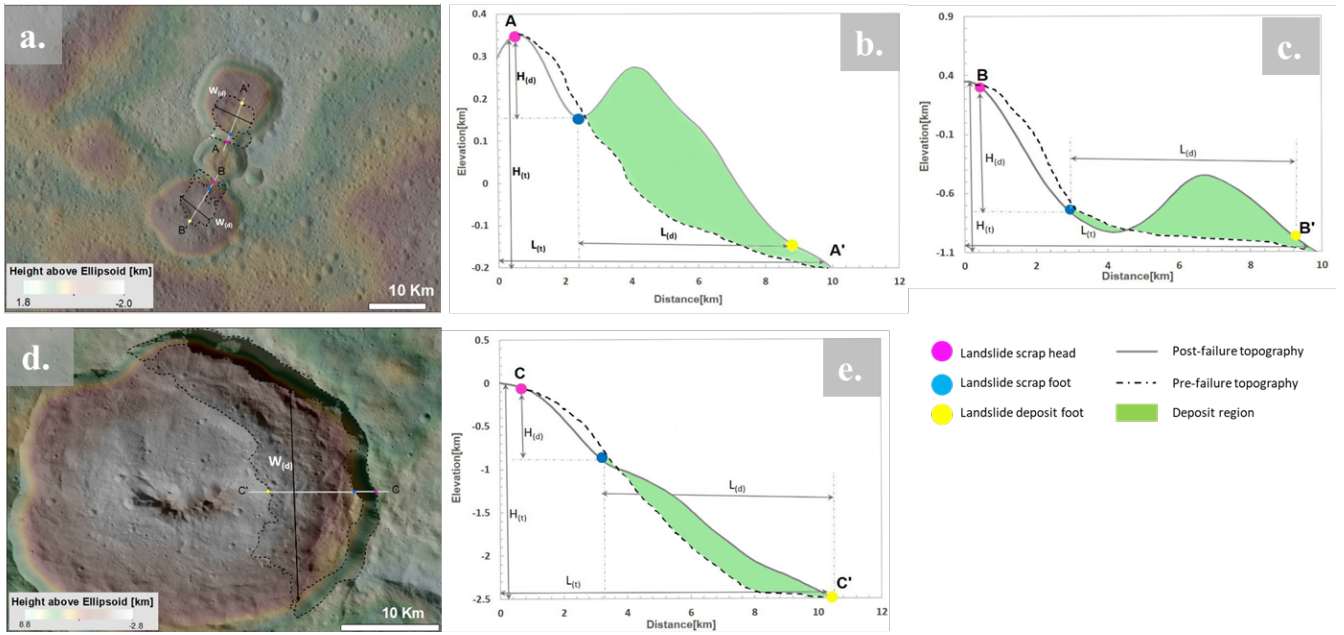

Figure B: 1 Example of *H/L* measurements. (a.) and (d.) show mass wasting examples with corresponding elevation information in (b., c.) and (d.). Both scenarios are exemplary for Vesta and Ceres. $H_{(d)}$: drop-height of deposit, $H_{(t)}$: total height of the rim, $L_{(d)}$: deposit run-out length, $L_{(t)}$: total run-out length of the deposit. To calculate the *H/L* value, we used the drop height and deposit length. For colors and lines in (a.) and (d.) please refer to the legend. In (a.) and (d.) black dashed polygons highlight the region of mass wasting (including the scarp and deposit), black line shows the width of the deposit, perpendicular to the movement direction and grey line is of topographic profile which elevation information is given in (b.), (c.) and (e.).

b. Slump

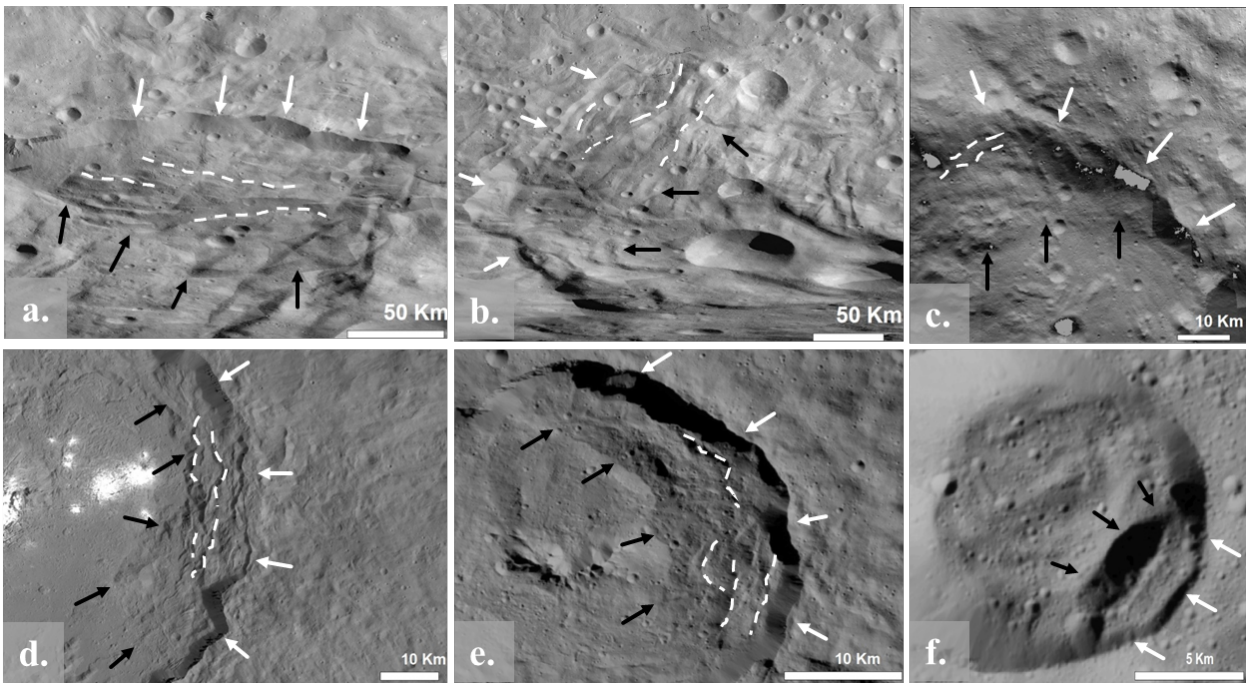

Figure B: 2 Representative examples of slumping features on Vesta (a.-c.) and on Ceres (d.-f.). Geomophorphological examples for the locations are as follows (a.) lat.: -53.82; long.: 241.63 (b.) lat.: -50.49; long.: 335.81 (c.) lat.: -69.41; long.: 75.41 (d.) lat.: 19.82; long.: 239.33 (e.) lat.: -32.35, long.: 88.38; (f.) lat.: 43.57, long.: 34.93. The white arrows indicate the main scarp from where the slumping material has been dispatched, the black arrows indicate the margins up to which the material has moved and white dash line highlight the step like patterns within slump deposit.

c. Slides

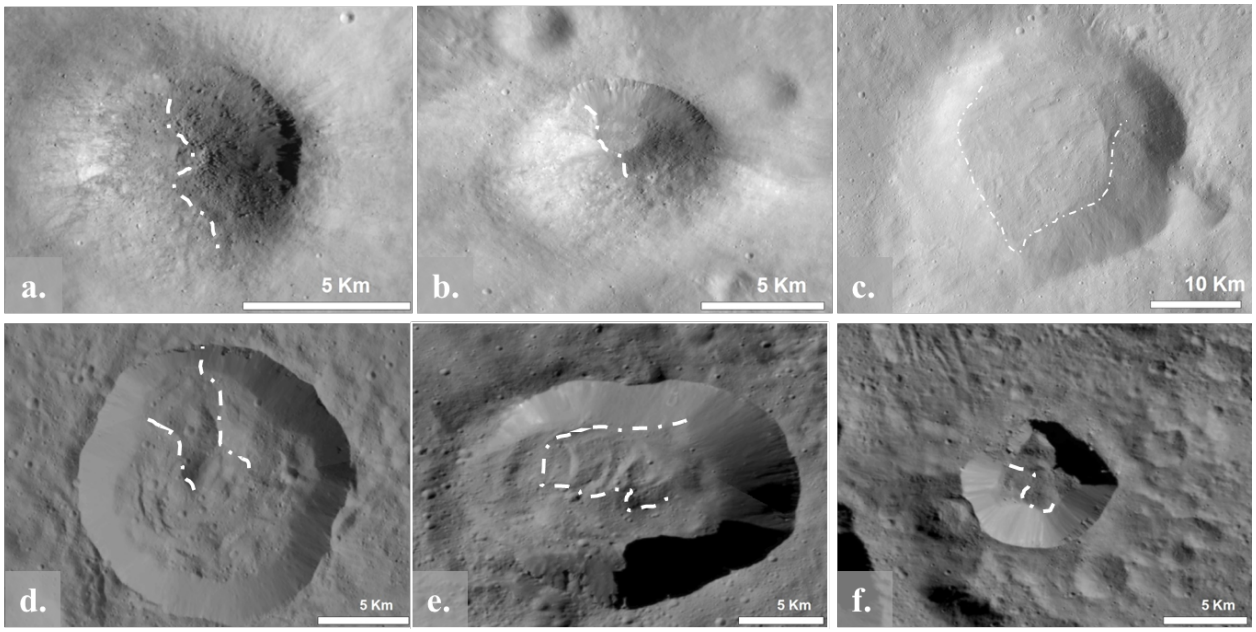

Figure B: 3 Representative examples of slide features on Vesta (a.-c.) and on Ceres (d.-f.). Geomophorphological examples for the locations are as follows (a.) lat.: -26.78; long: 10.46 (b.) lat: -34.41; long.: 107.88 (c.) lat.: -23.42; long: 191.59 (d.) lat.: -11.40; long: 119.06 (e.) lat.: 43.64; long.: 202.55 (f.) lat.: -35.64; long.: 306.96. White dashed-dotted lines indicate the region up to which the material has spread. Black dashed lines indicate transverse ridges near the terminal of deposits. Note that on Vesta sliding features can be composed of blocky material including boulders (in a., b.). On Ceres boulders are visible in f. nearby northern rim.

d. Flow-like movements

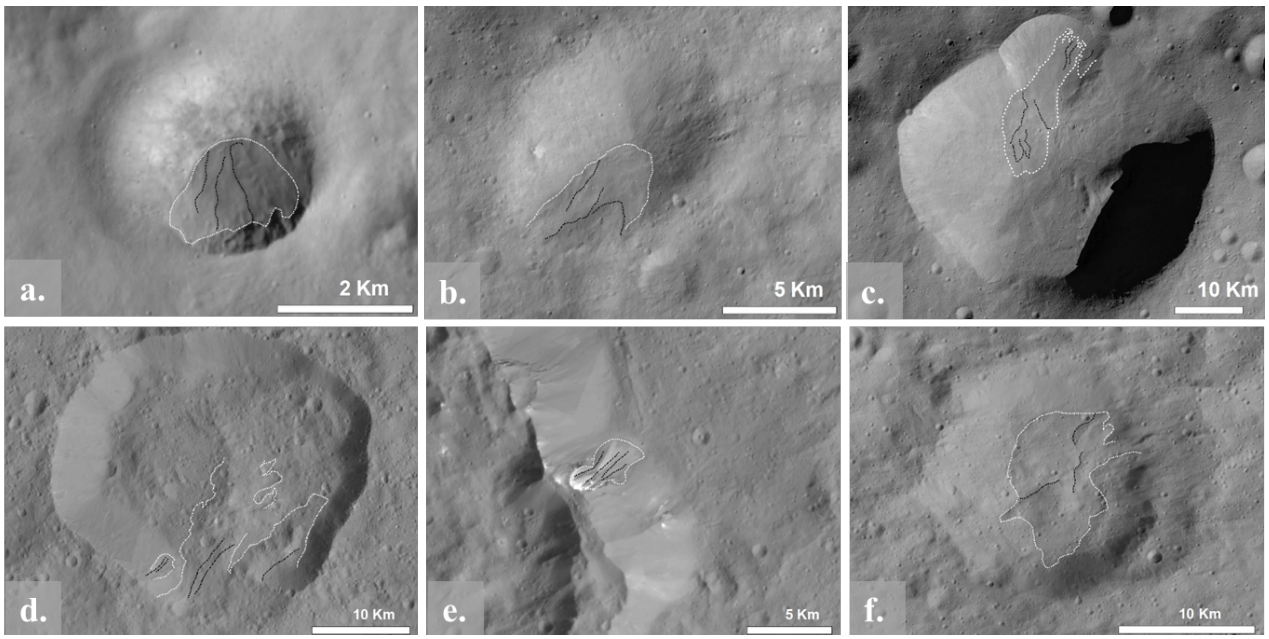

Figure B: 4 Representative examples of flow-like movements on Vesta (a.-c.) and on Ceres (d.-f.). Geomophorphological examples for the locations are as follows (a.) lat.: -9.16; long.: 329.56 (b.) lat.: -1.16; long.: 325.20 (c.) lat.: 16.74; long.: 96.76 (d.) lat: 12.71; long.: 15.09 (e.) lat.: 20.63; long.: 132.19 (f.) lat.: 27.66; long.: 118.10. The white dotted lines highlight the spreading margins of the deposits and black dotted lines denote striations.